DYNAMIC BEHAVIOUR OF RIGID-PLASTIC BEAMS

Thesis submitted in accordance with the requirements of the University of Liverpool for the degree of Doctor of Philosophy by Jianhui Liu.

September 1986

ABSTRACT

The shear and bending response and finite deflection behaviour of a clamped beam struck by a mass at any point on the span are presented in Chapter 3 and Chapter 4 of this thesis, respectively. The interaction effect of bending moment, shear force and membrane force corresponding to a cubic shaped yield surface may be obtained in a simple way by combining Chapter 3 with Chapter 4 when the effect of membrane forces is ignored in the shear sliding phases. A theoretical procedure has been developed in Chapter 5 to predict the threshold external dynamic energy for the onset of a tensile tearing failure and shear failure of a clamped beam struck by a mass at any point of the span.

A total of 260 aluminium alloy and steel beam specimens were tested with the impact points varied from the midpoint of the beam to the immediate vicinity of the supports. The experimental data are reported and discussed in Chapters 2 and 6.

It is found that the theoretical analyses which are developed in Chapters 3 to 5 give reasonable agreement with the corresponding test results.

ACKNOWLEDGEMENTS

The work described in this thesis was carried out during the period October 1983 to September 1986 in the Department of Mechanical Engineering at the University of Liverpool, under the supervision of Professor N. Jones, whose guidance was greatly appreciated.

I am indebted to Liverpool University for the award of a Research Studentship and to the Chinese Government for the tuition fees. I am extremely grateful to my wife, Mrs. Xiaoyu Li for her invaluable help. My gratitude is also extended to Mr. R. S. Birch and W. S. Jouri who provided technical assistance, and Miss E. A. Mooney for her typing of this thesis. I also wish to express my gratitude to Huazhong University of Science and Technology for a leave of absence.

CONTENTS

NOTATION

σ_0, σ_0'	static and dynamic yield stresses, respectively
ε	uniaxial strain
ε_m	limit elongation of material (or fracture elongation of material) defined in Figs. 6
k	coefficient for estimating shear failure ($0 < k \leqslant 1$)
H	thickness of beam
B	width of beam
ℓ	half span of beam
ℓ_1, ℓ_2	lengths of parts of beam defined in Fig. 9a ($\ell_1 \leqslant \ell_2$)
V_0	initial impact velocity of striker or initial impulsive velocity
x	axial coordinate
W	transverse displacement of beam
W_0	transverse displacement at the impact point or at the centre of the beam
W_1, W_2	transverse displacements at right side section and left side section of beam adjacent to the impact point, respectively
W_f or W_m	maximum permanent deformation
a_1, a_2	location of the right side and left side travelling plastic hinges defined in Figs. 10a and 43a, respectively
$\bar{m}$	mass per unit length of beam
G	mass of striker
M_0	fully plastic bending moment of cross section
M_1, M_2	bending moment on right and left sides of beam, respectively

Q_0	fully plastic transverse shear force of cross section
Q_1, Q_2	transverse shear force on right and left sides of beam, respectively
Q_{10}, Q_{20}	shear force at right side section and left side section adjacent to the impact point defined in Fig. 10b, respectively
T	time
T_ℓ	time when travelling plastic hinges reach the supports
T_f	time when displacement of beam ceases
$(\ )'$	$\frac{\partial(\ )}{\partial T}$ in Chapters 3 and 4 or $\frac{\partial(\ )}{\partial z}$ in Appendix I.
t	$\frac{M_0 T}{G V_0 \ell_1}$
$(\dot{\ })$	$\frac{\partial(\ )}{\partial t}$
z	$\frac{x}{\ell_1}$
z_1, z_2	$\frac{a_1}{\ell_1}, \frac{a_2}{\ell_1}$
r	$\frac{\ell_1}{\ell_2}$
$\bar{w}, \bar{w}_0, \bar{w}_1, \bar{w}_2$	$\frac{w}{\ell_1}, \frac{w_0}{\ell_1}, \frac{w_1}{\ell_1}, \frac{w_2}{\ell_1}$
g	$\frac{\bar{m} \ell_1}{G}$
q, q_{10}, q_{20}	$\frac{Q}{Q_0}, \frac{Q_{10}}{Q_0}, \frac{Q_{20}}{Q_0}$
u	$\frac{G V_0^2}{2 M_0}$
ν_1, ν_2	$\frac{Q_0 \ell_1}{2 M_0}, \frac{Q_0 \ell_2}{2 M_0}$
m, m_1, m_2	$\frac{M}{M_0}, \frac{M_1}{M_0}, \frac{M_2}{M_0}$

θ	rotate angular of beam
t_s	time when shear sliding ceases
t_{1s}, t_{2s}	time when shear sliding at right side and left side of the impact point ceases, respectively
t_1, t_2	time when right side and left side travelling hinges reach the right-hand and left-hand supports, respectively
t_f	time when displacement of beam ceases
$\bar{W}_{1s}, \bar{W}_{2s}$	shear sliding displacements at right side and left side of the impact point, respectively
q_{1min}	minimum value of shear force on right side of beam
q_{2max}	maximum value of shear force on left side of beam
$\bar{W}_f$	$\frac{W_f}{\ell_1}$
$\bar{z}_2$	defined by equation (3-44j)
$\dot{\bar{W}}_3$	velocity at the middle travelling plastic hinge defined in Figs. 14a, 15a, etc.
z_0	location of the middle travelling plastic hinge
N	membrane force of beam
N_0	fully plastic membrane force of cross section
n	$\frac{N}{N_0}$
$\bar{\lambda}$	$\frac{\bar{m}\ell^2 V_0^2}{M_0 H}$
λ	$\frac{GV_0^2\ell_1}{8M_0H}$ or $\frac{GV_0^2\ell_1}{2BH^2\sigma_0}$ for rectangular cross section
γ	$\frac{N_0\ell_1}{4M_0}$
$\bar{W}_{01}$	displacement at the impact point when the right side travelling plastic hinge reaches the right-hand support

$\bar{W}_{02}$	displacement at the impact point when the left side travelling hinge reaches the left-hand support
$\bar{W}_{0f}$	displacement at the impact point when the motion of beam stops
e	distance from the neutral line to the central line of beam cross section
$\bar{\ell}$	plastic tension length on the upper surface or lower surface of beam
$\varepsilon_1, \varepsilon_2$	tensile strain when W = H and W = $\frac{\ell_1}{2}$, respectively
$\Delta\ell_{1b}, \Delta\ell_{1m}$	increased length due to bending moment and membrane force with time ΔT, respectively
λ_t, λ_s	threshold external dynamic energy for the onset of tensile tearing failure and shear failure, respectively
p	load
F	force between the tup and beam
H'	initial drop height

CHAPTER 1

INTRODUCTION

The rigid-plastic method of analysis has been used widely to examine the dynamic plastic response of beams, plates, shells and other structures subject to short duration, high intensity loading [1-5], which arise in the fields of structural crashworthiness, energy absorbing systems and the safety of nuclear and chemical plant, etc. Lee and Symonds [6] first introduced this method for the analysis of beams under transverse impact. The techniques of analysis have also been incorporated successfully into many design procedures and design codes [7]. Ignoring material elasticity leads to significant simplifications for many problems and appears reasonable, provided the external dynamic energy is at least 3 times larger than the maximum amount of strain energy which can be absorbed by a structure in a wholly elastic manner [8].

Parkes examined the dynamic response of a cantilever beam struck by a mass at its tip [9] and a clamped beam struck at any point on the span [10]. If the striker mass is large compared with the beam mass, the moving hinge phases are very short and most of the external energy is absorbed by plastic deformation during the final phase of motion in which the beam rotates about the supports. Reference [9] also found that the permanent deformation is larger when the gravitational effects are considered. Reference [10] ignored some cases in which the bending moments near the impact point may be larger than the

plastic limit moment. These cases are considered in Chapters 3 and 4 of this thesis. The dynamic response of a beam struck by a mass were also discussed in references [11-15].

There are many other investigations into the dynamic plastic response of beams with different loads and different support conditions [1-5]. Two approaches can be used to analyse the dynamic response of beam; one uses linear and angular momentum equations and the other employs the equilibrium equations of a beam element. In most cases, velocities and permanent deformations are more easily obtained from the first approach, but the static admissibility conditions can be more easily checked from the second approach since velocities and permanent deformations are obtained from consideration of the shear force and bending moment expressions.

Many papers have been published on the dynamic plastic response of circular plates and annular plates [1-5], but few investigations have been conducted on square and rectangular plates [16-20]. Conroy [21] discussed the dynamic response of a simply supported circular plate subjected to a dynamic circular loading in the central region and obtained permanent deformations of plate when the radial bending moment M_r is not negative in the plate. In other words, the external loading P is less than some certain value P_2. Her work can be extended for loads with $P>P_2$ but a numerical method is required to solve the differential equations. Some researchers also have examined plates struck by a mass [20,22,23].

The dynamic response of shells [1-5], beam grillages [24,25] and various energy absorbing devices [5,26] have also been studied.

Although ignoring material elasticity is a significant simplification, analytical solutions for many problems of dynamic response are still very difficult due to the complexity of this class of problems. Some numerical procedures [1-5] and some approximate methods [1-5] have been developed.

Transverse shear forces according to classical (bending only) theories are initially infinite at the boundaries of loaded zones in rigid-plastic beams, plates and shells subjected to an impulsive load [13,27,28] or struck by a mass [9-15]. However, by way of contrast, the transverse shear forces for a statically loaded structure are finite because they must be in equilibrium with the total external transverse load. This situation is responsible for the observation that transverse shear forces exercise a more important influence on the response of dynamically loaded rigid-plastic structures than on the static-plastic behaviour. Indeed beams, for example, may fail due to excessive transverse shear forces at the supports when subjected to impulsive velocities [29] or at the impact point when struck by a mass [30]. Transverse shear effects play an important role in a structure which responds with higher modal deformation forms [31] and dominate the behaviour of ideal fibre-reinforced beams [32,33] and plates [34].

The transverse shear effects of beams struck by a

mass were examined by Symonds [13], Jones and Oliveira [14] and Oliveira [15], etc. Nonaka [12] analysed some interaction effects in a rigid-plastic beam which carried a concentrated mass at the centre subjected to an impulsive load. His results can be directly used for a clamped beam with a uniform cross-section struck by a mass if the concentrated mass m_o and impulse I are replaced by the mass and its impulse at the instant when it contacts the beam, respectively. It is doubtful whether the static admissibility conditions of shear force were correctly checked for the second and third phases of motion, since inertial forces and transverse shear forces shown in Fig. 6-8 of reference [12] for second and third phases of motion are not correct [55].

Plastic yield criteria of beams relating the generalized stresses M and Q were examined by several authors [35] with local or non-local theories. It is shown in Reference [35] that a number of local and non-local theories give similar curves in $M/M_o - Q/Q_o$ plane for beams with rectangular cross-sections, but there is a large difference between the local and non-local theories for beams with I shaped cross-sections. The non-local interaction curves for I-beams are non-convex if the maximum shear force Q_o is based on the total cross-sectional area. Oliveira and Jones [35] suggested that one may select whichever $M/M_o - Q/Q_o$ curve for beams with rectangular cross-section is the most convenient and a suitable compromise from an engineering viewpoint between local and non-local theories might be achieved for I-beams when using a local theory with a maximum transverse

shear force based only on the web area.

Recently, Jones further developed bound methods with transverse shear effects in the dynamic plastic behaviour of structures [36]. He shows that the simple bound theorems provide excellent estimates of the response durations and permanent displacements of impulsively loaded beams, circular plates and cylindrical shells when transverse shear effects are important and also provide exact agreement with the behaviour of all the dynamic ideal fibre-reinforced structures examined.

Jones and Oliveira examined the influence of rotatory inertia of dynamical loading beams [14,15], circular plates [37] and cylindrical shells [28]. Their results show that the influence of rotatory inertia is less important than some other influences and can be neglected from an engineering viewpoint for most practical cases.

Bending only solutions or shear and bending solutions give good agreement with some experimental results [9-12], provided the maximum permanent deformation is small compared with the thickness or there is no axial restraint on the supports. As previously stated, ignoring material elasticity is reasonable when the external dynamic energy is very large compared with the energy that could be stored elastically in the structure. On the other hand, large external energy will cause large deformation then the influence of finite deflections, or geometry changes, can introduce in-plane or membrane forces which might exercise an important influence on the structural behaviour. This phenomenon

is particularly important for axially restrained beams and cylindrical shells and for circular and rectangular plates subjected to transverse dynamic loads [7].

Symonds and Mentel [38] examined finite deformations of simply supported and clamped beams subjected to an impulsive loading. They assumed that the normal force N on a cross-section is a constant along the beam, provided the deformation is small compared to the half span of a beam. This assumption is also used in some other examinations of finite deformation effects [12,39,40]. References [17,38] show that membrane forces play a dominant role when maximum permanent deformations are larger than the corresponding thickness of clamped beams and plates or larger than half thickness of simply supported beams and plates at least for beams governed by the parabolic interaction yield curve ('exact' yield curve) shown in Fig. 1 of reference [40]. Solutions relating to approximative square yield curves, shown in Fig. 1 of reference [40], do bound the 'exact' solutions [17,39,40] and also give good agreements with experimental results [17,40].

Nonaka [12] developed a one degree-of-freedom theoretical solution for beams struck by a mass, in which the first phase of motion with travelling hinges is ignored unless the mass is small. The one degree-of-freedom theoretical method leads to some simplifications and enabled him to more easily analyse the influence of both finite deflection and strain rate sensitivity. Some approximate theoretical procedures have been developed to estimate the dynamic plastic behaviour of

arbitrary shaped plates (including beams as a special case) [17] and shells [41] undergo finite displacements and have provided reasonable estimates of the available experimental results. Oliveira [20] has examined the influence of finite deflections of beams and rectangular plates struck by a falling mass at the centre using a mode approximation technique and an energy approach. A large difference might occur between these two methods when the mass of a falling body is much larger than the mass of the whole beam.

Another important complicating factor on the dynamic behaviour of structures is the dependence of yield stress on strain rate. Hot rolled mild steel, for example, is notoriously strain rate sensitive since the yield stress is double the corresponding 'static' yield stress at a strain rate of 40 s^{-1}, approximately [42]. On the other hand, aluminium 6061T6 is essentially strain rate insensitive at usual strain rates encountered in practice [42]. Therefore, the correction for the dependence of yield stress on strain rate should be made in the rigid-plastic theory for those strain rate sensitive materials.

Parkes [9,10] and Ezra [11] have catered for the influence of strain rate in their examinations on cantilever, clamped and simply supported beams struck by a mass. The 'dynamic' yield moment with the influence of strain rate sensitivity is obtained by multiplying the corresponding 'static' yield moment with a constant dynamic factor based on a mean rate of strain [10] at the outer fibre during the entire response. This

procedure is not strictly correct since the strain rate may vary through the depth of a beam [40] and even the strain rate at the outer fibre would change with time. Nevertheless, Symonds [42] demonstrated that a mode approximation with stationary plastic hinges of finite width could be used to develop an accurate theoretical procedure for viscoplastic cantilever beams and indeed Parkes [9,10] and Ezra [11] obtained good agreement between their theories and experimental work. Nonaka [12] assumed that plastic strains occur uniformly in triangular regions in the middle and at the supports for his one degree-of-freedom model of a beam. The Cowper-Symonds empirical expression

$$\frac{\sigma_o'}{\sigma_o} = 1 + \left(\frac{\dot{\varepsilon}}{D}\right)^{1/P} \qquad (1)$$

is employed for considering the influence of strain rate sensitivity, where σ_o' and σ_o are 'dynamic' and 'static' yield stresses, $\dot{\varepsilon}$ is the uniaxial strain rate and D and P are material constants. Equation (1) is also used in many other papers [26,39,40,42,43]. Many simplifications have been developed over the years [1-5] since material strain rate effects are a highly non-linear phenomenon which make theoretical analyses difficult.

The influence of material strain hardening has also been examined [1-5]. It appears that material strain hardening is not important for moderate strains or permanent transverse deflections of beams unless a material hardens significantly [7].

Symonds [42] and Perrone [43] suggested that a product-type mathematical representation could be used to describe a strain

hardening rate-sensitive material; thus

$$\frac{\sigma_c'}{\sigma_o} = f(\dot{\varepsilon})g(\varepsilon) \qquad (2)$$

where $f(\dot{\varepsilon})$ and $g(\varepsilon)$ are strain-rate sensitive and strain hardening relations, respectively.

Menkes and Opat [44] conducted an experimental investigation into dynamic plastic response and failure of fully clamped aluminium beams subjected to uniformly distributed velocities over the entire span. On the basis of these experimental tests, Menkes and Opat classified the three failure modes for fully clamped beams with rectangular cross-section as

Mode 1: large inelastic deformation of the entire beam;

Mode 2: tearing (tensile failure) of the beam at the supports;

Mode 3: transverse shear failure of the beam material at the supports.

It appears likely that similar types of failure modes exist for other kinds of structures and for beams with different loadings, but the failure locations may be different.

As previously stated, large inelastic deformation as a feature of dynamic behaviour has been widely discussed for a variety of structures subjected to different dynamic loads. However, most theoretical methods and most numerical schemes for the dynamic behaviour of structures use a material with an unlimited ductility. Clearly, this is a severe idealisation for

real materials [44]. Few papers [29] have been published on the dynamic behaviour of structures made from a material with a limited elongation. The reason may be that it is difficult to correctly estimate the maximum strain in structures. Jones [29] used his former work [17] with Nonaka's assumption [12], in which plastic strains occur in triangular regions in the middle and at the supports, to estimate the threshold velocity for the onset of mode 2 behaviour of clamped beams subjected to uniformly distributed loading. He obtained reasonable agreement between his theoretical predictions and Menkes and Opat's experimental tests.

Instead of an 'exact' amount of shear sliding which cause shear failure in structures, a vague criterion $W_s = kH$, where W_s is the magnitude of shear sliding, H is thickness of beam and plate and $0 < k \leqslant 1$, is usually given [15,28,37,45] because of paucity of both theoretical and experimental work. It appears nobody has examined the value of the coefficient k for a particular problem. Nevertheless, Jones [29] did obtain a reasonable prediction on shear failure with k=1 compared to Menkes and Opat's experimental tests [44].

It shows that Mode 3 failures can occur at lower velocities than Mode 2 failures when ratio $2\ell/H$ is rather small [29]. It also appears that this phenomenon may occur with higher rupture strains materials. Indeed, equations (15) and (24) in reference [29] predict that Mode 3 failure precede Mode 2 failures provided the limit elongation

$$\varepsilon_m > \frac{1}{3} - \frac{3}{8}\left(\frac{H}{\ell}\right)^2 - \left(\frac{1}{\sqrt{6}} - \frac{1}{2}\right)\left(\frac{H}{\ell}\right). \qquad (3)$$

It is clear that Mode 2 failures cannot occur if Mode 3 failures precede Mode 2 failures since transverse shear forces are dominant in the early stages of motion when the displacement of a structure remains small (small strain) [45].

It should be noted from Menkes and Opat's experimental tests [44] that some of the beams exhibited failures which involved both the tearing and shearing modes when subjected to the impulsive velocities which lay between the smallest velocities required for the Mode 2 and Mode 3 failures [29]. The mixed failure of tearing and shearing also might occur before the pure tearing failure (Mode 2) and the pure shear failure (Mode 3) for some dynamic problems since the reduced cross-sectional area after shear sliding would have a reduced bending moment carrying capacity.

A lot of experimental work has been done with the development of theoretical analysis on dynamic behaviour of structures [1-5]. Duwez, Clark and Bohnenblust [46] performed some experimental tests on simply supported long beams deformed due to an impact load at the centre. Parkes [10] reported some experimental test results on clamped beams without axial restraints struck transversely by a 'heavy' (4 lb.) or a 'light' (0.005 lb.) mass at 3 different points. Nonaka [12] conducted some tests on beams with and without axial constraints (fully clamped and clamped) subjected to an impulsive load on the centre concentrated mass. Most of these tests on beams yielding large

plastic strain, but no broken specimens were reported in these papers [46,10,12]. Parkes [9] and Bodner and Symonds [8] conducted some experimental tests on cantilever beams struck by a falling mass at the tip. Some researchers who were interested in deformations and perforation velocities of plates struck by a mass in the middle have performed experimental tests [47]. Beams and plates subjected to impulsive loading are also an important topic and many experimental tests have been done over the past years [8,40,44,48-52]. Most experimental tests give good agreement with corresponding available theoretical analyses [8-12,48-52, etc.], therefore, some theoretical analyses are further confirmed by experimental tests.

Jones [53] examined the scaling of geometrically similar structures subjected to large dynamic loads which cause an inelastic material response. It appears that the wholly ductile dynamic response (without fracture) of small-scale models and full-scale prototypes might conform to the principle of elementary geometrical scaling. However, the well known size effect associated with material strain rate sensitivity should be taken into account and might be exacerbated in structures with load-deflection relationships which decrease after an initial peak value. It shows from experimental tests [54] that geometrical scaling is not satisfied when tearing, cutting or ductile-brittle transitions occur during a structure response.

In this thesis, the main attention is focussed on the dynamic response of clamped beams struck by a mass at any

point of the beam span. This is an important practical problem which arises in a number of industries including nuclear, offshore and naval architecture. This subject might be particularly useful for ship collision since the longitudinal members of ships can sometimes be idealised as beams.

The theoretical work of Parkes [10], Symonds [13], Nonaka [12] and Oliveira [15] has been further developed and extended to shear and bending response and finite deflection of clamped beam struck by a mass at any point of its span. Furthermore, the phenomenon of beam failures is discussed. A series of experimental tests (total over 250 specimens) has been conducted with external dynamic energies which cause not only large inelastic response but also fracture of the beam specimens.

CHAPTER 2

EXPERIMENTAL DETAILS

2.1 Introduction

A wide range of experimental facilities are available for dynamic testing in the Department of Mechanical Engineering at Liverpool University [56]. The drop hammer rig can achieve impact velocities up to 12 ms^{-1}. The tup mass can be varied between 5 kg and 210 kg and electronic instruments are available to record the test results which can be processed using various microcomputer facilities.

The experimental tests on clamped beams which were struck by a falling mass, which are reported in this thesis, were conducted on the above drop hammer rig. A total of 260 specimens of aluminium alloy and steel was tested.

2.2 General Arrangement and Equipment

The experimental arrangement is shown in Fig. 1. The drop hammer has a variable drop height up to a maximum value of 9 m. The tup impact face area is 130 mm x 150 mm with a typical maximum specimen height of 300 mm. The width between the two vertical guides is 130 mm. There are ten levels of height designed in this rig. The tup can also be stopped at any intermediate height by pushing the stop button switch and the corresponding height can be read from a ruler which is attached

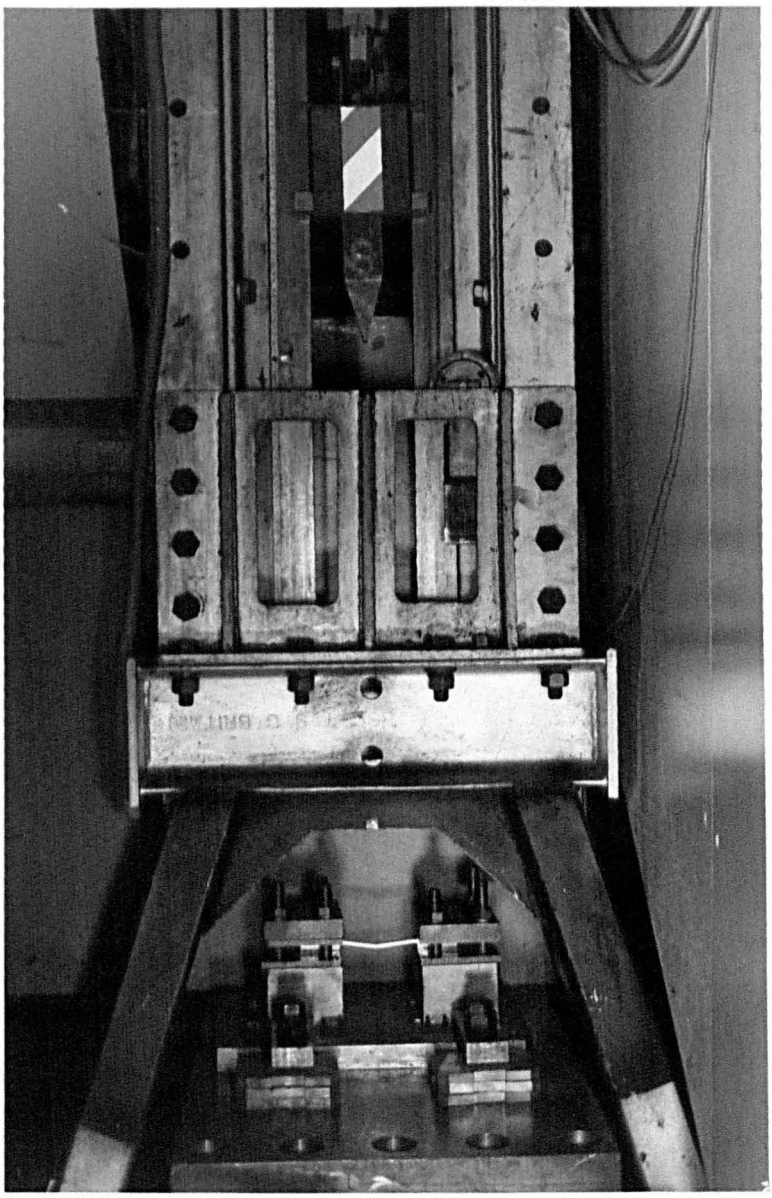

FIG. 1 The experimental arrangement.

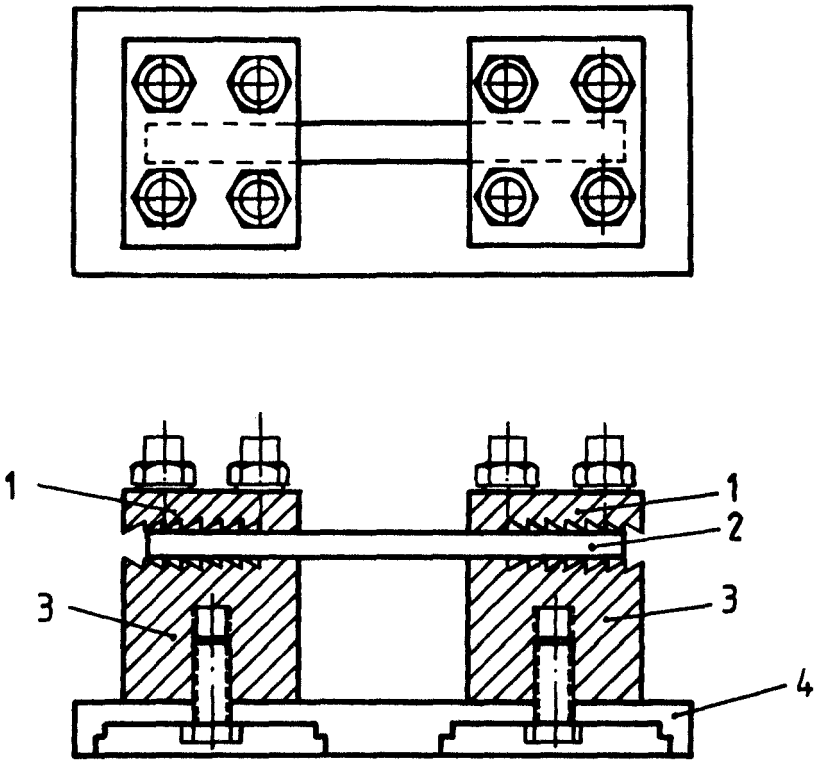

FIG. 2 The specimen holder. 1) steel cover plates, 2) beam specimen, 3) steel stocks, and 4) thick steel plates.

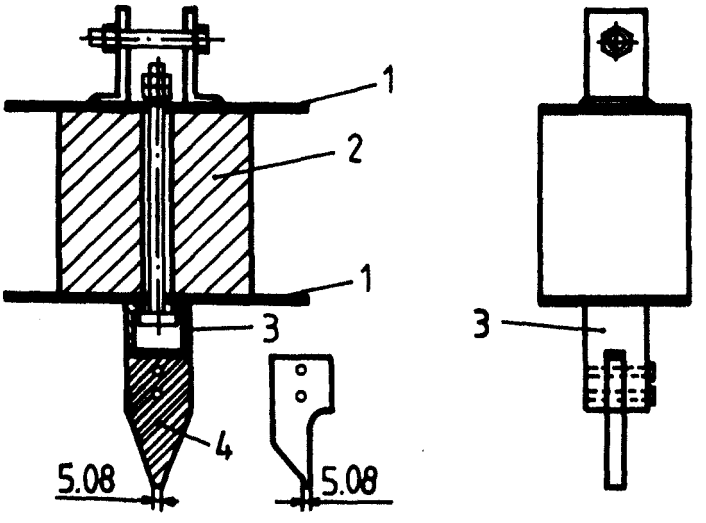

FIG. 3 The tup. 1) steel sheets, 2) wood stock, 3) tup head connector, and 4) tup heads.

to the rig. A remote control for the motion of the tup is available. A specimen was held in a specimen holder, shown in Fig. 2, which was designed to obtain the desired clamped boundary conditions. The specimen holder consists of three parts; two covers, two steel blocks and one thick steel plate. There are four holes in each cover and each steel block. Four bolts hold the specimen. In order to prevent sliding between specimen and the holder, the covers and steel blocks were serrated. The connection between the thick steel plate and the steel blocks are made through four elongated holes in the plate and two tapped holes in each block. The elongated holes in the plate allow the span between two blocks to be varied. The specimen holder was placed on the platform of the base of the rig and was tightened by bolts to prevent it from moving during the test. The tup shown in Fig. 3 consists of two pieces of steel sheet, a wood block, a tup head connector and tup head. The steel sheet provides a guide for the tup. The tup head connector enables the tup head to be changed. Two tup heads were designed to satisfy the experimental requirement that a tup can strike at any point of the beam. The width of impact area is 5.08 mm shown in Fig. 3. The total weight of the tup is 5 kg for both designs.

2.3 Specimen and Material Properties

The two kinds of specimens shown in Fig. 4 were designed in order to assess the effectiveness of clamping. The large end specimen shown in Fig. 4a models an ideally clamped beam since the deformation at the supports would be negligible in comparison with that in the beam sections. However, the flat end specimen

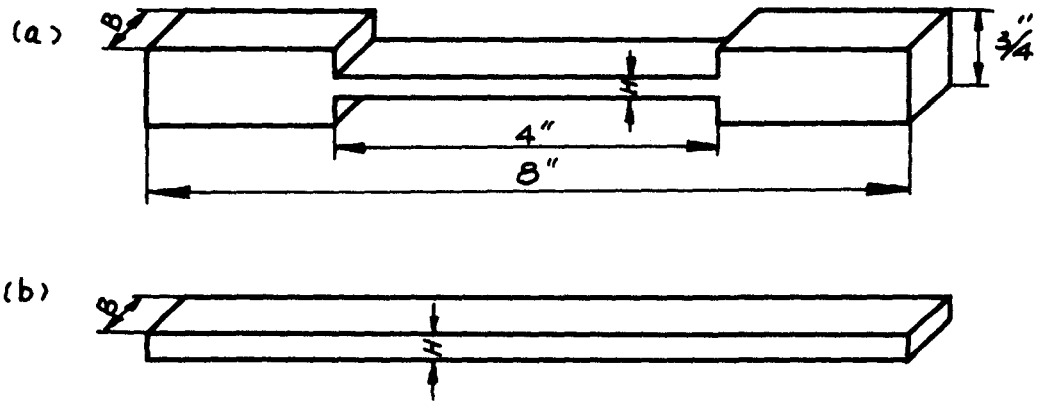

FIG. 4 Beam specimens. (a) large end specimen; (b) flat end specimen.

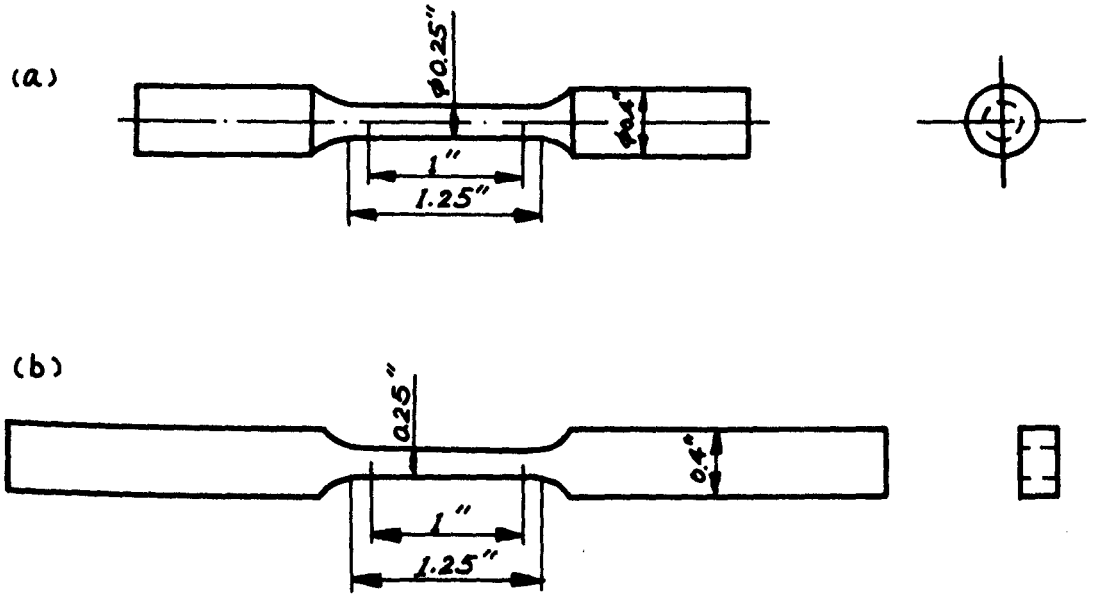

FIG. 5 Static tension test specimens. (a) standard 0.25 in-round specimen; (b) standard 0.25 in-wide plate specimen.

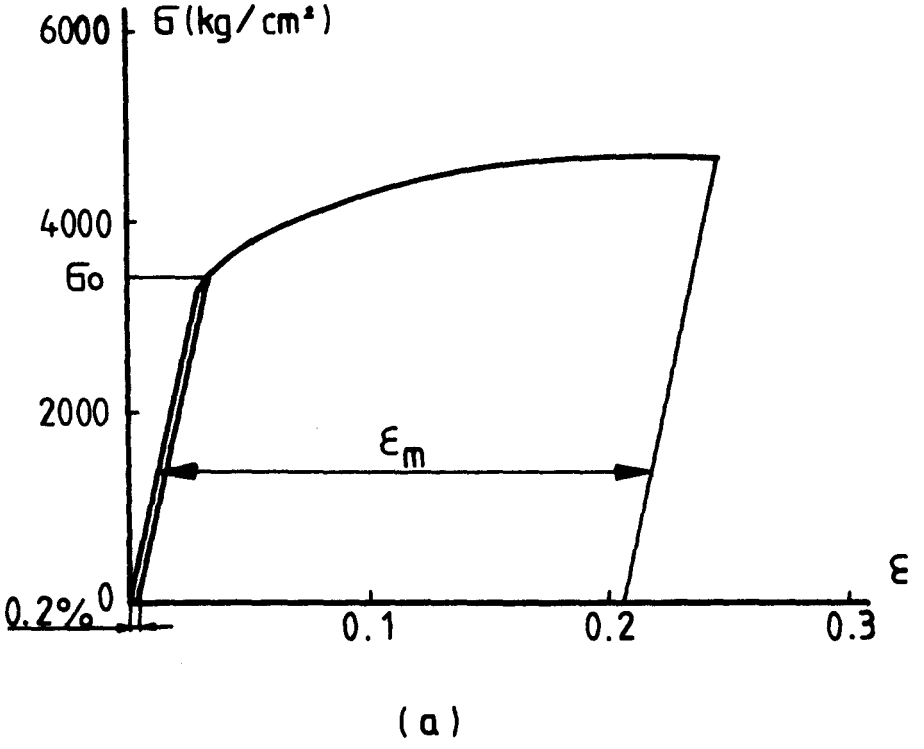

(a)

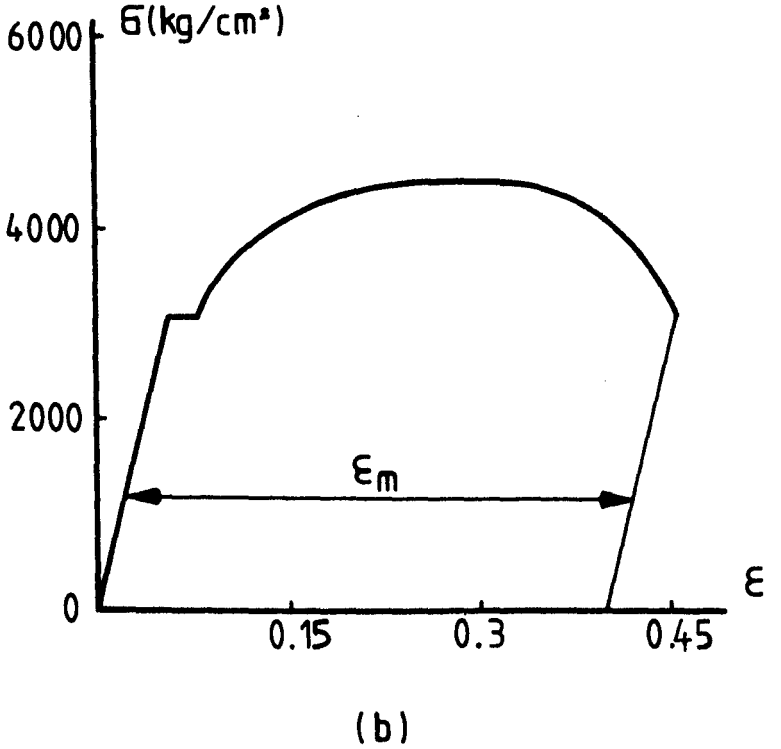

(b)

FIG. 6 Stress-strain curves. (a) aluminium alloy; (b) steel.

Type of Beam	Material	Thickness (in)	Specimen Number	Original Material	Yield Stress N/mm^2	UTS N/mm^2	Elongation ε_m (%)
Large End Beams	Aluminium Alloy	0.15	AI 1-7	Thick Aluminium Plate	181 and 183; average 182	321 and 315; average 318	Approximate 19%
		0.2	AII 1-12				
		0.25	AIII 1-6				
		0.3	AIV 1-6				
	Steel	0.15	SI 1-6	Thick Steel Plate	321 and 327; average 324	504 and 498; average 501	Approximate 31%
		0.2	SII 1-12				
		0.25	SIII 1-6				
		0.3	SIV 1-6				
Flat End Beams	Aluminium Alloy	0.15	AℓI 1-25	Aluminium Bar 1	348 and 361; average 354.5	466 and 485; average 475.5	Approximate 19%
		0.2	AℓII 1-25				
		0.25	AℓIII 1-25				
		0.3	AℓIV 1-25	Aluminium Bar 2	average from 4 tests 412	average from tests 553	Approximate 15%
	Steel	0.15	STI 1-25	Steel Bar 1	335 and 339; average 337	461 and 468; average 464.5	Approximate 39%
		0.2	STII 1-25				
		0.25	STIII 1-25	Steel Bar 2	229,301 303 and 304; average 302	444,447 443.5 and 441; average 444	Approximate 40%
		0.3	STIV 1-25				

Table 1. The specimen details and some mechanical properties of materials.

is more easily machined and saves machining time. A total of 60 large end specimens and 200 flat end specimens of aluminium alloy and steel were tested.

The beam width was chosen as B=0.4 in (10.16 mm). The span of beam is 4 in (101.6 mm) (the total length of specimen is 8 in (203.2 mm)). The thickness of beam was varied from 0.15 in (3.81 mm) to 0.3 in (7.62 mm). The dimensions and other details of the specimens were shown in Table 1.

The large end specimen was made from one aluminium alloy thick plate BS1470-HS15 and one steel thick plate BS4360-43A, while the flat end specimen was made from similar materials but from different bar materials. At least two static tensile tests were conducted for each piece of material in order to obtain the mechanical properties. The static tensile tests were carried out on the Dartec testing machine, which is installed in the Department of Mechanical Engineering at Liverpool University, at average strain rates of approximately 5×10^{-4} s^{-1}. The tensile test specimens are standard 0.25-in-round specimen made from thick plates and bars with original thickness of 0.5 in and standard 0.25-in-wide plate specimen made from bars with original thickness of 0.3 in. The static tensile test specimens are shown in Fig. 5. The typical stress-strain curves for aluminium alloy and steel are shown in Fig. 6. Some of the test data are given in Table 1. It shows that the test results are different with different bars. A distinct yield flow region appeared in the stress-strain curves of the steel, while aluminium alloy strain hardens. The yield stresses are obtained from the average values

of stress in the yield flow region of the stress-strain curves for steel, while for aluminium alloy the yield stresses are obtained from stress-strain curves using offset method with 0.2% strain.

Six large end specimens and six flat end specimens of aluminium alloy and steel were statically loaded in the Dartec testing machine until failure. The load was applied at different points of the beam and the locations from the right-hand support are ℓ_1 = 0.5 in, 1.0 in and 2 in. The load-deflection curves are shown in Figs. 7 and 8. These show that when a beam broke at the support a clear unloading region appears in the load-deflection curves, while for a beam which breaks at the loading point the load continuously increased with the increase of the deflection of the beam until the beam failed and suddenly dropped to zero. It appears that tensile tearing governed the failures of the aluminium alloy beams and the large end steel beams except for the case when the load was applied at the centre of the beam or ℓ_1 = 2 in, while for flat end steel beams and the large end steel beam with ℓ_1 = 2 in, the failure was governed by shear*. Strain gauges were used on the flat end beams at some special points, e.g. at supports and the loading point. However, only limited data were recorded at each support and loading point since the strains at these points increased sharply and exceeded the allowable strain for the strain gauges when the maximum deformation of beam was small in comparison with that corresponding to beam failure.

---

* The failure of these beams is further discussed in Chapter 7.

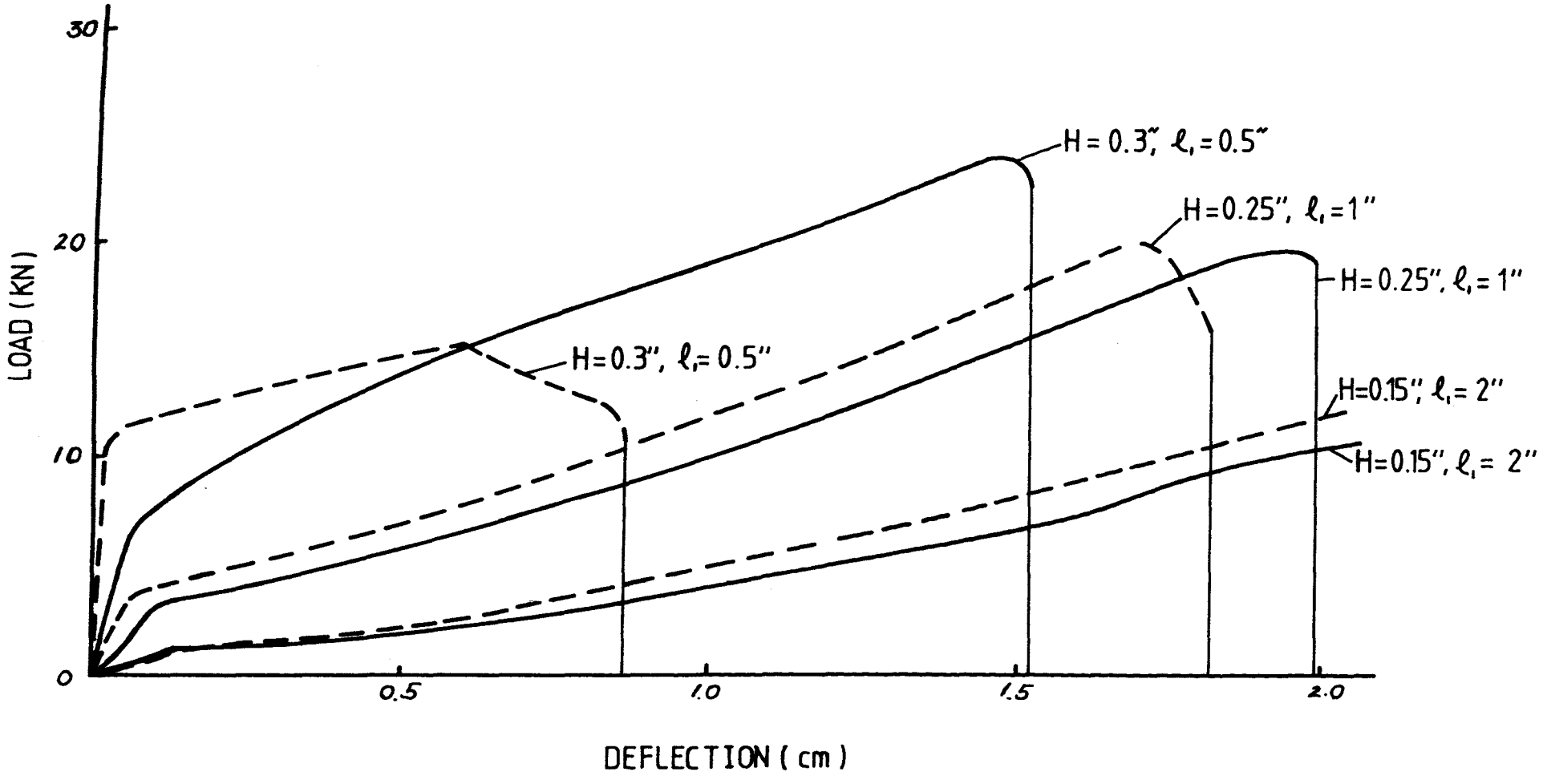

FIG. 7 Load-deflection curves for static test on steel beams.

—— flat end specimen; ---- large end specimen.

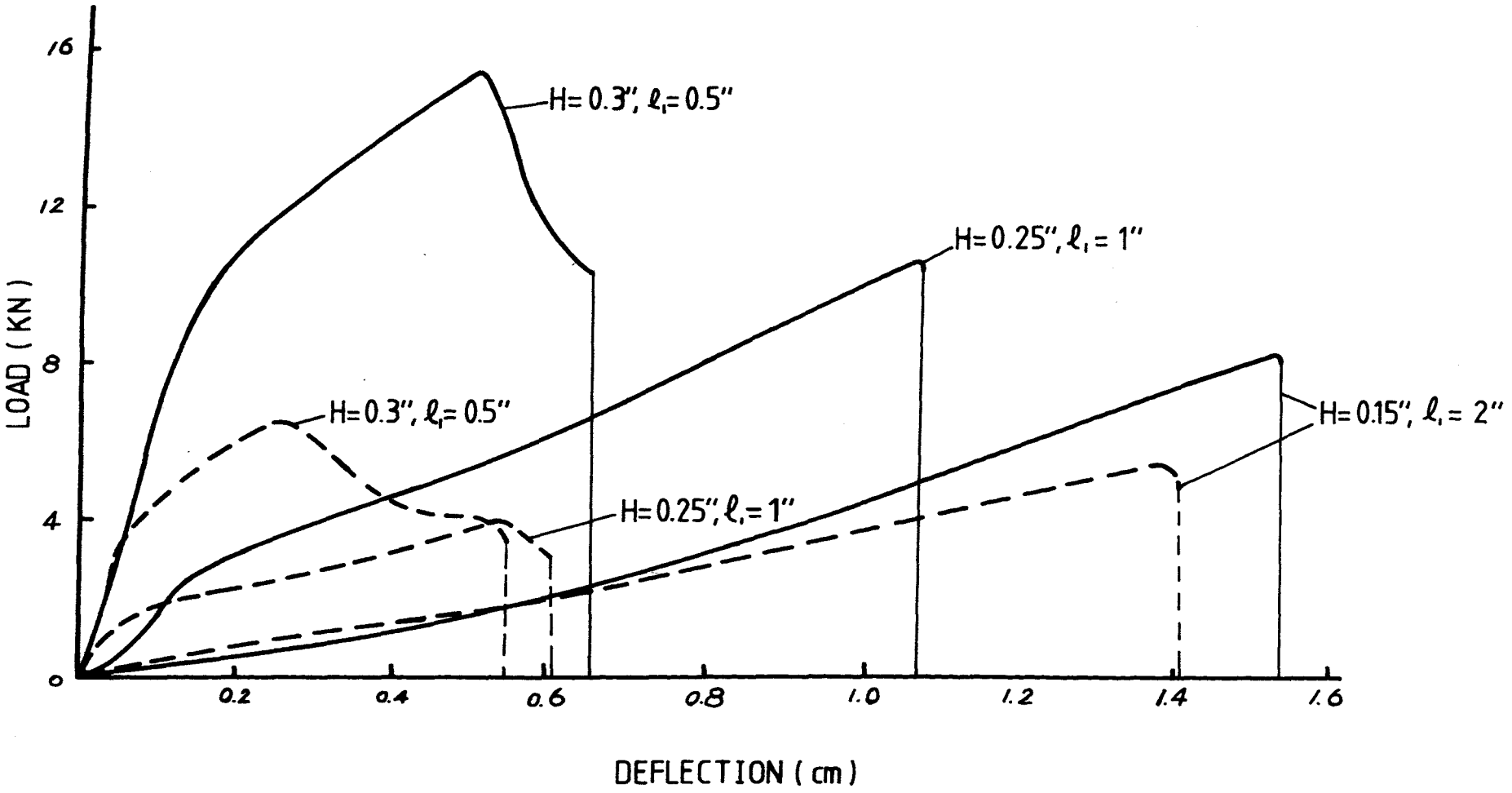

FIG. 8 Load-deflection curves for static test on aluminium alloy beams.

—— flat end specimen; ---- large end specimen.

2.4 Loading

The impact loads were applied on beams by the tup, or the striker. The large end beams with thickness of H = 0.15 in, 0.25 in, and 0.3 in were struck at the centre, while the beam with H = 0.2 in were impacted at both ℓ_1 = 2 in (the centre of beam) and ℓ_1= 0.5 in. The flat end beams with H = 0.15 in, 0.2 in, 0.25 in and 0.3 in were struck at ℓ_1 = 2 in, 1.5 in, 1 in, 0.5 in and 0.25 in. ℓ_1 = 2 in means that the impact point is at the centre of beam, while the impact point ℓ_1 = 0.25 in is very close to the support. The tests with the same specimen materials, same impact point and same thickness of beam were classified as a type of test. There were 50 types of test and at least four specimens of each type were tested with different impact velocities. A failure (cracked or broken beam) was sought for each type of test in order to examine the phenomenon of beam failures so that the range of external kinetic energy is from very low value (a small plastic deformation of beam) to a very high value (a cracked or broken beam was obtained).

2.5 Data Recording Instruments*

A considerable amount of experimental data, e.g. the velocity-time history at the impact point, motion of beam and strain-time relations at some particular points, were recorded during the tests.

---

* More details of these instruments are given in reference [56].

The velocity of the tup or the velocity at impact point of beam (it is assumed that the tup is in contact with beam) was measured using a laser doppler velocimeter. Transient signals were stored using DL1080 transient recorders. The DL1080 transient signals recorder is a digital instrument designed to capture single shot, low repetition and other analogue signals. After capture the signals are presented for continuous display on a CRO, analogue readout to an XY plotter, digital storage on an internal cassette recorder or digital output to an external peripheral processor. There are two independent signal inputs in the DL1080 transient recorder so that it is possible to sample both inputs simultaneously. The test data were recorded on mini-cassettes. On playback to DL1080 transient recorder's memory this data can be re-examined.

A Hadland high speed camera was used to take some films during tests. Different speeds with $\frac{1}{4}$ or half frame exposures were used. These films clearly show the motion of the beam and the tup during the entire response.

Several specimens with strain gauges at some particular points were tested. The strain gauge signals were amplified using 1 MHz Tektronic differential amplifiers. The amplified strain gauge signals were again stored in DL1080 transient recorders and were recorded on mini-cassettes with digital storage.

2.6 Data Processing, Analysis and Measurement of Deformation of Beam

Transient data from recorders can be processed on a BBC microcomputer. A series of software for signal processing is now available in the Department of Mechanical Engineering [56]. A 'Readit' programme transfers the data from the DL1080 transient recorder to the microcomputer's memory, and a 'Try8' programme is used to process this data. After filtering of frequency, the displacement of the beam at the impact point is obtained by integrating the velocity signal which was recorded during the test, and the acceleration or load is obtained by differentiating the velocity signal. The filtered velocity signal, displacement of beam at the impact point and load curves can be obtained by a printer or an XY plotter. The 'Readit', 'Try8' and some other programmes were written by Birch [56]. The strain gauge signals were processed with some similar software.

The films taken with the Hadland high speed camera can be analysed on a Vanguard motion analyser. The deformation profiles can be measured in this analyser and the data can be directly printed on a printer or transferred into a BBC microcomputer.

Most of the permanent deformation profiles were measured after the test by a travelling microscope. This microscope can travel in both x and y directions and measures the profile with an accuracy of 0.01 mm.

CHAPTER 3

SHEAR AND BENDING RESPONSE OF A RIGID-PLASTIC CLAMPED BEAM STRUCK BY A MASS AT ANY POINT OF ITS SPAN

3.1 Introduction

The dynamic response of a rigid-plastic clamped beam due to an impact loading has been examined by several authors [10,13-15]. The extension of this work to examine the shear and bending response of a clamped beam struck by a mass at any point of its span, shown in Fig. 9a, is presented in this Chapter.

The beam, which is of length $\ell_1 + \ell_2 = 2\ell$ and mass $\bar{m}$ per unit length, is struck at a point ℓ_1 from the right-hand support by a mass G shown in Fig. 9a. After impact the striker G is supposed to remain in contact with the beam. Therefore, the striker and the struck point of beam have the same velocity throughout the entire response and the initial velocity is Vo at the instant of first contact. The square yield curve relating to shear forces and bending moments shown in Fig. 9c, which is used in references [13-15], is employed herein. Without loss of generality ℓ_1 can be taken as less than ℓ_2.

A general velocity profile shown in Fig. 10a is assumed and is suitable for most cases discussed in Section 3.3. The corresponding equations of motion and the shear force and bending moment distributions are given in Section 3.2. The basic equations for the cases ignored by Parkes [10], in which a travelling bending

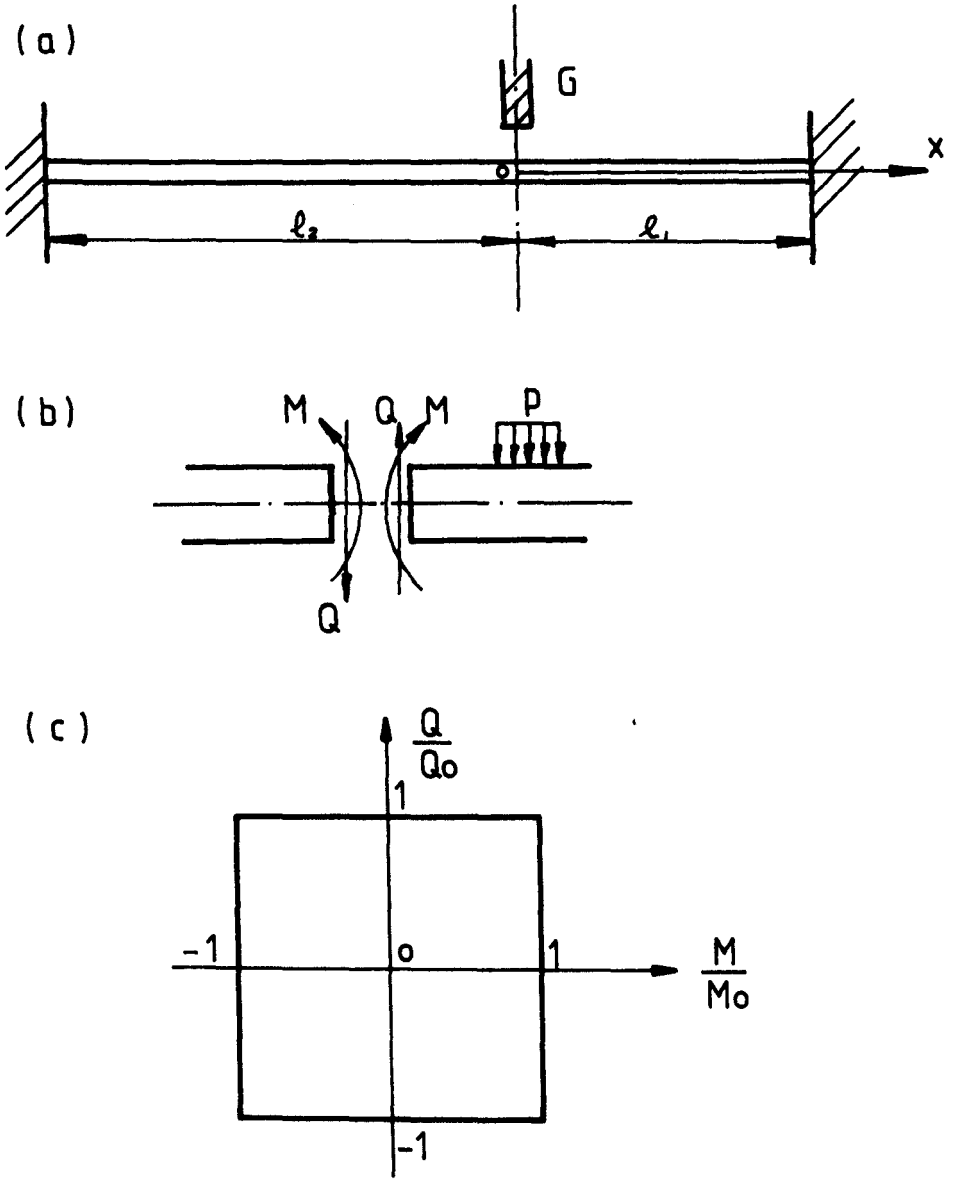

FIG. 9 Clamped beam struck by a body. (a) clamped beam, (b) definitions of bending moment M, shear force Q and load p, (c) yield curve.

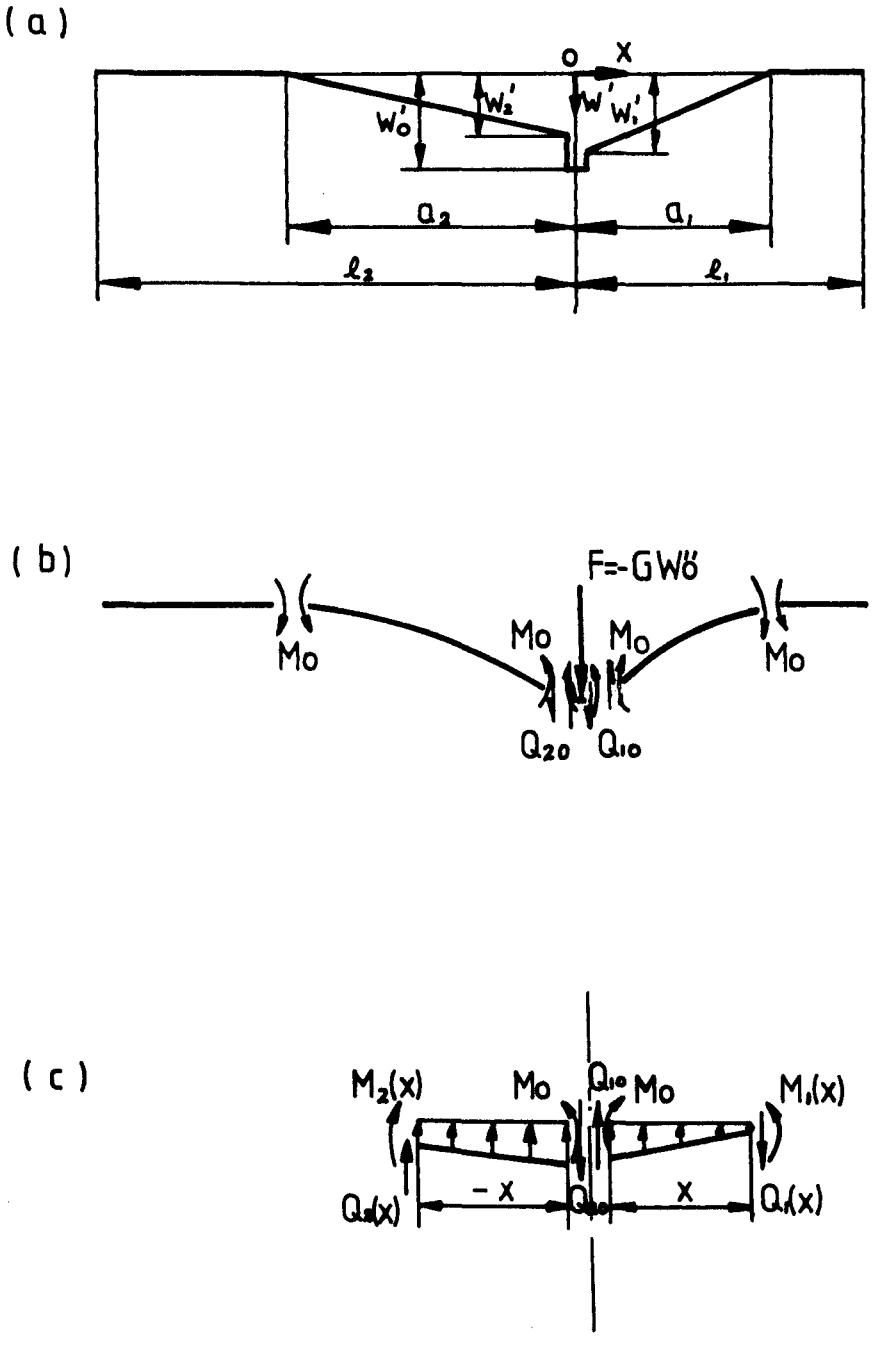

FIG. 10 Motion of beam with two plastic travelling hinges, one stationary plastic hinge and two shear hinges.

plastic hinge develops at $z = z_0$ or $z = -z_0$ instead of a stationary hinge at $z = 0$, are given in Section 3.3. Some continuity and discontinuity conditions of motion at plastic bending and shear hinges are also displayed in Section 3.2. Theoretical analysis and the method of solution are given in Sections 3.3 and 3.4, respectively, while discussion is given in Section 3.5. A detailed examination of the static admissibility of the solution is given in Appendix I.

3.2 Basic Equations

If a beam struck by a mass G yields a stationary bending hinge at the impact point x=0 with two travelling bending hinges at $x=a_1$ and $x=-a_2$ which move towards the supports, and two parts of beam between the stationary hinge and travelling hinges rotating as rigid bodies about the travelling hinges while the rest of beam beyond the travelling hinges is undeformed, the velocity profile shown in Fig. 10a can be written as

$$W'(x) = \begin{cases} 0 & -\ell_2 \leq x \leq -a_2^- \\ W_2'(1 + \frac{x}{a_2}) & -a_2^+ \leq x \leq 0^- \\ W_1'(1 - \frac{x}{a_1}) & 0^+ \leq x \leq a_1^- \\ 0 & a_1^+ \leq x \leq \ell_1 \end{cases} \tag{3-1}$$

where W_1' and W_2' are the velocities on the right and the left side adjacent to the impact point, respectively, i.e. $W' = W_2'$ at $x = 0^-$ and $W' = W_1'$ at $x=0^+$, $(\ )' = \frac{\partial(\ )}{\partial T}$ and T is time.

The linear and angular momentum equations for $0^+ \leqslant x \leqslant a_1^-$ and $-a_2^- \leqslant x \leqslant 0^-$ are

$$\frac{1}{3}\bar{m}\,a_1^2 W_1'' + \frac{1}{6}\bar{m}\,W_1' a_1' a_1 = -2M_0 - Q_{10}a_1 \tag{3-2a}$$

$$\frac{1}{2}\bar{m}\,(W_1'' a_1 + W_1' a_1') = -Q_{10} \tag{3-2b}$$

$$\frac{1}{3}\bar{m}\,a_2^2 W_2'' + \frac{1}{6}\bar{m}\,W_2' a_2' a_2 = -2M_0 + Q_{20}a_2 \tag{3-2c}$$

$$\frac{1}{2}\bar{m}\,(W_2'' a_2 + W_2' a_2') = Q_{20} \tag{3-2d}$$

since the shear force is equal to zero in a plastic hinge in Timoshenko beam if rotatory inertia is neglected and no external concentrated forces act on the plastic hinge and where Q_{10} and Q_{20} are defined in Fig. 10b.

The transverse equilibrium condition at the impact point gives

$$-Q_{10} + Q_{20} = -GW_0'' \tag{3-2e}$$

where W_0' is the velocity at the impact point $x = 0$.

According to transverse equilibrium condition and moment equilibrium condition with $M = -M_0$ at the supports of the beam, the shear force and bending moment distributions shown in Fig. 10c can be expressed as

$$Q_2(x) = 0$$
$$M_2(x) = -M_0 \qquad \text{for } -\ell_2 \leqslant x \leqslant -a_2 \tag{3-3a,b}$$

$$Q_2(x) = Q_{20} + \frac{\bar{m}}{2}[W_2'' + W''(x)]x$$
$$M_2(x) = M_0 + Q_{20}x + \frac{1}{3}\bar{m}\,W_2''x^2 + \frac{1}{6}\bar{m}\,W''(x)x^2 \qquad \text{for } -a_2 \leqslant x \leqslant 0 \tag{3-3c,d}$$

$$Q_1(x) = Q_{10} + \frac{1}{2}\bar{m}\,[W_1'' + W''(x)]x$$
$$M_1(x) = M_0 + Q_{10}x + \frac{1}{3}\bar{m}\,W_1''x^2 + \frac{1}{6}\bar{m}\,W''(x)x^2 \qquad \text{for } 0 \leqslant x \leqslant a_1 \tag{3-3e,f}$$

$$Q_1(x) = 0$$
$$M_1(x) = -M_0 \qquad \text{for } a_1 \leqslant x \leqslant \ell_1 \tag{3-3g,h}$$

since the shear forces and bending moments are continuous in whole beam [13,14] and where subscripts 1 and 2 indicate shear forces and bending moments on the right side and left side of impact point, respectively.

Equations (3-1), (3-2), (3-3) and (3-4) can be rewritten to

$$\dot{\bar{W}}(z) = \begin{cases} 0 & -\frac{1}{r} \leqslant z \leqslant -z_2^- \\ \dot{\bar{W}}_2(1 + \frac{z}{z_2}) & -z_2^+ \leqslant z \leqslant 0^- \\ \dot{\bar{W}}_1(1 - \frac{z}{z_1}) & 0^+ \leqslant z \leqslant z_1^- \\ 0 & z_1^+ \leqslant z \leqslant 1 \end{cases} \tag{3-4}$$

$$z_1 \ddot{\bar{W}}_1 + \frac{1}{2}\dot{\bar{W}}_1 \dot{z}_1 = -\frac{12u(1 + q_{10}\nu_1 z_1)}{g z_1} \tag{3-5a}$$

$$z_1 \ddot{\bar{W}}_1 + \dot{\bar{W}}_1 \dot{z}_1 = -8u\nu_1 q_{10}/g \tag{3-5b}$$

$$z_2 \ddot{\bar{W}}_2 + \frac{1}{2}\dot{\bar{W}}_2 \dot{z}_2 = -12u(1 - q_{20}\nu_1 z_2)/g z_2 \tag{3-5c}$$

$$z_2 \ddot{\bar{W}}_2 + \dot{\bar{W}}_2 \dot{z}_2 = 8u\nu_1 q_{20}/g \tag{3-5d}$$

$$-q_{10} + q_{20} = -\ddot{\bar{W}}_0/4u\nu_1 \tag{3-5e}$$

and

$$q_2(z) = 0$$
$$m_2(z) = -1 \qquad \text{for } -\frac{1}{r} \leqslant z \leqslant -z_2 \tag{3-6a,b}$$

$$q_2(z) = q_{20} + \frac{g}{8u\nu_1}[\ddot{\bar{W}}_2 + \ddot{\bar{W}}(z)]z$$
$$m_2(z) = 1 + 2q_{20}\nu_1 z + \frac{g}{6u}\ddot{\bar{W}}_2 z^2 + \frac{1}{12}\frac{g}{u}\ddot{\bar{W}}(z)z^2 \qquad \text{for } -z_2 \leqslant z \leqslant 0 \tag{3-6c,d}$$

$$q_1(z) = q_{10} + \frac{g}{8u\nu_1}[\ddot{\bar{W}}_1 + \ddot{\bar{W}}(z)]z$$
$$m_1(z) = 1 + 2q_{10}\nu_1 z + \frac{g}{6u}\ddot{\bar{W}}_1 z^2 + \frac{1}{12}\frac{g}{u}\ddot{\bar{W}}(z)z^2 \qquad \text{for } 0 \leqslant z \leqslant z_1 \tag{3-6e,f}$$

$$q_1(z) = 0$$
$$m_1(z) = -1 \qquad \text{for } z_1 \leqslant z \leqslant 1 \tag{3-6g,h}$$

where

$$z = \frac{x}{\ell_1},\ z_1 = \frac{a_1}{\ell_1},\ z_2 = \frac{a_2}{\ell_1},\ \nu_1 = \frac{Q_0\ell_1}{2M_0},\ u = \frac{GV_0^2}{2M_0},\ \bar{W} = W/\ell_1,$$

$$g = \frac{\bar{m}\ell_1}{G},\ q = \frac{Q}{Q_0},\ r = \frac{\ell_1}{\ell_2},\ m = \frac{M}{M_0},\ (\dot{}) = \frac{\partial(\ )}{\partial t} \text{ and } t = \frac{M_0}{GV_0\ell_1}T \qquad (3\text{-}7a\text{-}\ell)$$

At a bending plastic hinge $z = z^*$, the deformation and velocity must be continuous, the acceleration may be discontinuous but it must satisfy [6]

$$[\ddot{\bar{W}}]\Big|_{z=z^*} = \dot{z}^*[\dot{\theta}]\Big|_{z=z^*} \qquad (3\text{-}8a)$$

where [X] means the difference in X on either side of an interface travelling with a velocity $\dot{z}^*$, $\dot{\theta}$ is angular velocity at $z=z^*$ and it is positive according to clockwise rotation. At a shear hinge $Z=\bar{z}$, the velocity may be discontinuous to accommodate any transverse shear sliding, but the geometrical condition

$$[\frac{\partial \dot{\bar{W}}}{\partial z}]\Big|_{z=\bar{z}} = 0 \qquad (3\text{-}8b)$$

must be satisfied and the shear forces and bending moments are continuous at both bending hinges and shear hinges [13,14].

3.3 Theoretical Analysis

The general procedure for generating a theoretical solution for the dynamic response of beams is that a kinematically admissible velocity field which describes the motion of a beam is first postulated. The solution usually can then be obtained from the equilibrium equations or the linear and angular momentum equations with the initial and boundary conditions. Finally the static admissibility conditions have to be checked to examine if any

yield violations have occurred during entire response. If both kinematic and static admissibility conditions are satisfied, then the solution obtained is 'exact'.

It is evident from references [13-15] that the velocity profile of beam may change with the magnitude of $v_1 = \frac{Q_0 \ell_1}{2M_0}$ or $v_2 = \frac{Q_0 \ell_2}{2M_0}$ when the finite shear strength of materials is considered.

3.3.1 Case I, $v_2 \geq v_1 > 3$

A) Phase 1, shear sliding $0 \leq t < t_s$

After impact, shear sliding appears at both sides of the impact point ($z=0^-$ and $z=0^+$) where the shear forces $q_{10} = -q_{20} = -1$ and a stationary plastic hinge is formed at $z=0$ while two stationary plastic hinges appear at $z=z_1$ and $z=-z_2$. The velocity profile shown in Fig. 11a is the same as equation (3-4). Equations (3-4) and (3-5) with $q_{10} = -q_{20} = -1$ and $\dot{z}_1 = \dot{z}_2 = 0$ give

$$z_1^2 \ddot{\bar{W}}_1 = -\frac{12u\,(1 - v_1 z_1)}{g} \tag{3-9a}$$

$$z_1 \ddot{\bar{W}}_1 = 8uv_1/g \tag{3-9b}$$

$$z_2^2 \ddot{\bar{W}}_2 = -\frac{12u\,(1 - v_1 z_2)}{g} \tag{3-9c}$$

$$z_2 \ddot{\bar{W}}_2 = 8uv_1/g \tag{3-9d}$$

and

$$\ddot{\bar{W}}_0 = -8uv_1 \tag{3-9e}$$

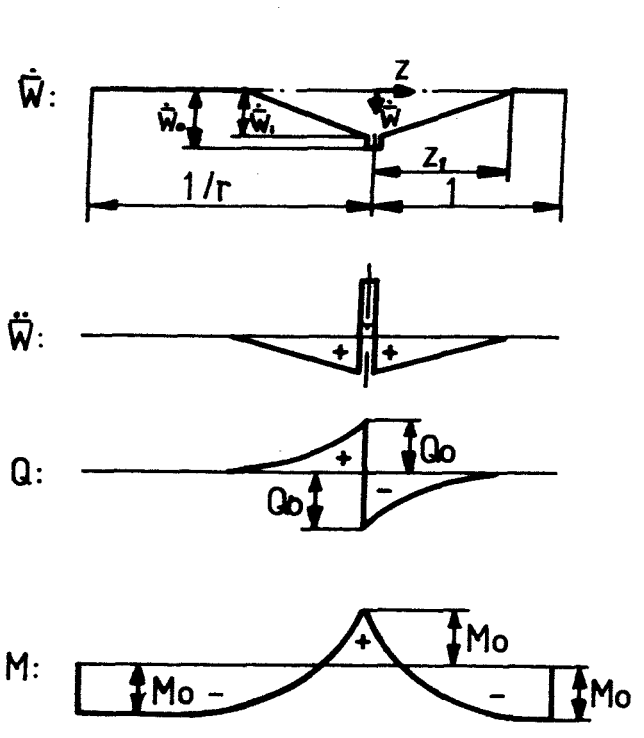

FIG. 11 First phase of motion for $\nu_2 \geq \nu_1 > 3$ (case I).

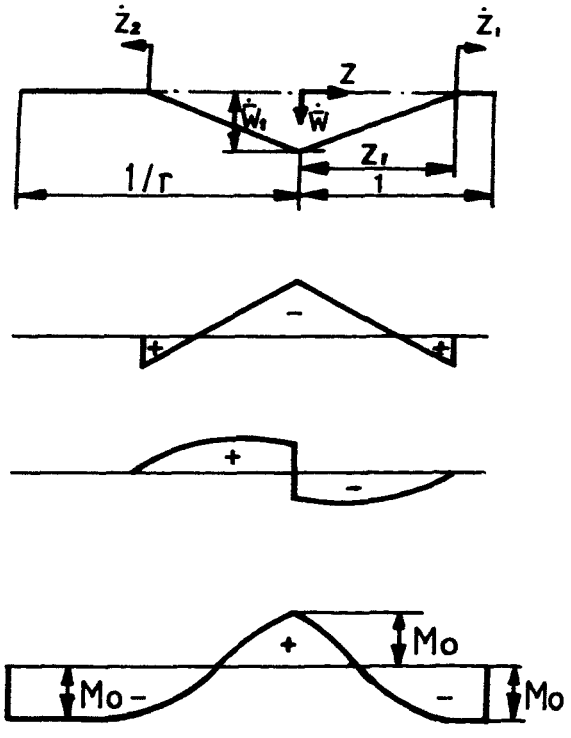

FIG. 12 Second phase of motion for case I.

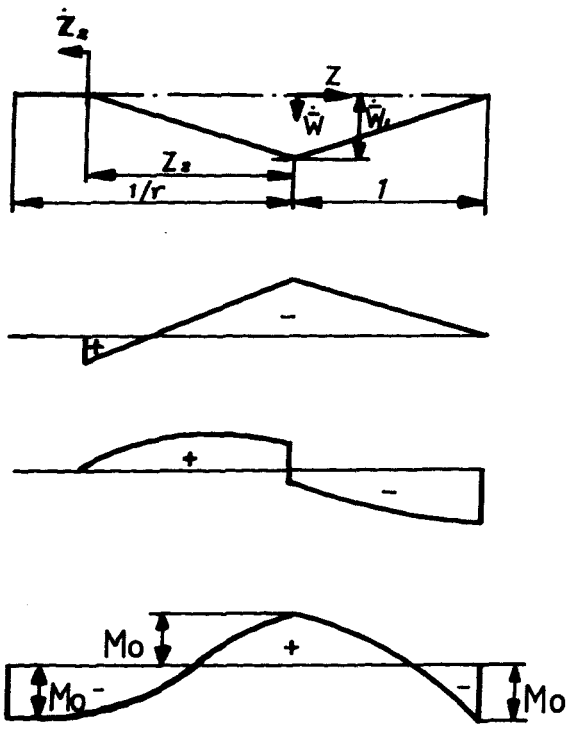

FIG. 13 Third phase of motion for case I.

Integrating equations (3-9) with respect to time t, we obtain

$$z_1 = \frac{3}{\nu_1}\,,\quad \dot{\bar{W}}_1 = \frac{8}{3}\frac{\nu_1^2 u}{g}\,t,\quad \dot{\bar{W}}_0 = 2u - 8u\nu_1 t$$
$$\bar{W}_1 = \frac{4}{3}\frac{\nu_1^2 u}{g}\,t^2\,,\quad \bar{W}_0 = 2ut - 4u\nu_1 t^2 \qquad (3\text{-}10a\text{-}e)$$

and $z_2=z_1$, $\dot{\bar{W}}_2=\dot{\bar{W}}_1$ and $\bar{W}_2=\bar{W}_1$ since the initial conditions $\dot{\bar{W}}_1=\dot{\bar{W}}_2=0$, $\bar{W}_1=\bar{W}_2=0$, $\dot{\bar{W}}_0=2u$ and $\bar{W}_0=0$ at $t=0$.

At $$t = t_s = \frac{3}{4}\frac{g}{\nu_1(\nu_1+3g)} \qquad (3\text{-}11a)$$

$\dot{\bar{W}}_1 = \dot{\bar{W}}_2 = \dot{\bar{W}}_0$, the shear sliding stops and the deformations in this phase are

$$\bar{W}_0(t_s) = \frac{3}{2}\frac{ug(\nu_1 + \frac{3}{2}g)}{\nu_1(\nu_1 + 3g)^2}\,,\quad \bar{W}_1(t_s) = \bar{W}_2(t_s) = \frac{3}{4}\frac{ug}{(\nu_1 + 3g)^2} \qquad (3\text{-}11b,c)$$

and $$\bar{W}_{1s} = \bar{W}_{2s} = \bar{W}_0(t_s) - \bar{W}_1(t_s) = \frac{3}{4}\frac{ug}{\nu_1(\nu_1 + 3g)} \qquad (3\text{-}11d)$$

where $\bar{W}_{1s}$ and $\bar{W}_{2s}$ are the maximum shear sliding on the right and left side of the impact point, respectively.

In this phase, equations (3-6) give*

$$-1 \leqslant q_1(z) \leqslant 0,\quad 0 \leqslant q_2(z) \leqslant 1,\quad -1 \leqslant m_1(z) \leqslant 1 \text{ and } -1 \leqslant m_2(z) \leqslant 1.$$

B) Phase 2, $t_s < t \leqslant t_1$

It is suggested from the end of phase 1 that $\dot{\bar{W}}_0 = \dot{\bar{W}}_1 = \dot{\bar{W}}_2$ and $z_1 = z_2$ but z_1 and z_2 are no longer constants in this phase and they are a function of the time t. The velocity profile in this phase is shown in Fig. 12.

---

* The examination of static admissibility conditions in this Chapter is given in Appendix I.

Equations (3-4) and (3-5) with $z_1 = z_2$, $q_{10} = -q_{20}$ and $\dot{\bar{W}}_0 = \dot{\bar{W}}_1 = \dot{\bar{W}}_2$ give

$$\frac{1}{12}\frac{g}{u}(\dot{\bar{W}}_1 z_1^2)'_t = 2 \qquad (3\text{-}12a)$$

and

$$(1 + gz_1)\,\dot{\bar{W}}_1 = 2u \qquad (3\text{-}12b)$$

since $z_1 = \frac{3}{\nu_1}$ and $\dot{\bar{W}}_1 = 2u\nu_1/(\nu_1+3g)$ at $t=t_s$.

Equations (3-12) can be rewritten to

$$\ddot{\bar{W}}_1 - 4u^2\ddot{\bar{W}}_1/\dot{\bar{W}}_1^2 - 24ug = 0 \qquad (3\text{-}13a)$$

and

$$\frac{1}{6}gz_1^2/(1 + z_1 g) = 2t \qquad (3\text{-}13b)$$

When $z_1 = 1$, equations (3-13b) and (3-12b) give

$$t_1 = \frac{1}{12}g/(1 + g) \qquad (3\text{-}14a)$$

$$\dot{\bar{W}}_1(t_1) = 2u/(1+g) \qquad (3\text{-}14b)$$

Integrating (3-13a) after multiplying $\dot{\bar{W}}_1$, we obtain

$$\frac{1}{2}\dot{\bar{W}}_1^2 - 4u^2\ln(\dot{\bar{W}}_1) - 24ug\,\bar{W}_1 = A \qquad (3\text{-}14c)$$

where $A = \frac{1}{2}\dot{\bar{W}}_1^2(t_s) - 4u^2\ln[\dot{\bar{W}}_1(t_s)] - 24ug\,\bar{W}_1(t_s)$

$$= 2u^2(\nu_1 - 3g)/(\nu_1 + 3g) - 4u^2\ln[2u\nu_1/(\nu_1 + 3g)] \qquad (3\text{-}14d)$$

Substituting (3-14b) into (3-14c), we obtain

$$\bar{W}_1(t_1) = \bar{W}_2(t_1) = \frac{u}{12g}\left\{\frac{1}{(1+g)^2} - (\nu_1-3g)/(\nu_1+3g) - 2\ln\left[\frac{\nu_1+3g}{\nu_1(1+g)}\right]\right\} \qquad (3\text{-}15)$$

Equations (3-6) give

$$q_{2max} = \frac{3}{\nu_1 z_1}\frac{(1 + gz_1)^2}{(2gz_1+1)(gz_1+2)} < \frac{3}{2\nu_1 z_1} < 1 \qquad (3\text{-}16a)$$

and $$q_{1min} = -q_{2max} > -1 \qquad (3\text{-}16b)$$

since $z_1 \geqslant \nu_1 > 3$, or $-1 < q_1 \leqslant 0$, $0 \leqslant q_2 < 1$ and $-1 \leqslant m_1 \leqslant 1$, $-1 \leqslant m_2 \leqslant 1$.

C) Phase 3, $t_1 < t \leqslant t_2$

The right side travelling plastic hinge arrives at the right-hand support at $t=t_1$ and will remain there in this phase. So, in this phase $z_1=1$, $\dot{z}_1=0$ and $\dot{\bar{W}}_0=\dot{\bar{W}}_1=\dot{\bar{W}}_2$. The velocity profile is shown in Fig. 13a.

Equation (3-5b) is not valid in this phase since the reactive force on the right-hand support acts on the hinge at $z=z_1=1$. Fortunately, we know $z_1=1$, $\dot{z}_1=0$ and we can obtain our solution from the rest of equations (3-5).

Equations (3-4), (3-5a) and (3-5c-e) with $z_1=1$, $\dot{z}_1=0$ and $\dot{\bar{W}}_0=\dot{\bar{W}}_1=\dot{\bar{W}}_2$ give

$$\frac{1}{12}\frac{g}{u}(\dot{\bar{W}}_1 z_2^2)'_t = 2 \qquad (3\text{-}17a)$$

and $$\frac{1}{4}\frac{g}{u}(z_2\dot{\bar{W}}_1)'_t = -\frac{1}{2u}\ddot{\bar{W}}_1 - \frac{g}{6u}\ddot{\bar{W}}_1 - 2 \qquad (3\text{-}17b)$$

Integrating equations (3-17), we obtain

$$\frac{g}{12u}\dot{\bar{W}}_1 z_2^2 = 2(t-t_1) + B \qquad (3\text{-}18a)$$

$$\frac{g}{4u}z_2\dot{\bar{W}}_1 + \frac{1}{2u}\dot{\bar{W}}_1 + \frac{g}{6u}\dot{\bar{W}}_1 = -2(t-t_1) + C \qquad (3\text{-}18b)$$

where $B = \frac{g}{12u}\dot{\bar{W}}_1(t_1)\, z_2^2(t_1)$ and $C = [\frac{g}{4u} z_2(t_1) + \frac{1}{2u} + \frac{g}{6u}]\dot{\bar{W}}_1(t_1)$

(3-18c,d)

Equations (3-18) give

$$\dot{\bar{W}}_1 = \frac{12u(B+C)}{gz_2^2 + 3gz_2 + 6 + 2g} \qquad (3\text{-}19)$$

Equations (3-19) and (3-17a) give

$$\dot{z}_2 = \frac{2(gz_2^2 + 3gz_2 + 6 + 2g)^2}{gz_2\,(3gz_2 + 12 + 4g)(B+C)} \qquad (3\text{-}20)$$

Combining equation (3-20) and equation (3-19) gives

$$\frac{\partial \bar{W}_1}{\partial z_2} = \frac{6ugz_2(3gz_2 + 12 + 4g)(B+C)^2}{(gz_2^2 + 3gz_2 + 6 + 2g)^3} \qquad (3\text{-}21)$$

since $\dot{\bar{W}}_1 = \frac{\partial \bar{W}_1}{\partial z_2}\dot{z}_2$.

Integrating equation (3-21), we obtain

$$\bar{W}_1 = \frac{1}{2} ug(B+C)^2 \left[\frac{36z_2 + 54}{(g-24)(gz_2^2 + 3gz_2 + 6 + 2g)} - \frac{18z_2 + 12 + {}^{36}/_{g}}{(gz_2^2 + 3gz_2 + 6 + 2g)^2} + \right.$$

$$\left. + \frac{3}{(g-24)} f(z_2)\right] \Bigg|_{z_2(t_1)}^{z_2} + \bar{W}_1(t_1) \qquad (3\text{-}22a)$$

where

$$f(z_2) = \begin{cases} \dfrac{24}{\sqrt{g(24-g)}}\ \text{arctg}\ [\dfrac{2gz_2 + 3g}{\sqrt{g(24-g)}}] & \text{for } g < 24 \\ \dfrac{12}{\sqrt{g(g-24)}}\ \ln[\dfrac{2gz_2 + 3g - \sqrt{g(g-24)}}{2gz_2 + 3g + \sqrt{g(g-24)}}] & \text{for } g > 24 \end{cases} \qquad (3\text{-}22b)$$

and B and C are defined by equations (3-18c,d).

From equations (3-6), we can obtain

$$q_{1min} = -\frac{1}{\nu_1}\frac{gz_2 + 4 + 2g + g/z_2}{gz_2 + 4 + 4g/3} = -\frac{3}{\nu_1}\frac{gz_{2/3} + 4/3 + 2g/3 + g/3z_2}{gz_2 + 4 + 4g/3} > -1$$

(3-23a)

$$q_{2max} = \frac{6}{\nu_1}\frac{(\frac{1}{6}gz_2^2 + \frac{1}{2}gz_2 + 1 + \frac{1}{3}g)^2}{z_2(gz_2 + 4 + \frac{4}{3}g)(\frac{1}{2}gz_2^2 + gz_2 + 1 + \frac{1}{3}g)} < \frac{3}{\nu_1} < 1$$

(3-23b)

since $z_2 \geq 1$ and $\nu_1 > 3$. Thus

$$-1 < q_1 \leq 0\ ,\quad -1 \leq m_1 \leq 1 \quad \text{if } \frac{4}{g} \geq \frac{2}{z_2} - z_2 \qquad (3\text{-}23c)$$

and

$$0 \leq q_2 < 1\ ,\quad -1 \leq m_2 \leq 1 \quad \text{if } \frac{3}{g} \geq \frac{1}{2}z_2^2 - 1 \qquad (3\text{-}23d)$$

Equations (3-23) shows that the solution given by equations (3-22) are valid only when $\frac{4}{g} \geq \frac{2}{z_2(t_1)} - z_2(t_1)$ since z_2 increases with time t and when $\frac{3}{g} \geq \frac{1}{2}z_2^2 - 1$.

For $\frac{4}{g} < \frac{2}{z_2(t_1)} - z_2(t_1)$, $\left.\frac{\partial m_1}{\partial z}\right|_{z=0^+} = 2\nu_1 q_{10} > 0$* and there is a yield violation of bending moment on the right side at z=0 since m_1=1 at z=0. The velocity profile shown in Fig. 13a is no longer valid. In this case, we assume that the velocity profile shown in Fig. 14a is

$$\dot{\bar{w}}(z) = \begin{cases} 0 & -\frac{1}{r} \leq z \leq -z_2^- \\ \dot{\bar{w}}_3 \frac{z_2+z}{z_2+z_0} & -z_2^+ \leq z \leq z_0^- \\ \dot{\bar{w}}_3 \frac{1-z}{1-z_0} & z_0^+ \leq z \leq 1 \end{cases} \qquad (3\text{-}24)$$

* see equations (9e) and (9f) in Appendix I.

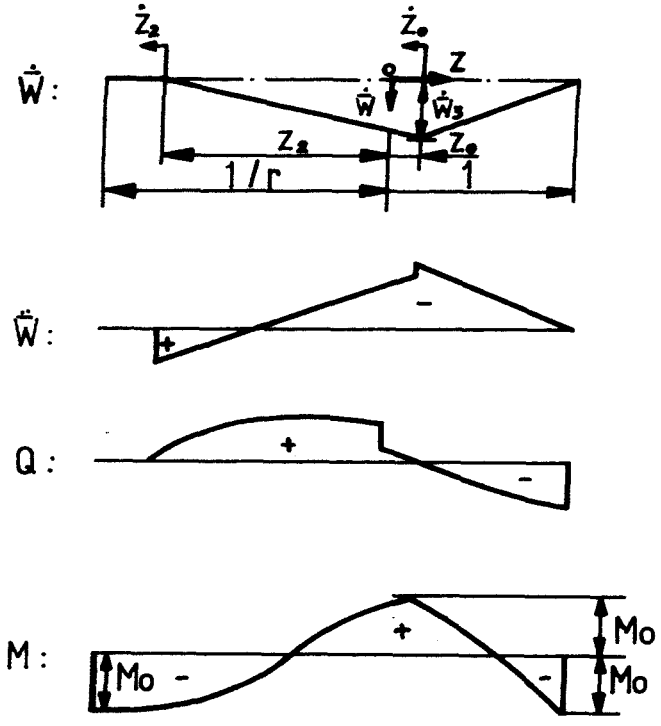

FIG. 14 Third phase of motion for case I when $\frac{4}{g} < \frac{2}{z_2(t_1)} - z_2(t_1)$.

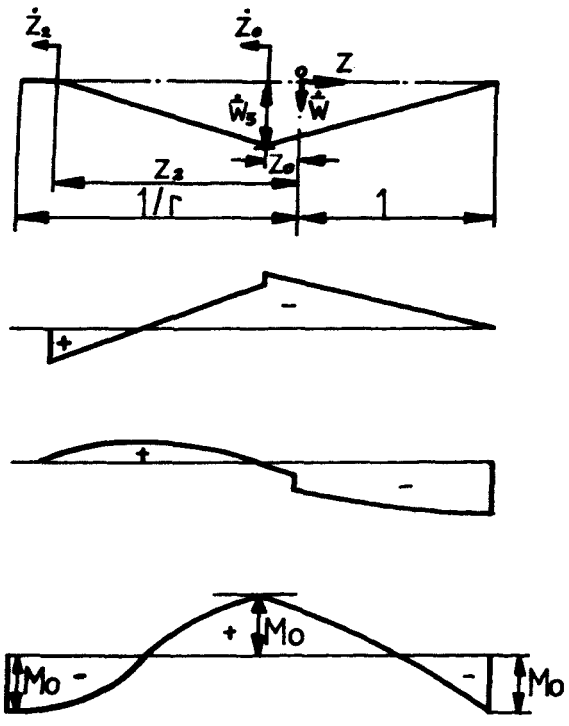

FIG. 15 Third phase of motion for case I when $\frac{3}{g} < \frac{1}{2} z_2^2 - 1$.

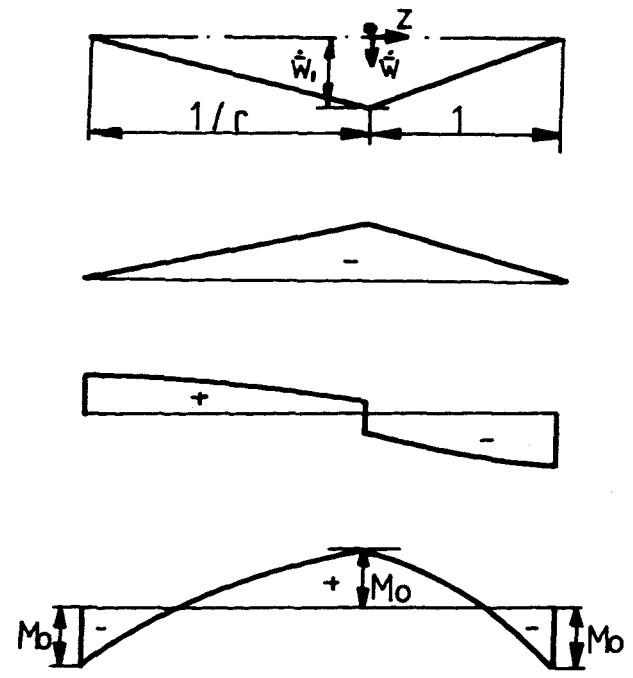

FIG. 16 Final phase of motion for case I.

which means that the plastic hinge at impact point z=0 now disappears and a new travelling plastic hinge occurs at $z=z_0$.

The linear and angular momentum equations of beam shown in Fig. 32a are

$$\frac{1}{6} g(1-z_0)^2 \ddot{\bar{W}}(z_0^+) = -2u \tag{3-25a}$$

$$\frac{1}{6} g(z_2+z_0)^2 \ddot{\bar{W}}(z_0^-) + \frac{1}{12} g(z_2+z_0)^2 \ddot{\bar{W}}(-z_2^+) = -2u - \frac{1}{2} z_2 \ddot{\bar{W}}(0) \tag{3-25b}$$

and $$\frac{1}{2} g[\ddot{\bar{W}}(z_0^-) + \ddot{\bar{W}}(-z_2^+)](z_2+z_0) + \ddot{\bar{W}}(0) = 0 \tag{3-25c}$$

where $\ddot{\bar{W}}(X)$ indicates the acceleration at z=X and can be obtained from equation (3-24).

Equations (3-24) and (3-25) give

$$\ddot{\bar{W}}_3 = \frac{12u}{g} \frac{[(z_0-z_2-2)(z_2+z_0)^2 g-4(z_0-z_0z_2+z_2^2)]}{[g(z_2+z_0)^3+4(z_2^2-z_0z_2+z_0^2)](z_2+1)(1-z_0)} \tag{3-26a}$$

$$\dot{\bar{W}}_3\dot{z}_0 = -\frac{12u}{g} \frac{[g(z_2+z_0)^2(z_2^2+2z_2z_0-z_0^2-2+4z_0)+4(z_2^3+2z_0^2-z_0)]}{[g(z_2+z_0)^3+4(z_2^2-z_0z_2+z_0^2)](z_2+1)(1-z_0)} \tag{3-26b}$$

$$\dot{\bar{W}}_3\dot{z}_2 = \frac{12u}{g} \frac{[2g(z_2+z_0)^2+4z_2]}{[g(z_2+z_0)^3+4(z_2^2-z_0z_2+z_0^2)]} . \tag{3-26c}$$

A numerical method has to be employed to solve equations (3-26) until $z_0=0$. The initial conditions at $t=t_1$ are $z_2=1$, $\dot{\bar{W}}_3=\dot{\bar{W}}_3(t_1)$ and

$z_0(t_1)$ is determined by equation (3-26b) with $\dot{z}_0(t_1)=0$. The static admissibility conditions need to be checked during numerical calculation*.

For $\frac{3}{g} < \frac{1}{2} z_2^2 - 1$, $\left.\frac{\partial m_2}{\partial z}\right|_{z=0^-} = 2\nu_1 q_{20} < 0$ and a yield violation occurs in the bending moment on the left side at z=0. The velocity profile is shown in Fig. 15a

$$\dot{\bar{W}}(z) = \begin{cases} 0 & -\frac{1}{r} \leqslant z \leqslant -z_2^- \\ \dot{\bar{W}}_3 \frac{z_2+z}{z_2-z_0} & -z_2^+ \leqslant z \leqslant -z_0^- \\ \dot{\bar{W}}_3 \frac{1-z}{1+z_0} & -z_0^+ \leqslant z \leqslant 1 \end{cases} \qquad (3\text{-}27)$$

is assumed which indicates that the plastic hinge at the impact point z=0 is now transferred to $z=-z_0$.

The linear and angular momentum equations of beam shown in Fig. 32b are

$$\frac{g}{6}(1+z_0)^2 \ddot{\bar{W}}(-z_0^+) = -2u - \frac{1}{2}\ddot{\bar{W}}(0) \qquad (3\text{-}28a)$$

$$\frac{g}{6}(z_2-z_0)^2 \ddot{\bar{W}}(-z_0^-) + \frac{g}{12}\ddot{\bar{W}}(-z_2^+)(z_2-z_0)^2 = -2u \qquad (3\text{-}28b)$$

and $$\frac{g}{2}[\ddot{\bar{W}}(-z_0^-) + \ddot{\bar{W}}(-z_2^+)](z_2-z_0) = 0 \qquad (3\text{-}28c)$$

Equations (3-27) and (3-28) give

$$\ddot{\bar{W}}_3 = -4u \frac{(1+z_0)^2(2+z_0+z_2) + \frac{6}{g}}{(z_2-z_0)(z_2+1)[\frac{1}{3}g(1+z_0)^3+1]} \qquad (3\text{-}29a)$$

---

* see equations (11) in Appendix I.

$$\dot{\bar{W}}_3\dot{z}_0 = 4u\,\frac{(1+z_0)^2[(z_2-z_0)^2 - 2(z_0+1)^2] - 6(1+z_0)/g}{(z_2-z_0)(z_2+1)[\frac{1}{3}g(1+z_0)^3 + 1]} \qquad (3\text{-}29b)$$

$$\text{and } \dot{\bar{W}}_3\dot{z}_2 = \frac{24u}{g(z_2-z_0)} \cdot \qquad (3\text{-}29c)$$

Equations (3-29) also need a numerical method to solve until $z_2 = \frac{1}{r}$ at $t=t_2$. This type of movement starts with $z_0=0$ when

$$z_2 = \sqrt{\frac{6}{g} + 2} \qquad (3\text{-}30)$$

which is obtained from $\frac{3}{g} = \frac{1}{2}z_2^2 - 1$ given by equation (3-23d), and the initial conditions of $\dot{\bar{W}}_3$ and $\bar{W}_3$ are defined by equations (3-19) and (3-22) with z_2 given by equation (3-30). The static admissibility conditions should be checked during numerical calculation*.

D) Phase 4, $t_2 < t \leqslant t_f$

The left side travelling plastic hinge reaches the left-hand support at $t=t_2$ and two parts of the beam rotate as rigid bodies in this phase of motion. The velocity profile is shown in Fig. 16a.

Equations (3-4), (3-5a), (3-5c) and (3-5e) with $z_1=1$, $\dot{z}_1=0$, $z_2 = \frac{1}{r}$, $\dot{z}_2=0$ and $\dot{\bar{W}}_0=\dot{\bar{W}}_1=\dot{\bar{W}}_2$ give

$$[\frac{1}{3}(1+r)g+r]\ddot{\bar{W}}_1 = -4ur(1+r) \qquad (3\text{-}31)$$

Integrating equation (3-31), we obtain

$$\dot{\bar{W}}_1 = -\frac{4ur(1+r)}{\frac{1}{3}(1+r)g+r}(t-t_2) + \dot{\bar{W}}_1(t_2) \qquad (3\text{-}32a)$$

---

* see equations (13) in Appendix I.

and $$\bar{W}_1 = -\frac{2ur(1+r)}{\frac{1}{3}(1+r)g+r}(t-t_2)^2 + \dot{\bar{W}}_1(t_2)(t-t_2) + \bar{W}_1(t_2) \qquad (3\text{-}32b)$$

At $t=t_f$, $\dot{\bar{W}}=0$ and

$$t_f = \frac{\dot{\bar{W}}_2(t_2)[\frac{1}{3}(1+r)g+r]}{4ur(1+r)} + t_2 \qquad (3\text{-}33)$$

Finally, we obtain the maximum permanent deformation in the beam

$$\bar{W}_{1f} = \frac{1}{2}\frac{[\frac{1}{3}(1+r)g+r]}{4ur(1+r)}\dot{\bar{W}}_1^2(t_2) + \bar{W}_1(t_2) \qquad (3\text{-}34)$$

Equations (3-6) give

$$q_{1min} = -\frac{1}{\nu_1}\frac{(\frac{1}{2}g + \frac{1}{3}\frac{g}{r} + 1 + \frac{1}{6}gr)}{\frac{1}{3}g + \frac{1}{3}\frac{g}{r} + 1} = -\frac{3}{\nu_1}\frac{(\frac{g}{6} + \frac{1}{9}\frac{g}{r} + \frac{1}{3} + \frac{1}{18}gr)}{\frac{1}{3}g + \frac{1}{3}\frac{g}{r} + 1} > -1 \qquad (3\text{-}35a)$$

$$q_{2max} = \frac{1}{\nu_1}\frac{\frac{1}{3}gr + \frac{1}{2}g + 1 + \frac{1}{6}\frac{g}{r}}{\frac{1}{3}g + \frac{1}{3}\frac{g}{r} + 1} \leqslant -q_{1min} < 1 \qquad (3\text{-}35b)$$

since $\nu_1 > 3$ and $r \leqslant 1$, therefore, $-1 < q_1 < 0$, $-1 \leqslant m_1 \leqslant 1$ (3-35c)

and $0 < q_2 < 1$, $-1 \leqslant m_2 \leqslant 1$ if $\frac{3}{g} \geqslant \frac{1}{r^2} - 1$. (3-35d)

For $\frac{3}{g} < \frac{1}{r^2} - 1$, $\left.\frac{\partial m_2}{\partial z}\right|_{z=0^-} = 2\nu_1 q_{20} < 0$ and a yield violation of bending moment occurs on the left side of the impact point z=0. The velocity profile shown in Fig. 16a is no longer valid. A new velocity profile shown in Fig. 17a may be expressed in the form

$$\dot{\bar{W}}(z) = \begin{cases} \dot{\bar{W}}_3 \frac{1+zr}{1-z_0 r} & -\frac{1}{r} \leqslant z < -z_0^- \\ \dot{\bar{W}}_3 \frac{1-z}{1+z_0} & -z_0^+ \leqslant z \leqslant 1 \end{cases} \qquad (3\text{-}36)$$

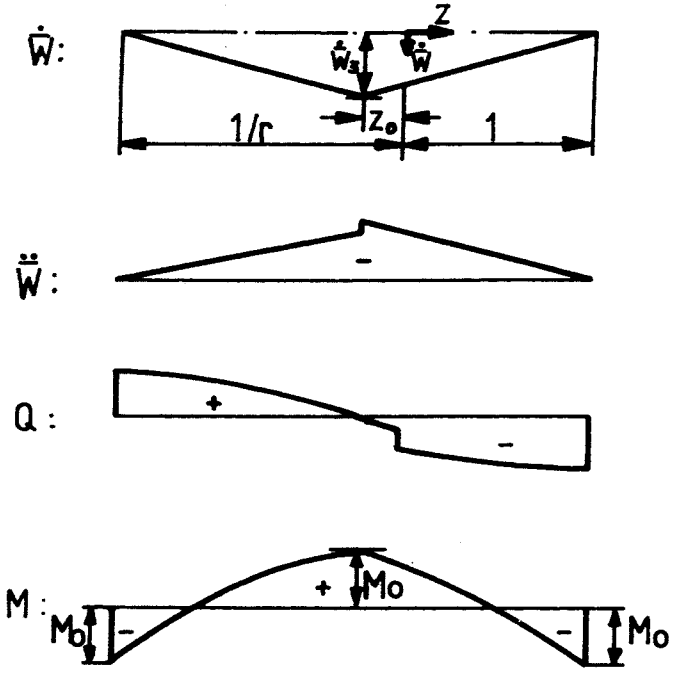

FIG. 17 Final phase of motion for case I when $\frac{3}{g} < \frac{1}{r^2} - 1$.

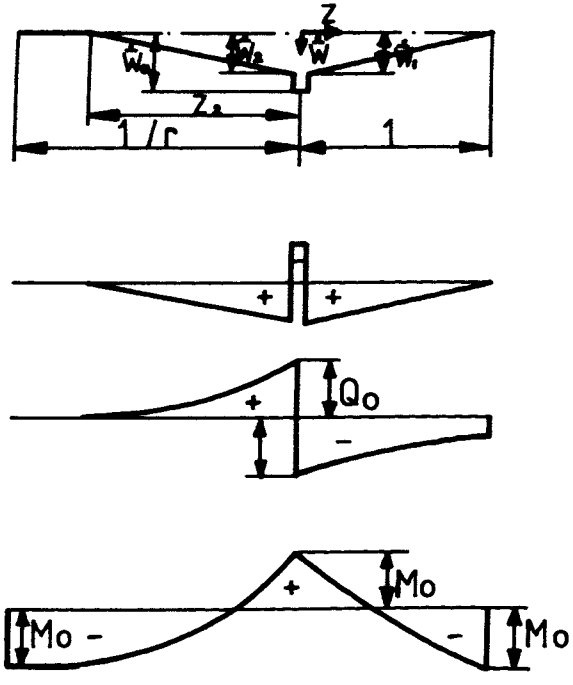

FIG. 18 First phase of motion for $1 < \nu_1 \leqslant 3$ and $\nu_2 > 3$ (case II).

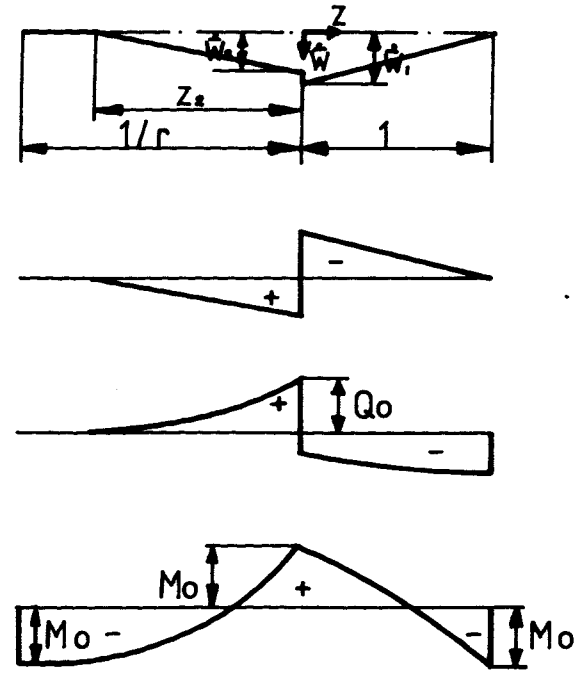

FIG. 19 Motion of case II for $1.5 \leqslant \nu_1 < 3$ when $t_{s1} < t \leqslant t_{s2}$.

is postulated which means the stationary plastic hinge at the impact point z=0 disappears and a new travelling plastic hinge now occurs at $z = -z_0$.

The linear and angular momentum equations of beam shown in Fig. 32c give

$$\ddot{\bar{W}}_3 = -4u \frac{(1 + z_0)^2 (1 + \frac{1}{r}) + \frac{3}{g}}{(\frac{1}{r} - z_0)(\frac{1}{r} + 1)[\frac{1}{3} g(1 + z_0)^3 + 1]} \qquad (3\text{-}37a)$$

and $$\dot{\bar{W}}_3 \dot{z}_0 = 4u \frac{(1 + z_0)^2 (1 + \frac{1}{r})(\frac{1}{r} - 1 - 2z_0) - 3(1 + z_0) \frac{1}{g}}{(\frac{1}{r} - z_0)(\frac{1}{r} + 1)[\frac{1}{3} g(1 + z_0)^3 + 1]} \qquad (3\text{-}37b)$$

Equations (3-37) can be solved by a numerical method until the movement of beam stops at $\dot{\bar{W}}_3 = 0$. The initial conditions are that $\dot{\bar{W}}_3 = \dot{\bar{W}}_3(t_2)$ and $z_0(t_2)$ is defined by equation (3-37b) with $\dot{z}_0 = 0$. The static admissibility conditions should be checked during the numerical calculation*.

3.3.2 Case II, $1 \leq \nu_1 < 3$ and $\nu_2 > 3$

Equation (3-10a) shows that if $\nu_1 < 3$ the velocity profile introduced in phase I of case I is no longer valid since z_1 must be less than 1 (or equal to 1, we will discuss when $z_1 = 1$ in this section). Equation (3-10) gives $z_1 = 1$ when $\nu_1 = 3$. Therefore, we assume that a stationary plastic hinge occurs at the right-hand support when $\nu_1 \leq 3$. Equations (3-4), (3-5a) and (3-5c-e) with $z_1 = 1$ and $\dot{z}_1 = 0$ give

$$\frac{1}{12} \frac{g}{u} (\dot{\bar{W}}_2 z_2^2)'_t = 2 \qquad (3\text{-}38a)$$

---

* see equations (17) in Appendix I.

$$q_{20} = \frac{1}{8}\frac{g}{u\nu_1}(\dot{\bar{W}}_2 z_2)_t' \qquad (3\text{-}38b)$$

$$\frac{1}{6}\frac{g}{u}\ddot{\bar{W}}_1 = -2 - 2\nu_1 q_{10} \qquad (3\text{-}38c)$$

and

$$q_{20} - q_{10} = -\frac{1}{4}\frac{1}{u\nu_1}\ddot{\bar{W}}_0 \qquad (3\text{-}38d)$$

K) Phase 1, shear sliding

a) $0 \leqslant t \leqslant t_{s1}$

After impact the mechanics of motion are the same as those described in phase 1 of case I except the plastic hinge which is located on the right side of impact point now remains at the right-hand support z=1. The velocity profile is shown in Fig. 18a.

Equations (3-38) with $q_{10} = -1$ and $q_{20} = 1$ give

$$z_2 = \frac{3}{\nu_1},\ \dot{\bar{W}}_0 = 2u - 8\nu_1 ut,\ \dot{\bar{W}}_1 = \frac{12u}{g}(\nu_1 - 1)t\ , \qquad (3\text{-}39a\text{-}c)$$

$$\dot{\bar{W}}_2 = \frac{8}{3}\frac{u}{g}\nu_1^2 t\ ,\ \bar{W}_0 = 2ut - 4u\nu_1 t^2\ ,\ \bar{W}_1 = -\frac{6u}{g}(1-\nu_1)t^2 \qquad (3\text{-}39d\text{-}f)$$

and

$$\bar{W}_2 = \frac{4}{3}\frac{u}{g}\nu_1^2 t^2 \qquad (3\text{-}39g)$$

since $\dot{\bar{W}}_0 = 2u$, $\dot{\bar{W}}_1 = \dot{\bar{W}}_2 = 0$ and $\bar{W}_0 = \bar{W}_1 = \bar{W}_2 = 0$ at t=0. Compared with equations (3-39c) and (3-39d), we obtain that $\dot{\bar{W}}_1 \geqslant \dot{\bar{W}}_2$ when $\frac{3}{2} \leqslant \nu_1 < 3$, otherwise, $\dot{\bar{W}}_1 < \dot{\bar{W}}_2$. Therefore, the shear sliding on the right side of the impact point first stops if $\frac{3}{2} \leqslant \nu_1 < 3$, while the left side one will stop at an earlier time when $1 < \nu_1 < \frac{3}{2}$. Equations (3-39b-d) for $\frac{3}{2} \leqslant \nu_1 \leqslant 3$, give $\dot{\bar{W}}_0 = \dot{\bar{W}}_1$ at

$$t = t_{s1} = \frac{g}{4\nu_1 g - 6(1-\nu_1)} \text{ and } \bar{W}_{1s} = \frac{ug}{4\nu_1 g - 6(1-\nu_1)}\ , \qquad (3\text{-}39h,i)$$

while for $1 < \nu_1 < \frac{3}{2}$, $\dot{\bar{W}}_0 = \dot{\bar{W}}_2$ at

$$t = t_{s1} = \frac{3g}{4\nu_1(\nu_1+3g)} \text{ and } \bar{W}_{2s} = \frac{3ug}{4\nu_1(\nu_1+3g)} \qquad (3\text{-}39j,k)$$

Equations(3-6) show that the static admissibility conditions are satisfied, i.e. $-1 \leqslant q_1 \leqslant 0$, $-1 \leqslant m_1 \leqslant 1$, $0 \leqslant q_2 \leqslant 1$ and $-1 \leqslant m_2 \leqslant 1$.

b) $t_{s1} < t \leqslant t_{s2}$

For $\frac{3}{2} \leqslant \nu_1 < 3$, shear sliding stops at $z=0^+$ when $t=t_{s1}$ while the other continues and the velocity profile is shown in Fig. 19a. Equations (3-38) with $\dot{\bar{W}}_0 = \dot{\bar{W}}_1$ and $q_{20} = 1$ give

$$\dot{\bar{W}}_1 = -\frac{12u(1+\nu_1)}{(3+g)}t + \frac{6u}{3+g}, \quad \dot{\bar{W}}_2 = \frac{8}{3}\frac{u}{g}\nu_1^2 t, \quad z_2 = \frac{3}{\nu_1} \qquad (3\text{-}40a\text{-}c)$$

$$\bar{W}_1 = -\frac{6u(1+\nu_1)}{(3+g)}t^2 + \frac{6u}{3+g}t - \frac{3}{2}\frac{ug}{(3+g)(2\nu_1 g-3+3\nu_1)} \qquad (3\text{-}40d)$$

$$\bar{W}_2 = \frac{4}{3}\frac{u}{g}\nu_1^2 t^2 \qquad (3\text{-}40e)$$

and $$\dot{\bar{W}}_2 = \dot{\bar{W}}_1 \text{ at } t = t_{s2} = \frac{9g}{12\nu_1^2+4\nu_1^2 g+18g+18\nu_1 g} \qquad (3\text{-}40f)$$

Equations (3-6) give

$$q_{1min} = -\frac{g\nu_1+3g+6}{\nu_1(2g+6)} \geqslant -1 \text{ if } \frac{3}{g} \geqslant \frac{3-\nu_1}{2(\nu_1-1)}$$

$0 \leqslant q_2 \leqslant 1$, $-1 \leqslant m_1 \leqslant 1$ and

$-1 \leqslant q_1 \leqslant 0$, $-1 \leqslant m_1 \leqslant 1$ if $\frac{3}{g} \geqslant \nu_1$.

If $\frac{3}{g} \geqslant \nu_1$, the static admissibility conditions are satisfied

since $\frac{3}{g} \geqslant \frac{3-\nu_1}{2(\nu_1-1)}$ for $\frac{3}{2} \leqslant \nu_1 \leqslant 3$. The following motion is the same as phase 3 and phase 4 in case I with $t_1 = t_{s2}$, $z_2(t_1) = \frac{3}{\nu_1}$ and $\dot{\bar{w}}_1(t_1) = \dot{\bar{w}}_1(t_{s2})$. The static admissibility conditions (3-23) and (3-35) are also satisfied with $\nu_1 \geqslant \frac{3}{2}$ and $z_2 > 1$.

If $\frac{3}{g} < \nu_1$, the solution of equations (3-40) corresponds to a yield violation of bending moment on the right side of the impact point since $\left.\frac{\partial m_1}{\partial z}\right|_{z=0^+} = 2\nu_1 q_{10} > 0$. Therefore, a new velocity profile shown in Fig. 20a

$$\dot{\bar{w}}(z) = \begin{cases} 0 & -\frac{1}{r} \leqslant z \leqslant -z_2^- \\ \dot{\bar{w}}_2(1 + \frac{z}{z_2}) & -z_2^+ \leqslant z \leqslant 0^- \\ \dot{\bar{w}}_1 + (\dot{\bar{w}}_3 - \dot{\bar{w}}_1)\frac{z}{z_0} & 0^+ \leqslant z \leqslant z_0^- \\ \dot{\bar{w}}_3 \frac{1-z}{1-z_0} & z_0^+ \leqslant z \leqslant 1 \end{cases} \tag{3-41}$$

is postulated. The linear and angular momentum equations of beam shown in Fig. 33a are

$$g(1-z_0)^2 \ddot{\bar{w}}(z_0^+) = -12u \tag{3-42a}$$

$$2gz_0^2 \ddot{\bar{w}}(z_0^-) + gz_0^2 \ddot{\bar{w}}(0^+) = -12u + 12um_2(0) \tag{3-42b}$$

$$2gz_2^2 \ddot{\bar{w}}(0^-) + gz_2^2 \ddot{\bar{w}}(-z_2^+) = -12u - 12um_2(0) \tag{3-42c}$$

$$gz_0[\ddot{\bar{w}}(0^+) + \ddot{\bar{w}}(z_0^-)] + 2\ddot{\bar{w}}(0^+) = -8u\nu_1 \tag{3-42d}$$

and $$gz_2[\ddot{\bar{w}}(0^-) + \ddot{\bar{w}}(-z_2^+)] = 8u\nu_1 \tag{3-42e}$$

where $\ddot{\bar{w}}(-z_2^+) = \dot{\bar{w}}_2\dot{z}_2/z_2$, $\ddot{\bar{w}}(0^-) = \ddot{\bar{w}}_2$, $\ddot{\bar{w}}(0^+) = \ddot{\bar{w}}_1$, $\ddot{\bar{w}}(z_0^-) = \ddot{\bar{w}}_3 - (\dot{\bar{w}}_3 - \dot{\bar{w}}_1)\dot{z}_0/z_0$ and $\ddot{\bar{w}}(z_0^+) = \ddot{\bar{w}}_3 + \dot{\bar{w}}_3\dot{z}_0/(1-z_0)$ are given by equation (3-41).

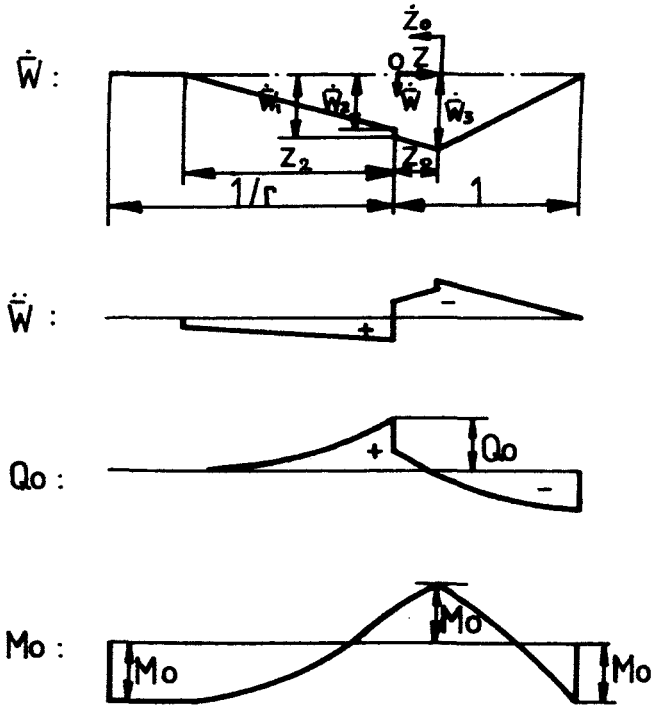

FIG. 20 Motion of case II for $1.5 \leqslant \nu_1 < 3$ when $t_{s1} < t \leqslant t_{s2}$, if $\frac{3}{g} < \nu_1$.

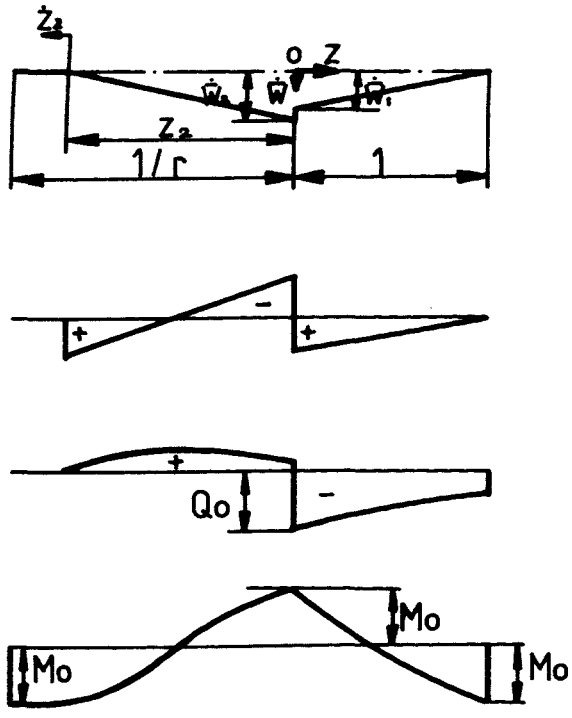

FIG. 21 Motion of case II for $1 < \nu_1 < 1.5$ when $t_{s1} < t \leqslant t_{s2}$.

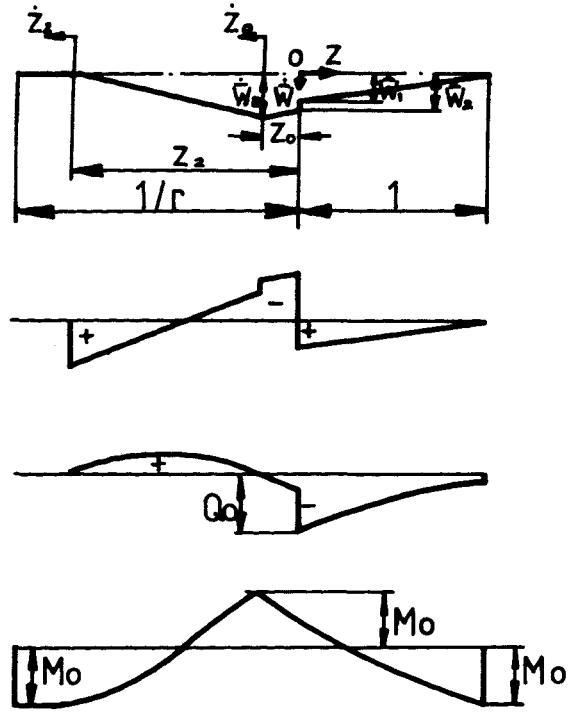

FIG. 22 Motion of case II for $1 < \nu_1 < 1.5$ when $t_{s1} < t \leqslant t_{s2}$, if $\frac{6}{g} < \nu_1 z_2^2$.

Equations (3-41) and (3-42) with geometrical condition at the shear hinge $z = 0^-$ give

$$\ddot{\bar{W}}_3 + \dot{\bar{W}}_3\dot{z}_0/(1-z_0) = -12u/[g(1-z_0)^2] \qquad (3\text{-}43a)$$

$$z_0^2\ddot{\bar{W}}_3 - z_0(\dot{\bar{W}}_3-\dot{\bar{W}}_1)\dot{z}_0 + \frac{1}{2}z_0^2\ddot{\bar{W}}_1 + z_2^2\ddot{\bar{W}}_2 + \frac{1}{2}z_2\dot{\bar{W}}_2\dot{z}_2 = -12u/g \qquad (3\text{-}43b)$$

$$z_0[\ddot{\bar{W}}_1 + \ddot{\bar{W}}_3 + (\dot{\bar{W}}_3 - \dot{\bar{W}}_1)\dot{z}_0/z_0] + 2\ddot{\bar{W}}_1/g = -8uv_1/g \qquad (3\text{-}43c)$$

$$\dot{\bar{W}}_2 z_0 = (\dot{\bar{W}}_3 - \dot{\bar{W}}_1)z_2 \qquad (3\text{-}43d)$$

and $$z_2\ddot{\bar{W}}_2 + \dot{\bar{W}}_2\dot{z}_2 = 8uv_1/g. \qquad (3\text{-}43e)$$

The equations (3-43) can be solved by a numerical method until $z_2 = \frac{1}{r}$ or $\dot{\bar{W}}_1 = \dot{\bar{W}}_2$. If the left side travelling hinge reaches the left-hand support before $\dot{\bar{W}}_1 = \dot{\bar{W}}_2$, the motion is still governed by equations (3-41), (3-42a-d) and (3-43a-d) with $z_2 = \frac{1}{r}$ and $\dot{z}_2 = 0$. Otherwise, the motion is the same as phase 3 and phase 4 of case I and the static admissibility conditions (3-23) and (3-35) are satisfied with $v_1 \geq \frac{3}{2}$ and $z_2 > 1$.

For $1 < v_1 < \frac{3}{2}$, the shear sliding at $z=0^-$ stops at $t=t_{s1}$ while the other continues. The velocity profile is shown in Fig. 21a. Equations (3-38) with $q_{10} = -1$ and $\dot{\bar{W}}_0 = \dot{\bar{W}}_2$ give

$$\dot{\bar{W}}_1 = \frac{12u}{g}(v_1-1)t, \quad \bar{W}_1 = \frac{6u}{g}(v_1-1)t^2, \qquad (3\text{-}44a,b)$$

$$\frac{1}{12}\frac{g}{u}\dot{\bar{W}}_2 z_2^2 = 2t \text{ and } \frac{1}{4uv_1}\dot{\bar{W}}_2 + \frac{g}{8uv_1}\dot{\bar{W}}_2 z_2 = \frac{1}{2v_1} - t \qquad (3\text{-}44c,d)$$

Equations (3-44c,d) give

$$\dot{\bar{W}}_2 = \frac{12u}{v_1 g z_2^2 + 6 + 3gz_2} \qquad (3\text{-}44e)$$

or $$\dot{\bar{W}}_2 = 2u + 3ugt - 4\nu_1 ut - \frac{1}{2}\sqrt{36u^2g^2t^2 - 96u^2g\nu_1 t^2 + 48u^2gt} \quad (3\text{-}44f)$$

and $$t = \frac{gz_2^2}{2\nu_1 gz_2^2 + 12 + 6gz_2} \quad (3\text{-}44g)$$

Integrating equation (3-44f) with respect to time t, we obtain

$$\bar{W}_2 = \left[2ut + \frac{3}{2}ugt^2 - 2\nu_1 ut^2 - \frac{2at+b}{4a}\sqrt{at^2+bt} + f(t)\right]\Bigg|_{t_{s1}}^{t} + \bar{W}_2(t_{s1}) \quad (3\text{-}44h)$$

where $a = 9g^2u^2 - 24g\nu_1 u^2$, $b = 12gu^2$

and

$$f(t) = \begin{cases} \dfrac{b^2}{8a\sqrt{a}} \ln(2at + b + 2\sqrt{a}\sqrt{at^2+bt}) & \text{for } a > 0 \\ \dfrac{b^2}{8a\sqrt{-a}} \arcsin\left(\dfrac{-2at-b}{b}\right) & \text{for } a < 0 \end{cases} \quad (3\text{-}44i)$$

Equations (3-44a) and (3-44c) give

$$\bar{z}_2 = \sqrt{\frac{2}{\nu_1 - 1}} \quad (3\text{-}44j)$$

when $\dot{\bar{W}}_1 = \dot{\bar{W}}_2$. Therefore, two types of motion can be followed which depend on the magnitude of $\bar{z}_2$.

If $\bar{z}_2 < \frac{1}{r}$ or $r^2 < \frac{1}{2}(\nu_1 - 1)$, $z_2(t_{s2}) = \bar{z}_2 = \sqrt{\frac{2}{\nu_1 - 1}}$ and $\dot{\bar{W}}_1 = \dot{\bar{W}}_2$ (3-45a,b)

at $$t_{s2} = \frac{1}{2\left[\frac{3}{2}\sqrt{2(\nu_1 - 1)} + \frac{3(\nu_1 - 1)}{g} + \nu_1\right]} \quad (3\text{-}45c)$$

The following motion is the same as phase 3 and phase 4 in case I with $t_1 = t_{s2}$, $z_2(t_1) = z_2(t_{s2})$ and $\dot{\bar{W}}_1(t_1) = \dot{\bar{W}}_1(t_{s2})$. The static admissibility conditions (3-23) and (3-35) are satisfied

with $z_2 \geq \sqrt{\frac{2}{\nu_1-1}}$, $1 < \nu_1 < \frac{3}{2}$ and $r^2 < \frac{1}{2}(\nu_1-1)$.

If $\bar{z}_2 \geq \frac{1}{r}$ or $r^2 \geq \frac{1}{2}(\nu_1-1)$, the travelling plastic hinge on the left side reaches the left-hand support before the shear sliding at $z=0^+$ stops. In other words, $\dot{\bar{W}}_2$ is still larger than $\dot{\bar{W}}_1$ when $z_2 = \frac{1}{r}$. Therefore, equations (3-44a-i) are valid until $z_2 = \frac{1}{r}$ at

$$t = \bar{t}_2 = \frac{g}{6gr+12r^2+2\nu_1 g} \tag{3-46a}$$

Then, the motion of beam is governed by equations (3-5a), (3-5c) and (3-5e) with $q_{10} = -1$, $z_1 = 1$, $\dot{z}_1 = 0$, $z_2 = \frac{1}{r}$, $\dot{z}_2 = 0$ and $\dot{\bar{W}}_0 = \dot{\bar{W}}_2$. The velocities and deformations of beam are

$$\dot{\bar{W}}_1 = \frac{12u}{g}(\nu_1-1)t, \quad \dot{\bar{W}}_2 = [\frac{2u}{r} - 4u(1+\nu_2)t]r^2/(\frac{1}{3}g+r) \tag{3-46b,c}$$

$$\bar{W}_1 = \frac{6u}{g}(\nu_1-1)t^2 \tag{3-46d}$$

and $$\bar{W}_2 = 2ur(t-\bar{t}_2)[1 - (r+\nu_1)(t+\bar{t}_2)]/(\frac{1}{3}g+r) + \bar{W}_2(\bar{t}_2) \tag{3-46e}$$

where $\bar{W}_2(\bar{t}_2)$ is obtained by substituting equation (3-46a) into (3-44h).

At $$t = t_{s2} = \frac{rg}{2[(\nu_1-1)(g+3r) + gr^2(1+\nu_2)]}, \tag{3-46f}$$

$\dot{\bar{W}}_1 = \dot{\bar{W}}_2$ and the shear sliding at $z=0^+$ stops. The following motion is the same as phase 4 of case I with $\dot{\bar{W}}_1(t_2) = \dot{\bar{W}}_1(t_{s2})$ and $\bar{W}_1(t_2) = \bar{W}_1(t_{s2})$. The static admissibility conditions (3-35) may not be satisfied, i.e. the absolute value of shear forces q_1 at the right-hand support may be slightly larger than the limit shear strength, if $\nu_1 < 1 + 0.5gr(1+r)/[g(1+r) + 3r]$, but we neglect this case herein.

For $1 < \nu_1 < \frac{3}{2}$, equations (3-6) shows that equations (3-44) and (3-46b-f) are valid only when $\frac{6}{g} \geqslant \nu_1 z_2^2$ and $\frac{3}{g} \geqslant \frac{\nu_1}{r^2}$, respectively. If $\frac{6}{g} < \nu_1 z_2^2$ (corresponding to equations (3-44)) or $\frac{3}{g} < \frac{\nu_1}{r^2}$ (corresponding to equations (3-46b-f)), a yield violation of bending moment occurs on the left side of impact point since $\left.\frac{\partial m_2}{\partial z}\right|_{z=0^-} = 2\nu_1 q_{20} < 0$. Therefore, a new velocity profile shown in Fig. 22a

$$\dot{\bar{W}}(z) = \begin{cases} 0 & \frac{1}{r} \leqslant z \leqslant -z_2^- \\ \dot{\bar{W}}_3 \frac{z_2+z}{z_2-z_0} & -z_2^+ \leqslant z \leqslant -z_0^- \\ (\dot{\bar{W}}_2-\dot{\bar{W}}_3) \frac{z}{z_0} + \dot{\bar{W}}_2 & -z_0^+ \leqslant z \leqslant 0^- \\ \dot{\bar{W}}_1(1-z) & 0^+ \leqslant z \leqslant 1 \end{cases} \tag{3-47}$$

is assumed which means that the bending moment at z=0 is now less than plastic limit moment but a new travelling hinge appears at $z = -z_0$. The linear and angular momentum equations of beam shown in Fig. 33b are

$$g\ddot{\bar{W}}_1 = -6u - 6um_1(0) + 12u\nu_1 \tag{3-48a}$$

$$gz_0[\ddot{\bar{W}}(-z_0^+) + \ddot{\bar{W}}_2] + 2\ddot{\bar{W}}_2 = -8u\nu_1 \tag{3-48b}$$

$$2gz_0^2\ \ddot{\bar{W}}(-z_0^+) + gz_0^2\ \ddot{\bar{W}}_2 = -12u + 12um_1(0) \tag{3-48c}$$

$$2g(z_2-z_0)^2\ \ddot{\bar{W}}(-z_0^-) + g(z_2-z_0)^2\ \ddot{\bar{W}}(-z_2^+) = -24u \tag{3-48d}$$

and $$\ddot{\bar{W}}(-z_0^-) + \ddot{\bar{W}}(-z_2^+) = 0 \tag{3-48e}$$

where $\ddot{\bar{W}}(-z_0^-) = \ddot{\bar{W}}_3 + \dot{\bar{W}}_3\dot{z}_0/(z_2-z_0)$, $\ddot{\bar{W}}(-z_0^+) = \ddot{\bar{W}}_3 + (\dot{\bar{W}}_2-\dot{\bar{W}}_3)\dot{z}_0/z_0$ and $\ddot{\bar{W}}(-z_2^+) = \dot{\bar{W}}_3\dot{z}_2/(z_2-z_0)$ are given by equation (3-47).

Equations (3-47) and (3-48) with the geometrical condition at the shear hinge $z=0^+$ give

$$\ddot{\bar{W}}_1 = 2u \frac{[2(z_0^2 + 2z_0 + \frac{2}{g})\nu_1 - 4(z_0 + \frac{1}{g})]}{\frac{2}{3} z_0^3 + \frac{1}{6} g z_0^4 + \frac{2}{3} g z_0 + \frac{2}{3}} \qquad (3\text{-}49a)$$

$$\ddot{\bar{W}}_2 = -2u \frac{[2(\frac{2}{3} z_0^3 + z_0^2 + \frac{2}{3})\nu_1 - 2z_0^2]}{\frac{2}{3} z_0^3 + \frac{1}{6} g z_0^4 + \frac{2}{3} g z_0 + \frac{2}{3}} \qquad (3\text{-}49b)$$

$$(\dot{\bar{W}}_2 - \dot{\bar{W}}_3) + \dot{\bar{W}}_1 z_0 = 0 \qquad (3\text{-}49c)$$

$$(z_2 - z_0)^2 \ddot{\bar{W}}_3 + (z_2 - z_0)(\dot{z}_0 + \frac{1}{2} \dot{z}_2)\dot{\bar{W}}_3 = -12u/g \qquad (3\text{-}49d)$$

$$\dot{\bar{W}}_3 \dot{z}_2 = 24u/[g(z_2 - z_0)] \qquad (3\text{-}49e)$$

Equations (3-49) can be solved by a numerical method. For $\frac{6}{g} < \nu_1 z_2^2$ (corresponding to equations (3-44)), this type of motion starts with $z_0=0$ when $z_2 = \sqrt{\frac{6}{g\nu_1}}$ and the other initial conditions can be obtained from equations (3-44) with $z_2 = \sqrt{\frac{6}{g\nu_1}}$. For $\frac{3}{g} < \frac{\nu_1}{r^2}$ (corresponding to equations (3-46)), the motion is governed by equations (3-47), (3-48a-d) and (3-49a-d) with $z_2 = \frac{1}{r}$ and $\dot{z}_2 = 0$, and the initial conditions are given by equations (3-44) with $t=\bar{t}_2$ which is defined by equation (3-46a). The static admissibility conditions should be checked during the numerical calculation*.

The shear deformations in this case discussed in this section are

$$\bar{W}_{2s} = \bar{W}_1(t_{s2}) + \bar{W}_{1s} - \bar{W}_2(t_{s2}) \quad \text{if } \frac{3}{2} \leqslant \nu_1 \leqslant 3 \qquad (3\text{-}50)$$

where $\bar{W}_{1s}$ is defined by equation (3-39i) and t_{s2} is the time when the shear sliding at $z=0^-$ stops; or

$$\bar{W}_{1s} = \bar{W}_2(t_{s2}) + \bar{W}_{2s} - \bar{W}_1(t_{s2}) \text{ if } 1 < \nu_1 < \frac{3}{2} \qquad (3\text{-}51)$$

---

* see equations (26) in Appendix I.

where $\bar{W}_{2s}$ is defined by equation (3-39k) and t_{s2} is the time when the shear sliding at $z=0^+$ stops.

3.3.3 Case III, $0 < \nu_1 \leqslant 1$ and $\nu_2 > 3$

Equation (3-39c) shows that $\dot{\bar{W}}_1 < 0$ and $\ddot{\bar{W}}_1 < 0$ when $\nu_1 < 1$. This is impossible since $q_1 < q_{10} = -1$ and yield violations of shear force will occur in $0^+ \leqslant z \leqslant 1$, if $\ddot{\bar{W}}_1 < 0$. Therefore, a new velocity profile shown in Fig. 23a is assumed, in which the part of beam on the right side of impact point remains stationary during the entire response. Equations (3-4) and (3-5c-e) with $\dot{\bar{W}}_1 = 0$ and $q_{10} = -1$ give

$$\frac{1}{12}\frac{g}{u}(\dot{\bar{W}}_2 z_2^2)'_t = 2 \qquad (3\text{-}52a)$$

$$q_{20} = \frac{1}{8}\frac{g}{u\nu_1}(\dot{\bar{W}}_2 z_2)'_t \qquad (3\text{-}52b)$$

and

$$q_{20} + 1 = -\frac{1}{4}\frac{}{u\nu_1}\ddot{\bar{W}}_0 \qquad (3\text{-}52c)$$

A) Phase 1, shear sliding

a) $0 \leqslant t \leqslant t_{s1}$

Two shear slidings occur at $z=0^-$ and $z=0^+$ after impact, shown in Fig. 23a. Equations (3-52) with $q_{20} = 1$ give

$$\dot{\bar{W}}_0 = 2u - 8u\nu_1 t,\ \dot{\bar{W}}_2 = \frac{8}{3}\frac{u}{g}\nu_1^2 t,\ z_2 = \frac{3}{\nu_1} \qquad (3\text{-}53a\text{-}c)$$

$$\bar{W}_0 = 2ut - 4u\nu_1 t^2 \text{ and } \bar{W}_2 = \frac{4}{3}\frac{u}{g}\nu_1^2 t^2 \qquad (3\text{-}53d,e)$$

since $\dot{\bar{W}}_0 = 2u$, $\dot{\bar{W}}_2 = 0$, $\bar{W}_0 = 0$ and $\bar{W}_2 = 0$. Equations (3-53a) and (3-53b) give $\dot{\bar{W}}_0 = \dot{\bar{W}}_2$ at

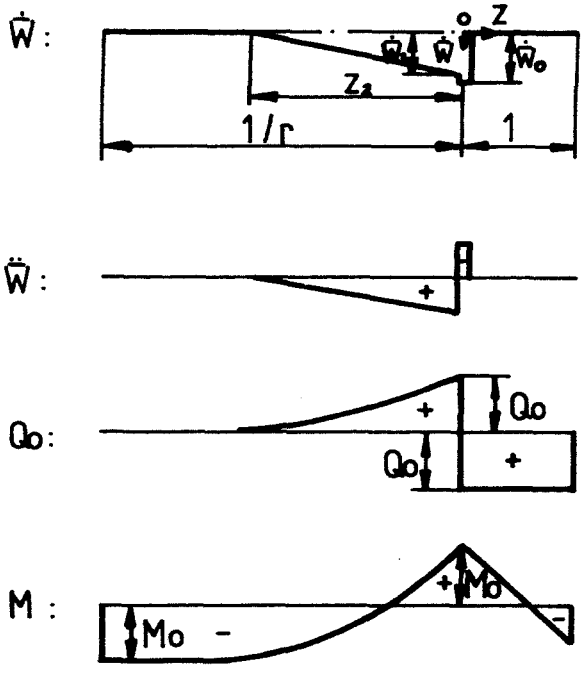

FIG. 23 First phase of motion for $0 < \nu_1 \leqslant 1$ and $\nu_2 > 3$ (case III).

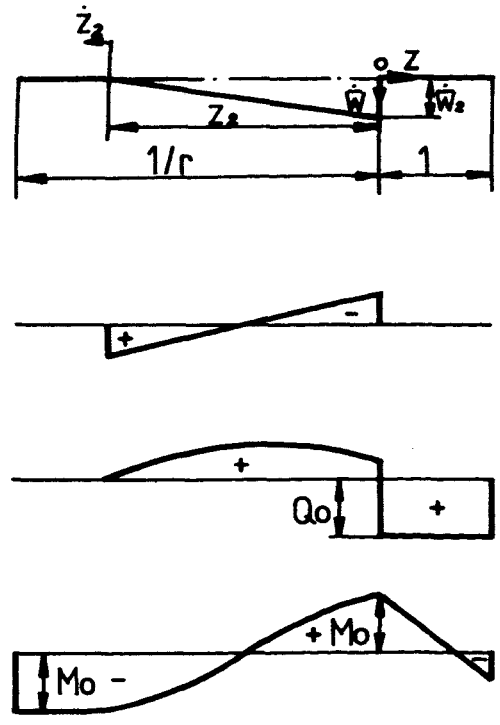

FIG. 24 Motion of case III when $t_{s1} < t \leqslant t_2$.

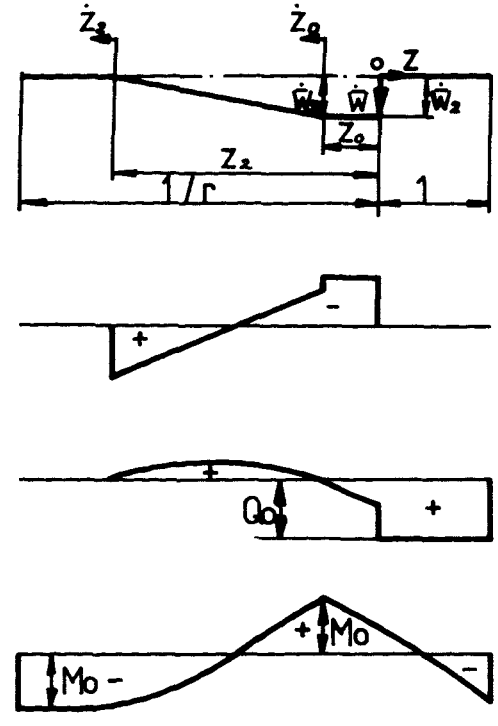

FIG. 25 Motion of case III when $t_{s1} < t \leqslant t_2$, if $\frac{6}{g} < \nu_1 z_2^2$.

$$t = t_{s1} = \frac{3}{4}\frac{g}{v_1(v_1+3g)} \text{ and } \bar{W}_{2s} = \frac{3ug}{4v_1(v_1+3g)} \qquad (3\text{-}53f,g)$$

The static admissibility conditions can be proved to be satisfied by equations (3-6) with $q_1 = q_{10} = -1$, $-1 \leqslant m_1 \leqslant 1$, $0 \leqslant q_2 \leqslant 1$ and $-1 \leqslant m_2 \leqslant 1$.

b) $\underline{t_{s1} < t \leqslant t_2}$

The shear sliding at $z=0^-$ stops at $t=t_{s1}$ and the following motion shown in Fig. 24a is still governed by equations (3-52) with $\dot{\bar{W}}_0 = \dot{\bar{W}}_2$. The equations (3-44c-i) are valid in this case and the velocities $\dot{\bar{W}}_1$ and $\dot{\bar{W}}_2$ and the deformations $\bar{W}_1$ and $\bar{W}_2$ can be obtained from equations (3-44a,b,e,h) with t_{s1} given by equation (3-53f) until

$$t = t_2 = \frac{g}{6gr+12r^2+2v_1 g} \qquad (3\text{-}54)$$

since equations (3-38) is the same as equations (3-52) when $q_{10} = -1$ and $\dot{\bar{W}}_1 = 0$, where t_2 is the time when the travelling plastic hinge reaches the left-hand support. It shows from previous analysis in case II that equations (3-44) are valid only when $\frac{6}{g} \geqslant v_1 z_2^2$.

$\underline{\text{If } \frac{6}{g} < v_1 z_2^2}$, equations (3-44) are no longer valid since $\left.\frac{\partial m_2}{\partial z_2}\right|_{z=0^-} = 2v_1 q_{20} < 0$. Therefore, a new velocity profile shown in Fig. 25a.

$$\dot{\bar{W}}(z) = \begin{cases} 0 & -\frac{1}{r} \leqslant z \leqslant -z_2^- \\ \dot{\bar{W}}_3 \frac{z_2+z}{z_2-z_0} & -z_2^+ \leqslant z \leqslant -z_0^- \\ \dot{\bar{W}}_2 & -z_0^+ \leqslant z \leqslant 0^- \\ 0 & 0^+ \leqslant z \leqslant 1 \end{cases} \qquad (3\text{-}55)$$

is postulated, where $\dot{\bar{W}}_2 = \dot{\bar{W}}_3$ according to geometrical conditions at shear hinge. The linear and angular momentum equations of beam shown in Fig. 34 are

$$z_0 g \ddot{\bar{W}}_2 + \ddot{\bar{W}}_2 + 4u\nu_1 = 0 \qquad (3\text{-}56a)$$

$$2g(z_2-z_0)^2 \ddot{\bar{W}}(-z_0^-) + g(z_2-z_0)^2 \ddot{\bar{W}}(-z_2^+) = -24u \qquad (3\text{-}56b)$$

$$\ddot{\bar{W}}(-z_0^-) + \ddot{\bar{W}}(-z_2^+) = 0 \qquad (3\text{-}56c)$$

where $$\ddot{\bar{W}}(-z_0^-) = \ddot{\bar{W}}_2 + \frac{\dot{z}_0 \dot{\bar{W}}_2}{z_2-z_0} \text{ and } \ddot{\bar{W}}(-z_2^+) = \frac{\dot{\bar{W}}_2 \dot{z}_2}{z_2-z_0} \qquad (3\text{-}56d,e)$$

since $\dot{\bar{W}}_2 = \dot{\bar{W}}_3$.

Equations (3-56) give

$$(z_2-z_0)^2 \ddot{\bar{W}}_2 + (z_2-z_0)(\dot{z}_0 + \frac{1}{2}\dot{z}_2)\dot{\bar{W}}_2 = -\frac{12u}{g} \qquad (3\text{-}57a)$$

$$(gz_0+1)\ddot{\bar{W}}_2 = -4u\nu_1 \qquad (3\text{-}57b)$$

and $$\dot{\bar{W}}_2 \dot{z}_2 = {}^{24u}/_{[g(z_2-z_0)]} \qquad (3\text{-}57c)$$

Equations (3-57) can be solved by a numerical method until $z_2 = \frac{1}{r}$. This kind of motion starts with $z_0 = 0$ when $z_2 = \sqrt{\frac{6}{g\nu_1}}$ and the other initial conditions can be obtained from equations (3-44e-i). Equations (3-55), (3-56) and (3-57) are only valid when $m_1(1) \geq -1$ or

$$(gz_0+1)(1-\nu_1) \geq \frac{1}{2} g\nu_1 z_0^2 \qquad (3\text{-}57d)$$

and the other static admissibility conditions must be checked during the numerical calculation*.

---

* see equations (30) in Appendix I.

If equation (3-57d) is not satisfied, the motion of beam is controlled by equations (3-47), (3-48) and (3-49).

c) $t_2 < t \leqslant t_f$

The travelling plastic hinge at $z = -z_2$ reaches the left-hand support at $t = t_2$ which is defined by equation (3-54). The following motion is that the right part of beam still remains stationary while the left part rotates about the left-hand support, and the shear sliding at $z=0^+$ continues.

Equations (3-4), (3-5c) and (3-5e) with $\dot{\bar{w}}_1 = 0$, $\dot{\bar{w}}_0 = \dot{\bar{w}}_2$, $q_{10} = -1$, $z_2 = \frac{1}{r}$ and $\dot{z}_2 = 0$ give

$$\dot{\bar{w}}_2 = -\frac{12u(r+v_1)r}{g+3r}(t-t_2) + \dot{\bar{w}}_2(t_2) \qquad (3\text{-}58a)$$

$$\bar{w}_2 = \frac{-6u(r+v_1)r}{g+3r}(t-t_2)^2 + \dot{\bar{w}}_2(t_2)(t-t_2) + \bar{w}_2(t_2) \qquad (3\text{-}58b)$$

Equation (3-58a) gives that $\dot{\bar{w}}_2 = 0$ when

$$t = t_f = \dot{\bar{w}}_2(t_2)(g+3r)/[12u(r+v_1)r] + t_2 \qquad (3\text{-}58c)$$

The maximum permanent deformation

$$\bar{w}_{2f} = \frac{(g+3r)}{24u(r+v_1)r}\dot{\bar{w}}_2^2(t_2) + \bar{w}_2(t_2) \qquad (3\text{-}58d)$$

is obtained from equations (3-58b,c). The shear sliding at $z=0^+$ is

$$\bar{w}_{1s} = \bar{w}_{2f} + \bar{w}_{2s} \qquad (3\text{-}59)$$

where $\bar{w}_{2s}$ is defined by equation (3-53g).

Equations (3-6) show that the static admissibility conditions

are satisfied and the solution given in equations (3-58) is 'exact', provided $\frac{3}{g} \geqslant {}^{\nu}1/r^2$.

If $\frac{3}{g} < {}^{\nu}1/r^2$, the motion of beam is governed by equations (3-57a) and (3-57b) with $z_2 = \frac{1}{r}$ and $\dot{z}_2 = 0$. The initial conditions are that $\dot{\bar{w}}_2 = \dot{\bar{w}}_2(t_2)$ and z_0 is defined by equations (3-57a) and (3-57b) with $\dot{z}_0 = 0$.

3.3.4 Case IV, $1 < \nu_1 \leqslant \nu_2 \leqslant 3$

Equations (3-39a) shows that if $\nu_2 < 3$ the velocity profile introduced in phase 1 of case II is no longer valid since z_2 must be less than $\frac{1}{r}$ (or equal to $\frac{1}{r}$, but when $z_2 = \frac{1}{r}$ we will discuss in this section). In this case we assume that $z_1 = 1$, $\dot{z}_1 = 0$, $z_2 = \frac{1}{r}$, $\dot{z}_2 = 0$.

Equations (3-4), (3-5a), (3-5c) and (3-5d) with $z_1 = 1$, $\dot{z}_1 = 0$, $z_2 = \frac{1}{r}$ and $\dot{z}_2 = 0$ give

$$\ddot{\bar{w}}_1 = -\frac{12u(1+q_{10}\nu_1)}{g} \tag{3-60a}$$

$$\ddot{\bar{w}}_2 = -\frac{12u(r-q_{20}\nu_1)r}{g} \tag{3-60b}$$

and

$$-q_{10} + q_{20} = -\frac{\ddot{\bar{w}}_0}{4u\nu_1} \tag{3-60c}$$

A) Phase 1, shear sliding

a) $0 \leqslant t \leqslant t_{s1}$

Two shear hinges occurs on both sides of the struck point of beam, i.e. shear sliding occurs at $z=0^-$ and $z=0^+$ where shear

force $q_{10} = -1$ and $q_{20} = 1$, respectively. Two parts of beam rotate about the supports. The velocity profile is shown in Fig. 26a.

Equations (3-60) with $q_{10} = -1$ and $q_{20} = 1$ give

$$\dot{\bar{W}}_0 = 2u - 8u\nu_1 t,\ \dot{\bar{W}}_1 = \frac{12u}{g}(\nu_1-1)t,\ \dot{\bar{W}}_2 = \frac{12ur}{g}(\nu_1-r)t \qquad (3\text{-}61a\text{-}c)$$

$$\bar{W}_0 = 2ut - 4u\nu_1 t^2,\ \bar{W}_1 = \frac{6u}{g}(\nu_1-1)t^2,\ \bar{W}_2 = \frac{6ur}{g}(\nu_1-r)t^2 \qquad (3\text{-}61d\text{-}f)$$

since $\dot{\bar{W}}_0 = 2u$, $\dot{\bar{W}}_1 = \dot{\bar{W}}_2 = \bar{W}_0 = \bar{W}_1 = \bar{W}_2 = 0$ at $t = 0$.

It is shown from equations (3-61b) and (3-61c) that

if $\nu_1 \geqslant 1 + r$, $\dot{\bar{W}}_1 \geqslant \dot{\bar{W}}_2$ and $\dot{\bar{W}}_1 = \dot{\bar{W}}_0$ at $t = t_{s1} = \frac{g}{4\nu_1 g - 6 + 6\nu_1}$;

(3-62a)

if $\nu_1 < 1 + r$, $\dot{\bar{W}}_1 < \dot{\bar{W}}_2$ and $\dot{\bar{W}}_2 = \dot{\bar{W}}_0$ at $t = t_{s1} = \frac{g}{6r(\nu_1-r)+4\nu_1 g}$

(3-62b)

The shear deformations are

$$\bar{W}_{1s} = \frac{ug}{4\nu_1 g - 6 + 6\nu_1} \qquad \text{if } \nu_1 \geqslant 1 + r \qquad (3\text{-}62c)$$

$$\bar{W}_{2s} = \frac{ug}{6r(\nu_1-r)+4\nu_1 g} \qquad \text{if } \nu_1 < 1 + r \qquad (3\text{-}62d)$$

Equations (3-6) shows that the static admissibility conditions are satisfied.

b) $t_{s1} < t \leqslant t_{s2}$

If $\nu_1 \geqslant 1 + r$, the shear sliding at $z=0^+$ stops at $t=t_{s1}$, where t_{s1} is defined in equation (3-62a), while the shear sliding at $z=0^-$

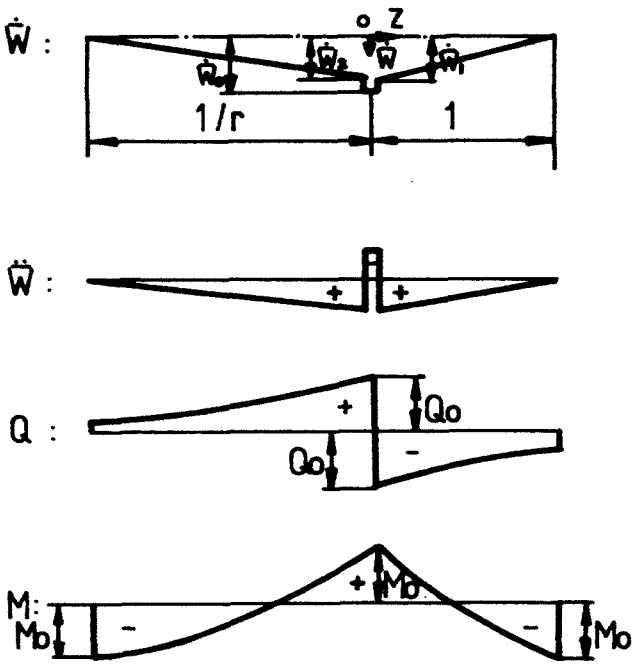

FIG. 26 First phase of motion for $1 < \nu_1 \leqslant \nu_2 \leqslant 3$ (case IV).

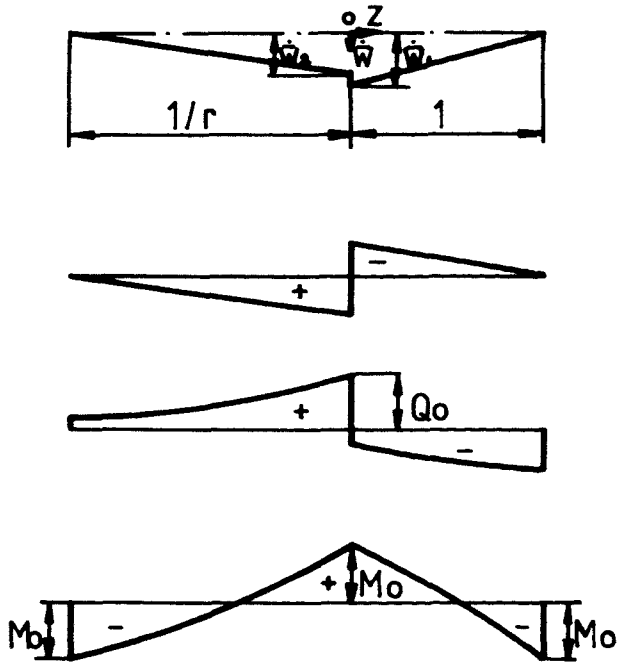

FIG. 27 Motion of case IV for $\nu_1 \geqslant 1 + r$ when $t_{s1} < t \leqslant t_{s2}$.

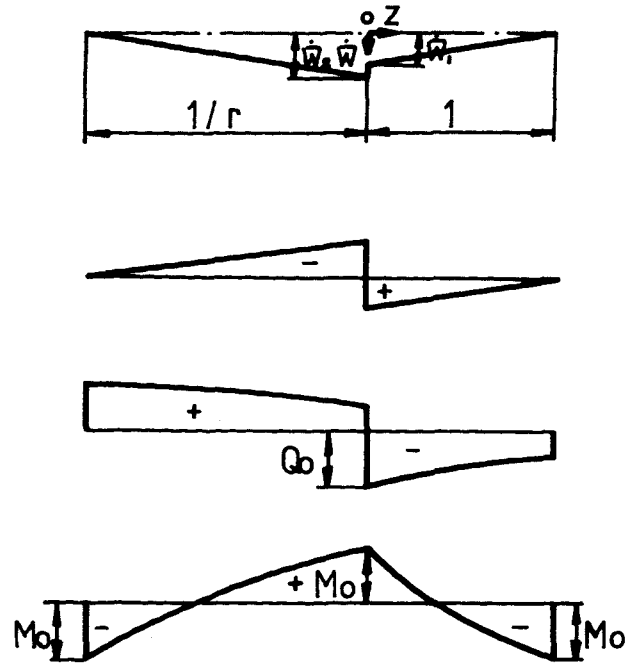

FIG. 28 Motion of case IV for $\nu_1 < 1 + r$ when $t_{s1} < t \leqslant t_{s2}$.

continues. The velocity profile is shown in Fig. 27a.

Equations (3-60) with $q_{20} = 1$ and $\dot{\bar{W}}_1 = \dot{\bar{W}}_0$ give

$$\dot{\bar{W}}_1 = -\frac{12u(\nu_1+1)}{3+g}\,t + \frac{6u}{3+g},\quad \dot{\bar{W}}_2 = \frac{12ur}{g}\,(\nu_1-r)t, \qquad (3\text{-}63a,b)$$

$$\bar{W}_1 = -\frac{6u(\nu_1+1)}{3+g}\,t^2 + \frac{6u}{3+g}t - \frac{3}{2}\frac{ug}{(3+g)(2\nu_1 g-3+3\nu_1)} \qquad (3\text{-}63c)$$

and $$\bar{W}_2 = \frac{6ur}{g}\,(\nu_1-r)t^2 \qquad (3\text{-}63d)$$

The shear sliding at $z=0^-$ stops at

$$t = t_{s2} = \frac{g}{2}\frac{1}{r(\nu_1-r)(3+g)+g(1+\nu_1)} \qquad (3\text{-}63e)$$

when $\dot{\bar{W}}_1 = \dot{\bar{W}}_2$.

Equations (3-6) shows that

$$q_{1\min} = -\frac{1}{\nu_1}\frac{g\nu_1+3g+6}{2g+6} \gtrless -1 \quad \text{if } \nu_1 \gtrless \frac{3(2+g)}{6+g} \qquad (3\text{-}63f)$$

$0 < q_2 \leqslant 1,\quad -1 \leqslant m_2 \leqslant 1$

and $-1 \leqslant m_1 \leqslant 1$ if $\frac{3}{g} \geqslant \nu_1$.

If $\frac{3}{g} < \nu_1$, the solution given by equations (3-63) is no longer valid since $\left.\frac{\partial m_1}{\partial z}\right|_{z=0^+} = 2\nu_1 q_{10} > 0$ and a yield violation of bending moment occurs on the right side of impact point. In this case, the motion of beam is controlled by equations (3-43a-d) with $\dot{z}_2 = 0$ and $z_2 = \frac{1}{r}$.

Equation (3-63f) shows that the absolute value of shear force at $z = 1$ may be slightly larger than 1 in a very narrow range of

$\frac{4}{3} < \nu_1 < \frac{3}{2}^*$ if $\frac{3}{g} \geqslant \nu_1$, but we neglect this case herein.

If $\nu_1 < 1 + r$, the shear sliding at $z=0^-$ stops at $t = t_{s1}$, where t_{s1} is defined by equation (3-62b), while the shear sliding at $z=0^+$ continues. The velocity profile is shown in Fig. 28a.

Equations (3-60) with $q_{10} = -1$ and $\dot{\bar{W}}_2 = \dot{\bar{W}}_0$ give

$$\dot{\bar{W}}_1 = \frac{12u}{g}(\nu_1-1)t, \quad \dot{\bar{W}}_2 = -\frac{12u(r+\nu_1)r}{3r+g}t + \frac{6ur}{3r+g}, \qquad (3\text{-}64a,b)$$

$$\bar{W}_1 = \frac{6u}{g}(\nu_1-1)t^2 \qquad (3\text{-}64c)$$

and

$$\bar{W}_2 = -\frac{6u(r+\nu_1)r}{3r+g}t^2 + \frac{6ur}{3r+g}t - \frac{3ur}{3r+g}t_{s1}. \qquad (3\text{-}64d)$$

The shear sliding at $z=0^+$ stops at

$$t = t_{s2} = \frac{rg}{(\nu_1-1)(3r+g)+r^2g(1+\nu_2)} \qquad (3\text{-}64e)$$

when $\dot{\bar{W}}_1 = \dot{\bar{W}}_2$.

Equations (3-6) shows that

$$q_{2max} = \frac{3rg+6r^2+\nu_1 g}{2\nu_1(g+3r)} \leqslant 1, \text{ if } \nu_1 \geqslant \frac{3r(g+2r)}{g+6r} \qquad (3\text{-}64f)$$

$$-1 \leqslant q_1 < 0, \quad -1 \leqslant m_1 \leqslant 1$$

and $\quad -1 \leqslant m_2 \leqslant 1$, if $\frac{3}{g} \geqslant \frac{\nu_1}{r^2}$.

If $\frac{3}{g} < \frac{\nu_1}{r^2}$, the solution given by equations (3-64) is no longer

---

* It is clear that $\nu_1 > \frac{4}{3}$ since $\nu_1 \geqslant 1 + r$ and $r = \frac{\nu_1}{\nu_2} > \frac{1}{3}$. Equation (3-63f) shows that $q_{1min} \geqslant -1$ if $\nu_1 \geqslant \frac{3(2\nu_1+3)}{(6\nu_1+3)}$ or $\nu_1 \geqslant \frac{3}{2}$ since $\frac{3}{g} \geqslant \nu_1$. Therefore $|q_{1min}|$ may be larger than 1 only in $\frac{4}{3} < \nu_1 < \frac{3}{2}$.

valid since $\left.\frac{\partial m_2}{\partial z}\right|_{z=0^-} = 2\nu_1 q_{20} < 0$ and a yield violation of bending moment occurs on the left side of impact point. In this case, the motion of beam is governed by equations (3-49a-d) with $z_2 = \frac{1}{r}$ and $\dot{z}_2 = 0$.

Equation (3-64f) shows that the maximum shear force q_{2max} which occurs at $z = -\frac{1}{r}$ may be larger than 1 for $1 < \nu_1 < \frac{3}{2} r^*$ if $\frac{3}{g} \geqslant \nu_1$, but we neglect this case herein.

B) Phase 2, $t_{s2} < t \leqslant t_f$

The motion of this phase is the same as that of phase 4 in case I. The absolute value of shear force q_1 at z=1 may be larger than 1 for $1 < \nu_1 < 1 + \frac{1}{2} r^2$ if $\frac{3}{g} \geqslant \frac{1}{r^2} - 1$, but this case is neglected herein.

The shear deformations in this case are that

$$\bar{W}_{2s} = \bar{W}_1(t_{s2}) + \bar{W}_{1s} - \bar{W}_2(t_{s2}) \quad \text{if } \nu_1 \geqslant 1 + r \tag{3-65}$$

where $\bar{W}_{1s}$ is defined by equation (3-62c) and t_{s2} is the time when the shear sliding at $z=0^-$ stops; or

$$\bar{W}_{1s} = \bar{W}_2(t_{s2}) + \bar{W}_{2s} - \bar{W}_1(t_{s2}) \quad \text{if } \nu_1 < 1 + r \tag{3-66}$$

where $\bar{W}_{2s}$ is defined by equation (3-62d) and t_{s2} is the time when the shear sliding at $z=0^+$ stops.

---

* Equation (3-64f) shows that $q_{2max} \leqslant 1$ if $\nu_1 \geqslant \frac{3r^2+2r\nu_1}{r+2\nu_2}$ or $\nu_1 \geqslant \frac{3}{2} r$ since $\frac{3}{g} \geqslant \nu_1$.

3.3.5 Case V, $0 < \nu_1 \leq 1$ and $1 < \nu_2 \leq 3$

It is assumed according to equation (3-53c) that $\dot{z}_1 = 0$, $z_1 = 1$, $\dot{z}_2 = 0$ and $z_2 = \frac{1}{r}$. Equations (3-4), (3-5c) and (3-5e) with $\dot{z}_2 = 0$, $z_2 = \frac{1}{r}$ and $q_{10} = -1$ give

$$\ddot{\bar{w}}_2 = -12u(r-q_{20}\nu_1)r\ /g \tag{3-67a}$$

and

$$q_{20} = -1 - \frac{1}{4u\nu_1}\ddot{\bar{w}}_0 \tag{3-67b}$$

A) Phase 1, shear sliding

a) $0 \leq t \leq t_{s1}$

Two shear slidings occur at $z=0^-$ and 0^+ after impact and the velocity profile is shown in Fig. 29a. Equations (3-67) with $q_{20} = 1$ give

$$\dot{\bar{w}}_0 = 2u - 8u\nu_1 t,\ \dot{\bar{w}}_2 = \frac{12u(\nu_1-r)r}{g}\,t \tag{3-68a,b}$$

$$\bar{w}_0 = 2ut - 4u\nu_1 t^2 \text{ and } \bar{w}_2 = \frac{6u(\nu_1-r)r}{g}\,t^2 \tag{3-68c,d}$$

since $\dot{\bar{w}}_0 = 2u$, $\dot{\bar{w}}_2 = \bar{w}_0 = \bar{w}_2 = 0$.

The shear sliding at $z=0^-$ stops at

$$t = t_{s1} = \frac{g}{6(\nu_1-r)r+4\nu_1 g} \tag{3-68e}$$

when $\dot{\bar{w}}_0 = \dot{\bar{w}}_2$ and the shear deformation at $z=0^-$ is

$$\bar{w}_{2s} = \frac{ug}{6(\nu_1-r)r+4\nu_1 g} \tag{3-68f}$$

Equations (3-6) show that the static admissibility conditions are satisfied with

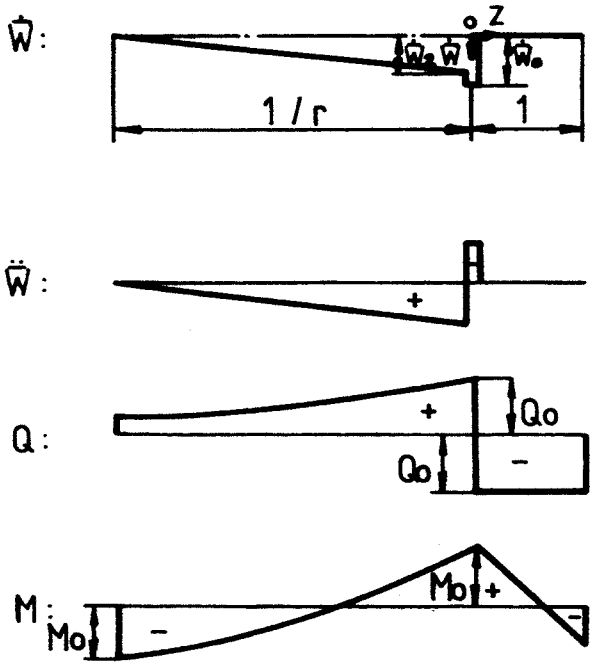

FIG. 29 First phase of motion for $0 < \nu_1 \leqslant 1$ and $1 < \nu_2 \leqslant 3$ (case V).

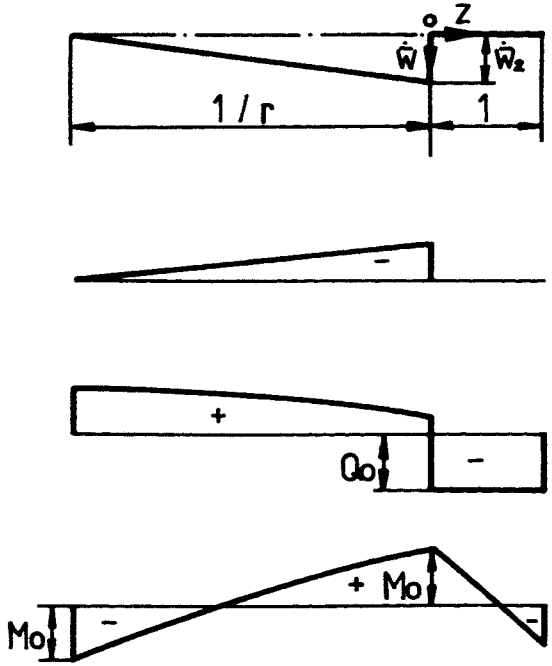

FIG. 30 Motion of case V when $t_{s1} < t \leqslant t_f$, if $\frac{3}{g} \geqslant \frac{1}{r^2}$.

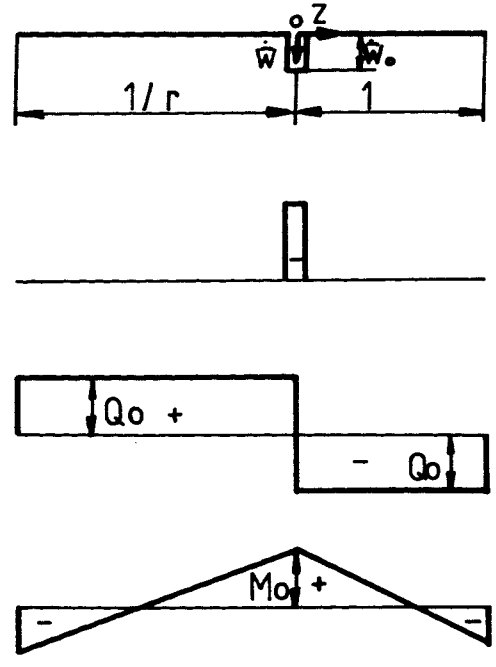

FIG. 31 Motion of case IV ($0 < \nu_1 \leqslant \nu_2 \leqslant 1$).

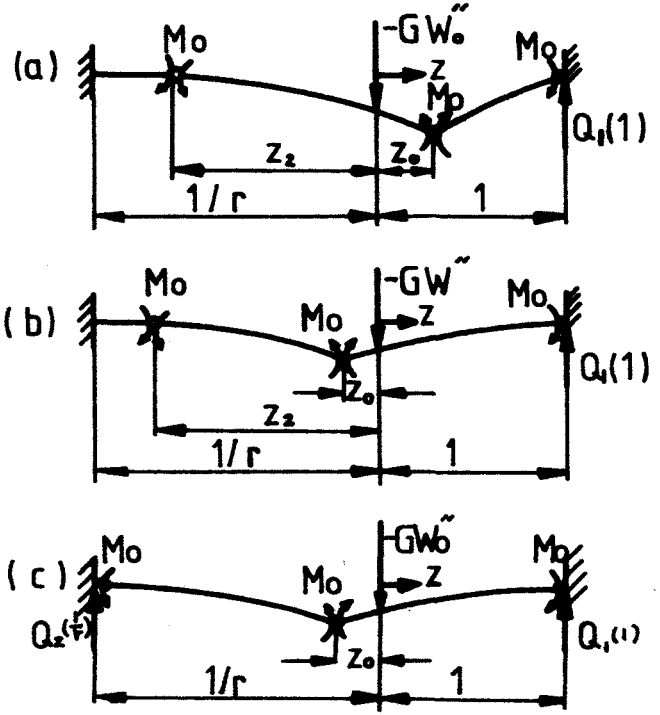

FIG. 32 Mechanisms of motion for case I. (a) $\frac{4}{g} < \frac{2}{z_2(t_1)} - z_2(t_1)$; (b) $\frac{3}{g} < \frac{1}{2} z_2^2 - 1$; and (c) $\frac{3}{g} < \frac{1}{r^2} - 1$.

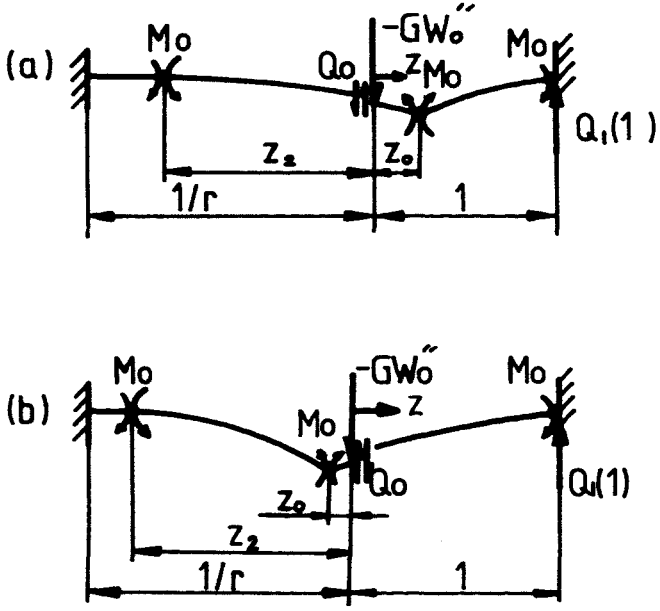

FIG. 33 Mechanisms of motion for case II. (a) $\frac{3}{g} < \nu_1$; (b) $\frac{6}{g} < \nu_1 z_2^2$.

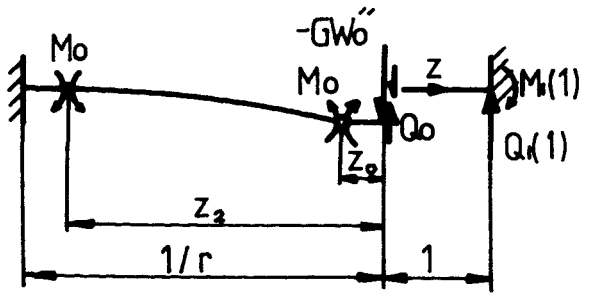

FIG. 34 Mechanisms of motion for case III when $\frac{6}{g} < \nu_1 z_2^2$.

$$q_1 = -1,\ 0 \leqslant q_2 \leqslant 1,\ -1 \leqslant m_1 \leqslant 1 \text{ and } -1 \leqslant m_2 \leqslant 1.$$

b) $t_{s1} < t \leqslant t_f$

The shear sliding at $z=0^-$ stops at $t=t_{s1}$ but the other one at $z=0^+$ continues. The right part of beam remains stationary, while the left rotates about the left-hand support. The velocity profile is shown in Fig. 30a.

Equations (3-67) with $\dot{\bar{W}}_0 = \dot{\bar{W}}_2$ give

$$\dot{\bar{W}}_2 = -\frac{12(r+\nu_1)ur}{g+3r}\,t + \frac{6ur}{g+3r} \tag{3-69a}$$

$$\bar{W}_2 = -\frac{6(r+\nu_1)ur}{g+3r}\,t^2 + \frac{6ur}{g+3r}\,t - \frac{3ur}{g+3r}\,t_{s1} \tag{3-69b}$$

The motion of the beam stops at

$$t_f = \frac{1}{2(r+\nu_1)} \tag{3-69c}$$

when $\dot{\bar{W}}_2 = 0$ and the permanent deformation is

$$\bar{W}_{2f} = \frac{3ur(\nu_1-r)}{(r+\nu_1)[6(\nu_1-r)r+4\nu_1 g]} \tag{3-69d}$$

Equations (3-6) shows that equations (3-69) are valid only when $\frac{3}{g} \geqslant \frac{\nu_1}{r^2}$ because of the static admissibility conditions. (The absolute value of shear force q_2 at $z = -\frac{1}{r}$ may be larger than 1 for $1 < \nu_2 < \frac{3}{2}$ if $\frac{3}{g} \geqslant \frac{\nu_1}{r^2}$, but this case is neglected herein.)

If $\frac{3}{g} < \frac{\nu_1}{r^2}$, there is a violation of the bending moment at the left side of impact point since $\left.\frac{\partial m_2}{\partial z}\right|_{z=0^-} = 2\nu_1 q_{20} < 0$. In this case the motion of beam is governed by equations (3-57a,b) with $z_2 = \frac{1}{r}$

and $\dot{z}_2 = 0$, provided inequality (3-57d) is satisfied. Otherwise, it is governed by equations (3-49a-d).

The shear deformation at $z=0^+$ in this case is

$$\bar{W}_{1s} = \bar{W}_2(t_f) + \bar{W}_{2s} \tag{3-70}$$

where $\bar{W}_{2s}$ is defined by equation (3-68f) and t_f is the time when the motion of beam stops.

3.3.6 Case VI, $0 < \nu_1 \leq \nu_2 \leq 1$

Equation (3-68b) shows that $\dot{\bar{W}}_2 < 0$ and $\ddot{\bar{W}}_2 < 0$ when $\nu_2 = \frac{\nu_1}{r} < 1$. This is impossible since $q_2 > q_{20} = 1$ and yield violations of shear force will occur in $-\frac{1}{r} < z < 0^-$ if $\ddot{\bar{W}}_2 < 0$. Therefore, a new velocity profile shown in Fig. 31a is assumed, in which two shear slidings occur at $z=0^-$ and $z=0^+$ and the struck point of beam moves transversely downwards with the striker while the rest of beam remains stationary. Equation (3-5e) with $q_{10} = -q_{20} = -1$ give

$$\dot{\bar{W}}_0 = 2u - 8u\nu_1 t \text{ and } \bar{W}_0 = 2ut - 4u\nu_1 t^2 \tag{3-71a,b}$$

since $\dot{\bar{W}}_0 = 2u$ and $\bar{W}_0 = 0$ at $t = 0$.

The motion of beams stops at

$$t_f = \frac{1}{4\nu_1} \tag{3-71c}$$

when $\dot{\bar{W}}_0 = 0$. The maximum permanent deformation of beam is

$$\bar{W}_{0f} = \frac{u}{4\nu_1} \tag{3-71d}$$

Equations (3-6) show that the static admissibility conditions

are satisfied with $q_1 = -1$, $q_2 = 1$, $-1 \leqslant m_1 \leqslant 1$, $-1 \leqslant m_2 \leqslant 1$.

3.4 Calculation

A computer programme was written to generate results for the response of a beam struck by a mass at any point of its span. A flow diagram showing the solution method is given in Fig. 35.

The maximum permanent deformations and shear sliding deformations of most cases can be directly obtained from the theoretical analysis in Section 3.3, while for the remaining cases with a travelling plastic hinge occurs at $z = -z_0$ or $z = z_0$ instead of a stationary plastic hinge at $z = 0$, a numerical method has to be employed. In the numerical programme the approximations

$$\ddot{\bar{W}} = \frac{\dot{\bar{W}}_{n+1} - \dot{\bar{W}}_n}{\Delta t}, \quad \dot{z}^* = \frac{z^*_{n+1} - z^*_n}{\Delta t} \tag{3-72a,b}$$

and

$$\bar{W}_{n+1} = \bar{W}_n + \frac{(\dot{\bar{W}}_n + \dot{\bar{W}}_{n+1})\Delta t}{2} \tag{3-72c}$$

were employed with the dimensionless time step

$$\Delta t = \frac{M_0}{GV_0 \ell_1} \Delta T \tag{3-72d}$$

to simplify the differential equations, where z^* indicates locations of the plastic bending hinge. The static admissibility conditions are checked at each step.

With the aid of equations (3-72a,b), the differential equations appeared in Section 3.3 can be finally simplified as a nonlinear algebraic equation of z_{0n+1}. Therefore, a very simple method can be used to solve this nonlinear algebraic equation.

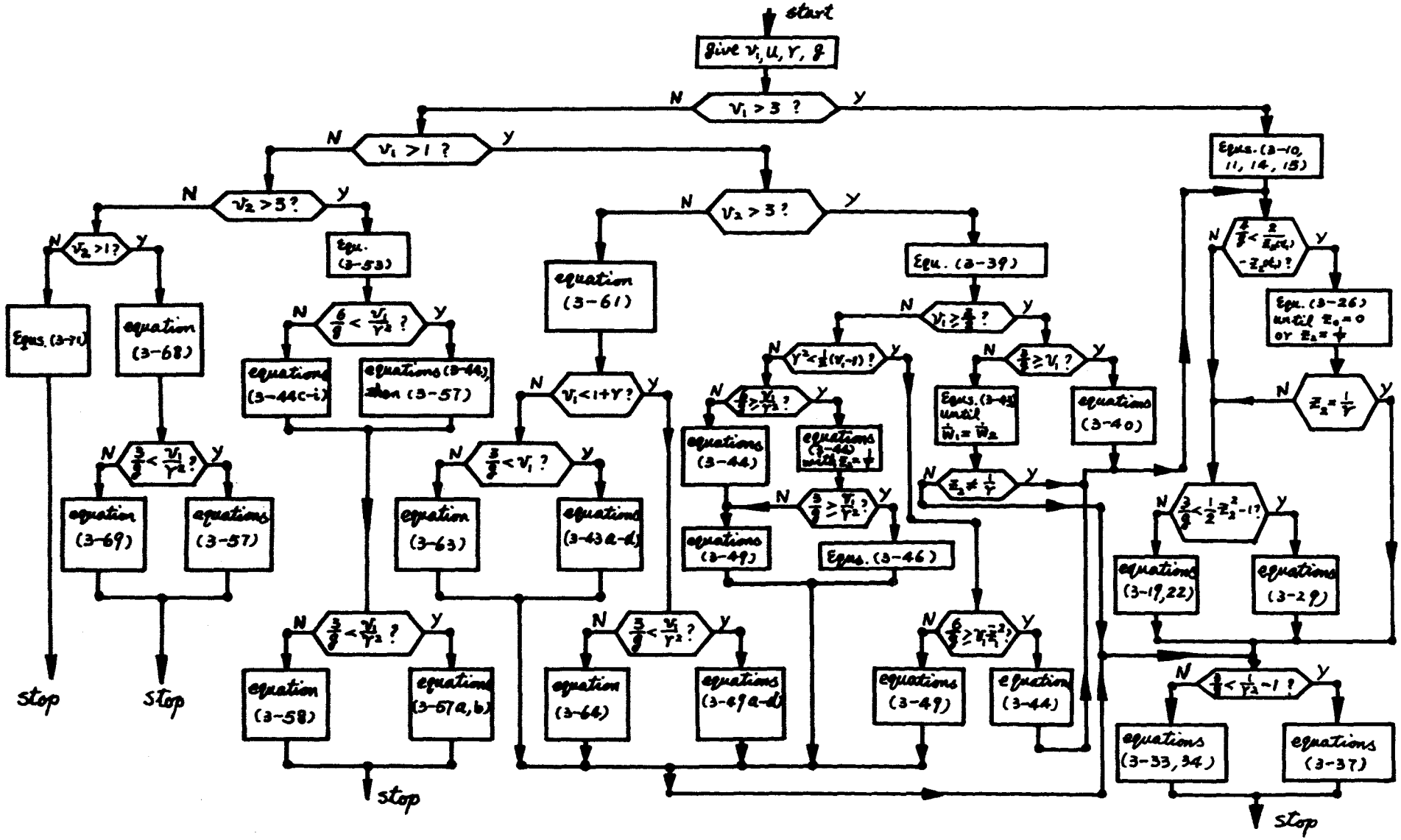

FIG. 35 Flow diagram showing the solution method of the computer programme.

An example of this simplification is given for equations (3-26).

Equations (3-26) give

$$\ddot{\bar{W}}_1(1-z_0) + \dot{\bar{W}}_1\dot{z}_0 = -\frac{12u}{g(1-z_0)} \qquad (3\text{-}73a)$$

and

$$[\ddot{\bar{W}}_1(z_2+z_0) - \dot{\bar{W}}_1\dot{z}_0](z_2-2z_0) + \dot{\bar{W}}_1\dot{z}_2(2z_2-z_0) = \frac{24u}{g} \qquad (3\text{-}73b)$$

Substituting equations (3-72a,b) into equations (3-73), we obtain

$$(\dot{\bar{W}}_{1n+1}-\dot{\bar{W}}_{1n})(1 - z_{0n+1}) + \dot{\bar{W}}_{1n+1}(z_{0n+1}-z_{0n}) = -\frac{12u\Delta t}{g(1-z_{0n+1})}$$

or $$\dot{\bar{W}}_{1n+1} = [\dot{\bar{W}}_{1n}(1-z_{0n+1})^2 - \frac{12u\Delta t}{g}]/[(1-z_{0n})(1-z_{0n+1})] \qquad (3\text{-}74a)$$

$$[(\dot{\bar{W}}_{1n+1}-\dot{\bar{W}}_{1n})(z_{2n+1}+z_{0n+1}) - \dot{\bar{W}}_1(z_{0n+1}-z_{0n})](z_{2n+1}-2z_{0n+1}) +$$

$$+ \dot{\bar{W}}_{1n+1}(z_{2n+1}-z_{2n})(2z_{2n+1}-z_{0n+1}) = \frac{24u\Delta t}{g}$$

or $$z_{2n+1} = \frac{b}{2a} + \frac{1}{2a}\sqrt{b^2-4ac} \qquad (3\text{-}74b)$$

where $a = 3\dot{\bar{W}}_{1n+1}-\dot{\bar{W}}_{1n}$, $b = az_{0n+1}-\dot{\bar{W}}_{1n+1}z_{0n} + 2\dot{\bar{W}}_{1n+1}z_{2n}$ (3-74c,d)

$$c = 2z_{0n+1}^2\dot{\bar{W}}_{1n}-2\dot{\bar{W}}_{1n+1}z_{1n}z_{1n+1}+\dot{\bar{W}}_{1n+1}z_{2n}z_{0n+1}-\frac{24u\Delta t}{g} \qquad (3\text{-}74e)$$

and the values of $\dot{\bar{W}}_{1n}$, z_{0n} and z_{2n} have been obtained in the last step.

Equation (3-26c) with equations (3-72a,b) give

$$\dot{\bar{W}}_{1n+1}(z_{2n+1}-z_{2n}) - \frac{12u\Delta t}{g}\frac{[2g(z_{2n+1}+z_{0n+1})^2+4z_{2n+1}]}{[g(z_{2n+1}+z_{0n+1})^3+4(z_{2n+1}^2-z_{0n+1}z_{2n+1}+z_{0n+1}^2]} = 0 \qquad (3\text{-}75)$$

Substituting equation (3-74a) into (3-74b) then substituting equations (3-74a,b) into (3-75), we obtain a nonlinear algebraic

equation of z_{0n+1}. Equation (3-75) seems very complex, but it is easily solved by computer with a given accuracy. Substituting z_{0n+1} which is obtained from equation (3-75) into equations (3-74a,b), we obtain the values of $\dot{\bar{W}}_{1n+1}$ and finally obtain $\bar{W}_{1n+1}$ with equation (3-72c).

Equations (3-26) and other differential equations which appear in Section 3.3 can also be solved by Runge-Kutta's method and other methods, but for equations (3-43) it is easier to obtain the solution by using equations (3-72) and the method described above.

3.5 Discussion

The theoretical predictions in Sections 3.2 and 3.3 extend Parkes' [10] and other authors' [13,15] work into shear and bending response of a rigid-plastic beam struck by a mass at any point of its span. It shows that according to the yield curve shown in Fig. 9c the number of deflection mechanisms of beam with a limited shear strength, shown in Figs. 36 and 37, is much larger than that with infinite shear strength. Fig. 36 shows that the deflection mechanism occurred in the first phase of motion may change with the different ratios of shear strength to bending moment v_1 and v_2. A flow diagram showing the change of deflection mechanisms with time t is given in Fig. 37.

According to Parkes' bending only solution [10], the transverse shear force is initial infinite at the impact point of the beam. However, for a real beam the shear strength is finite.

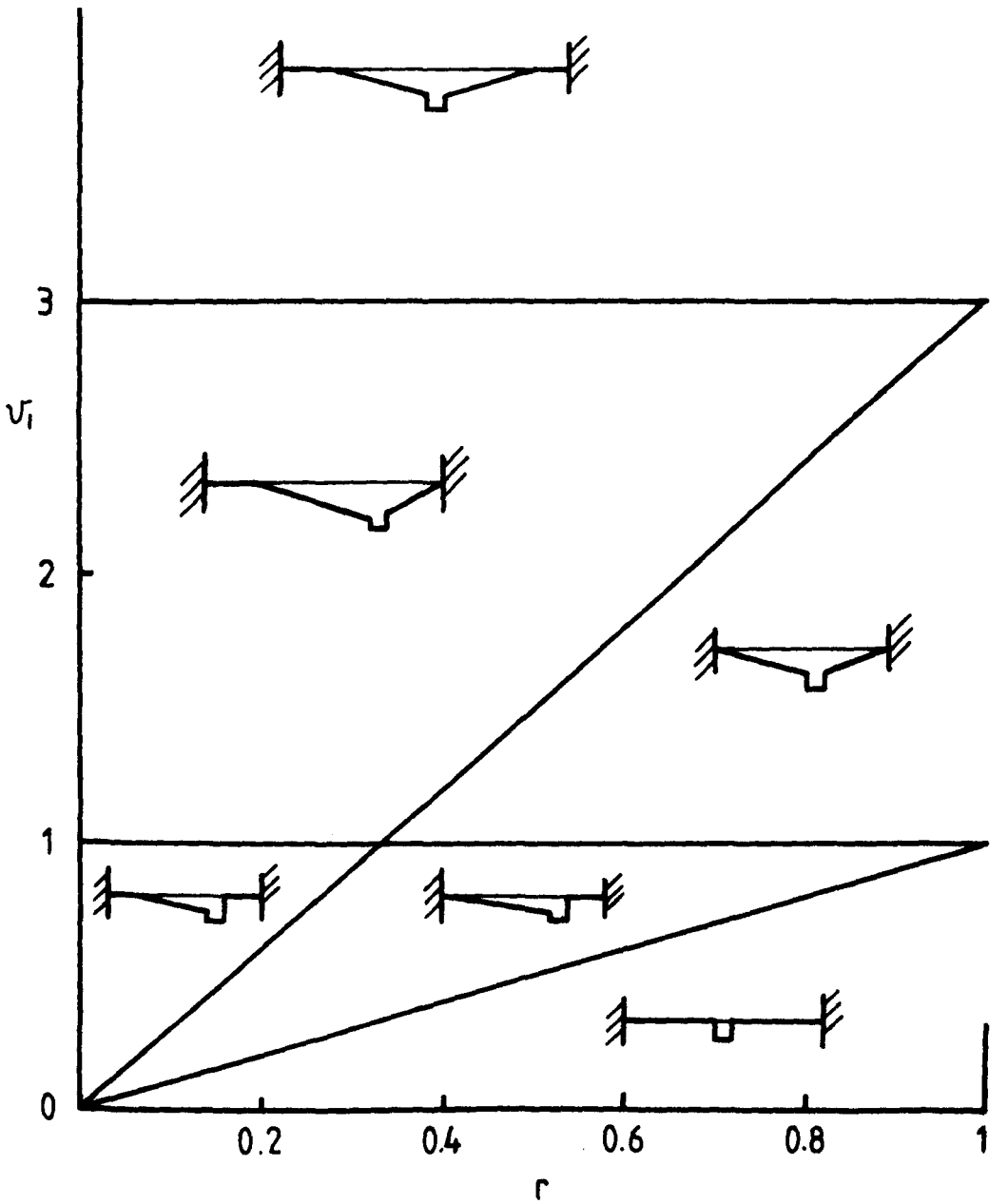

FIG. 36 Deflection mechanisms occurred in the first phase of motion of beam with a limited shear strength.

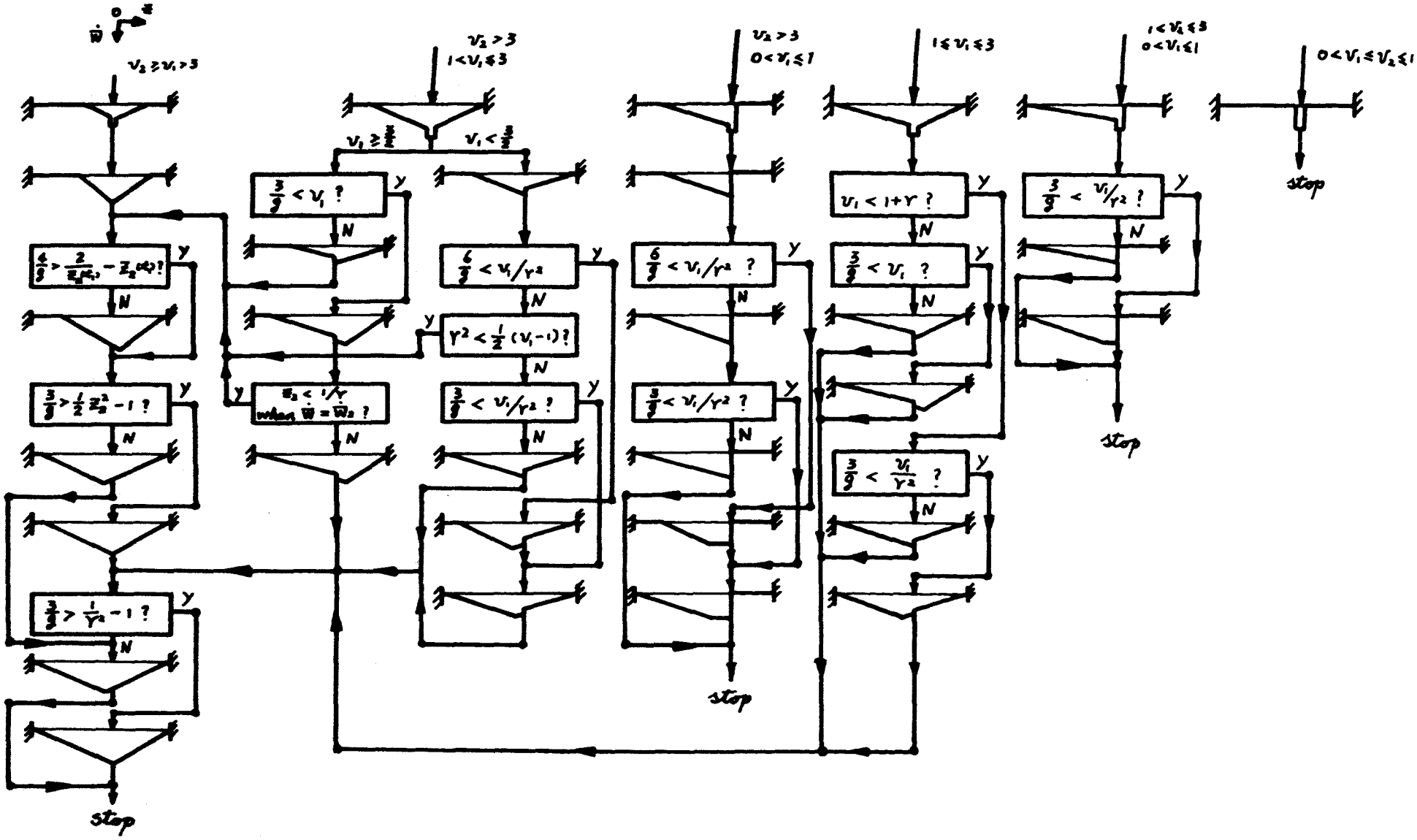

FIG. 37 Flow diagram showing the mechanisms of motion.

Therefore, some shear deformation may occur at the impact point. Figs. 38 and 39 shows that when the impact point is close to the support or when the mass ratio g is very large, the shear deformation may dominate the dynamic response and the beam would fail due to shear. Indeed, experimental results reported in Chapter 6 of this thesis show that some beams failed due to large shear deformation. The theoretical analysis in Sections 3.2 and 3.3 can be reduced to Parkes' results when v_1 and v_2 (the shear strength of beam) tend to infinity.

It is found that dependent on the ratio of mass g, the ratio of two part lengths of beam r and the ratio of shear strength to bending moment v_1, the shear forces Q_{10} and Q_{20}, which locate at $x = 0^+$ and $x = 0^-$, respectively, may change their values from negative to positive or from positive to negative when a stationary plastic hinge is assumed to remain at the impact point $x = 0$. In other words, Q_{10} may be larger than zero and Q_{20} may be less than zero. Therefore, the bending moment at both sides of the impact point $x = 0$ may be larger than the plastic limit moment M_0 since $\frac{\partial M}{\partial x} = Q$ and $M = M_0$ at $x = 0$. For these cases which were ignored by Parkes [10], new velocity profiles with a travelling plastic bending hinge occurred at $z = -z_0$ or $z = z_0$ instead of the stationary hinge occurred at $z = 0$ are assumed in Section 3.3 of this Chapter. The limitation of Parkes' result is shown in Fig. 40 according to the rigid-plastic yield condition. It shows that when the impact point is at the centre of the beam there is no limitation, but for other cases Parkes' solution has some limitation, especially when the mass of the striker is very

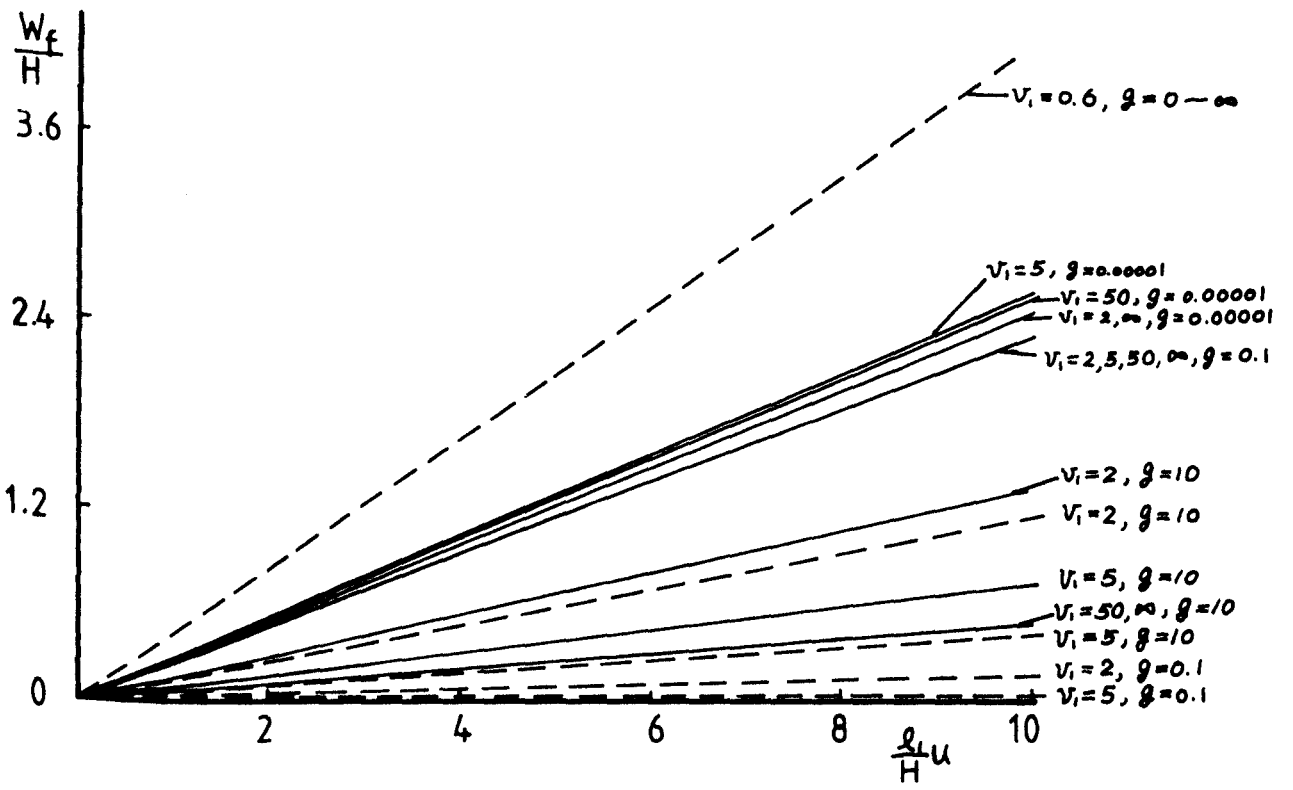

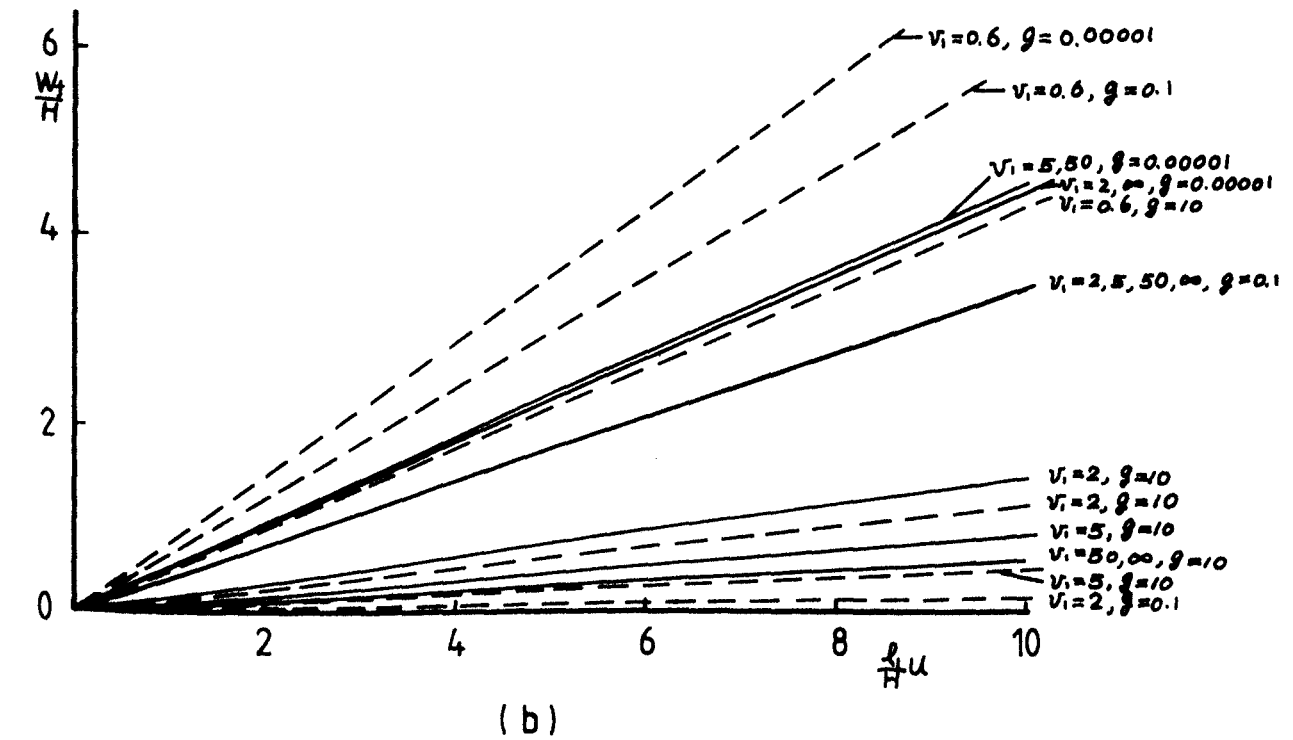

FIG. 38 Variation of maximum permanent deformation $\frac{W_f}{H}$ with external dynamic energy $u\frac{\ell_1}{H}$. (a) r = 1 and (b) r = 0.1, —— maximum permanent deformation; ---- shear sliding deformation.

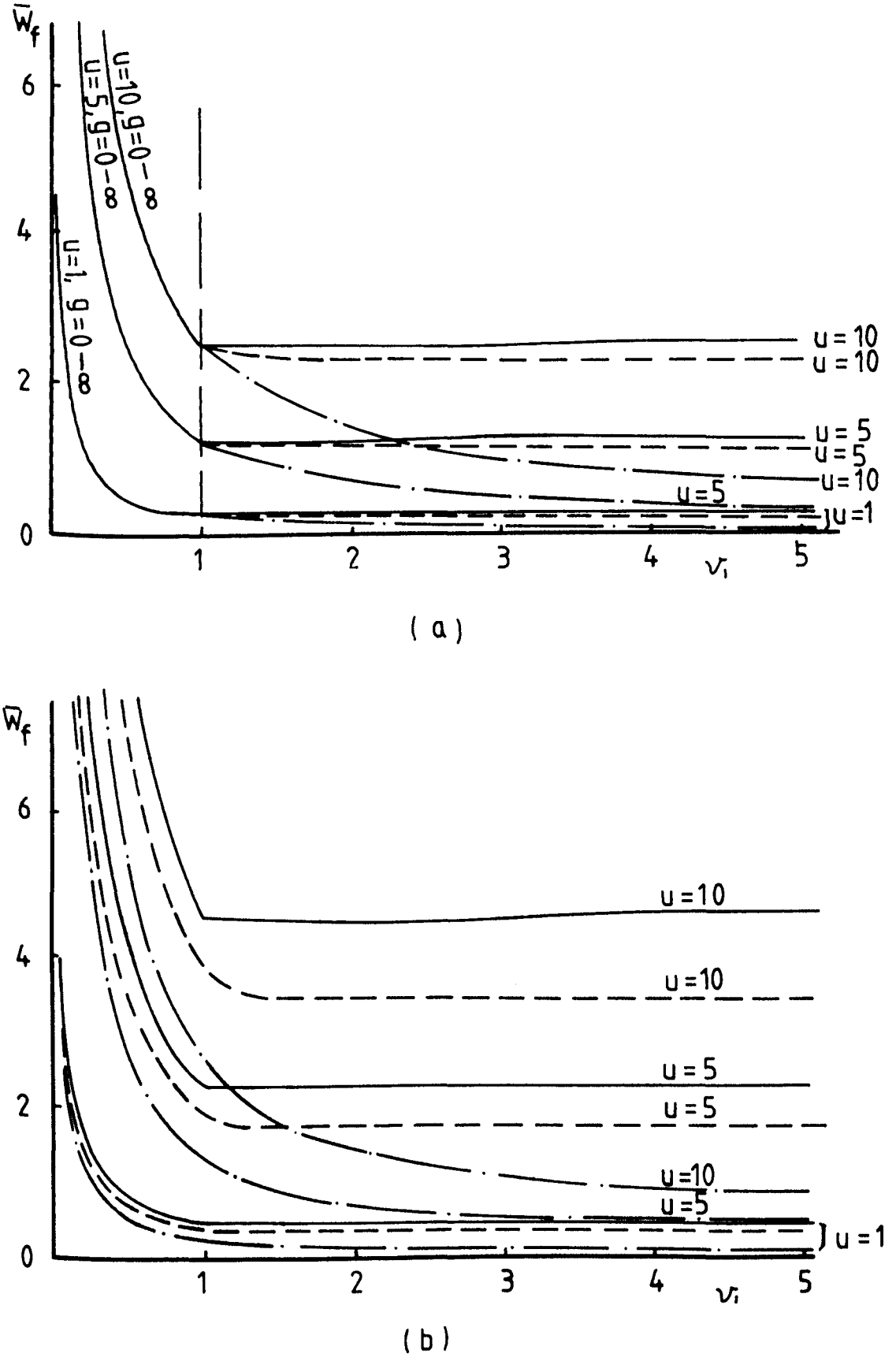

FIG. 39 Variation of maximum permanent deformation $\bar{W}_f$ with ν_1. (a) r = 1 and (b) r = 0.1, —— g = 0.00001; ---- g = 0.1; —·— g = 10.

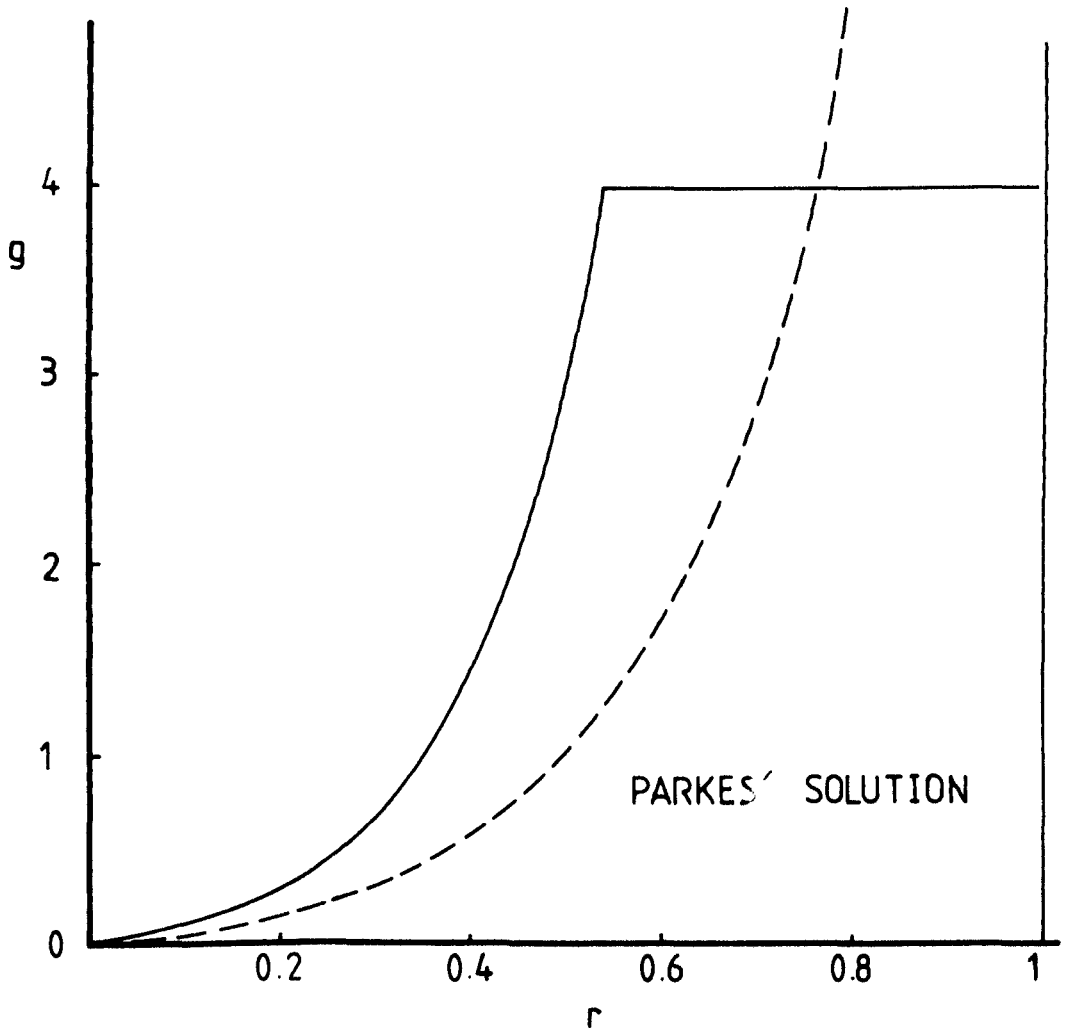

FIG. 40 Valid area for Parkes' solution [10]. —— valid area for second phase of motion; ---- valid area for final (third) phase of motion.

small.

It shows that the theoretical analysis in Section 3.3 satisfies the required kinematic relation given in Section 3.2 and satisfies the boundary and initial conditions. Thus, it is kinematically admissible. It also shows that the static admissibility conditions are satisfied except for $1 < \nu_1 < \frac{3}{2}$ or $1 < \nu_2 < \frac{3}{2}$. Therefore, the theoretical analysis given in Section 3.3 is exact except for $1 < \nu_1 < \frac{3}{2}$ or $1 < \nu_2 < \frac{3}{2}$. When $1 < \nu_1 < \frac{3}{2}$ or $1 < \nu_2 < \frac{3}{2}$, the shear force at the right-hand support or at the left-hand support may be slightly larger than the limit shear strength. Therefore, new velocity profiles have to be assumed, but these cases are neglected in our analysis. However, this is not a practically important case when $1 < \nu_1 < \nu_2 < \frac{3}{2}$ because $H < \ell_1 < \ell_2 < \frac{3}{2}$ for rectangular cross section beam with $Q_0 = \frac{1}{2}BH\sigma_0$ and $M_0 = \frac{1}{4}BH^2\sigma_0$. Furthermore, equations (3-35a), (3-63f) and (3-64f) show that the maximum absolute value of shear force may only be slightly larger than Q_0, or $q_{1min} \simeq -1$ and $q_{2max} \simeq 1$, since the ratio of mass $g = \frac{m\ell_1}{G}$ should be small when $h < \ell_1 < \frac{3}{2}h$.

A wide range for $\nu_1 = 0.2\text{-}50$, $r = 0.01\text{-}1$, $u = 0.01\text{-}10$ and $g = 0.00001\text{-}10$ are assumed and the corresponding dynamic behaviour of beam struck by a body are obtained. As we expected, the characteristics of the motion for the cases with a travelling plastic hinge occurring at $z = -z_0$ or $z = z_0$ are similar to that with a stationary plastic hinge at $z = 0$. The velocity $\dot{W}_0$ decreases and z_1 and z_2 increase gradually with time. In other words, the striker decelerates and two travelling

plastic hinges at $z = z_1$ and $z = -z_2$ move towards the supports. The static admissibility conditions are checked at each step and there are no violations of yield conditions.

It is shown from Fig. 38 that the maximum permanent deformation and shear sliding displacement from the theoretical analysis in Section 3.3 are in proportion to the initial kinetic energy u, but the maximum permanent deformation decreases, while shear sliding increases, with the increase of the mass ratio g, especially when g is large, the maximum permanent deformation decreases sharply, while shear sliding displacement increases sharply. Thus, shear influence play an important role when the mass ratio g is large, i.e. small G.

It is evident from Fig. 39 that the maximum permanent deformation increases sharply with decrease of the ratio of shear strength to bending moment ν_1 when $\nu_1 < 1$. Actually, the maximum deformation equals shear sliding displacement when $\nu_1 < 1$. Therefore, the shear influence dominates the dynamic response of a rigid-plastic beam struck by a mass. The beam would be broken when shear sliding displacement $W_s = kH$, where $0 < k \leqslant 1$.

It shows from Fig. 41 that the maximum permanent deformation decreases sharply with increase r, provided g is small, but little change occurs when g is large.

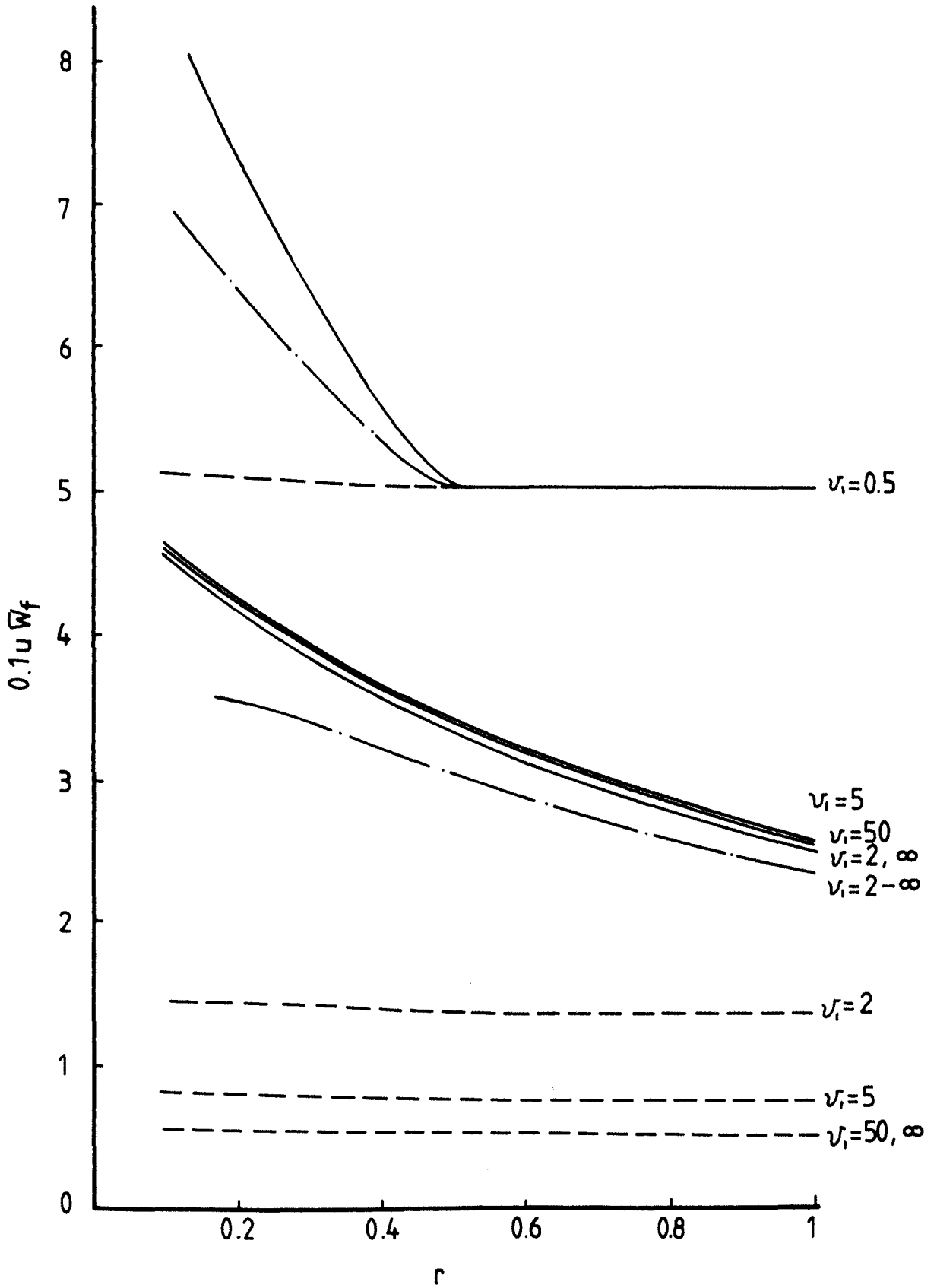

FIG. 41 Variation of maximum permanent deformation $\bar{W}_f$ with r.

—— g = 0.00001; —·— g = 0.1; ---- g = 10.

CHAPTER 4

FINITE DEFLECTION OF RIGID-PLASTIC BEAMS DUE TO DYNAMIC LOADING

4.1 Introduction

When a rigid-plastic beam with axial restraints at its supports is subjected to a large dynamic load, a large discrepancy between the theoretical analysis of a bending only solution, or shear and bending solution, and experimental results [12,40] may occur. In this case, the influence of finite deflections, or geometry changes, play an important role on the beam behaviour. This phenomenon has attracted some attention [12,17,37-40].

In this Chapter, we consider the influence of finite deflections on a clamped beam struck by a body at any point of its span shown in Fig. 42a and pin-ended beam subjected to a uniformly distributed impulsive loading as shown in Fig. 42b. The square yield curves shown in Fig. 42d, which are used by several authors [17,39,40] and give good agreement with experimental results [17,40], are employed herein. The membrane force N is assumed to be a constant along the beam. This assumption is used by Symonds and Mentel [38] and other authors [12,39,40] and follows from the in-plane equilibrium equations when axial inertia is neglected.

Symonds and Mentel [38] examined the effects of axial constraints for simply supported and clamped beams subjected to impulsive uniform loading using an 'exact' yield curve (parabolic

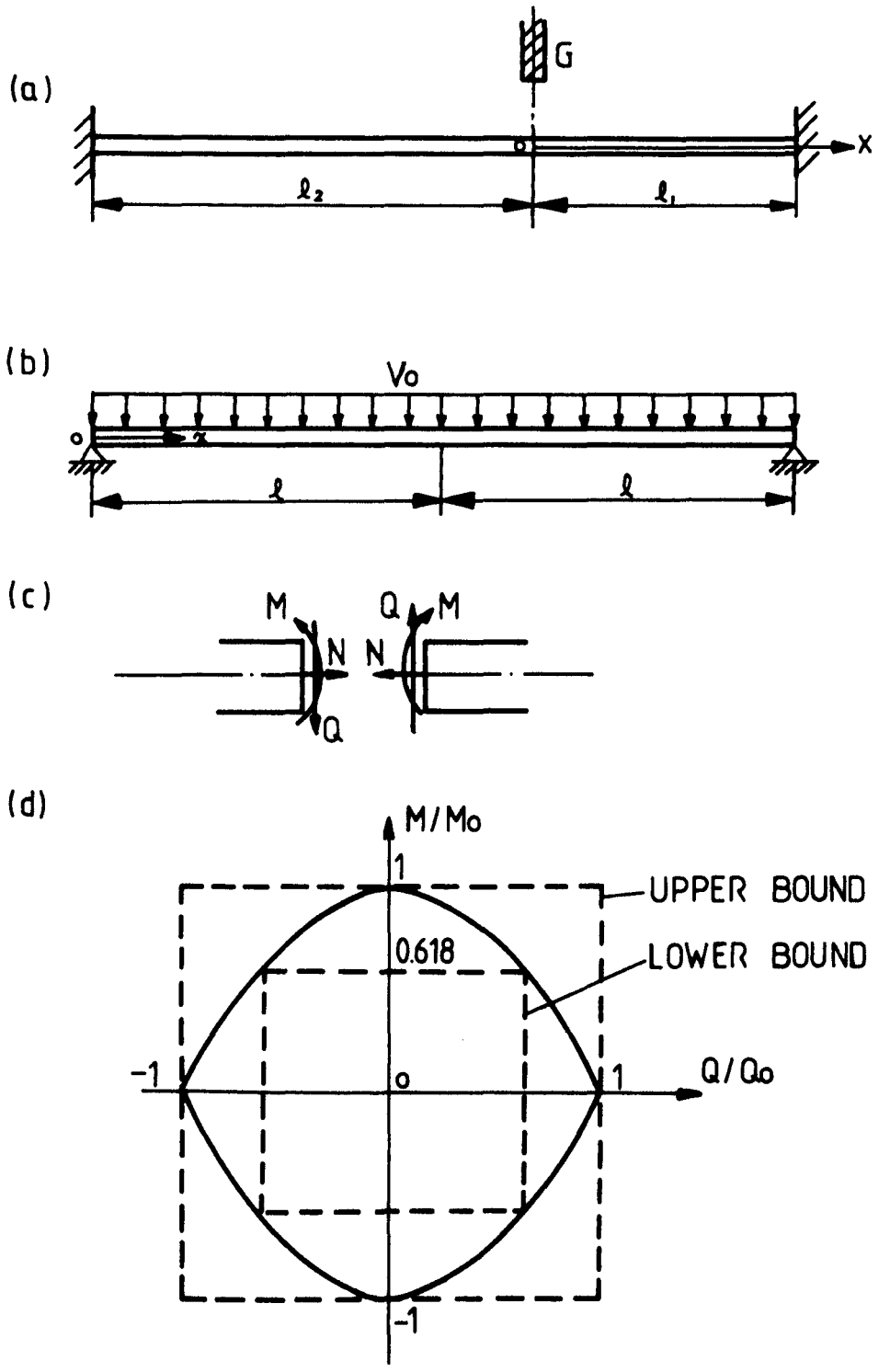

FIG. 42 (a) clamped beam struck by a mass, (b) simply supported beam subjected to an impulsive loading; (c) definitions of bending moment, a shear force, membrane force and loads; (d) yield curves.

curve) as shown in Fig. 42d. Jones [39] solved this problem from elementary equilibrium equations with square yield curve. Furthermore, this solution can be obtained from Jones' approximation method [17] when P_T tends to $\bar{m}V_0$. We discuss this problem again in Section 4.2. It is the purpose of the present work to show that an analytical solution can be more easily obtained from linear and angular momentum equations when the square yield curves are employed and to show how the solution relating to the square yield curves bound that relating to parabolic yield curve.

The influence of finite deflection on a clamped beam struck by a mass at any point of its span is examined in Section 4.3. Several authors [12,20,30] examined the influence of finite deflection of beam struck by a mass at the centre. It appears that the influence of finite deflections of a beam struck at any point of its span has not been examined, but Jones' approximation method developed in reference [17] can be used for this problem and the formula of maximum permanent deformation is given in reference [30]. All these formulae of maximum permanent deformation of a clamped beam with rectangular cross-section are listed in Appendix II and some results calculated from these formulae are plotted in Fig. 54.

4.2 Finite Deflection of Pin-Ended Beams Subjected to Impulsive Loading

Two phases of motion for a pin-ended beam subjected

to impulsive loading shown in Fig. 42b are assumed according to experimental evidence and previous analysis. In the first phase, two travelling plastic hinges originate from the supports at T=0 and travel towards the centre of beam. Therefore, there is a central position which translates at the initial velocity V_o, while segments at each end rotate as rigid bodies. The velocity profile is shown in Fig. 43a. The second phase starts when two travelling hinges meet at the centre of the beam. A stationary plastic hinge remains at the centre of the beam and two half beams rotate as rigid bodies, as shown in Fig. 44a, until all the initial kinetic energy is dissipated as plastic work. The membrane force N is assumed to equal the fully plastic tensile force of cross-section N_0 during the entire response [39,40]*. One half span of the beam is considered because of symmetry about the centre of the beam.

A) First phase, $0 \leqslant T \leqslant T_\ell$

In this phase, the velocity profile shown in Fig. 43a is

$$W' = \begin{cases} V_0 \dfrac{x}{a_2} & \text{for } 0 \leqslant x \leqslant a_2 \\ V_0 & \text{for } a_2 \leqslant x \leqslant \ell \end{cases} \qquad (4\text{-}1)$$

---

* When a parabolic yield curve as shown in Fig. 42d is employed, the membrane force N of beams may increase from zero to fully plastic tensile force of a rectangular cross section N_0 corresponding to the deformation W of beams varied from zero to full thickness H of a clamped beam or to half thickness $\frac{H}{2}$ of a simply supported beam and N will remain N_0 for $W > H$ or $W > \frac{H}{2}$ [12,17,38-40]. However, the difference may be small when the membrane force is assumed to remain N_0 in whole response of the beam, provided the permanent deformation W_f of the beam is large in comparison with the beam thickness.

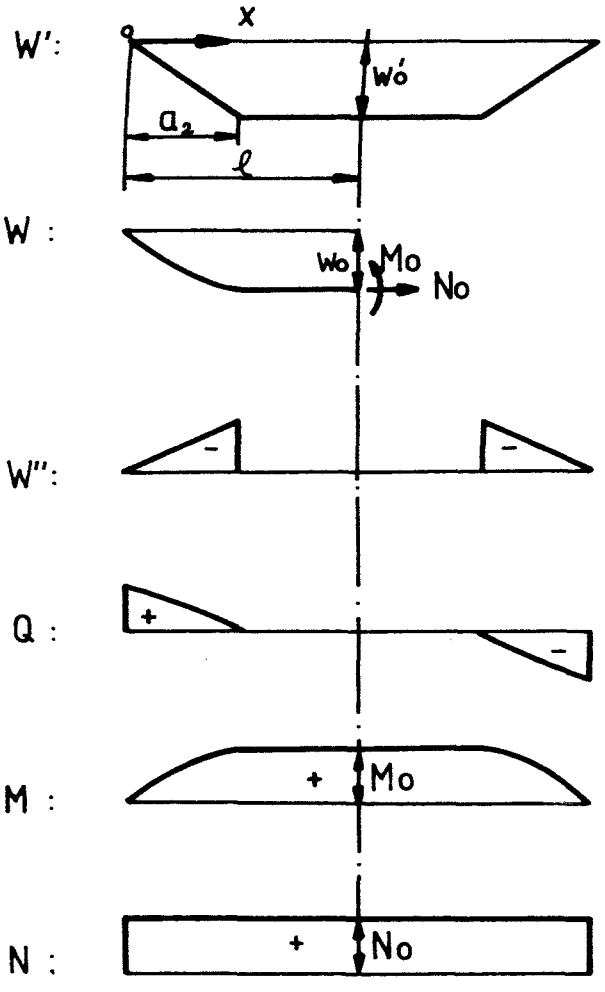

FIG. 43 First phase of motion of simply supported beam due to an impulsive loading.

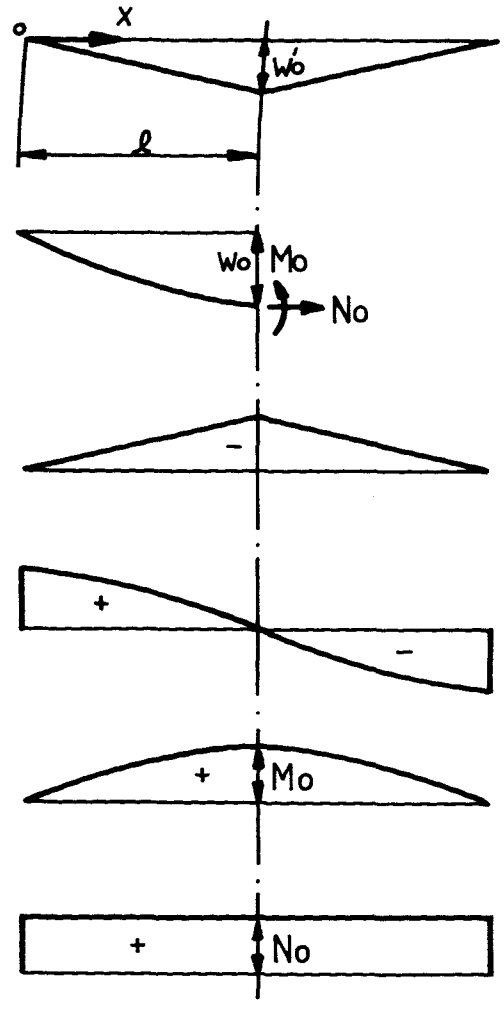

FIG. 44 Final phase of motion of simply supported beam due to an impulsive loading.

where V_0 is the initial impulsive velocity and a_2 is the location of the travelling plastic hinge.

The angular momentum equation about the support of the beam shown in Fig. 43b is

$$\int_0^{\ell} \bar{m}W''xdx = -M_0 - N_0W_0 \tag{4-2}$$

where W_0 is the displacement at the centre of the beam and

$$W_0 = V_0T \tag{4-3}$$

in this phase.

Integrating equation (4-2) with respect to time T after substituting equation (4-3) into equation (4-2), we obtain

$$\int_0^{\ell} \bar{m}W'xdx = -M_0T - \frac{1}{2} N_0V_0T^2 + \int_0^{\ell} \bar{m}V_0xdx \tag{4-4}$$

since $W' = V_0$ at T=0.

Equations (4-1) and (4-4) give

$$\frac{1}{6} \bar{m}V_0a_2^2 = M_0T + \frac{1}{2} N_0V_0T^2. \tag{4-5}$$

At $T=T_{\ell}$, $a_2=\ell$ and

$$T_{\ell} = -\frac{M_0}{N_0V_0} + \sqrt{\frac{M_0^2}{N_0^2V_0^2} + \frac{1}{3}\frac{\bar{m}\ell^2}{N_0}}. \tag{4-6}$$

The maximum deflection in this phase is

$$W_{0\ell} = V_0T_{\ell} = -\frac{M_0}{N_0} + \sqrt{\frac{M_0^2}{N_0^2} + \frac{1}{3}\frac{\bar{m}\ell^2V_0^2}{N_0}}. \tag{4-7}$$

B) Second phase, $T_\ell < T \leqslant T_f$

The two travelling plastic hinges coalesce when $a_2=\ell$ at $T=T_\ell$ and the velocity profile of following motion shown in Fig. 44a is

$$W' = W_0' \frac{x}{\ell} . \qquad \text{for } 0 \leqslant x \leqslant \ell \tag{4-8}$$

The angular momentum equation shown in Fig. 44b is

$$\frac{1}{3} \bar{m} \ell^2 W_0'' = -M_0 - N_0 W_0 . \tag{4-9}$$

Integrating equation (4-9) after multiplying by W_0', we obtain

$$\frac{1}{6} \bar{m} \ell^2 W_0'^2 + M_0 W_0 + \frac{1}{2} N_0 W_0^2 = \frac{1}{6} \bar{m} \ell^2 V_0^2 + M_0 W_{0\ell} + \frac{1}{2} N_0 W_{0\ell}^2 \tag{4-10}$$

since $W_0' = V_0$ and $W_0 = W_{0\ell}$ at $T=T_\ell$, where $W_{0\ell}$ is defined by equation (4-7). The motion stops when $W_0' = 0$ at $T=T_f$ and the maximum permanent displacement W_{0f} is defined by

$$\frac{1}{2} N_0 W_{0f}^2 + M_0 W_{0f} = \frac{1}{6} \bar{m} \ell^2 V_0^2 + M_0 W_{0\ell} + \frac{1}{2} N_0 W_{0\ell}^2$$

or

$$W_{0f} = \frac{M_0}{N_0} \left(-1 + \sqrt{1 + \frac{2}{3} \frac{\bar{m} \ell^2 V_0^2}{M_0} \frac{N_0}{M_0}}\right). \tag{4-11}$$

If $M_0 = \frac{1}{4} BH^2 \sigma_0$ and $N_0 = BH\sigma_0$ for beam with rectangular cross section, the maximum permanent deformation is

$$\frac{W_{0f}}{H} = \frac{1}{4} \left(-1 + \sqrt{1 + \frac{8}{3} \bar{\lambda}}\right) \tag{4-12}$$

where

$$\bar{\lambda} = \frac{\bar{m} \ell^2 V_0^2}{M_0 H} . \tag{4-13}$$

It can be shown that the analysis discussed in this section satisfies both static admissibility and kinematic admissibility

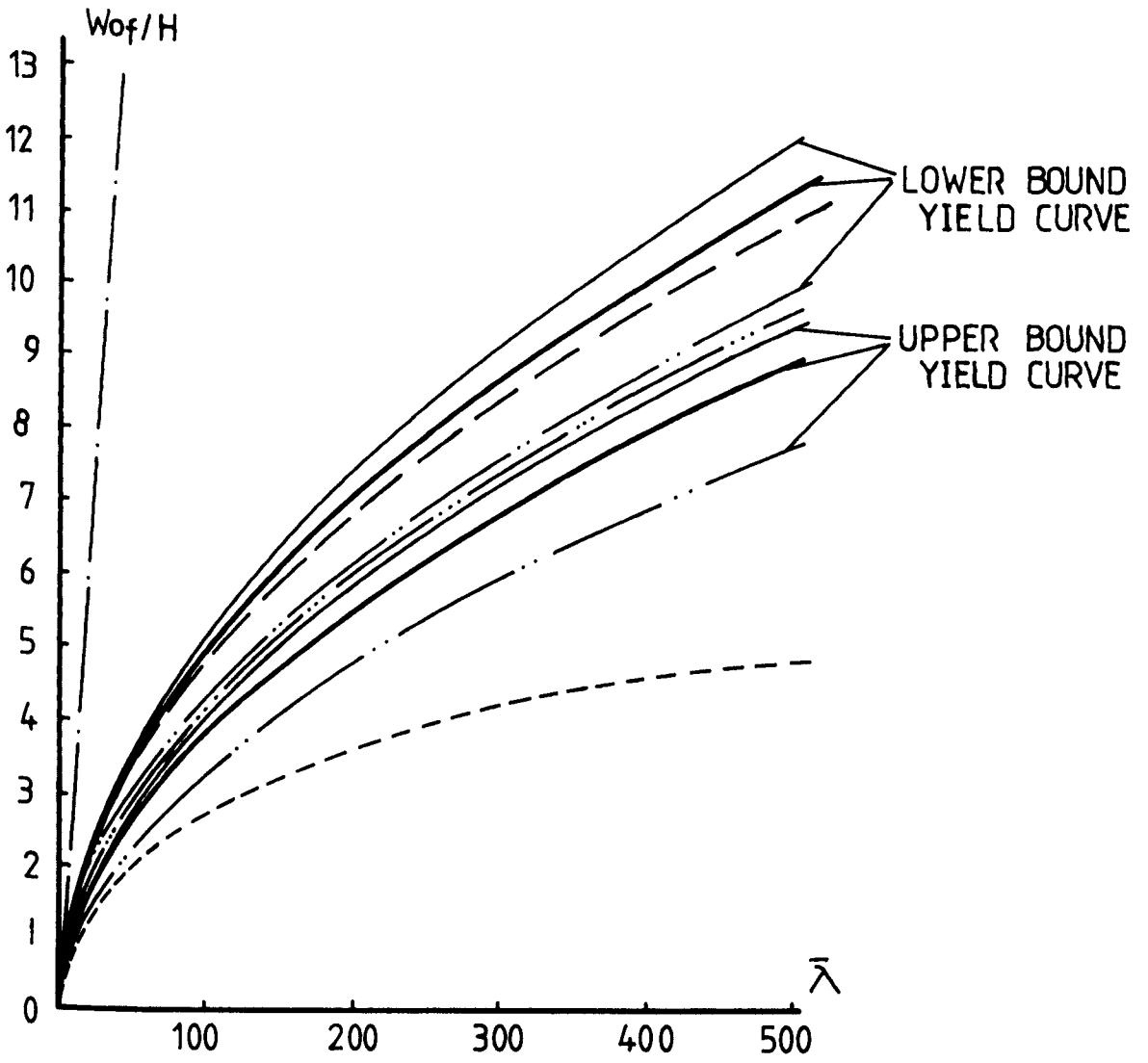

FIG. 45 Variation of maximum permanent deformation W_{0f}/H of a simply supported beam with external dynamic energy $\bar{\lambda}$.

—·— equation (27) of Ref. [39], simple bending only solution;

----- equation (25) of Ref. [38], excludes string phase;

—··— equation (37) of Ref. [39], square yield curve;

▬▬ equation (4-12), square yield curve;

——— equation (25) of Ref. [17], square yield curve;

— — — equation (50) of Ref. [38], includes string phase;

—···— equation (22) of Ref. [17], parabolic yield curve.

conditions during the entire response, relating to the square yield curve employed herein. Therefore, the results are correct. To obtain an upper bound on the deflection, using the inscribed square yield curve (lower bound yield curve), $\bar{\lambda}$ would be replaced by $\bar{\lambda}/0.618$. Several results are plotted in Fig. 45 and it shows that the simplified results obtained in this section give good agreement with other solutions [17,38,39]. It is quite clear that the axial constraints have a substantial effect for large deformations.

4.3 Finite Deflection of a Clamped Beam Struck by a Body At Any Point of its Span.

Three phases of motion for a clamped beam struck by a mass shown in Fig. 42a are assumed in this Section according to experimental evidence and previous analysis [10,57]. In the first phase, a stationary plastic hinge occurs at the impact point z=0, while two travelling plastic hinges originate from the impact point z=0 and travel towards the supports. Two parts of the beam between the stationary hinge and travelling hinges rotate as rigid bodies about the travelling hinges, while the rest of beam which is not disturbed and remains undeformed. The second phase of motion starts when the right side travelling hinges reaches the right-hand support at $t=t_1$, while the third phase starts when the left side travelling hinge reaches the left-hand support at $t=t_2$. The membrane force N is assumed to equal N_0 along the beam during the entire response.*

---

* see page 65 footnote.

A) First Phase, $0 \leqslant t \leqslant t_1$

The velocity profile shown in Fig. 46a is

$$\dot{\bar{W}} = \begin{cases} 0 & \text{for } -\frac{1}{r} \leqslant z \leqslant -z_2^- \\ \dot{\bar{W}}_0(1 + \frac{z}{z_2}) & \text{for } -z_2^+ \leqslant z \leqslant 0^- \\ \dot{\bar{W}}_0(1 - \frac{z}{z_1}) & \text{for } 0^+ \leqslant z \leqslant z_1^- \\ 0 & \text{for } z_1^+ \leqslant z \leqslant 1 \end{cases} \tag{4-14}$$

where $z_1 = z_2$ in this phase.

The linear and angular momentum equations* of beam are

$$z_1\ddot{\bar{W}}_0 + \dot{\bar{W}}_0\dot{z}_1 = -\ddot{\bar{W}}_0/g \tag{4-15a}$$

$$gz_1^2\ddot{\bar{W}}_0 + \frac{1}{2}gz_1\dot{z}_1\dot{\bar{W}}_0 + \frac{3}{2}z_1\ddot{\bar{W}}_0 = -12u(1 + 2\gamma\bar{W}_0) \tag{4-15b}$$

since

$$q_{10} = -q_{20} = \ddot{\bar{W}}_0/8u\nu_1, \tag{4-15c}$$

where $\gamma = \frac{N_0\ell_1}{4M_0}$ and the other non-dimensional characters are defined by equations (3-7).

Equations (4-15a,b) can be rewritten as

$$(\dot{\bar{W}}_0 z_1^2)'_t = \frac{24u}{g}(1 + 2\gamma\bar{W}_0) \tag{4-16a}$$

and

$$(1 + z_1 g)\dot{\bar{W}}_0 = 2u \tag{4-16b}$$

since $\dot{\bar{W}}_0 = 2u$ and $z_1 = 0$ at $t = 0$.

---

* The methods deriving these equations are similar to those discussed in Chapter 3, except the membrane force contributes to the angular momentum equations.

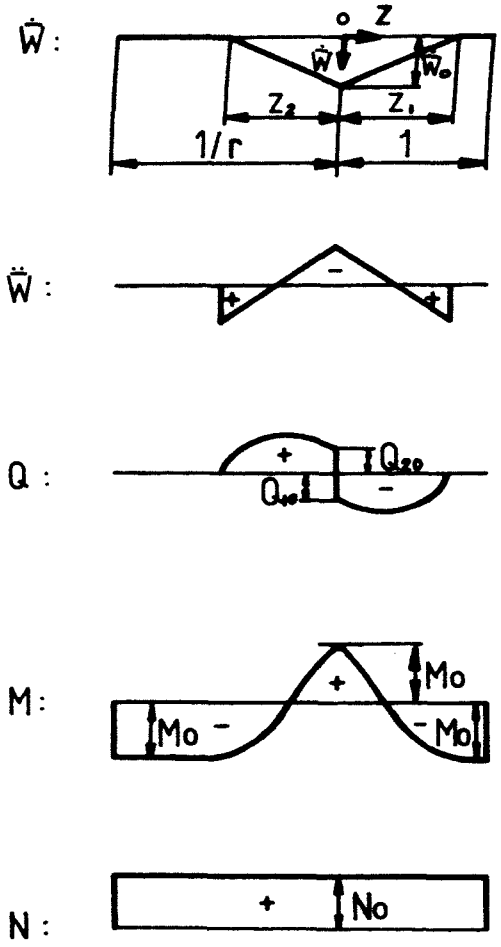

FIG. 46 First phase of motion of a clamped beam struck by a mass at any point.

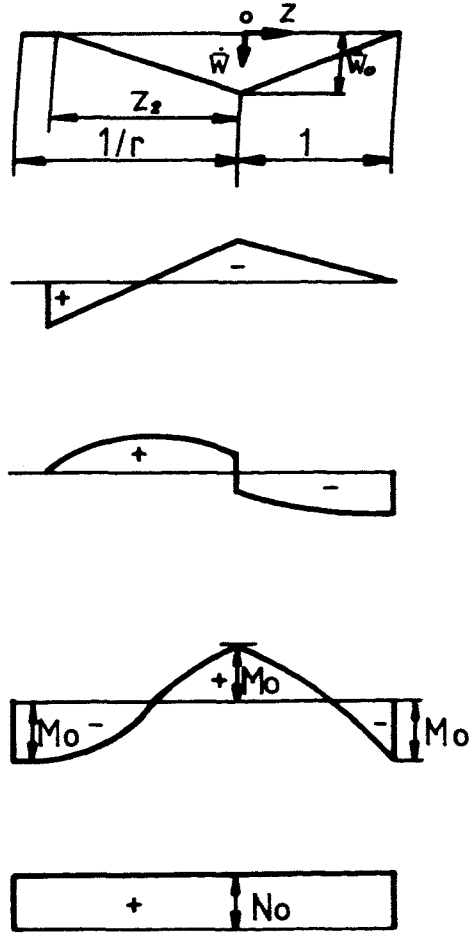

FIG. 47 Second phase of motion when $\frac{4}{g} \geqslant 1$.

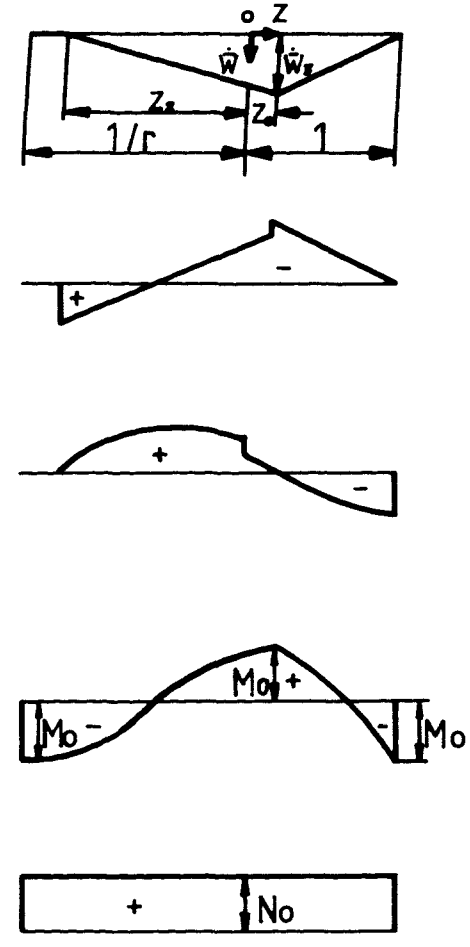

FIG. 48 Second phase of motion when $\frac{4}{g} < 1$.

Equations (4-16) give

$$\ddot{\bar{W}}_0 - 4u^2 \ddot{\bar{W}}_0/\dot{\bar{W}}_0^2 - 24ug - 48ug\gamma\bar{W}_0 = 0. \qquad (4\text{-}17)$$

Integrating (4-17) after multiplying by $\dot{\bar{W}}_0$, we obtain

$$\frac{1}{2}\dot{\bar{W}}_0^2 - 4u^2 \ln\dot{\bar{W}}_0 - 24ug\bar{W}_0 - 24ug\gamma\bar{W}_0^2 = 2u^2 - 4u^2 \ln(2u) \qquad (4\text{-}18)$$

since $\dot{\bar{W}}_0 = 2u$ and $\bar{W} = 0$ at $t = 0$.

At $t = t_1$, $z_1 = 1$ and velocity given by equation (4-16b) is

$$\dot{\bar{W}}_{01} = \frac{2u}{1+g}. \qquad (4\text{-}19)$$

Substituting equation (4-19) into equation (4-18), we obtain

$$24ug\bar{W}_{01} + 24ug\gamma\bar{W}_{01}^2 = \frac{2u^2}{(1+g)^2} - 4u^2 \ln\left(\frac{2u}{1+g}\right) - 2u^2 + 4u^2 \ln(2u)$$

or

$$\bar{W}_{01} = \frac{1}{2\gamma}\left\{-1 + \sqrt{1 - \frac{u\gamma}{3g}\left[\frac{g(2+g)}{(1+g)^2} + 2\ln\left(\frac{1}{1+g}\right)\right]}\right\}. \qquad (4\text{-}20)$$

It shows that in this phase the static admissibility conditions are satisfied* with $-1 \leqslant m \leqslant 1$ and $n = 1$ in $-\frac{1}{r} \leqslant z \leqslant 1$.

B) Second phase, $t_1 < t \leqslant t_2$

The right side travelling hinge reaches the right-hand support at $t=t_1$ and the following velocity profile shown in Fig. 47a is assumed

---

* The differentials of m with respect to z in this phase are similar to equations (7b) and (7d) in Appendix I, although there is an additional term $4\gamma[\bar{W}_0-\bar{W}(z)]$ in bending moment expressions and an additional term $-48u\gamma\bar{W}_0/(z_1^2 g+2z_1)$ in acceleration equations of $\bar{W}_0$. Nevertheless, $-1 \leqslant m \leqslant 1$ without any restrictions.

$$\dot{\bar{W}} = \begin{cases} 0 & \text{for } -\frac{1}{r} \leqslant z \leqslant -z_2^- \\ \dot{\bar{W}}_0(1 + \frac{z}{z_2}) & \text{for } -z_2^+ \leqslant z \leqslant 0^- \\ \dot{\bar{W}}_0(1-z) & \text{for } 0^+ \leqslant z \leqslant 1 \end{cases} \tag{4-21}$$

The linear and angular momentum equations with the transverse equilibrium equation at the impact point z = 0 and equation (4-21) give

$$(\dot{\bar{W}}_0 \dot{z}_2^2)_t' = 24u(1 + 2\gamma\bar{W}_0)/g \tag{4-22a}$$

and

$$(z_2\dot{\bar{W}}_0)_t' = -\ddot{\bar{W}}_0(\frac{2}{g} + \frac{2}{3}) - 8u(1+2\gamma\bar{W}_0)/g. \tag{4-22b}$$

Equations (4-22) give

$$3(z_2\dot{\bar{W}}_0)_t' + (\dot{\bar{W}}_0 z_2^2)_t' + \ddot{\bar{W}}_0(\frac{6}{g} + 2) = 0. \tag{4-23}$$

Integrating equation (4-23) with respect to time t, we obtain

$$\dot{\bar{W}}_0 = \frac{12u}{3gz_2+gz_2^2+6+2g} \tag{4-24}$$

since $z_2=1$ and $\dot{\bar{W}}_{01}$ is given by equation (4-19) at $t=t_1$.

Equation (4-23) also gives

$$\ddot{\bar{W}}_0 = -\frac{(3+2z_2)\, g\dot{\bar{W}}_0\dot{z}_2}{3gz_2+gz_2^2+6+2g}. \tag{4-25}$$

Substituting equation (4-25) into equation (4-22a), we obtain

$$\dot{z}_2 = \frac{24u(1+2\gamma\bar{W}_0)(3gz_2+gz_2^2+6+2g)}{gz_2\dot{\bar{W}}_0(3gz_2+12+4g)}. \tag{4-26}$$

Equations (4-24) and (4-26) give

$$\frac{\partial \bar{W}_0}{\partial z_2} = \frac{6ugz_2(3gz_2+12+4g)}{(1+2\gamma\bar{W}_0)(3gz_2+gz_2^2+6+2g)^3} \tag{4-27}$$

since $\dot{\bar{W}}_0 = \frac{\partial \bar{W}_0}{\partial z_2}\,\dot{z}_2$.

Equation (4-27) gives

$$\bar{W}_0 + \gamma\bar{W}_0^2 = \int_1^{z_2} \frac{6ugz_2(3gz_2+12+4g)}{(3gz_2+gz_2^2+6+2g)^3}\,dz_2 + \bar{W}_{01} + \gamma\bar{W}_{01}^2$$

or

$$\bar{W}_0 + \gamma\bar{W}_0^2 = \frac{1}{2}\,ug\left[\frac{36z_2+54}{(g-24)(gz_2^2+3gz_2+6+2g)} - \frac{18z_2+12+36/g}{(gz_2^2+3gz_2+6+2g)^2} + \right.$$

$$\left. + \frac{3}{(g-24)}\,f(z_2)\right]\Bigg|_1^{z_2} + \bar{W}_{01} + \gamma\bar{W}_{01}^2 \tag{4-28a}$$

where

$$f(z_2) = \begin{cases} \dfrac{24}{\sqrt{g(24-g)}}\ \text{arctg}\ \left[\dfrac{2gz_2+3g}{\sqrt{g(24-g)}}\right] & \text{for } g < 24 \\ \dfrac{24}{\sqrt{g(g-24)}}\ \ln\ \left[\dfrac{2gz_2+3g-\sqrt{g(g-24)}}{2gz_2+3g+\sqrt{g(g-24)}}\right] & \text{for } g > 24 \end{cases} \tag{4-28b}$$

and $\bar{W}_{01}$ is defined by equation (4-20).

It can be shown* that the bending moment and membrane force distributions corresponding to the solution of equation (4-28) satisfy

$$-1 \leqslant m_2 \leqslant 1 \text{ for } -\frac{1}{r} \leqslant z \leqslant 0, \text{ if } q_{20} \geqslant 0 \text{ or } \frac{3}{g} \geqslant \frac{1}{2}z_2^2 - 1 \tag{4-29a}$$

$$-1 \leqslant m_1 \leqslant 1 \text{ for } 0 \leqslant z \leqslant 1, \text{ if } q_{10} \leqslant 0 \text{ or } \frac{4}{g} \geqslant \frac{2}{z_2} - z_2 \tag{4-29b}$$

and $n = 1$ for $-\frac{1}{r} \leqslant z \leqslant 1$.

---

* The examination of static admissibility conditions is similar to equations (8) and (9) in Appendix I.

Therefore, the solution given by equations (4-28) are valid only when $\frac{4}{g} \geqslant 1$ and $\frac{3}{g} \geqslant \frac{1}{2} z_2^2 - 1$.

For $\frac{4}{g} < 1$, the analysis with the velocity profile (4-21) gives $\left.\frac{\partial m_1}{\partial z}\right|_{z=0^+} = 2\nu_1 q_{10} > 0$* and a yield violation of bending moment occurs in the right side part of the beam, since $m_1 = 1$ at $z=0$. It hints that a plastic hinge may occur in the right side of the impact point instead of the stationary plastic hinge at the impact point. A new velocity profile shown in Fig. 48a

$$\dot{\bar{W}} = \begin{cases} 0 & \text{for } -\frac{1}{r} \leqslant z \leqslant -z_2^- \\ \dot{\bar{W}}_3 \frac{z_2+z}{z_2+z_0} & \text{for } -z_2^+ \leqslant z \leqslant z_0^- \\ \dot{\bar{W}}_3 \frac{1-z}{1-z_0} & \text{for } z_0^+ \leqslant z \leqslant 1 \end{cases} \qquad (4\text{-}30)$$

is assumed. The linear and angular momentum equations of beam are

$$\frac{1}{6} g(1-z_0)^2 \ddot{\bar{W}}(z_0^+) = -2u(1+2\gamma\bar{W}_3) \qquad (4\text{-}31a)$$

$$\frac{1}{6} g(z_2+z_0)^2 \ddot{\bar{W}}(z_0^-) + \frac{1}{12} g(z_2+z_0)^2 \ddot{\bar{W}}(-z_2^+) = -2u(1+2\gamma\bar{W}_3) - \frac{1}{2} z_2 \ddot{\bar{W}}(0) \qquad (4\text{-}31b)$$

and $$\frac{1}{2} g[\ddot{\bar{W}}(z_0^-) + \ddot{\bar{W}}(-z_2^+)](z_2+z_0) + \ddot{\bar{W}}(0) = 0. \qquad (4\text{-}31c)$$

Equations (4-31) with (4-30) give

$$\ddot{\bar{W}}_3 = \frac{12u(1+2\gamma\bar{W}_3)}{g} \frac{[(z_0-z_2-2)(z_2+z_0)^2 g - 4(z_0-z_0z_2+z_2^2)]}{[g(z_2+z_0)^3 + 4(z_2^2-z_0z_2+z_0^2)](z_2+1)(1-z_0)} \qquad (4\text{-}32a)$$

---

* The examination of static admissibility conditions is similar to equations (8) and (9) in Appendix I.

$$\dot{\bar{W}}_3 \dot{z}_0 = -\frac{12u(1+2\gamma\bar{W}_3)}{g} \frac{[g(z_2+z_0)^2(z_2^2+2z_2z_0-z_0^2-2+4z_0)+4(z_2^3+2z_0^2-z_0)]}{[g(z_2+z_0)^3+4(z_2^2-z_0z_2+z_0^2)](z_2+1)(1-z_0)} \tag{4-32b}$$

$$\dot{\bar{W}}_3 \dot{z}_2 = \frac{12u(1+2\gamma\bar{W}_3)}{g} \frac{[2g(z_2+z_0)^2+4z_2]}{[g(z_2+z_0)^3+4(z_2^2-z_0z_2+z_0^2)]} . \tag{4-32c}$$

Equations (4-32) can be written to

$$C_1 \frac{\partial \dot{\bar{W}}_3}{\partial z_0} + C_2 \frac{\partial \dot{\bar{W}}_3}{\partial z_2} = C_3 \dot{\bar{W}}_3 \tag{4-33a}$$

since $\ddot{\bar{W}}_3 = \frac{\partial \dot{\bar{W}}_3}{\partial z_0}\frac{dz_0}{dt} + \frac{\partial \dot{\bar{W}}_3}{\partial z_2}\frac{dz_2}{dt}$, where

$$C_1 = -[g(z_2+z_0)^2(z_2^2+2z_2z_0-z_0^2-2+4z_0)+4(z_2^3+2z_0^2-z_0) \tag{4-33b}$$

$$C_2 = [2g(z_2+z_0)^2+4z_2](z_2+1)(1-z_0) \tag{4-33c}$$

and $$C_3 = [(z_0-z_2-2)(z_2+z_0)^2 g-4(z_0-z_0z_2+z_2^2)]. \tag{4-33d}$$

A numerical method has to be employed to solve equations (4-32) or equations (4-33) until $z_0=0$. The initial conditions at $t=t_1$ are $z_2=1$, $\dot{\bar{W}}_3 = \dot{\bar{W}}_3(t_1)$ and $z_0(t_1)$ is determined by equation (4-32b) with $\dot{z}_0(t_1) = 0$. The static admissibility conditions are checked during the numerical calculations.

For $\frac{3}{g} < \frac{1}{2} z_2^2 - 1$, the previous analysis with velocity profile (4-21) is no longer valid since $\left.\frac{\partial m_2}{\partial z}\right|_{z=0^-} = 2\nu_1 q_{20} < 0$ and a violation of bending moment occurs in the left side part of the beam. Therefore, a new velocity profile shown in Fig. 49a

$$\dot{\bar{W}} = \begin{cases} 0 & \text{for } -\frac{1}{r} \leqslant z \leqslant -z_2^- \\ \dot{\bar{W}}_3 \frac{z_2+z}{z_2-z_0} & \text{for } -z_2^+ \leqslant z \leqslant -z_0^- \\ \dot{\bar{W}}_3 \frac{1-z}{1+z_0} & \text{for } -z_0^+ \leqslant z \leqslant 1 \end{cases} \tag{4-34}$$

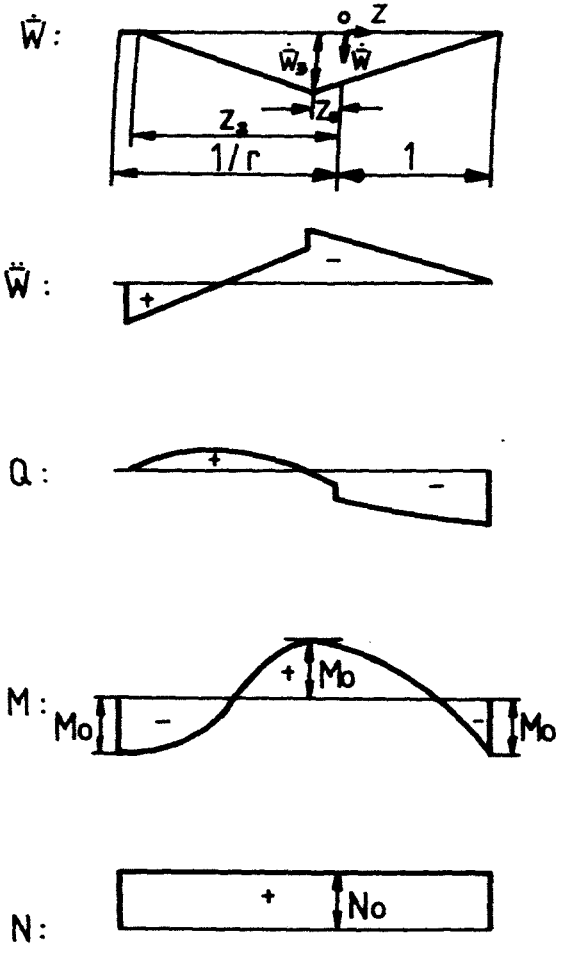

FIG. 49 Second phase of motion when $\frac{3}{g} < \frac{1}{2} z_2^2 - 1$.

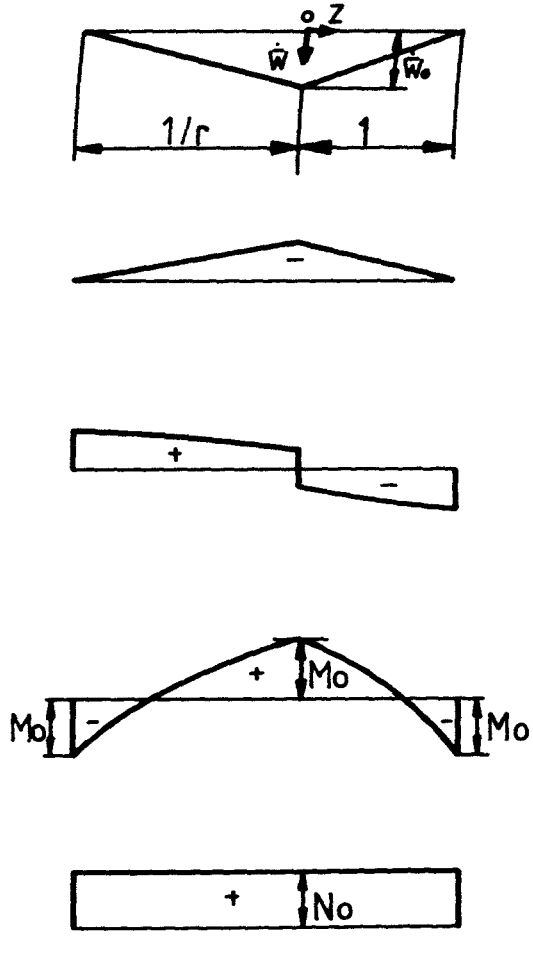

FIG. 50 Final phase of motion when $\frac{3}{g} \geqslant \frac{1}{r^2} - 1$.

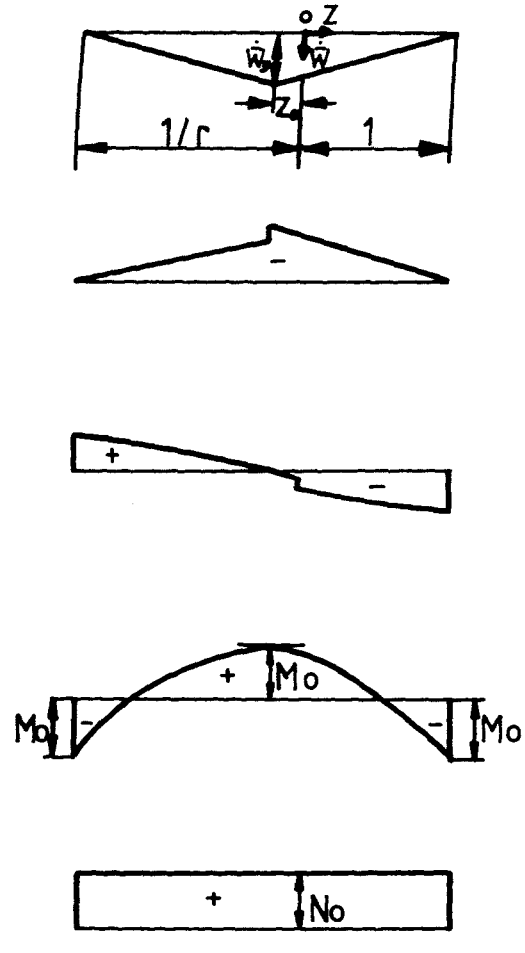

FIG. 51 Final phase of motion when $\frac{3}{g} < \frac{1}{r^2} - 1$.

is assumed. The linear and angular momentum equations of beam are

$$\frac{g}{6}(1+z_0)^2\ddot{\bar{W}}(-z_0^+) = -2u(1+2\gamma\bar{W}_3) - \frac{1}{2}\ddot{\bar{W}}(0) \tag{4-35a}$$

$$\frac{g}{6}(z_2-z_0)^2\ddot{\bar{W}}(-z_0^-) + \frac{g}{12}\ddot{\bar{W}}(-z_2^+)(z_2-z_0)^2 = -2u(1+2\gamma\bar{W}_3) \tag{4-35b}$$

and $$\frac{g}{2}[\ddot{\bar{W}}(-z_0^-)+\ddot{\bar{W}}(-z_2^+)](z_2-z_0) = 0. \tag{4-35c}$$

Equations (4-35) with equation (4-34) give

$$\ddot{\bar{W}}_3 = -4u(1+2\gamma\bar{W}_3)\frac{(1+z_0)^2(2+z_0+z_2)+\frac{6}{g}}{(z_2-z_0)(z_2+1)[\frac{1}{3}g(1+z_0)^3+1]} \tag{4-36a}$$

$$\dot{\bar{W}}_3\dot{z}_0 = 4u(1+2\gamma\bar{W}_3)\frac{(1+z_0)^2[(z_2-z_0)^2-2(z_0+1)^2]-6(1+z_0)/g}{(z_2-z_0)(z_2+1)[\frac{1}{3}g(1+z_0)^3+1]} \tag{4-36b}$$

and $$\dot{\bar{W}}_3\dot{z}_2 = \frac{24u(1+2\gamma\bar{W}_3)}{g(z_2-z_0)}. \tag{4-36c}$$

Equations (4-36) with $\ddot{\bar{W}}_3 = \frac{\partial\dot{\bar{W}}_3}{\partial z_0}\dot{z}_0 + \frac{\partial\dot{\bar{W}}_3}{\partial z_2}\dot{z}_2$ give

$$d_1\frac{\partial\dot{\bar{W}}_3}{\partial z_0} + d_2\frac{\partial\dot{\bar{W}}_3}{\partial z_2} = d_3\dot{\bar{W}}_3 \tag{4-37a}$$

where $$d_1 = (1+z_0)^2[(z_2-z_0)^2-2(z_0+1)^2]-6(1+z_0)/g \tag{4-37b}$$

$$d_2 = \frac{6}{g}(z_2+1)[\frac{1}{3}g(1+z_0)^3+1] \tag{4-37c}$$

and $$d_3 = -[(1+z_0)^2(2+z_0+z_2)+\frac{6}{g}]. \tag{4-37d}$$

A numerical method has to be employed to solve equations (4-36) or (4-37) until $z_2 = \frac{1}{r}$ at $t=t_2$. This type of motion starts with $z_0=0$ when

$$z_2 = \sqrt{\frac{6}{g} + 2} \tag{4-38}$$

which is obtained from $\frac{3}{g} = \frac{1}{2} z_2^2 - 1$. The initial conditions of $\dot{\bar{W}}_3$ and $\bar{W}_3$ are defined by equations (4-24) and (4-28) with z_2 given by equation (4-38). The static admissibility conditions should be checked during numerical calculation.

D) Phase 4, $t_2 < t \leqslant t_f$

The left side travelling hinge at $z = -z_2$ reaches the left-hand support at $t=t_2$ and two parts of the beam rotate as rigid bodies during this phase of motion until all the initial kinetic energy is dissipated as plastic work. The velocity profile shown in Fig. 50a is

$$\dot{\bar{W}} = \begin{cases} \dot{\bar{W}}_0 (1+rz) & \text{for } -\frac{1}{r} \leqslant z \leqslant 0 \\ \dot{\bar{W}}_0 (1-z) & \text{for } 0 \leqslant z \leqslant 1 \end{cases}$$

The linear and momentum equations of beam give

$$[\tfrac{1}{3} g(1+r)+r]\ddot{\bar{W}}_0 + 4u(1+r)r(1+2\gamma\bar{W}_0) = 0 . \tag{4-40}$$

Integrating equation (4-40) after multiplying by $\dot{\bar{W}}_0$, we obtain

$$\tfrac{1}{2} [\tfrac{1}{3} g(1+r)+r]\dot{\bar{W}}_0^2 + 4u(1+r)r(\bar{W}_0+\gamma\bar{W}_0^2) = A \tag{4-41a}$$

and $$A = \tfrac{1}{2}[\tfrac{1}{3} g(1+r)+r]\dot{\bar{W}}_{02}^2 + 4u(1+r)r(\bar{W}_{02}+\gamma\bar{W}_{02}^2) \tag{4-41b}$$

and $\dot{\bar{W}}_{02}$ and $\bar{W}_{02}$ are the velocity and displacement at the impact point when $z_2 = \frac{1}{r}$ at $t = t_2$. If $r = 1$, then $\dot{\bar{W}}_{02} = \dot{\bar{W}}_{01}$ and $\bar{W}_{02} = \bar{W}_{01}$ and they are defined by equations (4-19) and (4-20),

respectively. If $r \neq 1$, but $\frac{4}{g} \geqslant 1$ and $\frac{3}{g} \geqslant \frac{1}{2}\frac{1}{r^2} - 1$, then $\dot{\bar{W}}_{02}$ and $\bar{W}_{02}$ are defined by equations (4-24) and (4-28) with $z_2 = \frac{1}{r}$, respectively. Otherwise, $\dot{\bar{W}}_{02}$ and $\bar{W}_{02}$ is obtained from numerical calculation.

The motion of beam stops when $\dot{\bar{W}}_0 = 0$. Therefore, the maximum permanent deformation at the impact point can be obtained from equations (4-41) and is

$$\bar{W}_{0f} + \gamma \bar{W}_{0f}^2 = A/[4u(1+r)r]$$

or

$$\bar{W}_{0f} = \frac{1}{2\gamma}\left[-1 + \sqrt{1 + \frac{A\gamma}{u(1+r)r}}\right] \qquad (4\text{-}42)$$

where A is defined by equation (4-41b).

The bending moment and membrane force distribution expressions*show that

$$-1 \leqslant m_2 \leqslant 1 \quad \text{for} \quad -\frac{1}{r} \leqslant z \leqslant 0 \quad \text{if} \quad q_{20} \geqslant 0 \quad \text{or} \quad \frac{3}{g} \geqslant \frac{1}{r^2} - 1 \qquad (4\text{-}43a)$$

$$-1 \leqslant m_1 \leqslant 1 \quad \text{for} \quad 0 \leqslant z \leqslant 1 \quad \text{and} \quad n = 1 \quad \text{for} \quad -\frac{1}{r} \leqslant z \leqslant 1. \qquad (4\text{-}43b)$$

Therefore, the solution given by equation (4-42) is valid when $\frac{3}{g} \geqslant \frac{1}{r^2} - 1$.

For $\frac{3}{g} < \frac{1}{r^2} - 1$, the previous analysis with the velocity profile (4-39) gives $\left.\frac{\partial m_2}{\partial z}\right|_{z=0^-} = 2\nu_1 q_{20} < 0$ and a yield violation of bending moment occurs in the left side part of the beam, since $m_2=1$ at $z=0$. Therefore, a new velocity profile shown in Fig. 51a

---

* The examination of static admissibility conditions is similar to equations (14) and (15) in Appendix I.

$$\dot{\bar{W}} = \begin{cases} \dot{\bar{W}}_3 \dfrac{1+zr}{1-z_0 r} & \text{for } -\dfrac{1}{r} \leqslant z \leqslant -z_0^- \\ \dot{\bar{W}}_3 \dfrac{1-z}{1+z_0} & \text{for } -z_0^+ \leqslant z \leqslant 1 \end{cases} \tag{4-44}$$

is postulated. The linear and angular momentum equations of beam give

$$\ddot{\bar{W}}_3 = -4u(1+2\gamma\bar{W}_3) \frac{(1+z_0)^2(1+\frac{1}{r}) + \frac{3}{g}}{(\frac{1}{r} - z_0)(\frac{1}{r} + 1)[\frac{1}{3} g(1+z_0)^3 + 1]} \tag{4-45a}$$

and $$\dot{\bar{W}}_3 \dot{z}_0 = 4u(1+2\gamma\bar{W}_3) \frac{(1+z_0)^2(1+\frac{1}{r})(\frac{1}{r} - 1 - 2z_0) - 3(1+z_0)\frac{1}{g}}{(\frac{1}{r} - z_0)(\frac{1}{r} + 1)[\frac{1}{3} g(1+z_0)^3 + 1]}. \tag{4-45b}$$

It is reasonable to assume that $\dot{z}_0=0$ during the whole response of this case since the occurrence of this case only depends on g and r which are constants. Furthermore, the solution of this case with $\dot{z}_0=0$ does satisfy the statical admissibility conditions* as well as kinematic admissibility conditions. Therefore, equations (4-45) give

$$\ddot{\bar{W}} + 4ue(1+2\gamma\bar{W}_3) = 0 \tag{4-46a}$$

where $$e = \frac{(1+z_0)^2(1+\frac{1}{r}) + \frac{3}{g}}{(\frac{1}{r} - z_0)(\frac{1}{r} + 1)[\frac{1}{3} g(1+z_0)^3 + 1]} \tag{4-46b}$$

and $$z_0 = -\frac{3}{4} + \frac{1}{4r} + \frac{1}{2}\sqrt{\frac{1}{4} + \frac{1}{4r^2} + \frac{1}{2r} - \frac{6r}{g(1+r)}} \tag{4-46c}$$

which is obtained from equation (4-45b) with $\dot{z}_0=0$.

Integrating equation (4-46a) after multiplying by $\dot{\bar{W}}_3$, we obtain

---

* The examination of static admissibility is similar to equations (16) and (17) in Appendix I.

$$\frac{1}{2}\dot{\bar{W}}_3^2 + 4ue(\bar{W}_3+\gamma\bar{W}_3^2) = \frac{1}{2}\dot{\bar{W}}_{32}^2+4ue(\bar{W}_{32}+\gamma\bar{W}_{32}^2) \tag{4-47}$$

where $\dot{\bar{W}}_{32}$ and $\bar{W}_{32}$ indicate the velocity and displacement of the point $z = -z_0$ at $t=t_2$.

The motion stops when $\dot{\bar{W}}_3 = 0$ and the permanent deformation at $z = -z_0$ is determined by

$$4ue(\bar{W}_{3f}+\gamma\bar{W}_{3f}^2) = \frac{1}{2}\dot{\bar{W}}_{32}^2+4ue(\bar{W}_{32}+\gamma\bar{W}_{32}^2). \tag{4-48}$$

The maximum permanent deformation at impact point z=0 is

$$\bar{W}_{0f} = \bar{W}_{02} + (\bar{W}_{3f}-\bar{W}_{32})/(1+z_0). \tag{4-49}$$

It shows* that the static admissibility are satisfied with

$$-1 \leqslant m_2 \leqslant 1 \text{ in } -\frac{1}{r} \leqslant z \leqslant -z_0,\ -1 \leqslant m_1 \leqslant 1 \text{ in } -z_0 \leqslant z \leqslant 1$$

and $n = 1$ in $-\frac{1}{r} \leqslant z \leqslant 1$.

4.4 Discussion

A surprisingly simple solution for a simply supported beam with axial restraints subjected to an impulsive loading is obtained in Section 4.2 when the simplified square yield curves are employed. The results given by equation (4-12) give good agreement with other authors' previous work shown in Fig. 45. Therefore, the square yield curves are very useful from the engineering point of view since they simplify the analysis and give good predictions.

---

* The examination of static admissibility is similar to equations (16) and (17) in Appendix I.

The square yield curves are also employed in Section 4.3 to analyse the finite deflection of a clamped beam struck by a falling mass at any point of its span. The analytical solution can be obtained from Section 4.3 when $\frac{4}{g} \geq 1$ and $\frac{3}{g} \geq \frac{1}{2}\frac{1}{r^2} - 1$. Otherwise, a numerical method has to be employed to solve equations (4-32) or (4-33) and (4-36) or (4-37).

Equations (4-32) and (4-36) are more difficult to solve than equations (3-26) and (3-29) which are given in Chapter 3, since equations (4-32) and (4-36) are second-order differential equations, while equations (3-26) and (3-29) can be considered as first-order differential equations of $\dot{\bar{W}}_3$. One can use finite-difference methods to solve equations (4-32) and (4-36) directly, or use this method to solve the partial differential equations (4-33) and (4-37) and obtain $\dot{\bar{W}}_3$, then with equations (4-32b,c) or (4-36b,c) to obtain $\bar{W}_3$. However, after comparing the analytical results obtained in Section 3 of this Chapter with those in Case I of Chapter 3, one may assume that the deformation can be obtained by replacing $\bar{W}_3$, of which value obtained in Chapter 3, with $W_3 + \gamma\bar{W}_3^2$. It is shown that the velocity $\dot{\bar{W}}_3$ given by equations (3-26) or (3-29) are the same as that given by equations (4-32) or (4-36) with certain values of z_0 and z_2, since the same equations as equations (4-33) and (4-37) can be derived from equations (3-26) and (3-29), respectively. The solutions with $\frac{4}{g} \geq 1$ and $\frac{3}{g} \geq \frac{1}{2}\frac{1}{r^2} - 1$ are the same as those which ignored the influence of finite deflection, or geometrical change, if $\bar{W}_0 + \gamma\bar{W}_0^2$ is replaced by $\bar{W}_0$. Furthermore, the velocity $\dot{\bar{W}}_0$ at each phase with travelling plastic hinge,

$\dot{z}_1 \neq 0$ or $\dot{z}_2 \neq 0$, are exactly the same between N=0 and $N=N_0$, provided z_1 and z_2 are given*.

A wide range of γ, g and u was assumed and the corresponding maximum deformations are obtained. Some of these results are plotted in Figs. 52 and 53. The results from bending only solution are also plotted in Figs. 52 and 53. It shows that the differences between the bending only solution and the solution with influence of finite deflection increases sharply with the increase of external energy u. Fig. 53 shows that when u = 10 the results obtained from bending only solution can reach about ten times larger than that with the influence of finite deflection. However, this difference decreases with the increase of the mass ratio g.

When r = 1 or $\ell_1=\ell_2=\ell$, the maximum permanent deformation can be obtained from equation (4-42) in the form

$$\bar{W}_{0f} = \frac{1}{2\gamma}\{-1+\sqrt{1 + \frac{u}{3g}\gamma \left[\frac{g}{1+g} + 2\ln(1+g)\right]}\} \qquad (4\text{-}50)$$

For beams with rectangular cross-sections with $M_0 = \frac{1}{4} BH^2\sigma_0$ and $N_0=BH\sigma_0$, equation (4-50) can be written as

$$\frac{W_{0f}}{H} = \frac{1}{2}\{-1 + \sqrt{1 + \frac{u}{3g}\frac{\ell}{H}\left[\frac{g}{1+g} + 2\ln(1+g)\right]}\} \qquad (4\text{-}51)$$

The results which are obtained from equation (4-51) and other authors' previous work** are plotted in Fig. 54. It is clear that

---

* Equation (3-12b) and equation (4-16b), and equation (3-19) and equation (4-24) are the same, since B+C in equation (3-19) equals 1 when the shear strength of material is infinite.

** These formulae are listed in Appendix II.

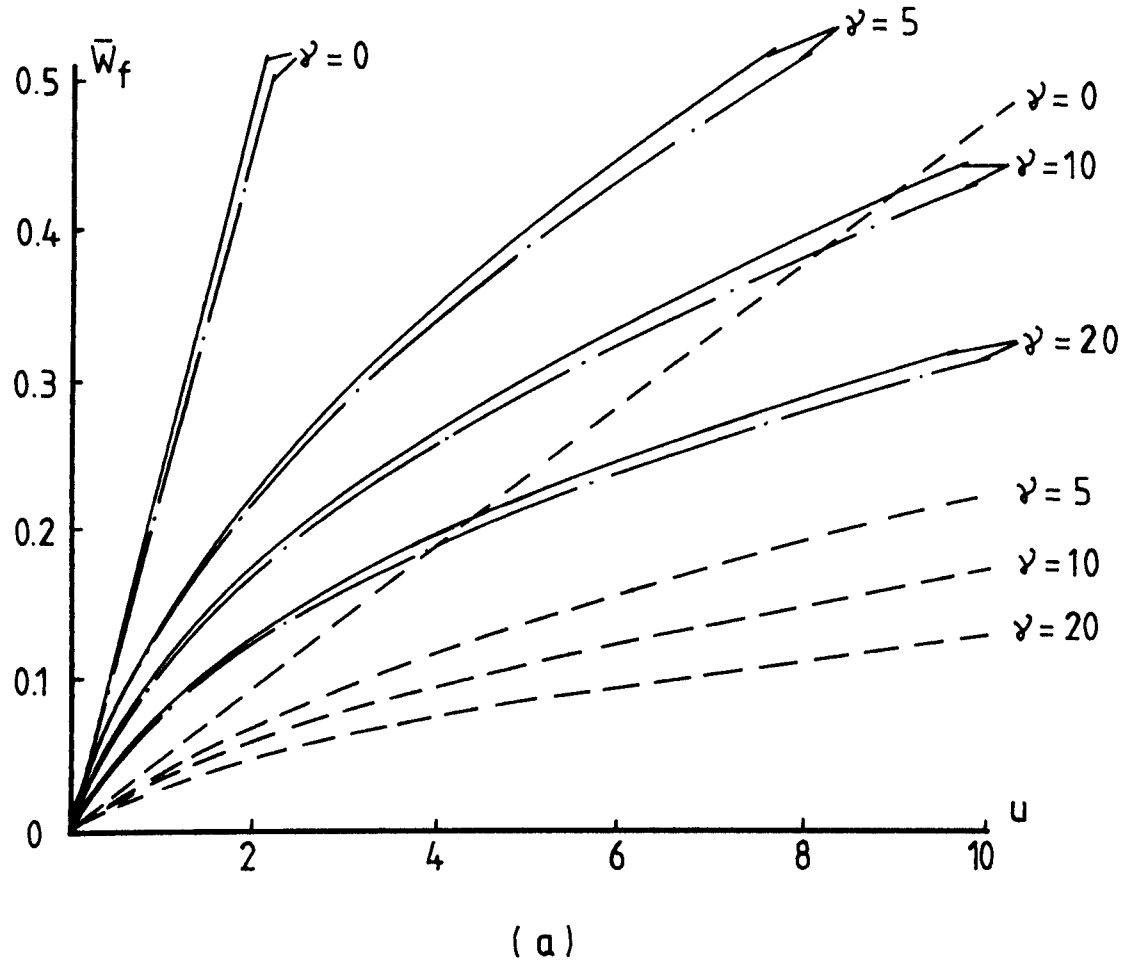

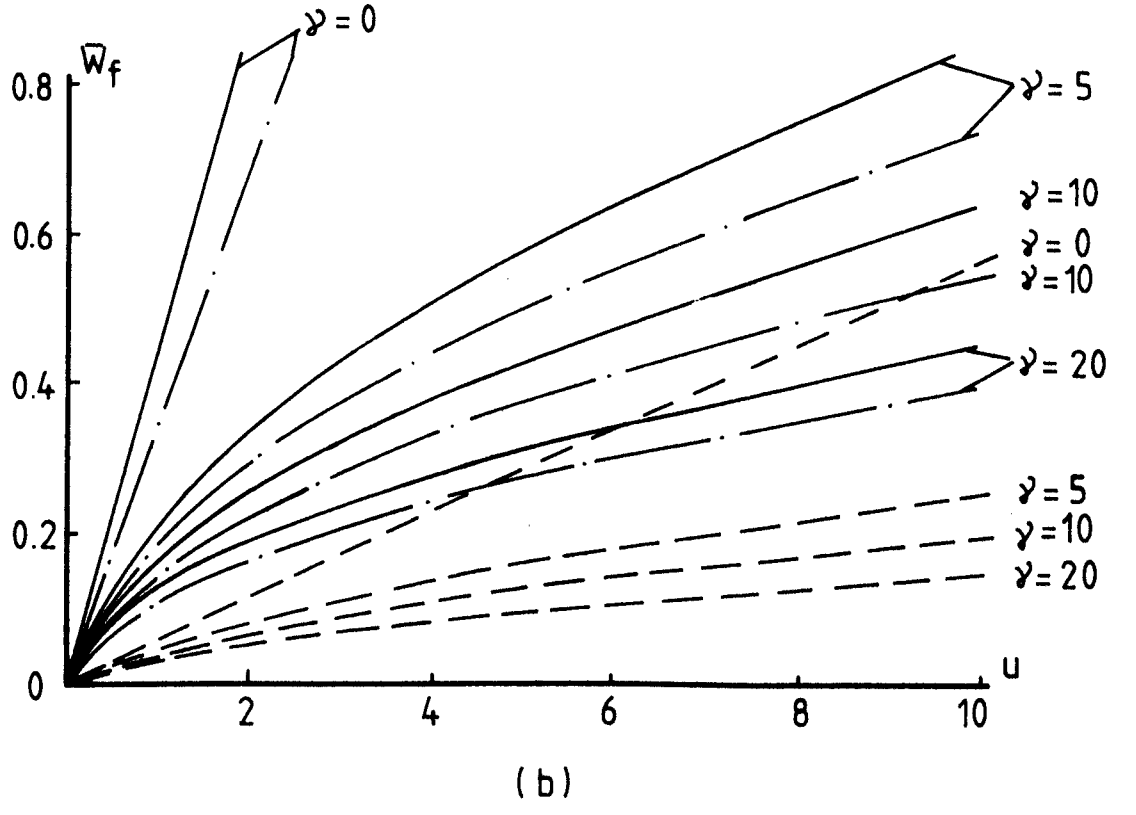

FIG. 52 Variation of maximum permanent deformation $\bar{W}_f$ of a clamped beam with external dynamic energy u. (a) r = 1 and (b) r = 0.1, ——— g = 0.00001; —·— g = 0.1; ---- g = 10.

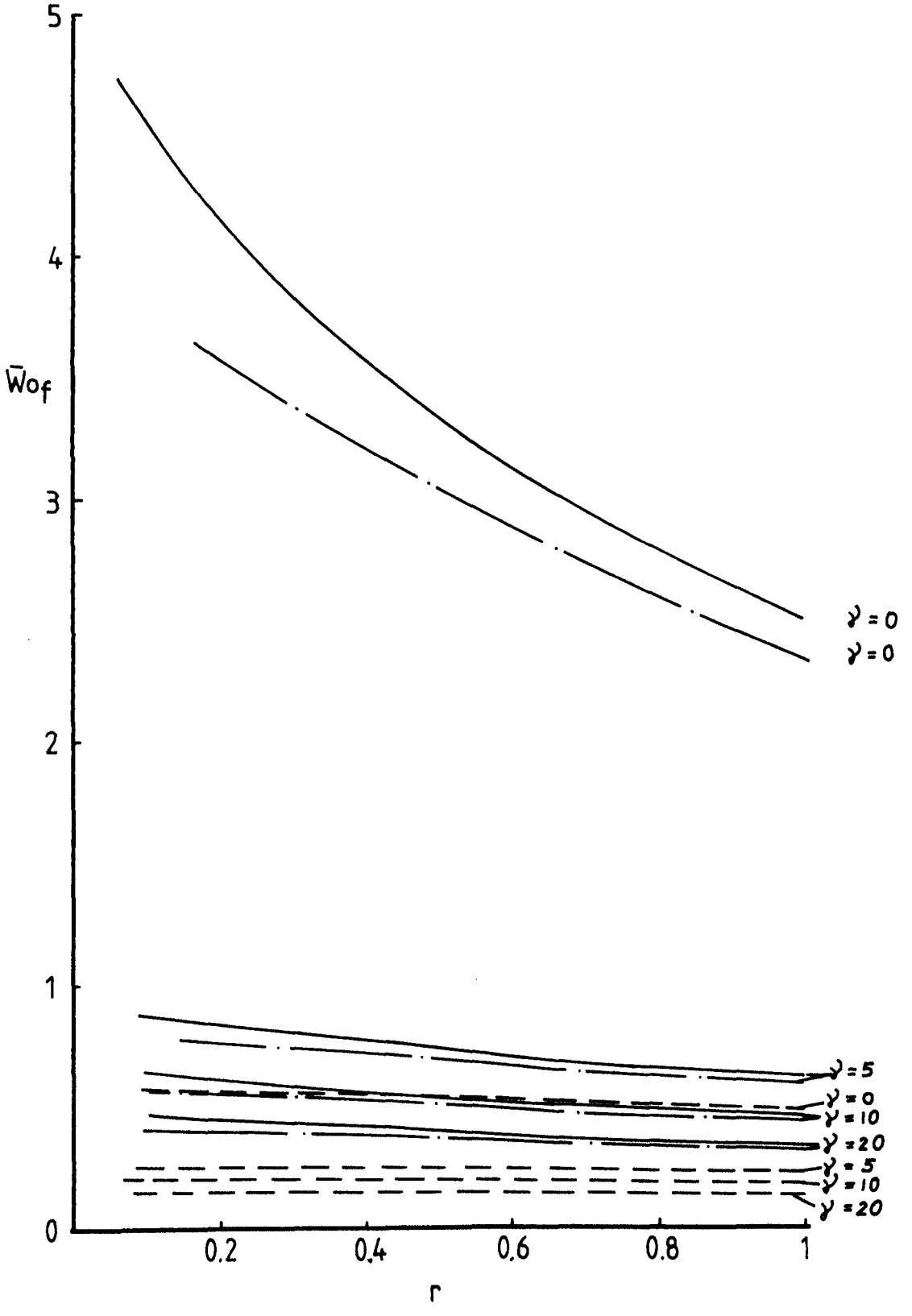

FIG. 53 Variation of maximum permanent deformation $\bar{W}_f$ with r when u = 10. —— g = 0.00001; —·— g = 0.1; ---- g = 10.

the results from equation (4-51) do bound well Nonaka's work in which the parabolic yield curve or 'exact' yield curve is employed [12].

Equation (4-19) shows that when $g \ll 1$, the first phase of motion hardly influences the entire response of beam since the value of velocity $\dot{\bar{W}}_0$ at the end of first phase is almost equal to its initial value 2u, i.e. $\dot{\bar{W}} \doteq 2u$ at the end of first phase. Thus, it is reasonable to neglect the influence of first phase and assume that two half beams rotate as rigid bodies during the entire response, provided $g \ll 1$. Indeed, Jones [30] and Oliveira [20] results give good predictions even when g=1, as shown in Fig. 54.

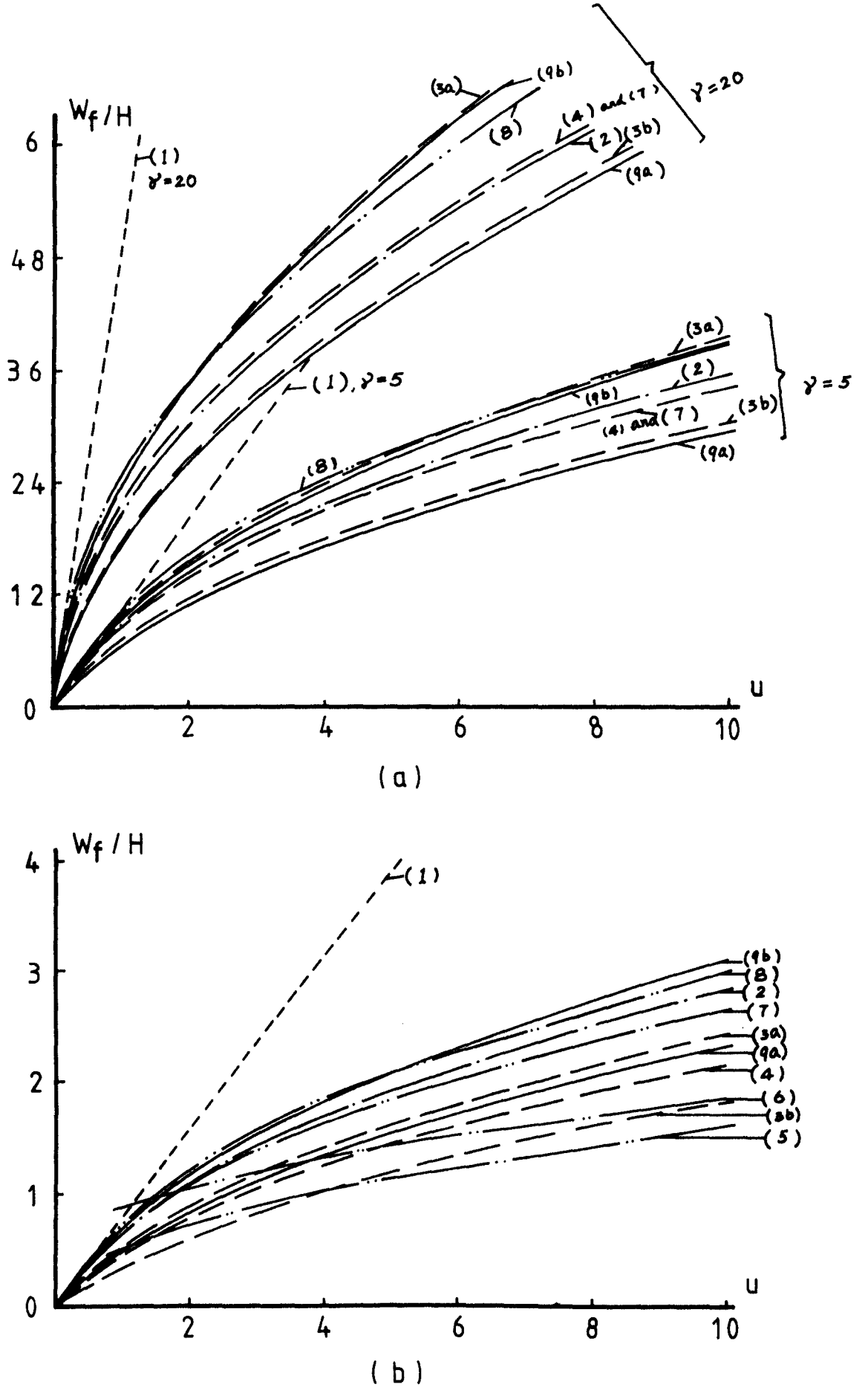

FIG. 54 Variation of maximum permanent deformation W_f/H with external dynamic energy u. (a) g = 0.00001, γ = 5 and 20; (b) g = 1, γ = 5. The symbol (X) indicates that the curve corresponds to the equation (X) given in Appendix II.

CHAPTER 5

THEORETICAL ASPECTS OF PLASTIC FAILURE OF A CLAMPED BEAM STRUCK BY A MASS AT ANY POINT OF ITS SPAN

5.1 Introduction

Jones [29] examined the plastic failure of a clamped beam subjected to an impulsive loading uniformly distributed over its span. His theoretical work is in good agreement with Menkes and Opat's experimental results [44].

The theoretical analysis of plastic failure of a clamped beam struck by a mass at any point of its span is presented in this Chapter. The triangular plastic regions at the supports and at the impact point of the beam which were assumed by Nonaka [12] are employed herein. Equation (1) of reference [30] is used to estimate the maximum permanent deformation of the beam since it is simple and provides a good estimate provided the mass ratio $g = \frac{\bar{m}\ell_1}{G}$ is not very small. The value of shear sliding is calculated from the theoretical analysis discussed in Chapter 3 of this thesis. The beam has a rectangular cross-section with depth H and width B.

5.2 Plastic Failure of Beams Due to Tensile Tearing

Most theoretical methods and most numerical schemes for the dynamic plastic behaviour of structures use a material having an unlimited ductility. Clearly, this is a severe idealisation for real materials since the structure may crack or break when the

maximum strain in the structure reaches the limit elongation of the structural material. Indeed, experimental results reported in reference [44] and in Chapter 6 of this thesis show that tensile tearing failure occurs in beams when the external dynamic energy is sufficient.

Few papers [29] have been published on the dynamic plastic behaviour of structures made from a material with a limited elongation. One reason is the difficulty of estimating the maximum allowable strain in a structure.

5.2.1 Plastic Regions

After examining his experimental beam specimens which were subjected to an impulsive velocity loading on a concentrated mass located at the centre, Nonaka [12] assumed that plastic strains occur in triangular regions at the supports and at the midspan of the beam. The assumed plastic region starts with two isosceles right triangles, shown in Fig. 55a, with the larger one on the tension side and the smaller one on the compressive side. With the increase of beam deformation the triangle on the tension side increases while the other on the compressive side decreases. The whole plastic region becomes one triangle in tension as shown in Fig. 55b when the deformation is equal to the beam thickness H. The plastic regions both at the supports and at the midspan then spread uniformly along the beam as indicated in Fig. 55b until the plastic regions extend over the whole span. At this stage the total length of a plastic region for half span of the beam is twice

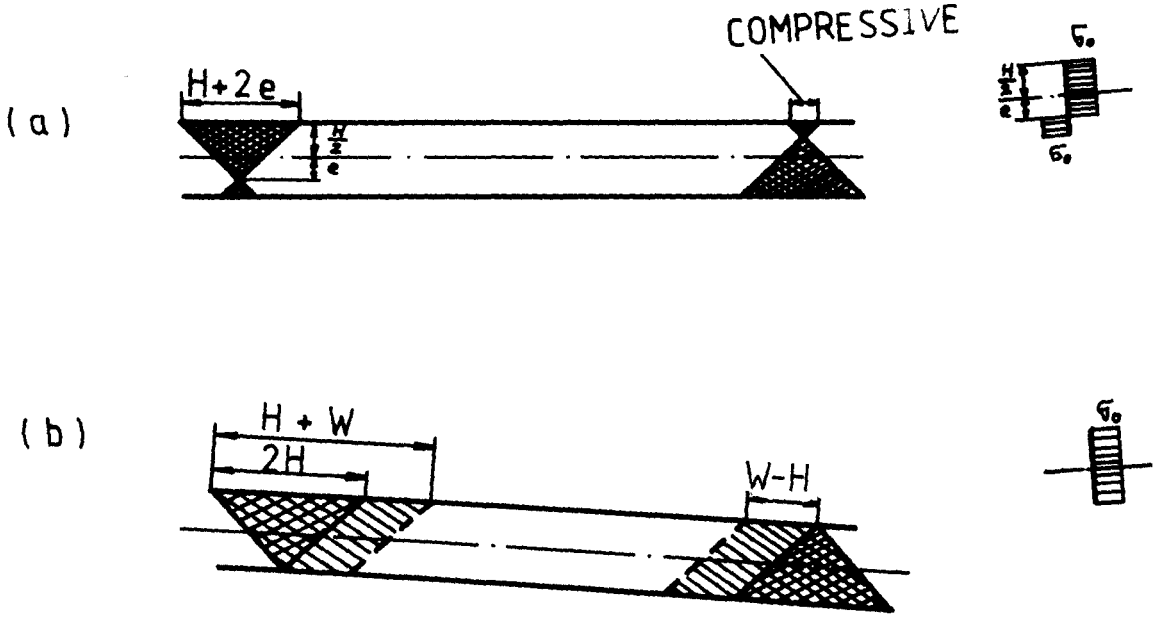

FIG. 55 Plastic regions. (a) for $0 \leqslant \frac{W}{H} \leqslant 1$ and (b) for $\frac{W}{H} \geqslant 1$.

the deformation at the beam centre. A similar sequence of triangular plastic region formation is also found at the supports and at the impact point of the beam struck by a falling tup, which will be reported in the next Chapter of this thesis. Instead of two triangular plastic regions at the midspan in reference [12], a large triangular plastic region occurs at the impact point of a clamped beam struck by a mass. It is assumed that the large triangular plastic region is the sum of two plastic regions at the supports and the distribution of the large plastic region to each part of the beam is equal to the plastic region at the support of this part of the beam.

Nonaka's assumption is used for the plastic tension length $\bar{\ell}$ on the upper or lower surface of the beam struck by a mass at any point of its span shown in Fig. 42a.

When the deformation of the beam is less than the beam thickness H, or $\frac{W}{H} \leqslant 1$, we have

$$N = 2\sigma_0 Be \quad \text{and} \quad \frac{N}{N_0} = \frac{N_0 W^*}{4M_0} \qquad (5\text{-}1,2)$$

where N is the membrane force, e is the distance from the neutral line to the central line of the beam cross section shown in Fig. 55a and W is the deformation at the impact point.

Equations (5-1) and (5-2) give

$$e = \frac{W}{2} \qquad (5\text{-}3)$$

---

* See equation (4) in reference [12] and also see references [58,59].

since $N_0 = \sigma_0 HB$ and $M_0 = \frac{1}{4}\sigma_0 H^2 B$ for rectangular section.

The length of the tensile plastic region on the upper or lower surface of the beam shown in Fig. 55a is

$$\bar{\ell} = 2(\frac{H}{2} + e) \qquad (5\text{-}4)$$

Equations (5-3) and (5-4) give

$$\bar{\ell} = H + W \quad \text{for } 0 \leqslant \frac{W}{H} \leqslant 1 \qquad (5\text{-}5a)$$

For $1 < \frac{W}{H} \leqslant \frac{\ell_1}{2H}$, the plastic regions spread along the beam shown in Fig. 55b and

$$\bar{\ell} = 2W \quad \text{for } 1 < \frac{W}{H} \leqslant \frac{\ell_1}{2H} \qquad (5\text{-}5b)$$

until the plastic regions extend to the whole beam at $\bar{\ell} = \ell_1$ or $\frac{W}{H} = \frac{\ell_1}{2H}$.

For $\frac{W}{H} > \frac{\ell_1}{2H}$, the plastic region remains

$$\bar{\ell} = \ell_1 \qquad \text{for } \frac{W}{H} > \frac{\ell_1}{2H} \qquad (5\text{-}5c)$$

until the motion of beam stops.

5.2.2 Maximum Tension Strain

a) for $0 \leqslant \frac{W}{H} \leqslant 1$

The increased length of an upper layer of plastic region at the support or lower layer of plastic region at the impact point of the beam between time T and T+ΔT, shown in Fig. 56a, can be expressed by

$$\Delta\ell_1 = \Delta\ell_{1b} + \frac{1}{2}\Delta\ell_{1m}, \qquad (5\text{-}6a)$$

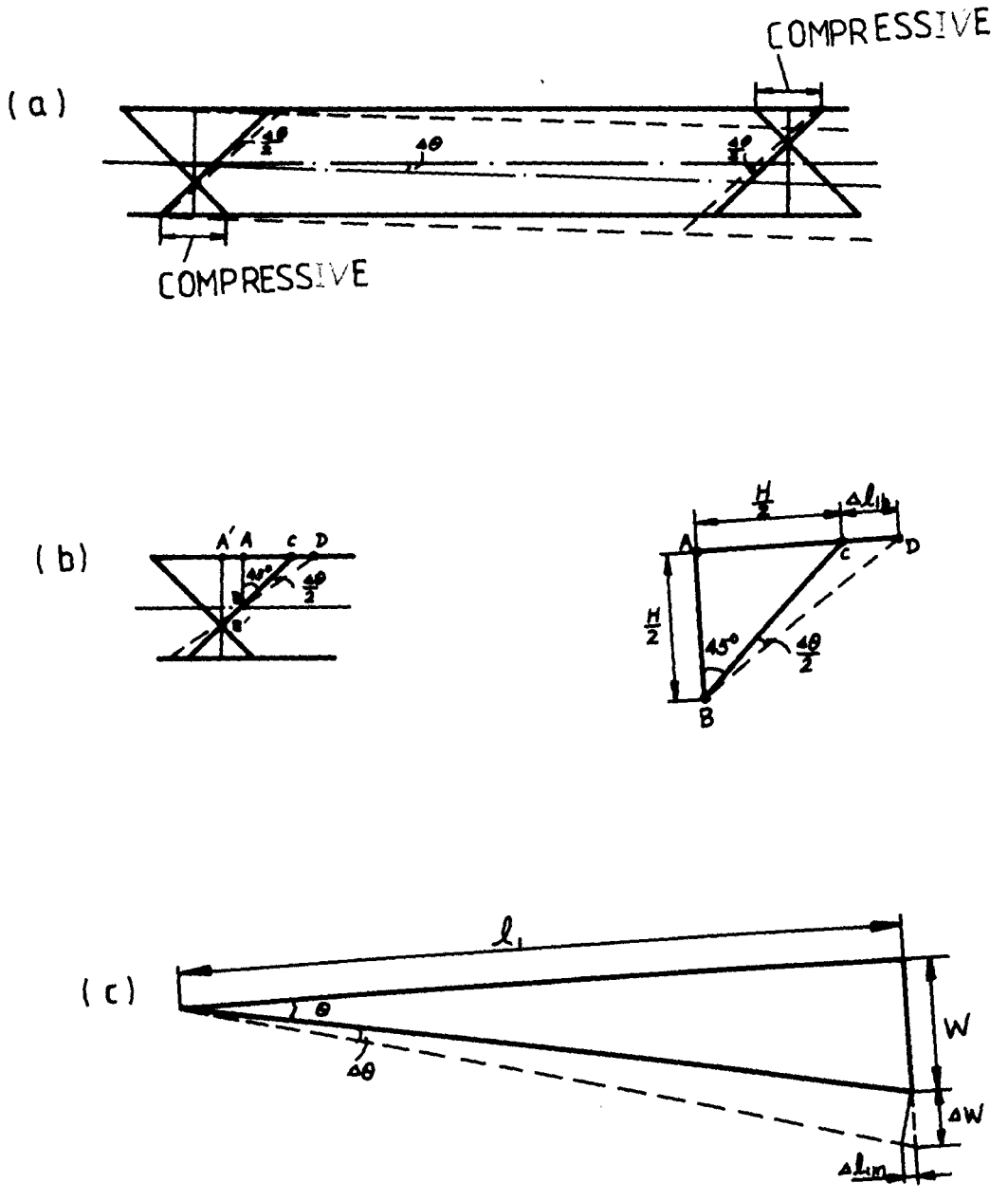

FIG. 56 The increased length of upper layer or lower layer of the beam between time T and T + ΔT. (a) the deformations of beam at time T and T + ΔT; (b) the increased length due to bending moment; (c) the increased length due to membrane force.

where $\Delta\ell_{1b} \simeq H\Delta\theta$ (5-6b)

is the increased length due to bending moment shown in Fig. 56b,

$$\Delta\ell_{1m} \simeq \Delta W \cdot \sin\theta = \Delta W \frac{W}{\sqrt{W^2+\ell_1^2}} \tag{5-6c}$$

is the increased length due to membrane force shown in Fig. 56c and

$$\Delta\theta \simeq \frac{\sqrt{\Delta W^2 - \Delta\ell_{1m}^2}}{\sqrt{W^2+\ell_1^2}} = \frac{\Delta W \ell_1}{W^2+\ell_1^2}. \tag{5-6d}$$

Equations (5-6) give

$$\Delta\ell_1 = \frac{1}{2}\left[H\frac{2\ell_1}{W^2+\ell_1^2} + \frac{W}{\sqrt{W^2+\ell_1^2}}\right]\Delta W. \tag{5-7}$$

Therefore, the increased strain between time T and T+ΔT is

$$\Delta\varepsilon = \frac{\Delta\ell_1}{\ell} = \frac{1}{2}\left[\frac{2H\ell_1}{W^2+\ell_1^2} + \frac{W}{\sqrt{W^2+\ell_1^2}}\right]\frac{\Delta W}{H+W} \tag{5-8}$$

and the maximum tension strain at time T is

$$\varepsilon = \int_0^W \frac{1}{2}\left[\frac{2H\ell_1}{W^2+\ell_1^2} + \frac{W}{\sqrt{W^2+\ell_1^2}}\right]\frac{dW}{H+W}$$

$$= \frac{H\ell_1}{(\ell_1^2+H^2)}\left\{\frac{1}{2}\ln\left[\frac{(W+H)^2\ell_1^2}{(W^2+\ell_1^2)H^2}\right] + \frac{H}{\ell_1}\operatorname{arctg}\frac{W}{\ell_1}\right\} + \frac{1}{2}\ln\left(\frac{W}{\ell_1} + \sqrt{1+\frac{W^2}{\ell_1^2}}\right)$$

$$- \frac{H}{2\sqrt{H^2+\ell_1^2}}\ln\left\{\frac{\left[\sqrt{H^2+\ell_1^2}\,(\ell_1+\sqrt{H^2+\ell_1^2}) - H^2\right](W+H)}{\left[\sqrt{H^2+\ell_1^2}\,(\sqrt{\ell_1^2+W^2}+\sqrt{H^2+\ell_1^2}) - H(W+H)\right]H}\right\} \tag{5-9}$$

When $\frac{W}{H} = 1$, the strain is

$$\varepsilon_1 = \frac{H\ell_1}{\ell_1^2+H^2}\left\{\frac{1}{2}\ln\left(\frac{4\ell_1^2}{H^2+\ell_1^2}\right) + \frac{H}{\ell_1}\operatorname{arctg}\frac{H}{\ell_1}\right\} + \frac{1}{2}\ln\left(\frac{H}{\ell_1} + \sqrt{1+\frac{H^2}{\ell_1^2}}\right)$$

$$- \frac{H}{2\sqrt{H^2+\ell_1^2}}\ln\left(1+\sqrt{1+H^2/\ell_1^2}\right) \tag{5-10}$$

(b) for $1 < \frac{W}{H} \leqslant \frac{\ell_1}{2H}$

When $\frac{W}{H} > 1$, the beam enters into the membrane state as shown in Fig. 55b. Therefore, $\Delta\ell_{1b} = 0$ and

$$\Delta\varepsilon = \frac{\Delta\ell_{1m}}{\bar{\ell}} = \frac{W}{\sqrt{W^2+\ell_1^2}} \frac{\Delta W}{\bar{\ell}}. \tag{5-11a}$$

Substituting equation (5-5b) into (5-11a), we obtain

$$\varepsilon = \int_H^W \frac{W}{\sqrt{W^2+\ell_1^2}} \frac{dW}{2W} + \varepsilon_1$$

$$= \frac{1}{2} \ln\left(\frac{W/\ell_1 + \sqrt{1+W^2/\ell_1^2}}{H/\ell_1 + \sqrt{1+H^2/\ell_1^2}}\right) + \varepsilon_1. \tag{5-11b}$$

When $\frac{W}{H} = \frac{\ell_1}{2H}$, the plastic regions extend to the whole beam and

$$\varepsilon_2 = \frac{1}{2} \ln\left[\frac{\frac{1}{2}(1+\sqrt{5})}{H/\ell_1 + \sqrt{1+H^2/\ell_1^2}}\right] + \varepsilon_1. \tag{5-12}$$

(c) for $\frac{W}{H} > \frac{\ell_1}{2H}$

Substituting equation (5-5c) into (5-11a), we obtain

$$\varepsilon = \int_{\frac{\ell_1}{2}}^W \frac{W\,dw}{\ell_1\sqrt{\ell_1^2+W^2}} + \varepsilon_2.$$

$$= \sqrt{\frac{W^2}{\ell_1^2} + 1} - \frac{1}{2}\sqrt{5} + \varepsilon_2. \tag{5-13}$$

5.2.3 The Maximum Permanent Deformation of the Beam

It may be shown that equation (1) in reference [30], which is obtained from Jones' previous work [17], agrees reasonably well with the theoretical analysis discussed in Chapter 4 of this thesis, provided the mass ratio g is not small*.

The maximum permanent deformation from equation (1) of reference [30] can be written

$$\frac{W_m}{H} = \frac{1}{2}[\sqrt{1+\lambda A} - 1] , \qquad (5\text{-}14a)$$

where

$$A = \frac{32}{3}\frac{r[3r+g(1+r)]}{(1+r)[2r+g(1+r)]^2} , \qquad (5\text{-}14b)$$

$$\lambda = \frac{GV_0^2 \ell_1}{2BH^3\sigma_0} , \quad g = \frac{\bar{m}\ell_1}{G} \text{ and } r = \ell_1/\ell_2. \qquad (5\text{-}14c\text{-}e)$$

5.2.4 Threshold External Dynamic Energy for Onset of Plastic Failure by Tensile Tearing.

Equations (5-9), (5-11b), (5-13) and (5-14) show that the tensile strain increases with the increase of the external dynamic energy λ. When the tensile strain reaches the limit strain ε_m of beam material, or the corresponding external dynamic energy is equal to some certain value λ_t, tensile tearing will occur. λ_t is the threshold external dynamic energy for onset of plastic failure due to tensile tearing.

---

* One can also use equation (7-1) in Chapter 7 of this thesis.

Dependent on the limit strain ε_m of material, the tensile tearing may start within three different ranges of deformation of the beam; $0 < \frac{W}{H} \leqslant 1$, $1 < \frac{W}{H} \leqslant \frac{\ell_1}{2H}$ or $\frac{W}{H} > \frac{\ell_1}{2H}$. If $\varepsilon_1 > \varepsilon_m$, the tensile tearing may start when $0 < \frac{W}{H} \leqslant 1$. If $\varepsilon_1 < \varepsilon_m$ and $\varepsilon_2 > \varepsilon_m$, the tensile tearing may start when $1 < \frac{W}{H} \leqslant \frac{\ell_1}{2H}$. If $\varepsilon_2 < \varepsilon_m$, the tensile tearing may start when $\frac{W}{H} > \frac{\ell_1}{2H}$.

(a) Plastic failure due to tensile tearing occurs when $0 < \frac{W_m}{H} \leqslant 1$.

In this case we can obtain the threshold external dynamic energy λ_t from equation (5-9) after substituting equations (5-14) into (5-9) and replacing ε in equation (5-9) with limit strain ε_m of beam material.

(b) Plastic failure occurs when $1 < \frac{W_m}{H} \leqslant \frac{\ell_1}{2H}$.

Equation (5-11b) can be written as

$$[H/\ell_1 + \sqrt{1+H^2/\ell_1^2}]e^{2(\varepsilon_m-\varepsilon_1)} = \frac{W}{\ell_1} + \sqrt{1 + W^2/\ell_1^2}$$

or
$$(B - \frac{W}{\ell_1})^2 = 1 + W^2/\ell_1^2, \qquad (5\text{-}15a)$$

where $B = [H/\ell_1 + \sqrt{1+H^2/\ell_1^2}]e^{2(\varepsilon_m-\varepsilon_1)}$ (5-15b)

and ε_1 is defined by equation (5-10).

Equations (5-15) give

$$\frac{W}{H} = \frac{1}{2}\frac{\ell_1}{H}(B - \frac{1}{B}). \qquad (5\text{-}16)$$

Substituting equations (5-14) into equation (5-16), we obtain

$$\frac{1}{2}[\sqrt{1+\lambda_t A} - 1] = \frac{1}{2}\frac{\ell_1}{H}\left(B - \frac{1}{B}\right)$$

or
$$\lambda_t = \frac{1}{A}\frac{\ell_1}{H}\left(B - \frac{1}{B}\right)\left[\frac{\ell_1}{H}\left(B - \frac{1}{B}\right) + 2\right], \qquad (5\text{-}17)$$

where A and B are defined in equation (5-14b) and (5-15b), respectively.

(c) Plastic failure occurs when $\frac{W_m}{H} > \frac{\ell_1}{2H}$

Equation (5-13) gives

$$\frac{W}{H} = \frac{\ell_1}{H}\sqrt{(\varepsilon_m + \frac{\sqrt{5}}{2} - \varepsilon_2)^2 - 1}\ , \qquad (5\text{-}18)$$

where ε_2 is defined in equation (5-12).

Substituting equations (5-14) into equation (5-18), we obtain

$$\lambda_t = \frac{C}{A}[C+2], \qquad (5\text{-}19a)$$

where
$$C = \frac{2\ell_1}{H}\sqrt{(\varepsilon_m + \frac{\sqrt{5}}{2} - \varepsilon_2)^2 - 1}. \qquad (5\text{-}19b)$$

5.3 Plastic Failure of Beams Due to Shear Sliding

It is shown in reference [29] that the shear failure may precede the tensile tearing failure, when the limit strain ε_m of the beam material is large enough, or provided the ratio $2\ell/H$ is sufficiently small. This phenomenon may occur in the present problem discussed herein.

The shear effect on a clamped beam struck by a mass at any point of its span has been discussed in Chapter 3. For most

cases, the value of shear sliding can be directly obtained from the theoretical analysis in Chapter 3. However, for a few cases a numerical method has to be employed in order to obtain the magnitude of shear sliding. Fortunately, this occurs only when the mass ratio is very large ($g = \frac{\bar{m}\ell_1}{G} > 3$) and when the impact point is close to the support ($\frac{\ell_1}{H} < 3$). These cases are neglected in the following analysis on the shear failure of beams.

Like other authors [15,28,37,45, etc.], we assume that shear failure occurs when the shear sliding $W_s = kH$, where $0 < k \leqslant 1$. Therefore, the threshold external dynamic energy λ_s for onset of shear failure corresponds to $W_s = kH$.

(a) $\nu_2 \geqslant \nu_1 \geqslant 3$

The shear sliding given by equation (3-11d) is

$$\frac{W_s}{H} = \frac{3g\lambda}{\nu_1(\nu_1+3g)} \tag{5-20}$$

since

$$u = 4\lambda \frac{H}{\ell_1} \tag{5-21}$$

Therefore, the threshold external dynamic energy for onset of shear failure is

$$\lambda_s = \frac{k\nu_1(\nu_1+3g)}{3g}. \tag{5-22}$$

(b) $1 < \nu_1 \leqslant \frac{3}{2}$ and $\nu_2 \geqslant 3$

For $r^2 < \frac{1}{2}(\nu_1-1)$, equation (3-51) with equations (3-39k), (3-44b) and (3-44h,i) give

$$\frac{W_s}{H} = 4\lambda A_1, \tag{5-23}$$

where $A_1 = F(t_{s2}) - F(t_{s1}) + \frac{3g(2\nu_1+3g)}{4\nu_1(\nu_1+3g)^2} - \frac{6}{g}(\nu_1-1)t_{s2}^2$, (5-24)

$$t_{s2} = \frac{1}{2}[\frac{3}{2}\sqrt{2(\nu_1-1)} + \frac{3(\nu_1-1)}{g} + \nu_1]^{-1}, \tag{5-25a}$$

$$t_{s1} = \frac{3g}{4\nu_1(\nu_1+3g)} \tag{5-25b}$$

$$F(t) = 2t + \frac{3}{2}gt^2 - 2\nu_1 t^2 - \frac{2at+b}{4a}\sqrt{at^2+bt} + f(t) \tag{5-26a}$$

$$f(t) = \begin{cases} \frac{b^2}{8a\sqrt{a}} \ln(2at + b + 2\sqrt{a}\sqrt{at^2+bt}) & \text{for } a > 0 \\ \frac{b^2}{8a\sqrt{-a}} \arcsin(\frac{-2at-b}{b}) & \text{for } a < 0 \end{cases} \tag{5-26b}$$

$$a = 9g^2 - 24g\nu_1 \text{ and } b = 12g. \tag{5-26c,d}$$

The threshold external dynamic energy is

$$\lambda_s = \frac{k}{4A_1} \tag{5-27}$$

where A_1 is defined in equation (5-24).

For $r^2 \geq \frac{1}{2}(\nu_1-1)$, equation (3-51) with equations (3-39k), (3-44h,i) and (3-46d,e) give

$$\frac{W_s}{H} = 4\lambda B_1, \tag{5-28}$$

where $B_1 = F(t_2) - F(t_{s1}) + \frac{3g(2\nu_1+3g)}{4\nu_1(\nu_1+3g)^2} - \frac{6}{g}(\nu_1-1)t_{s2}^2 +$

$$+ 2r(t_{s2}-t_2)[1 - (r+\nu_1)(t_{s2}+t_2)]/(\frac{1}{3}g+r), \tag{5-29}$$

$$t_{s2} = \frac{1}{2} rg[(\nu_1-1)(g+3r) + gr^2(1+r_2)]^{-1}, \qquad (5\text{-}30)$$

$$t_2 = g(6gr + 12r^2 + 2\nu_1 g)^{-1}, \qquad (5\text{-}31)$$

F(t) and t_{s1} are defined in equations (5-26) and (5-25b), respectively. Therefore,

$$\lambda_s = \frac{k}{4B_1}. \qquad (5\text{-}32)$$

where B_1 is defined by equation (5-29).

(c) $\frac{3}{2} < \nu_1 < 3$ and $\nu_2 > 3$

Equation (3-50) with equations (3-39h,i) and (3-40) gives

$$\frac{W_s}{H} = 4\lambda C_1, \qquad (5\text{-}33)$$

where

$$C_1 = \frac{1}{(3+g)} [27g(12\nu_1^2+4\nu_1^2 g+18g+18\nu_1 g)^{-1}+g^2(4\nu_1 g-6+6\nu_1)^{-1}]. \qquad (5\text{-}34)$$

So that,

$$\lambda_s = \frac{k}{4C_1}. \qquad (5\text{-}35)$$

(d) $0 < \nu_1 \leq 1$ and $\nu_2 > 3$

Equation (3-59) with equations (3-53), (3-44) and (3-58) gives

$$\frac{W_s}{H} = 4\lambda D_1, \qquad (5\text{-}36)$$

where $D_1 = F(t_2) - F(t_{s1}) + \frac{3g(2\nu_1+3g)}{4\nu_1(\nu_1+3g)^2} + \frac{6u(g+3r)r^3}{(r+\nu_1)(\nu_1 g+6r^2+3gr)^2}$ (5-37)

and $F(t)$, t_{s1} and t_2 are defined by equations (5-26), (5-25b) and (5-31), respectively.

The threshold dynamic energy is

$$\lambda_s = \frac{k}{4D_1} \tag{5-38}$$

where D_1 is defined by equation (5-37).

(e) $\underline{1 < \nu_1 \leqslant \nu_2 \leqslant 3}$

For $\nu_1 \geqslant 1 + r$, equation (3-65) with equations (3-62a,c) and (3-63) gives

$$\lambda_s = \frac{k}{4E_1}, \tag{5-39}$$

where $E_1 = \frac{g}{3+g}\left[\frac{3}{2}\frac{1}{r(\nu_1-r)(3+g)+g(1+\nu_1)} + \frac{g}{(4\nu_1 g-6+6\nu_1)}\right]$. (5-40)

For $\nu_1 < 1 + r$, equation (3-66) with equations (3-62b,d) and (3-64) gives

$$\lambda_s = \frac{k}{4E_2}, \tag{5-41}$$

where $E_2 = \frac{g}{3r+g}\left[\frac{3}{2}\frac{r^2}{(\nu_1-1)(3r+g)+gr(r+\nu_1)} + \frac{g}{6r(\nu_1-r)+4\nu_1 g}\right]$. (5-42)

(f) $\underline{0 < \nu_1 \leqslant 1 \text{ and } 1 < \nu_2 \leqslant 3}$

Equation (3-70) with equations (3-68f) and (3-69d) gives

$$\lambda_s = \frac{k}{4F_1}, \tag{5-43}$$

where $$F_1 = \frac{3r(\nu_1-r)+g(r+\nu_1)}{(r+\nu_1)[6(\nu_1-r)r+4\nu_1 g]}. \tag{5-44}$$

(g) $0 < \nu_1 \leqslant \nu_2 \leqslant 1$

Equation (3-71d) gives

$$\lambda_s = k\nu_1 \tag{5-45}$$

5.4 Discussion

The tensile tearing failure and shear failure of clamped beams struck by a mass at any point of the span are discussed in this Chapter.

Nonaka's assumption about the plastic regions in the beam has been employed in the present problem. Of course, when the impact point is very close to the right-hand support, the plastic region at the right-hand support may differ from Nonaka'a assumption due to the proximity of the support. However, the experimental results reported in the next Chapter show that triangular plastic regions did develop at the supports and at the impact point provided $\ell_1 \geqslant 0.5$ in. Furthermore, when the impact point is very close to the support the beam may fail in another mode of failure rather than in tensile tearing failure.

With the increase of the limit strain ϵ_m of beam material or with the decrease of ℓ_1, the shear failure may replace the

tensile tearing failure. The shear failure occurs when the shear sliding in the beam $W_s \geq kH$. Unfortunately, k is an unknown coefficient and must be obtained empirically. However, Jones [29] did obtain a reasonable prediction on shear failure with k=1 compared to Menkes and Opat's experimental tests [44].

Instead of pure shear failure and pure tensile tearing failure, the beam may fail due to the combined influence of tensile and shear effects. Further theoretical work is required in order to predict the mixed failure due to a combination of tearing and shearing.

CHAPTER 6

EXPERIMENTAL RESULTS

The range and some experimental results of the dynamic tests on clamped beams struck by a falling tup at different points of the span are listed in Tables 2-5. The experimental data on flat end beams of steel and aluminium alloy are presented in Tables 2 and 3, respectively, while the data on large end specimens of steel and aluminium alloy are given in Tables 4 and 5, respectively. W_f is the maximum permanent deformation of a beam and was measured after test using a travelling microscope. ℓ_1 is the location of the impact point from the right-hand support and V_0 is the initial impact velocity measured using a laser doppler velocimeter.

During the tests, the tup was carefully lowered to near contact with the beam and the beam which was held in the beam holder was set at its test position by reference to the tup head. The tup was then lifted to the drop height H′ after setting up the laser doppler velocimeter, DL1080 transient recorders and other data recording instruments. After another check of the instruments, the tup was released and dropped vertically along the rig guide rails and struck the beam specimen with an initial impact velocity V_0.

It was found that the actual impact point may slightly deviate from the desired point. The values of ℓ_1, which were measured from the beam specimens after the test, are listed in

Speci. No.	Impact Velocity V_0 (m/s)	Impact point ℓ_1 (mm) before test	Impact point ℓ_1 (mm) after test	λ	$\frac{W_f}{H}$	Comment
STI1	5.3366	50.8	50.2	18.88	3.622	
STI2	6.2868	50.8	50.6	26.4	4.14	
STI3	7.211	50.8	50.3	34.53	4.7	
STI4	7.9529	50.8	50.28	41.99	5.19	
STI5	8.6005	50.8	49.76	48.6	5.66	
STI6	5.3366	38.1	34.5	12.97	3.33	
STI7	6.2868	38.1	37	19.31	4.14	
STI8	7.211	38.1	41.1	28.22	4.7	
STI9	7.9529	38.1	36.6	30.56	4.98	
STI10	8.6916	38.1	38.2	38.1	5.56	
STI11	3.3289	50.8	50.6	7.4	2.24	
STI12	3.3289	38.1	39	5.71	2.15	
STI13	3.3289	25.4	25.8	3.77	1.88	
STI14	5.3366	25.4	24.26	9.12	2.99	
STI15	6.2868	25.4	25.6	13.36	3.59	
STI16	7.0287	25.4	25.5	16.63		broken at the impact point due to shear
STI17	3.3029	12.7	13.7	1.97	1.27	
STI18	5.3366	12.7	13.2	4.96	2.236	
STI19	4.4385	12.7	13.2	3.43	1.8	
STI20	3.3029	6.35	7.22	1.04	0.853	
STI21	5.1772	6.35	7.87	2.79	1.706	
STI22	4.624	6.35	8.2	2.31	1.426	
STI23	9.43	50.8	50.8	59.64		broken at the impact point due to shear
STI24						static test
STI25	7.3932	50.8	50.2	36.22	4.73	test with strain gauges

Table 2-1. Experimental Details of Flat End Steel Beam with Thickness H = 0.15 in (3.81 mm).

Speci. No.	Impact Velocity V_0 (m/s)	Impact point ℓ_1 (mm) before test	Impact point ℓ_1 (mm) after test	λ	$\frac{W_f}{H}$	Comment
STII1	5.3366	50.8	49.73	7.89	2.26	
STII2	7.211	50.8	51.2	14.83	2.97	
STII3	8.6916	50.8	48.6	20.45	3.6	
STII4	9.248	50.8	47.6	22.68	3.853	
STII5	9.9867	50.8	50.51	28.06	4.22	cracked at the impact point due to shear
STII6	5.3366	38.1	37.86	6.01	2.1083	
STII7	7.211	38.1	36.14	10.47	2.88	
STII8	7.9529	38.1	35.63	12.55	3.23	
STII9	9.248	38.1	37.21	17.73	3.75	
STII10	10.543	38.1	37.1	22.97		broken at the impact point due to shear
STII11	3.3289	50.8	50.45	3.11	1.4026	
STII12	3.3289	38.1	41.7	2.57	1.327	
STII13	3.3289	25.4	25.64	1.58	1.1067	
STII14	5.3366	25.4	24.29	3.85	1.8049	
STII15	6.2868	25.4	23.32	5.13	2.1346	
STII16	7.0287	25.4	28.68	7.89	2.69	
STII17	3.3289	12.7	12.56	0.775	0.687	
STII18	5.1772	12.7	13.1	1.96	1.27	
STII19	7.9529	12.7		4.47		broken at the impact point due to shear
STII20	6.2868	12.7	12.245	2.7	1.67	
STII21	3.3289	6.35	5.704	0.35	0.3374	
STII22	5.1772	6.35	8.112	1.21	0.93	
STII23	6.2868	6.35	7.86	1.73	1.194	
STII24	7.9529	12.7	14.307	5.04	2.366	the motion was recorded in film no. 7
STII25	7.3932	50.8	45.9	13.97	2.795	test with strain gauges

Table 2-2. Experimental Details of Flat End Steel Beam with Thickness H = 0.2 in (5.08 mm).

Speci. No.	Impact Velocity V_0 (m/s)	Impact point ℓ_1 (mm) before test	Impact point ℓ_1 (mm) after test	λ	$\frac{W_f}{H}$	Comment
STIII1	3.3289	50.8	50.6	1.754	0.9072	
STIII2	5.1772	50.8	50.9	4.346	1.5893	
STIII3	7.0287	50.8	49.6	7.796	2.155	
STIII4	9.8012	50.8	45.8	14.017	2.982	
STIII5	10.911	50.8		19.248		broken at the impact point due to shear
STIII6	3.3289	38.1	40.6	1.431	0.8805	
STIII7	5.1772	38.1	34.8	2.965	1.4855	
STIII8	7.0287	38.1	35.5	5.589	2.0209	
STIII9	9.8012	38.1	41.4	12.652	2.9241	
STIII10	3.3289	25.4	26.3	0.929	0.7157	
STIII11	6.2868	25.4	26.1	3.283	1.578	
STIII12	9.248	25.4	29	7.881	2.397	
STIII13	3.3289	12.7	13.6	0.478	0.43	
STIII14	6.2869	12.7	14	1.764	1.135	
STIII15	9.248	12.7	12.2	3.316	1.56	
STIII16	3.3289	6.35	5.3	0.187	0.211	
STIII17	6.2868	6.35	6.3	0.793	0.68	cracked at the impact point due to shear
STIII18	5.3366	6.35	5.5	0.495	0.5139	
STIII19						static test
STIII20	11.467	50.8	45.5	19.041	3.283	film No.2. sliding occurred between the beam and the holder
STIII21	11.467	50.8		21.259		broken at the impact point due to shear. film No.4
STIII22	10.728	25.4	26.4	9.67		broken at the impact point due to shear
STIII23	8.877	12.7	13	3.265	1.687	
STIII24	7.3932	25.4	29.4	5.118	1.9307	with strain gauges
STIII25	7.3932	12.7	19.4	3.375	1.4976	with strain gauges

Table 2-3. Experimental Details of Flat End Steel Beam with Thickness H = 0.25 in (6.35 mm).

Speci. No.	Impact Velocity V_0 (m/s)	Impact point ℓ_1 (mm) before test	Impact point ℓ_1 (mm) after test	λ	$\frac{W_f}{H}$	Comment
STIV1	3.3289	50.8	48.1	0.982	0.5752	
STIV2	5.1772	50.8	50.5	2.492	1.145	
STIV3	7.0287	50.8	49.7	4.526	1.5923	
STIV4	9.8012	50.8	49.3	8.72	2.3049	
STIV5	10.911	50.8	51.1	11.196	2.5226	
STIV6	3.3289	38.1	41.2	0.84	0.5563	
STIV7	5.1772	38.1	38.2	1.888	1.057	
STIV8	7.0287	38.1	39.3	3.576	1.5205	
STIV9	9.8012	38.1	34.9	6.175	2.1136	
STIV10	10.911	38.1	38.4	8.42	2.4167	
STIV11	3.3289	25.4	26.7	0.545	0.4101	
STIV12	6.2868	25.4	27.3	1.987	1.1327	
STIV13	10.3576	25.4	29.1	5.75	2.07	
STIV14	3.3289	12.7	15.3	0.314	0.2807	
STIV15	6.2868	12.7	19	1.383	0.949	
STIV16	9.248	12.7	13.3	2.095	1.3777	
STIV17	3.3289	6.35	8.4	0.171	0.1656	
STIV18	6.2868	6.35	7.4	0.539	0.5189	
STIV19	7.9529	6.35	9.5	1.107	0.832	
STIV20	9.248	6.35		1.003		broken at the impact point due to shear
STIV21	11.653	50.8	49.3	12.33	2.6567	
STIV22	11.2818	25.4	25.4	5.954		broken at the impact point due to shear
STIV23						static test
STIV24	10.7286	12.7	16.6	3.191	1.6403	
STIV25	7.3932	50.8	45.4	4.571	1.5551	with strain gauges

Table 2-4. Experimental Details of FLat End Steel Beam with Thickness H = 0.3 in (7.62mm).

Speci. No.	Impact Velocity V_0 (m/s)	Impact point ℓ_1 (mm) before test	Impact point ℓ_1 (mm) after test	λ	$\frac{W_f}{H}$	Comment
ALI1	5.3366	50.8	50.7	18.134	4.28556	
ALI2	5.3366	38.1		13.616		broken at the support due to tensile tearing
ALI3	4.624	50.8	49.3	13.228		broken at the impact point due to tensile tearing
ALI4	4.4385	50.8	49.6	12.262	3.10617	
ALI5	4.8095	50.8	49.8	14.456		broken at the impact point due to tensile tearing
ALI6	3.8853	50.8	50.7	9.604	2.8976	
ALI7	3.329	38.1	41.4	5.758	2.7575	
ALI8	3.8853	38.1	39.4	7.464	2.7627	cracked at the impact point due to tensile tearing
ALI9	4.3458	38.1	37.1	8.793		broken at the impact point due to tensile tearing
ALI10	2.668	50.8	44.6	3.984	2.068	
ALI11	1.7767	50.8	50.1	1.985	1.1976	
ALI12	1.7767	38.1	40.5	1.604	1.1446	
ALI13	1.8418	6.35	7.2	0.307	0.2318	
ALI14	2.668	6.35	7.7	0.688	0.6417	cracked at the support due to tensile tearing
ALI15	4.4385	25.4	24.9	6.156		broken at the impact point due to tensile tearing
ALI16	5.7336	50.8		20.957		broken at the support due to tensile tearing. with one strain gauge
ALI17	1.7767	25.4	24.5	0.971	0.846	
ALI18	2.668	25.4	25.6	2.287	1.5816	
ALI19	3.81	25.4	24.8	4.518	2.5856	
ALI20	1.7767	12.7	13.3	0.527	0.7039	
ALI21	2.668	12.7	13.8	1.233	0.995	cracked at the support due to tensile tearing
ALI22	3.81	12.7	12.7	2.315		broken at the support due to tensile tearing
ALI23	3.3029	12.7	12.6	1.725		broken at the impact point due to tensile tearing
ALI24						static test
ALI25	5.7336	50.8	46.9	19.348	4.3963	with strain gauges

Table 3-1. Experimental Details of FLat End Aluminium Beam with Thickness H = 0.15 in (3.81mm).

Speci. No.	Impact Velocity V_0 (m/s)	Impact point ℓ_1 (mm) before test	Impact point ℓ_1 (mm) after test	λ	$\frac{W_f}{H}$	Comment
ALII1	5.3366	50.8	49.7	7.4935	2.714	
ALII2	6.2868	50.8		10.63		broken at the impact point due to tensile tearing
ALII3	4.624	50.8	51.2	5.796	2.2813	
ALII4	5.7336	50.8	50.8	8.841		broken at the impact point due to tensile tearing
ALII5	5.548	50.8	48.8	7.952		broken at the impact point and at the support due to tensile tearing
ALII6	3.7	50.8	51.4	3.725	1.7006	
ALII7	3.1434	38.1	40.2	2.103	1.4154	
ALII8	4.253	38.1	41.9	4.012	2.1283	
ALII9	4.8095	38.1	41.4	5.07	2.353	
ALII10	5.3366	38.1	40.2	6.061	2.4543	
ALII11	1.7767	50.8	50.5	0.844	0.5287	
ALII12	1.7767	38.1	39.3	0.657	0.6291	
ALII13	1.7767	25.4	25	0.418	0.3957	
ALII14	2.668	25.4	25.4	0.957	0.8069	
ALII15	3.81	25.4	28.2	2.167	1.7504	
ALII16	4.702	25.4	27.4	3.207		broken at the impact point due to tensile tearing
ALII17	1.7767	12.7	13.6	0.227	0.2659	
ALII18	2.668	12.7	14.1	0.531	0.573	
ALII19	3.3029	12.7	14.6	0.843	0.7112	cracked at the support due to tensile tearing
ALII20	1.893	6.35	5.5	0.104	0.1307	
ALII21	2.729	6.35	5.8	0.229	0.2364	
ALII22	3.4138	6.35	8.3	0.514	0.5244	
ALII23	3.7	12.7	16.8	1.218	1.2835	cracked at the impact point due to tensile tearing
ALII24	11.2818	50.8		34.231		broken at the impact point
ALII25	11.653	50.8		36.521		broken at the impact point

Table 3-2. Experimental Details of Flat End Aluminium Beam with Thickness H = 0.2 in (5.08mm).

Speci. No.	Impact Velocity V_0 (m/s)	Impact point ℓ_1 (mm) before test	Impact point ℓ_1 (mm) after test	λ	$\frac{W_f}{H}$	Comment
ALIII1	5.3366	50.8	49.9	3.821	1.7024	
ALIII2	6.2868	50.8	52.2	5.592	2.0315	
ALIII3	7.0287	50.8	49.3	6.602		broken at the impact point due to tensile tearing
ALIII4	1.7767	50.8	50.9	0.436	0.3731	
ALIII5	3.81	50.8	50.9	2.003	1.2	
ALIII6	1.7767	38.1	39.9	0.341	0.4384	
ALIII7	3.81	38.1	40.9	1.609	1.3406	
ALIII8	5.1772	38.1	41.7	3.03	1.871	
ALIII9	6.355	38.1	39	4.27	1.9676	
ALIII10	1.7767	25.4	27.3	0.234	0.2931	
ALIII11	3.82	25.4	28.3	1.119	0.9783	
ALIII12	5.3366	25.4	27.2	2.1	1.5831	
ALIII13	6.355	25.4	24	2.627		broken at the impact point due to tensile tearing
ALIII14	1.8483	12.7	16	0.148	0.1471	
ALIII15	3.8853	12.7	15.5	0.634	0.649	
ALIII16	5.1772	12.7	13.9	1.01	1.019	cracked at the support due to tensile tearing
ALIII17	4.7167	12.7	13.3	0.802	0.8183	
ALIII18	1.8483	6.35	9.5	0.088	0.1096	
ALIII19	3.3289	6.35	7	0.21	0.2813	
ALIII20	4.7167	6.35	7.8	0.47	0.606	
ALIII21						static test
ALIII22	7.0287	50.8		6.8027		broken at the impact point due to tensile tearing. film No.6
ALIII23	5.3366	12.7	12.7	0.98	1.1276	film No.10
ALIII24	5.734	12.7	16.1	1.435	1.3874	
ALIII25	6.1046	12.7	14.7	1.485		broken at the impact point due to tensile tearing

Table3-3. Experimental Details of Flat End Aluminium Beam with Thickness H = 0.25 in (6.35mm).

Speci. No.	Impact Velocity V_0 (m/s)	Impact point ℓ_1 (mm) before test	Impact point ℓ_1 (mm) after test	λ	$\frac{W_f}{H}$	Comment
ALIV1	5.3366	50.8	49.1	1.887	1.1291	
ALIV2	6.2868	50.8	48.8	2.603	1.5421	cracked at the impact point due to tensile tearing
ALIV3	1.7767	50.8	51.3	0.219	0.1692	
ALIV4	3.81	50.8	50.8	0.995	0.7265	
ALIV5	1.7767	38.1	41.1	0.175	0.1625	
ALIV6	3.81	38.1	39.6	0.776	0.6627	
ALIV7	5.3366	38.1	38.4	1.476	1.1184	cracked at the impact point due to tensile tearing
ALIV8	6.355	38.1	37.5	2.044		broken at the impact point due to tensile tearing
ALIV9	1.7767	25.4	29.8	0.127	0.1328	
ALIV10	3.81	25.4	26.7	0.523	0.572	
ALIV11	5.3366	25.4	25.9	0.996	0.8938	cracked at the impact point due to tensile tearing
ALIV12	1.7767	12.7	17.3	0.074	0.0611	
ALIV13	3.3029	12.7	16.1	0.237	0.243	
ALIV14	4.253	12.7	15.1	0.369	0.4222	
ALIV15	5.3366	12.7	13.7	0.527	0.6147	cracked at the support due to tensile tearing
ALIV16	1.7767	6.35	9.1	0.039	0.0416	
ALIV17	3.3029	6.35	7.2	0.106	0.1719	
ALIV18	4.253	6.35	6.1	0.149	0.2734	cracked at the support due to tensile tearing
ALIV19	5.3366	6.35	4	0.154		broken at the impact point due to shear
ALIV20						static test
ALIV21	6.658	50.8	50.8	3.04		broken at the impact point due to tensile tearing
ALIV22	5.734	25.4	27.4	1.216		broken at the impact point due to tensile tearing
ALIV23	5.734	12.7		0.564		the tup impacted on bolts of the holder
ALIV24	5.734	25.4	28.9	1.286	1.1745	with two strain gauges
ALIV25	5.734	50.8	49.1	2.1794	1.2703	with strain gauges

Table 3-4. Experimental Details of Flat End Aluminium Beam with Thickness H = 0.3 in (7.62mm).

Speci. No.	Impact Velocity V_0 (m/s)	Impact point ℓ_1 (mm) before test	Impact point ℓ_1 (mm) after test	λ	$\frac{W_f}{H}$	Comment
SI1						static test
SI2	8.6916	50.8	48.2	49.9513	5.7014	cracked at the impact point due to shear
SI3	9.248	50.8	49	57.5281		broken at the impact point due to shear
SI4	3.1434	50.8	49.3	6.6907	2.1517	
SI5	5.7336	50.8	48.3	21.8152	3.7386	
SI6	7.3932	50.8	48.5	36.411	4.4987	
SII1	9.8012	50.8	45.5	25.301	4.1083	film No.1
SII2	10.543	50.8	48.1	30.931		broken at the impact point due to shear. film No.3
SII3	7.0287	12.7	11.4	3.262	1.26	cracked at the support due to tensile tearing. film No.8
SII4	3.1434	50.8	49.7	2.8434	1.39	
SII5	7.3932	50.8	48.2	15.244	3.06	
SII6	7.3932	12.7	19.5	6.1853	1.9329	cracked at the support due to tensile tearing
SII7	7.7674	12.7	12.7	4.4374		broken at the support due to tensile tearing
SII8	3.1434	12.7	19.5	1.1142	0.5785	
SII9	5.7336	12.7	14.4	2.814	1.317	cracked at the support due to tensile tearing
SII10	7.3932	50.8	45.1	14.284	2.6929	with strain gauges
SII11	5.7336	12.7	10.3	1.962		broken at the support due to tensile tearing. with strain gauges
SII12	7.3932	50.8	48.7	15.329	2.748	with one strain gauge
SIII1						static test
SIII2	3.1434	50.8	48.4	1.4192	0.8377	
SIII3	11.096	50.8	45.8	16.736	3.1323	
SIII4	11.467	50.8	50.8	19.787		broken at the impact point due to shear
SIII5	8.877	50.8	49.9	11.665	2.5465	
SIII6	6.6578	50.8	45.7	6.01	1.8567	
SIV1						static test
SIV2	11.467	50.8	49.1	11.0846	2.3933	
SIV3	9.248	50.8	45	6.6018	2.016	
SIV4	3.1434	50.8	49.3	0.8361	0.4156	
SIV5	11.6528	50.8	48.6	11.3295	2.4131	
SIV6	6.6578	50.8	47.3	3.6	1.416	

Table 4. Experimental Details of Large End Steel Beam with Thickness H=0.15 in (3.81mm),0.2 in (5.08mm),0.25 in (6.35mm) and o.3 in (7.62mm).

Speci. No.	Impact Velocity V_0 (m/s)	Impact point ℓ_1 (mm) before test	Impact point ℓ_1 (mm) after test	λ	$\frac{W_f}{H}$	Comment
AI1						static test
AI2	4.4385	50.8	50.2	24.2014	4.4579	cracked at the support due to tensile tearing
AI3	4.995	50.8	50.6	30.988		broken at the support due to tensile tearing
AI4	1.7767	50.8	48.6	3.7505	1.8971	
AI5	3.1434	50.8	49.3	11.8987	3.342	
AI6	3.7	50.8	48.8	16.334	3.777	
AI7	10.7287	50.8	49	142.958		broken at the support due to tensile tearing
AII1	5.3366	50.8	47.9	14.0675	3.3065	cracked at the support due to tensile tearing. film No.5
AII2	5.3366	6.35	6.35	1.863		broken at the support due to tensile tearing. film No.9
AII3	1.7767	50.8	47	1.5333	1.1171	
AII4	5.7336	50.8	48.4	16.3943		broken at the support due to tensile tearing
AII5	4.4385	50.8	50.4	10.2437	2.8189	
AII6	3.7	12.7	11.2	1.5815		broken at the support due to tensile tearing
AII7	3.514	12.7	14.2	1.8086		broken at the support
AII8	3.023	12.7	18.4	1.725	1.2717	cracked at the support
AII9	8.877	12.7	16.2	13.167		broken at the support
AII10	1.7767	12.7	16.7	0.5441	0.6711	
AII11	5.3366	50.8	50.8	14.9223		broken at the support. with strain gauges
AII12	5.3366	50.8	50.8	14.9223		broken at the support. with one strain gauge
AIII1						static test
AIII2	6.2868	50.8	49.9	10.419	2.7097	cracked at the support
AIII3	6.6578	50.8	49.9	11.6755	2.826	cracked at the support
AIII4	7.211	50.8	47.1	12.92		broken at the support
AIII5	1.7767	50.8	49.4	0.824	0.685	
AIII6	5.7336	50.8	47.5	8.2463	2.334	
AIV1						static test
AIV2	7.211	50.8	48.6	7.7152		broken at the support
AIV3	6.6578	50.8	48.7	6.5911	2.0705	cracked at the support
AIV4	1.7767	50.8	48.5	0.4674	0.3948	
AIV5	5.7336	50.8	49.9	5.0131	1.7371	
AIV6	4.4385	50.8	48.8	2.938	1.375	

Table 5. Experimental Details of Large End Aluminium Beam with Thickness H=0.15 in, 0.2 in, 0.25 in and 0.3 in.

Tables 2-5 and are taken as the actual values of ℓ_1 and were used in the calculation of λ and other parameters. It was also found that the tup may slide along the beam during the impact, provided the impact point was close to the support, but this effect had not been measured.

The external kinetic energy which acted on beam specimens depends on the initial drop height H′ or initial impact velocity V_0 (one value of tup mass 5 kg was used in all the tests). The drop height H′ of the tup in the test varied from 0.17 m to 7.2 m and the corresponding initial impact velocity V_0 varied from 1.78 ms^{-1} to 11.65 ms^{-1}, approximately. It was found that the velocities from the laser doppler velocimeter were smaller than the classical values calculated using the initial drop height. This difference is up to 2.7% and is largely attributed to friction between the tup and vertical guides of the drop hammer rig.

At least three unbroken beams after impact with different velocities V_0 were sought for each type of test (one type of test means that the beam specimens are of the same thickness and same boundary condition - flat end or large end which were made from the same material and were impacted at the same point of the span). After several *trial tests*, it was found that the aluminium alloy beams failed more easily than the steel beams. Therefore, the lowest initial impact velocity was chosen as 1.78 ms^{-1} for the aluminium alloy beams and 3.33 ms^{-1} for the steel beams, or the corresponding lowest drop height was 0.17 m and 0.576 m, respectively. Initial impact velocities, or initial

drop heights, for the remaining tests were chosen by reference to permanent deformations of the previously tested beams. The lowest impact velocity was used for the first test of each test type. It was then sought to obtain a cracked beam or a beam which had just broken. These beams were subjected to an initial impact velocity which is slightly higher than the maximum impact velocity which the beam can support without failure. Of course, it is difficult to obtain this velocity, but some broken beams were subjected to an impact velocity which was close to the maximum impact velocity. How close the impact velocity is to the maximum impact velocity can be estimated from the velocity time history curve captured by the laser doppler velocimeter shown for two cases in Figs. 57a and 57b, or in comparison between two parts of the broken beam shown in Figs. 57a and 57b since the rest of kinetic energy of the tup was dissipated by one part of the beam after it broke. The impact velocities for the rest of this type of test were chosen between the lowest velocity and the velocity corresponding to beam failure.

Although the specimen holder was serrated, there were still some sliding between the specimens and the holder when the initial impact velocity was very high. It may be better to prevent sliding by using beam specimens having the support ends made longer to cover the whole width of the holder stocks and holder covers shown in Fig. 2. Nevertheless, it appears that the sliding was small and for most tests no sliding occurred at all.

The motion of ten beams with different end conditions (flat

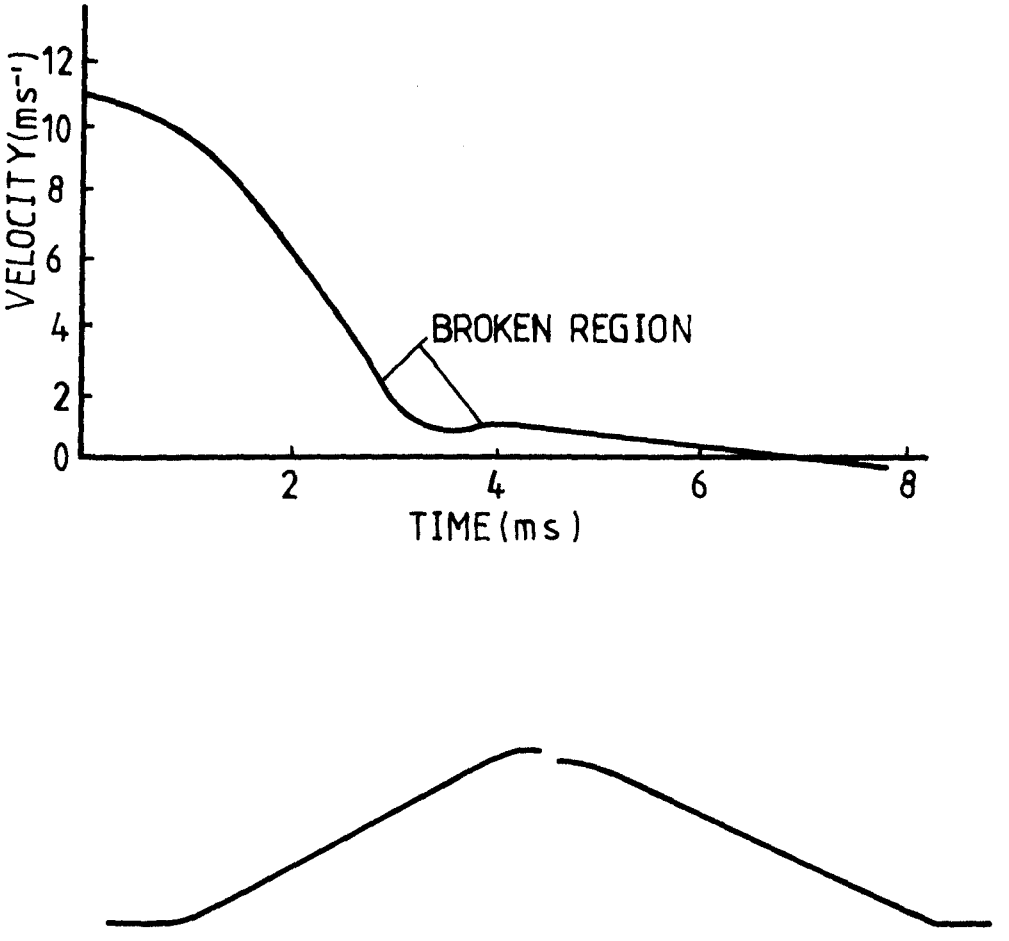

FIG. 57a The impact velocity was close to the maximum impact velocity which the beam can support without failure. The upper figure is the velocity-time history trace and the lower one is the permanent deformation profile of two parts of the broken beam. The beam specimen No. was STIII5.

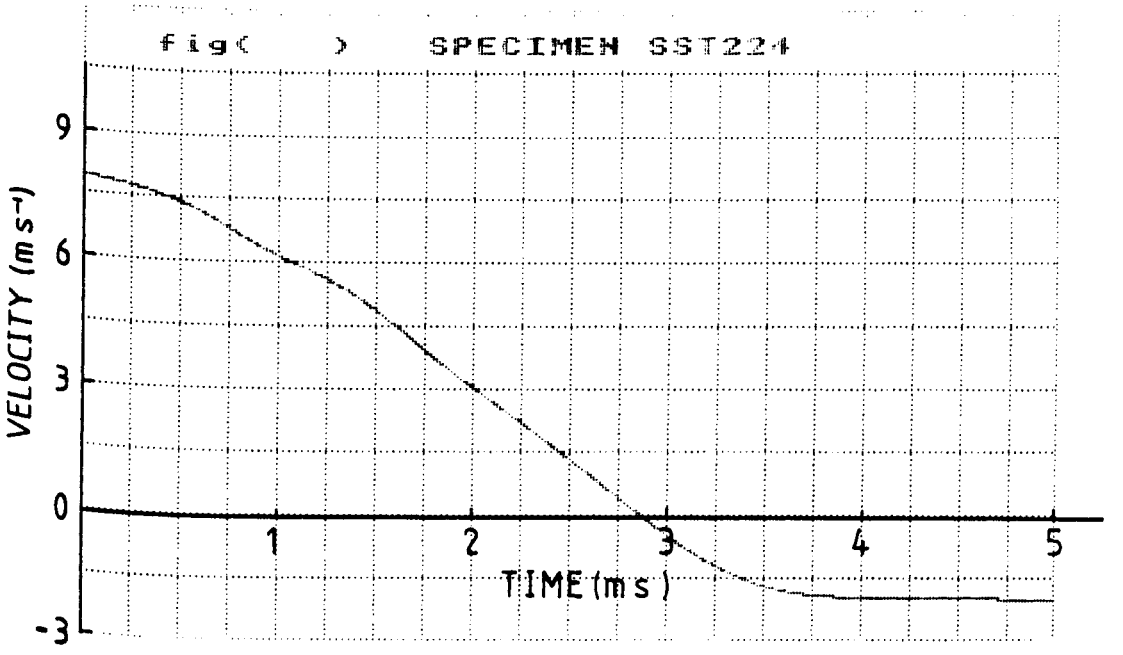

FIG. 65a Velocity-time history trace which was captured by the laser doppler velocimeter and was recorded by DL1080 transient recorder. Specimen No. STII24.

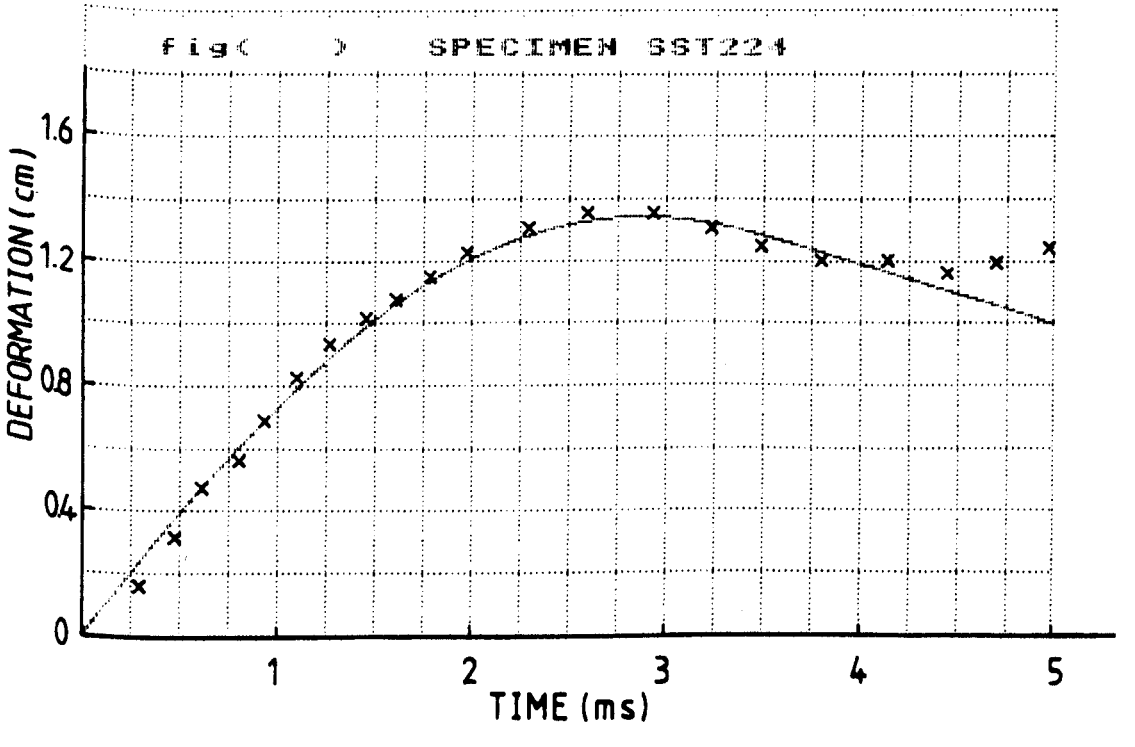

FIG. 65b Deformation-time history trace obtained by integrating the velocity trace in Fig. 65a using a computer program 'try 8'. x; the deformation measured from film. Specimen No. STII24.

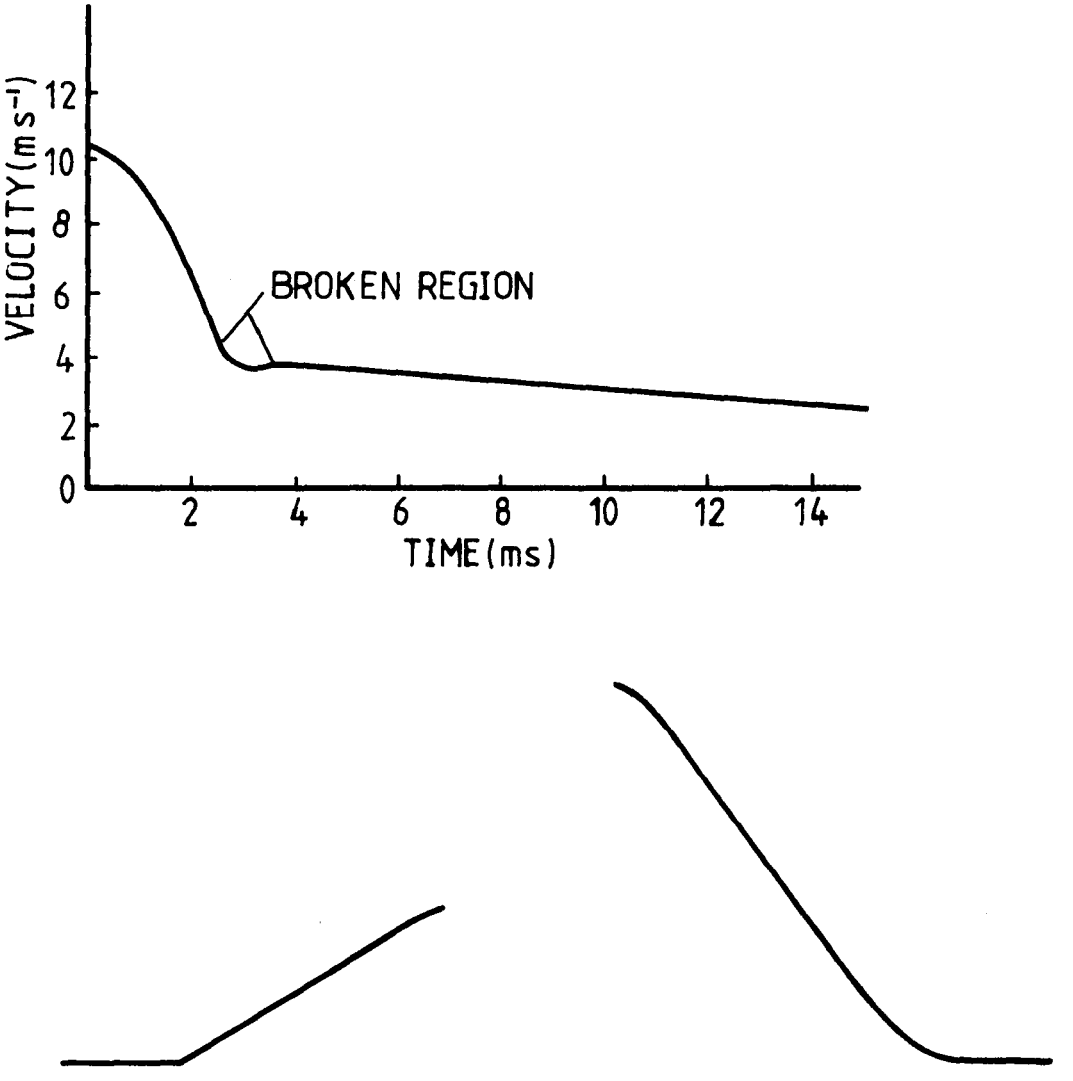

FIG. 57b The impact velocity was higher than the maximum impact velocity which the beam can support without failure. The beam specimen No. was STII 10.

end or large end) and different materials were recorded using the Hadland high speed camera. The impact point was ℓ_1 = 2 in (50.8 mm) and 0.5 in (12.7 mm). It was the purpose to record the transverse displacement-time history of the beam and the bending plastic hinge travelling in the beam. Therefore, quarter and half frame exposures were used with a camera speed of about 7000 frames per second. The films taken with quarter frame exposure gave more detail on the early response of beam but lost the data of the later motion of the beam since some parts of beam picture were superimposed on the following picture when the deformation of the beam was large. However, the films taken with half frame exposure clearly show the motion of the beam during the entire response. The motion of the tup can also be seen in these films. Some sliding between specimens and the holder were also recorded in some of the films. Some displacement profile-time history curves and some displacement-time history curves at the impact which were measured from the films are plotted in Figs. 58-61.

Ten specimens with 5 or 6 strain gauges stuck on each specimen were dynamically tested. The arrangement of strain gauges and tests is shown in Fig. 62. In order to measure the bending moment in the beam, two pairs of strain gauges were stuck on both upper and lower surfaces* of the beam at the support, except when the location of the impact point ℓ_1 is 0.5 in, and at the centre of half span of the beam or at the centre of the beam (defined as middle strain gauges), respectively. For flat end beams, one half length of the strain gauge on upper surface at

---

* The surface which is in contact with the tup is defined as upper surface of the beam and the surface on the other side of the beam is lower surface.

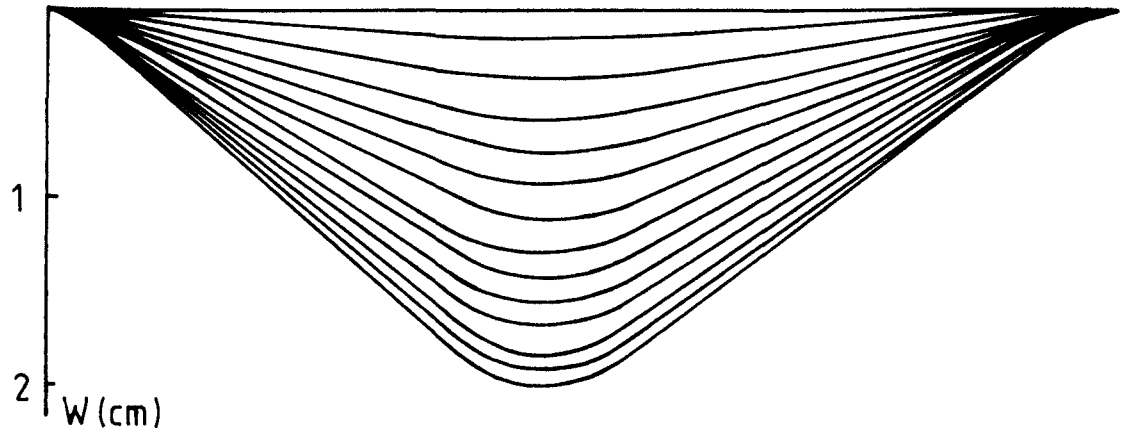

(a)

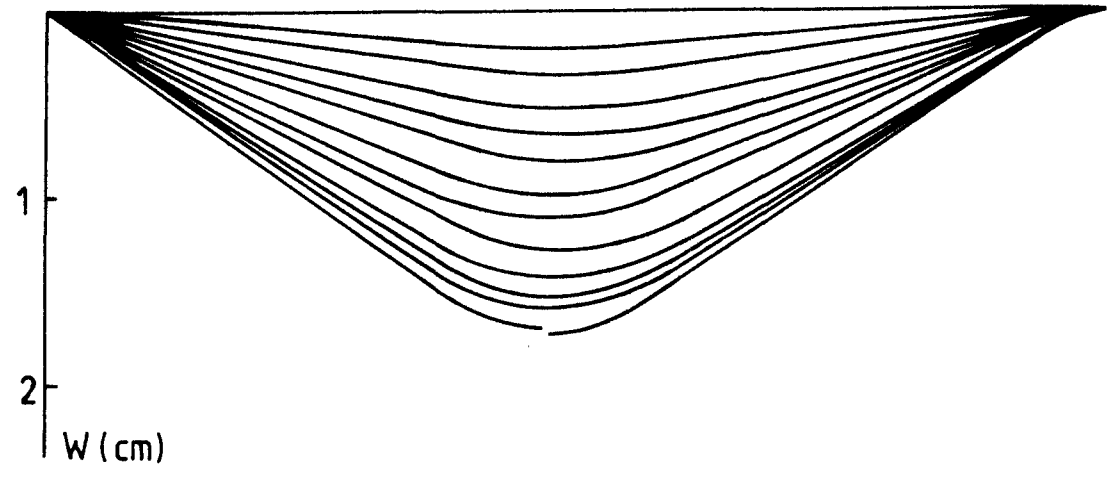

(b)

FIG. 58 Deformation profile-time history curves of beam with the impact point ℓ_1 = 2 in (50.8 mm). (a) large end beam, specimen No. SII2; (b) flat end beam, specimen No. STIII21.

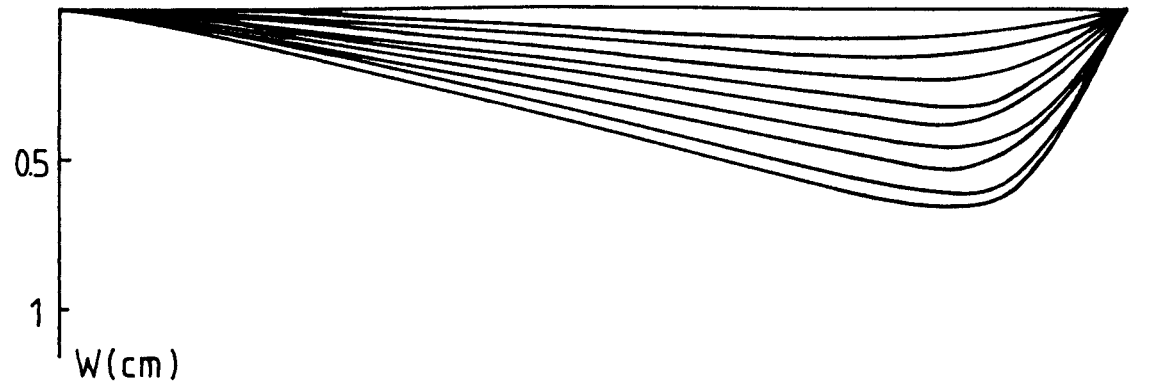

(a)

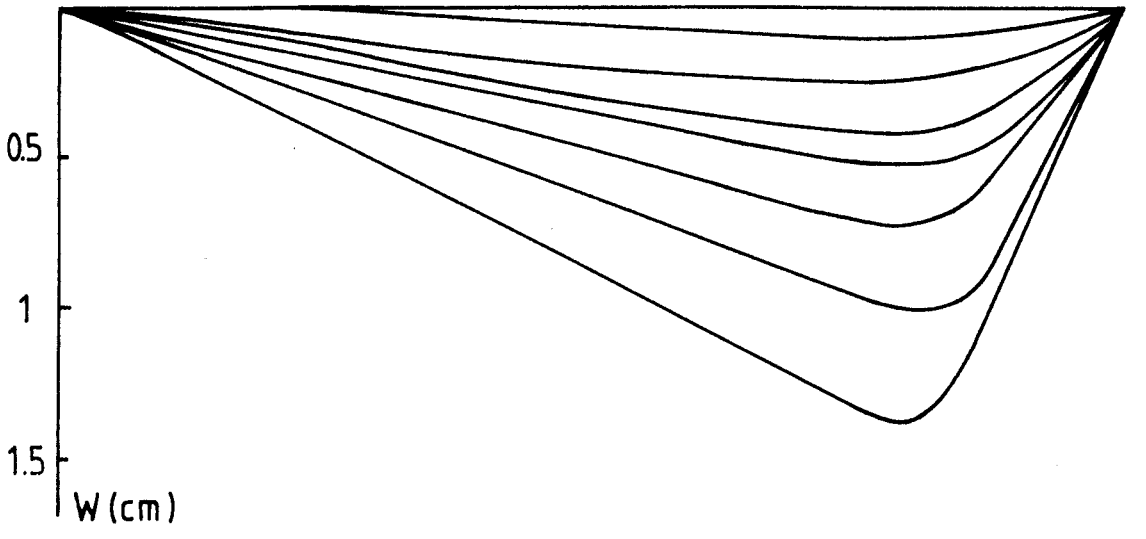

(b)

FIG. 59 Deformation profile-time history curves of beam with the impact point ℓ_1 = 0.5 in (12.7 mm). (a) large end beam, specimen No. SII3; (b) flat end beam, specimen No. STII24.

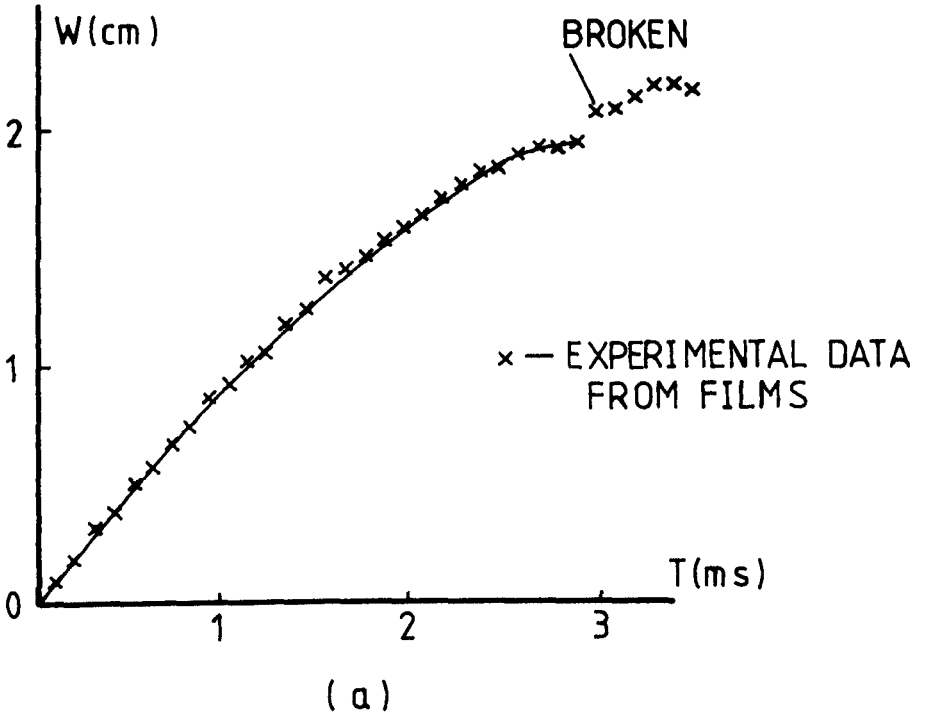

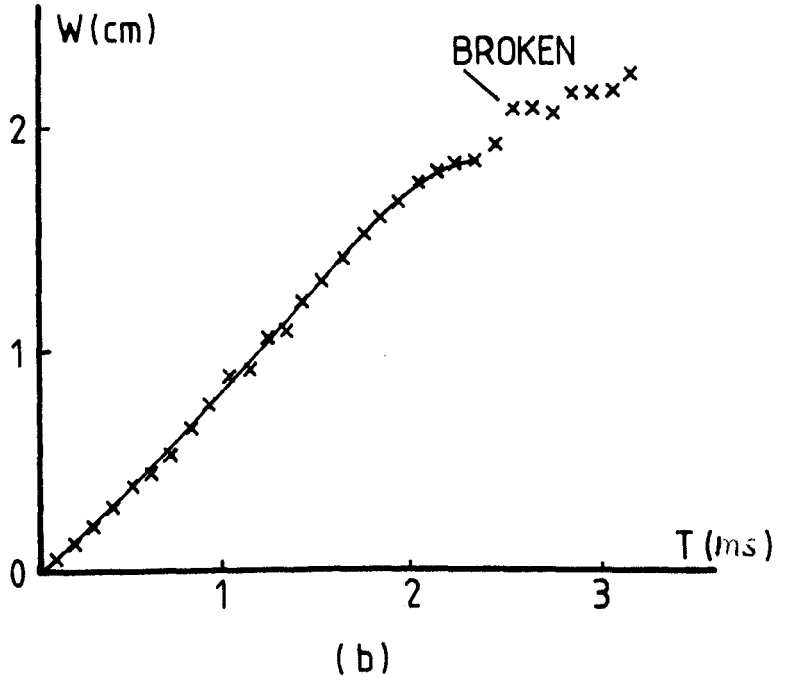

FIG. 60 Maximum deformation-time history traces of beam with the impact point ℓ_1 = 2 in (50.8 mm). (a) large end beam, specimen No. SII2; (b) flat end beam, specimen No. STIII21.

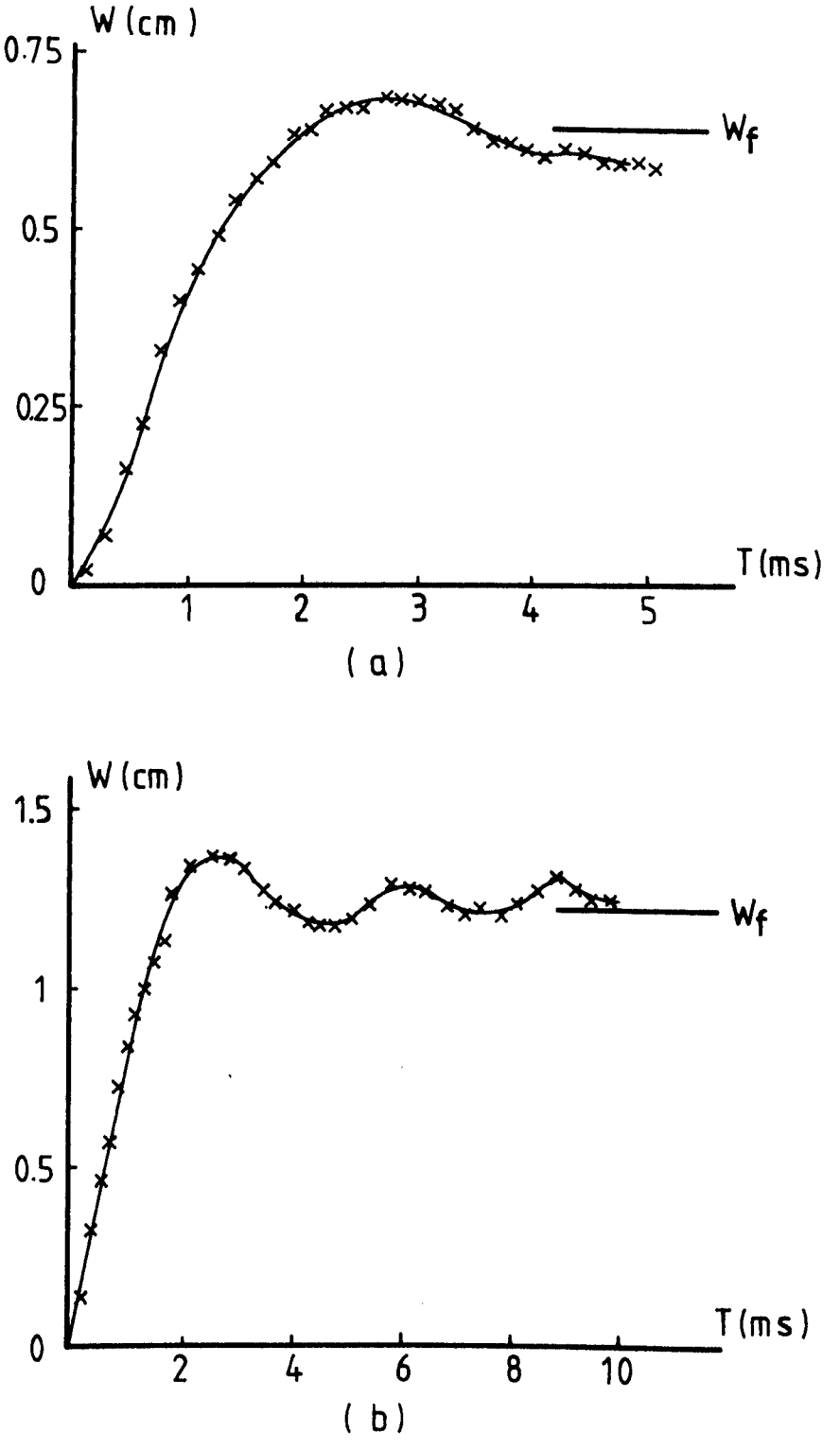

FIG. 61 Maximum deformation-time history traces of beam with the impact point ℓ_1 = 0.5 in (12.7 mm). (a) large end beam, specimen No. SII3; (b) flat end beam, specimen No. STII24.

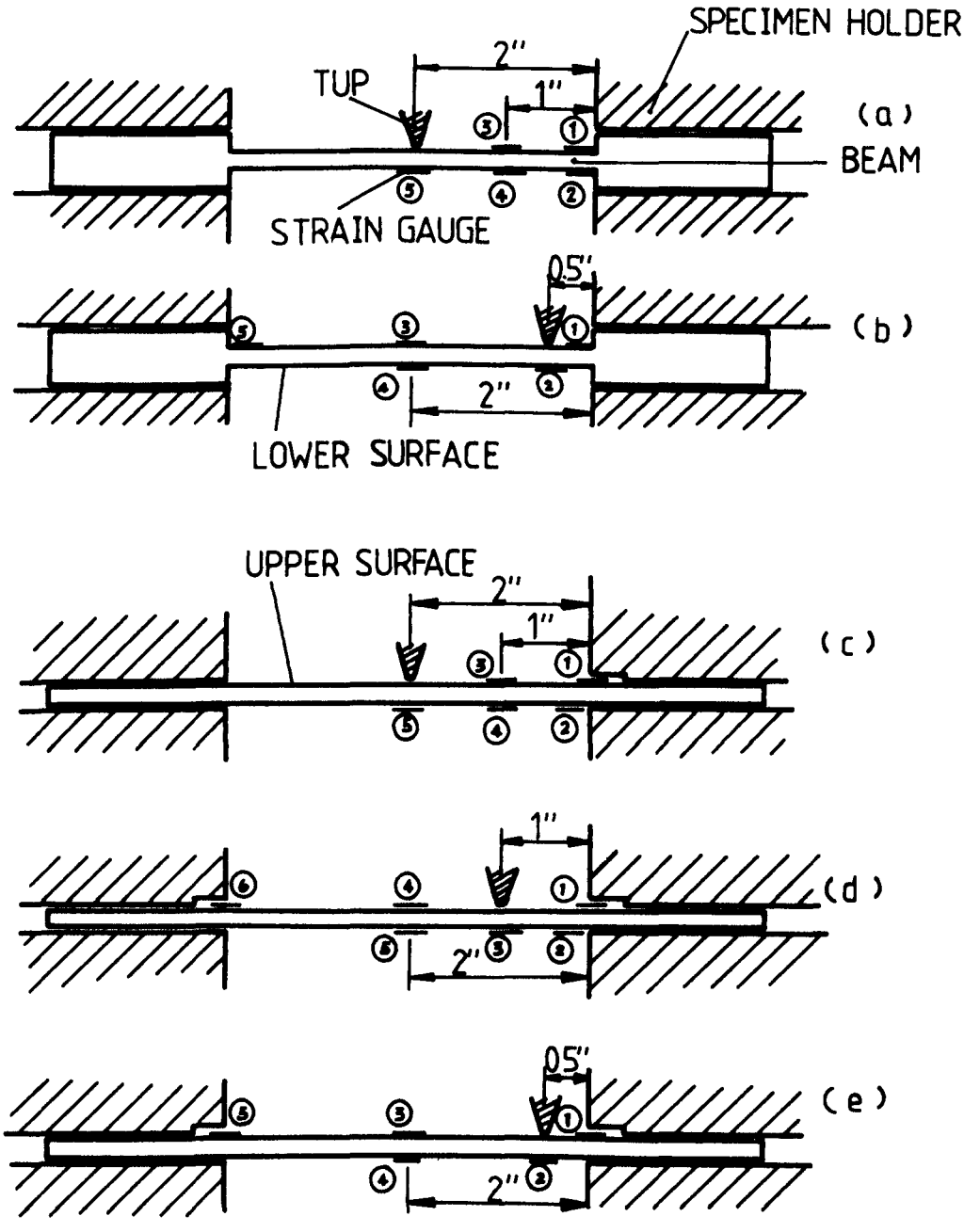

FIG. 62 The arrangement of strain gauges. (a) ℓ_1 = 2 in (50.8 mm) and the test specimens were AII11 and SII10; (b) ℓ_1 = 0.5 in (12.7 mm) and the test specimen was SII11; (c) ℓ_1 = 2 in and the test specimens were AℓI25, AℓIV25, STI25, STII25 and STIV25; (d) ℓ_1 = 1 in (25.4 mm), specimen was STIII24; (e) ℓ_1 = 0.5 in, specimen was STIII25.

the support was inserted into the holder since it was found that almost half of the triangular plastic region at the support occurred in the support end of the beam shown in Fig. 63.

6.1 Deformations of the Beam

The deformation shapes of the steel and aluminium beams were similar, but there was a slight difference between the flat end beam and the large end beam. However, the difference was very small and only occurred in a small region near the supports shown in Figs. 58 and 59. Triangular plastic regions can be clearly seen at the supports and at the impact point of the beam and some typical shapes are shown in Fig. 63.

6.1.1 Motion of the beam

When a beam was impacted by the tup at the centre, like the results reported by Duwez et al. [46] and Reid and Hendry [57], a V-shaped deformation spread, or two travelling plastic hinges travelled, from the impact point towards the built-in ends and it is classified as the first phase of motion. The first phase of motion occurred in a very short time compared with the duration of the beam response and the travelling plastic hinges reached the built-in ends almost at the instant when the tup first touched the beam since for our tests the beams are thicker and shorter and the tup is much heavier than that used by Duwez et al. [46] and Reid and Hendry [57]. Therefore, the motion of the beam was governed by those two parts of beam which separated from the impact point and rotated as rigid bodies around the supports

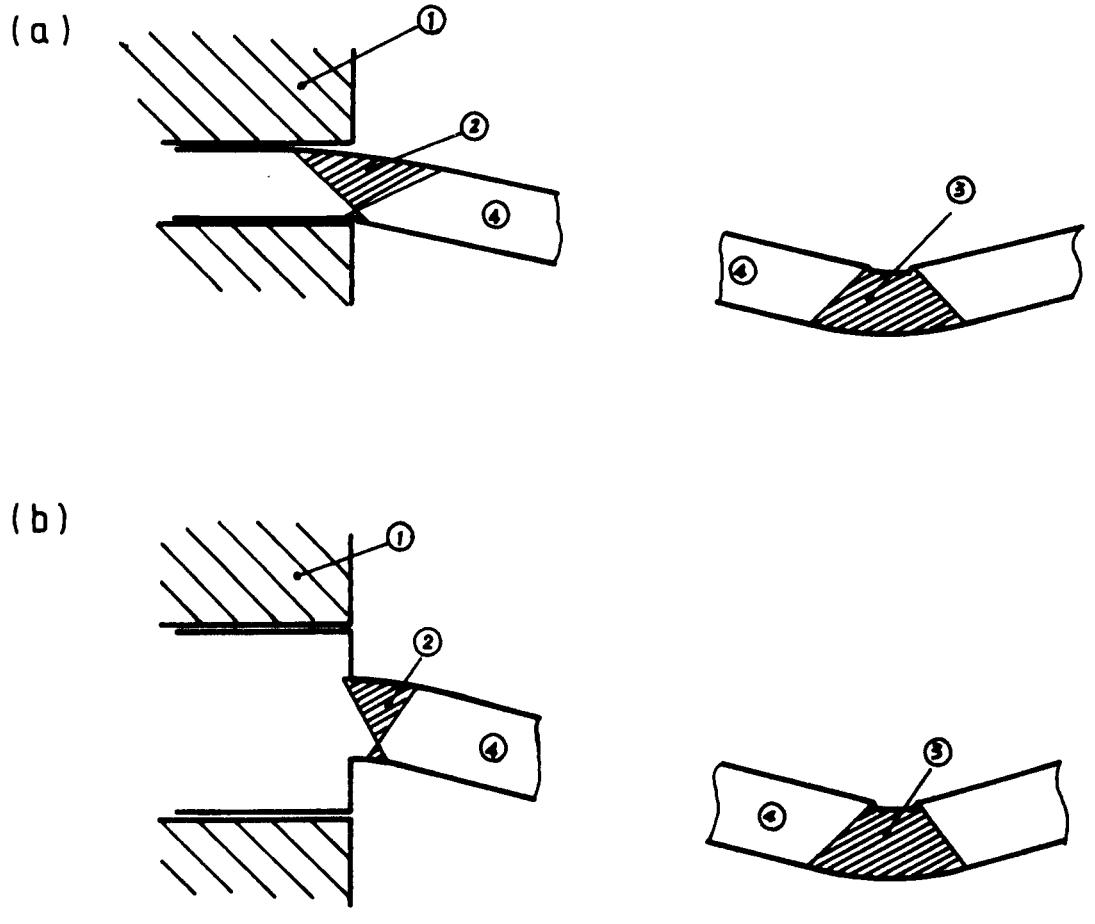

FIG. 63 The plastic regions of the beam at the support and at the impact point. (a) flat end beam and (b) large end beam, 1) the specimen holder, 2) plastic region at the support, 3) plastic region at the impact point, 4) beam specimen.

(this is classified as the second phase of motion), until the beam fractured or reached its maximum plastic deformation and started to vibrate elastically about its final position.

The first phase of motion occurred so quickly that it is not even clear in the films taken by the high speed camera with quarter frame exposures at the speed about 7000 frames per second. Fortunately, this phenomenon appears in the strain traces. The strain traces shown in Fig. 64 were recorded from strain gauges which were stuck on the upper and lower surfaces at the same point of the beam, respectively. It shows that at first the strain gauge on upper surface was increasingly stretched and the other one on lower surface was increasingly compressed, then after a short time of about 0.04 ms the situation was suddenly totally changed, i.e. the strain gauge on upper surface became to be compressed while the other one to be stretched. The interval from tension to compression for the upper surface strain gauge or from compression to tension for the lower surface strain gauge may contribute to the duration of the first phase of motion and it is about 0.04 ms for the case corresponding to the traces shown in Fig. 64.

It is clear from the deformation profile-time history plotted in Fig. 58 that in a very short time after the impact on the beam at the centre $\ell_1 = 2$ in the two halves of the beam moved as rigid bodies except for points near the impact point and the supports. When the impact point ℓ_1 was 1.5 in (38.1 mm), 1.0 in (25.4 mm) and even 0.5 in (12.7 mm), the motion of the beam was similar to that with the impact point $\ell_1 = 2$ in but the two

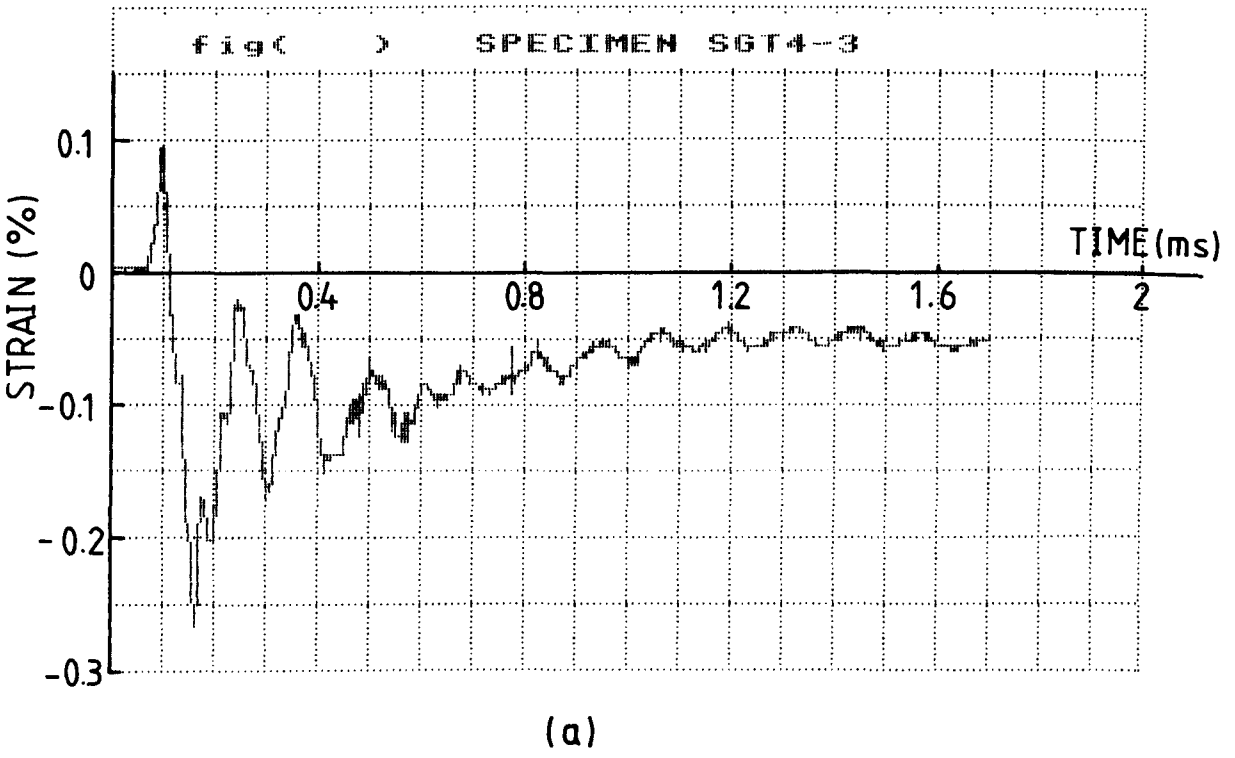

(a)

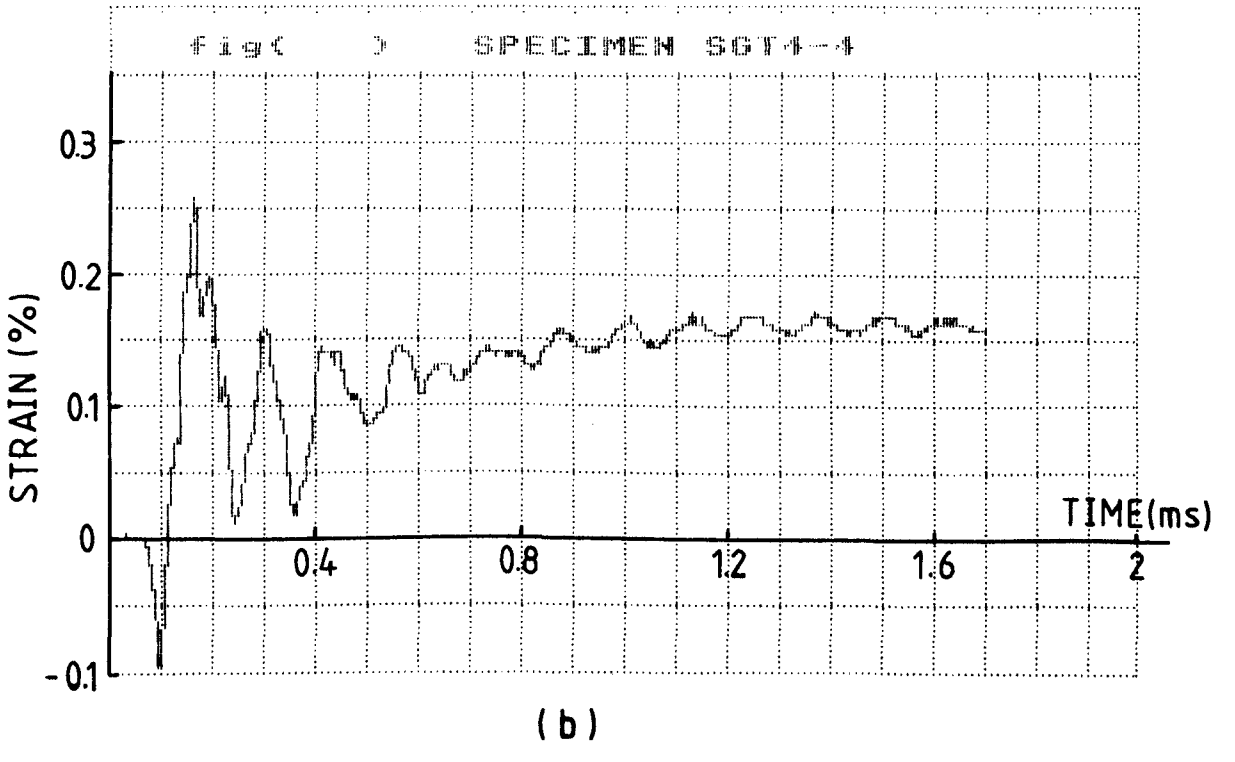

(b)

FIG. 64 Strain traces obtained from middle strain gauges, specimen No. STIV25. (a) strain on upper surface of the beam; (b) strain on lower surface of the beam.

travelling plastic hinges did not reach the supports simultaneously and the interval in which the hinges all reached the supports was longer. Fig. 59 shows some deformation profile-time history traces of beams with the impact point at ℓ_1 = 0.5 in (12.7 mm). When the impact point ℓ_1 was 0.25 in (6.35 mm), no straight line motion of the beam appeared on the right part of the beam since the impact point was too close to the right-hand support and the effect of the support was large.

The films show that the tup was in contact with the beam until the beam reached its maximum plastic deformation, then it rebounded two or three times and finally rested on the beam, while for the broken beams the tup was in contact with the beam during the entire response. The maximum deformation of the beam occurred during the first impact of the tup and the rebound of the tup hardly influences the response of the beam.

Fig. 65a shows some velocity-time history traces which were captured by the laser doppler velocimeter and were recorded by DL1080 transient recorders. These traces are actually the velocity-time history of the tup, but the positive portion of these traces is also the velocity of the beam at the impact point since the tup remained in contact with the beam at the impact point. It shows that the velocity decreased sharply during 3 ms, approximately, after impact. However, the velocity reduced slowly during the first third of a millisecond after impact which may occur because the plastic regions at the impact point and at the supports, shown in Figs. 63, were not large enought to allow

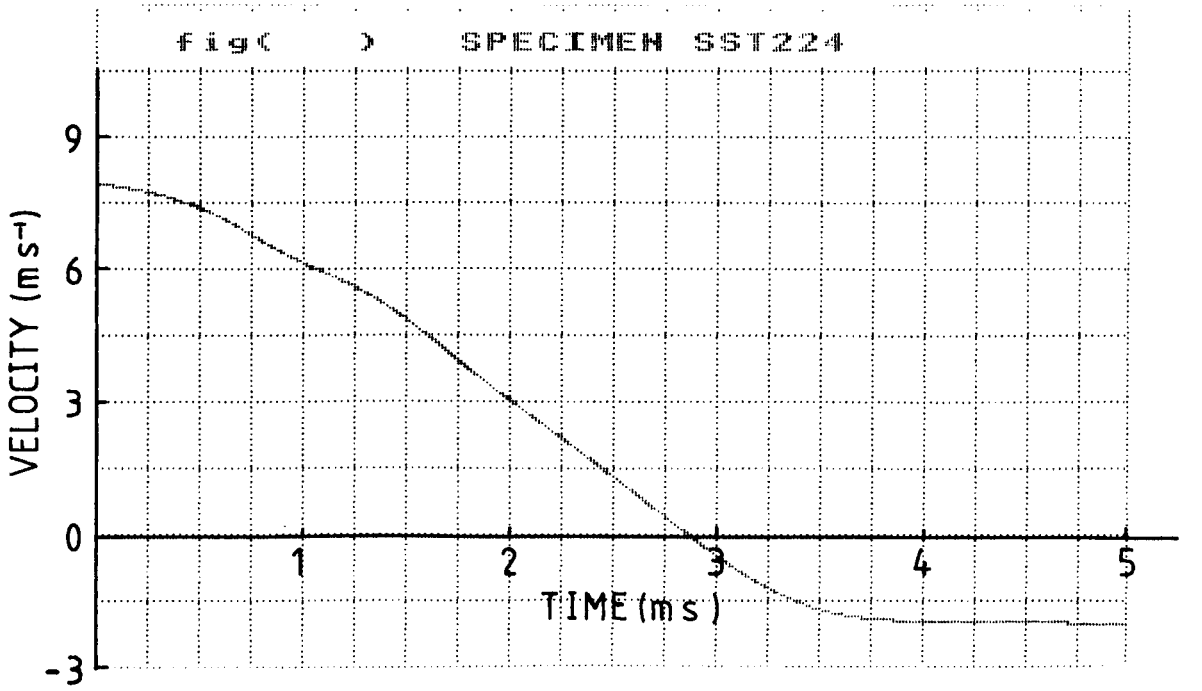

FIG. 65a Velocity-time history trace which was captured by the laser doppler velocimeter and was recorded by DL1080 transient recorder. Specimen No. STII24.

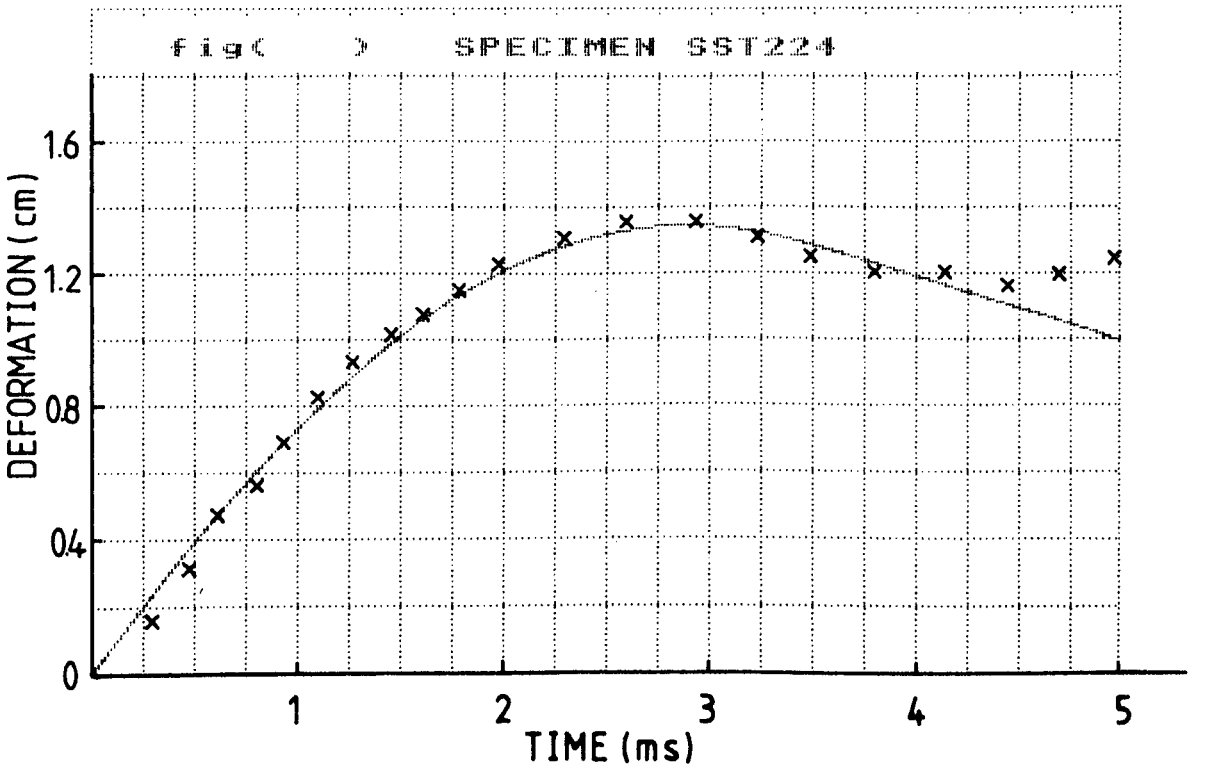

FIG. 65b Deformation-time history trace obtained by integrating the velocity trace in Fig. 65a using a computer program 'try 8'. x; the deformation measured from film. Specimen No. STII24.

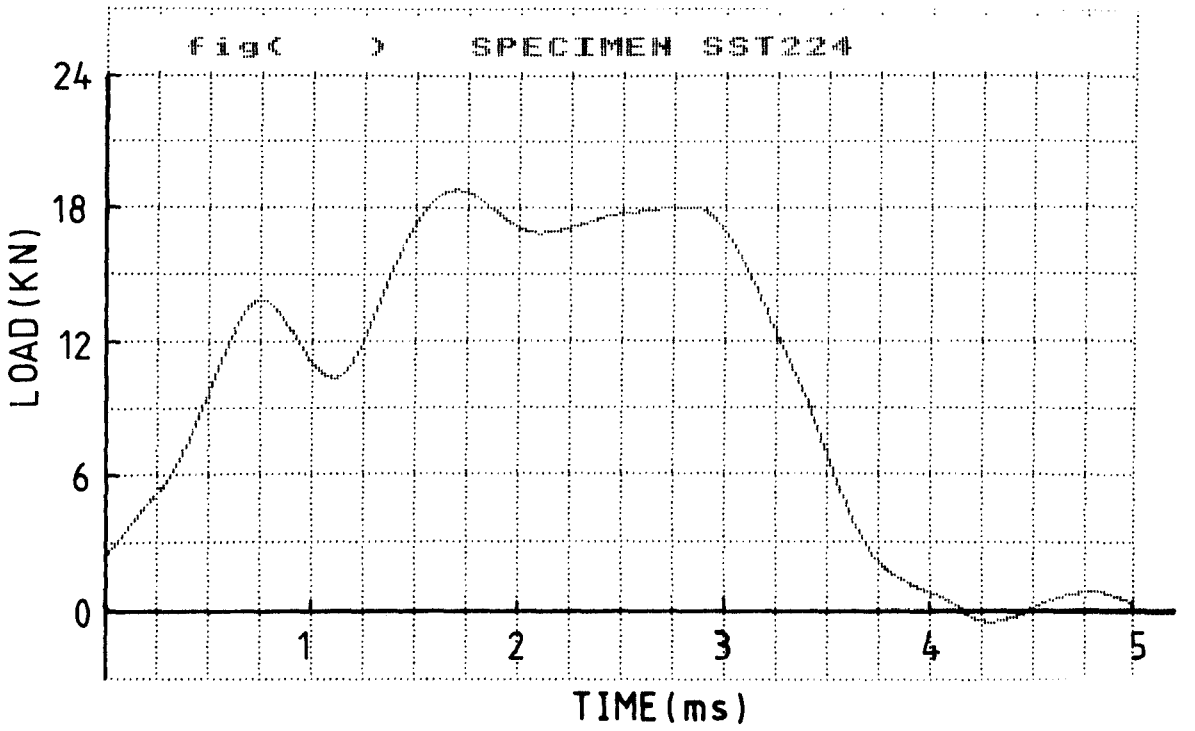

FIG. 65c Load-time history trace between the tup and the beam specimen. Specimen No. STII24.

the beam to rotate as rigid bodies. This phenomenon also appeared in deformation profile-time history traces shown in Figs. 58 and 59 where for first 2 or 3 deformation profile curves there are no clear 'plastic hinges' appeared at the impact point.

The deformation-time history curve of the beam at the impact point is plotted in Fig. 65b. This curve was obtained by integrating the velocity trace shown in Fig. 65a using the computer programme 'try 8'. The data which were measured from the film are also plotted in Fig. 65b. It is clear that the computer results are in fair agreement with the film data until the beam reached its maximum deformation. After that a large difference appeared because the tup separated from the beam and rebounded upwards. The loads between the tup and the beam, which were obtained by differentiating the velocity using 'try 8', are plotted in Fig. 65c.

It is evident from the film data and the strain gauge traces that after reaching its maximum deformation the beam started to vibrate elastically. The vibration decayed sharply and the beam soon reached its permanent deformation position, shown in Figs. 61 and 83.

6.1.2 Permanent deformation of the beam

The kinetic energy of the tup was dissipated as plastic work of the beam and caused a permanent deformation, provided the kinetic energy is large.

Figs. 66-70 show that consistent experimental results for

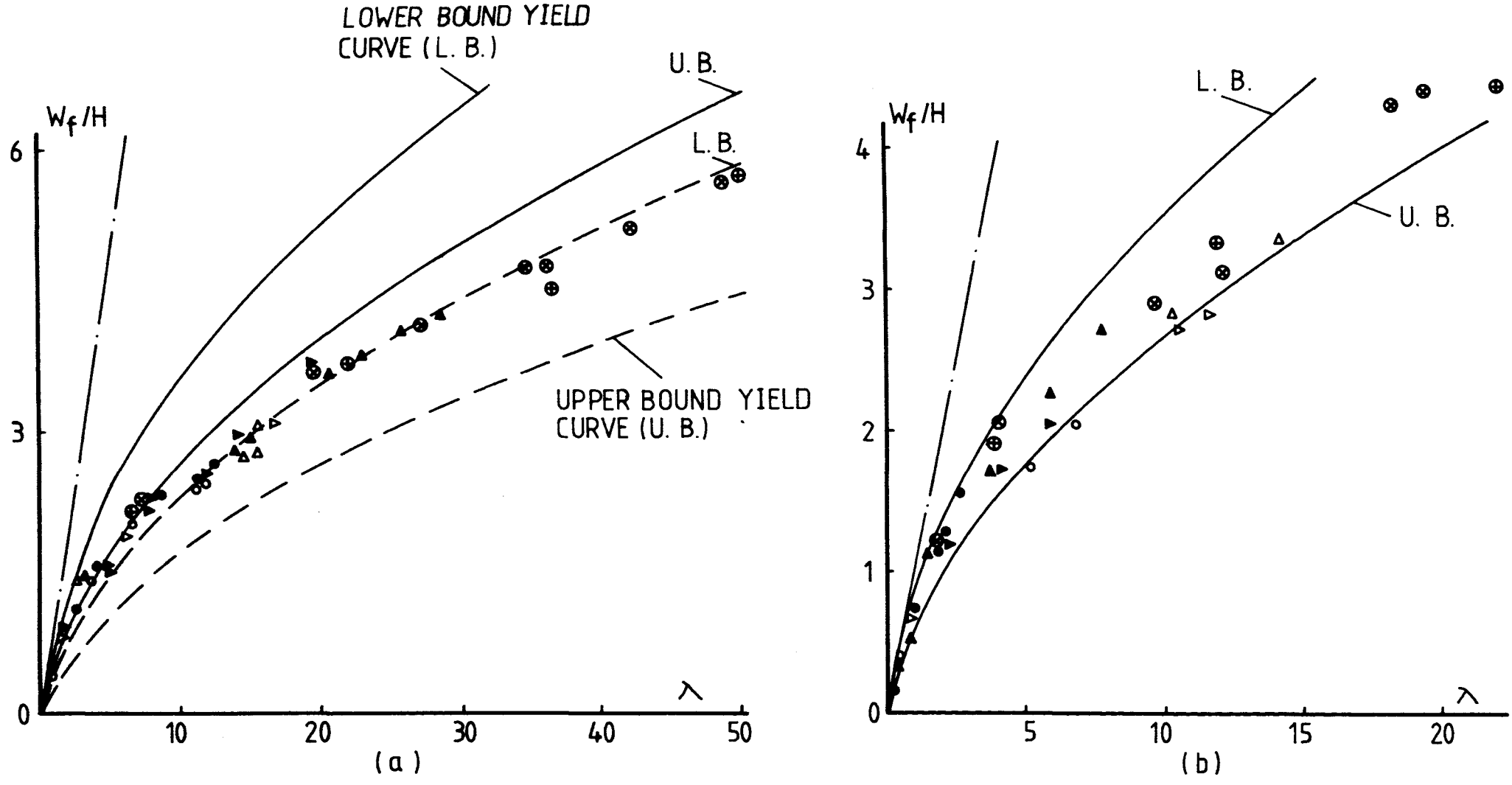

FIG. 66 Variation of maximum permanent deformation W_f/H with external dynamic energy λ when ℓ_1 = 2 in (a) steel beams, (b) aluminium alloy beams.
Theoretical predictions; — — bending only solution [10], ——— equation (7-1) with static yield stress σ_o, ---- equation (7-1) with dynamic yield stress given by equation (7-3).
Experimental results;

⊗ - flat end, H = 0.15 in; ⊕ - large end, H = 0.15 in;
▲ - flat end, H = 0.2 in; Δ - large end, H = 0.2 in;
▶ - flat end, H = 0.25 in; ▷ - large end, H = 0.25 in;
● - flat end, H = 0.3 in; ○ - large end, H = 0.3 in;

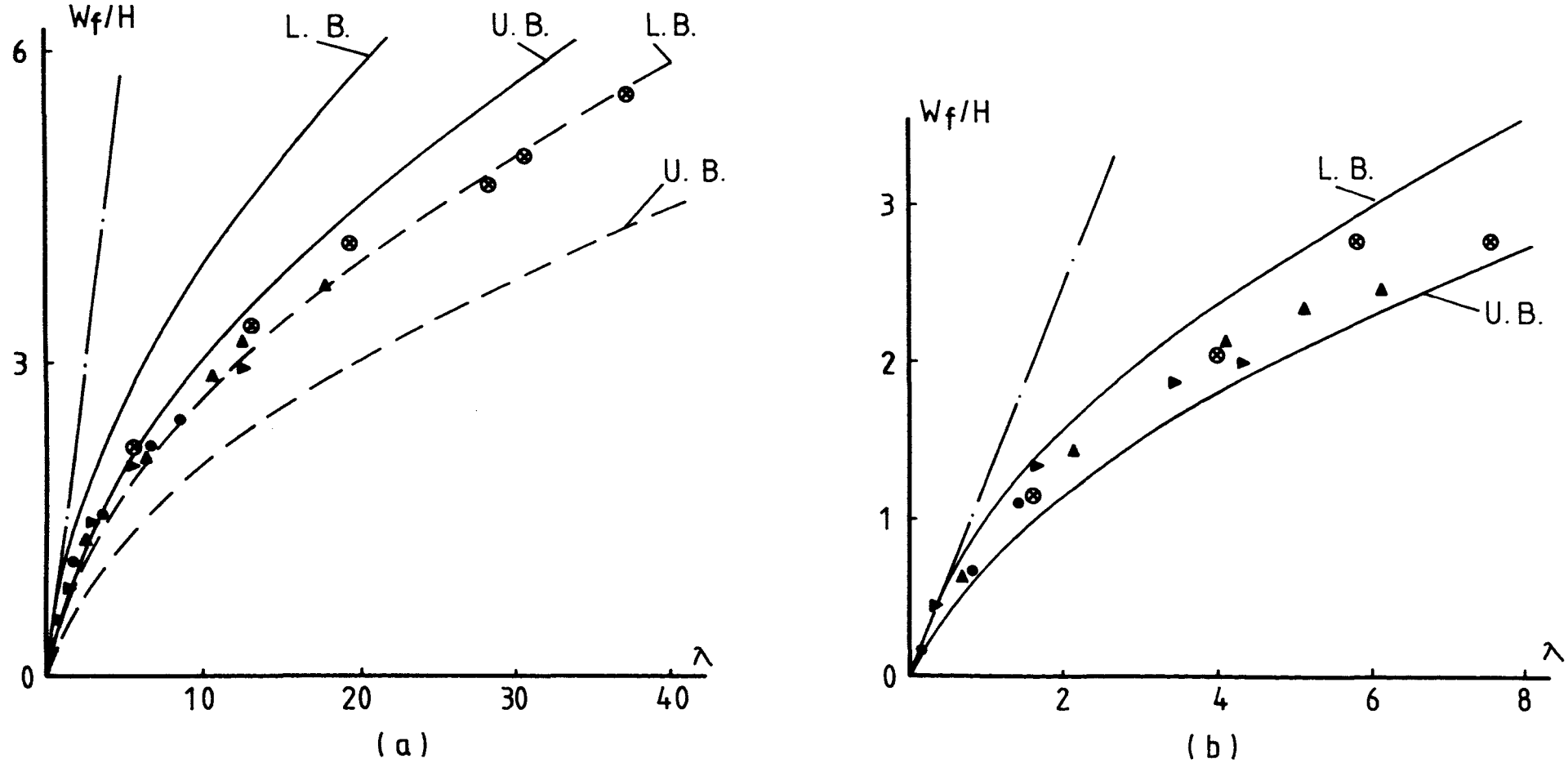

FIG. 67 Variation of $\frac{W_f}{H}$ with λ when ℓ_1 = 1.5 in. (a) steel beams, (b) aluminium alloy beams.

The symbols are the same as that in Fig. 66.

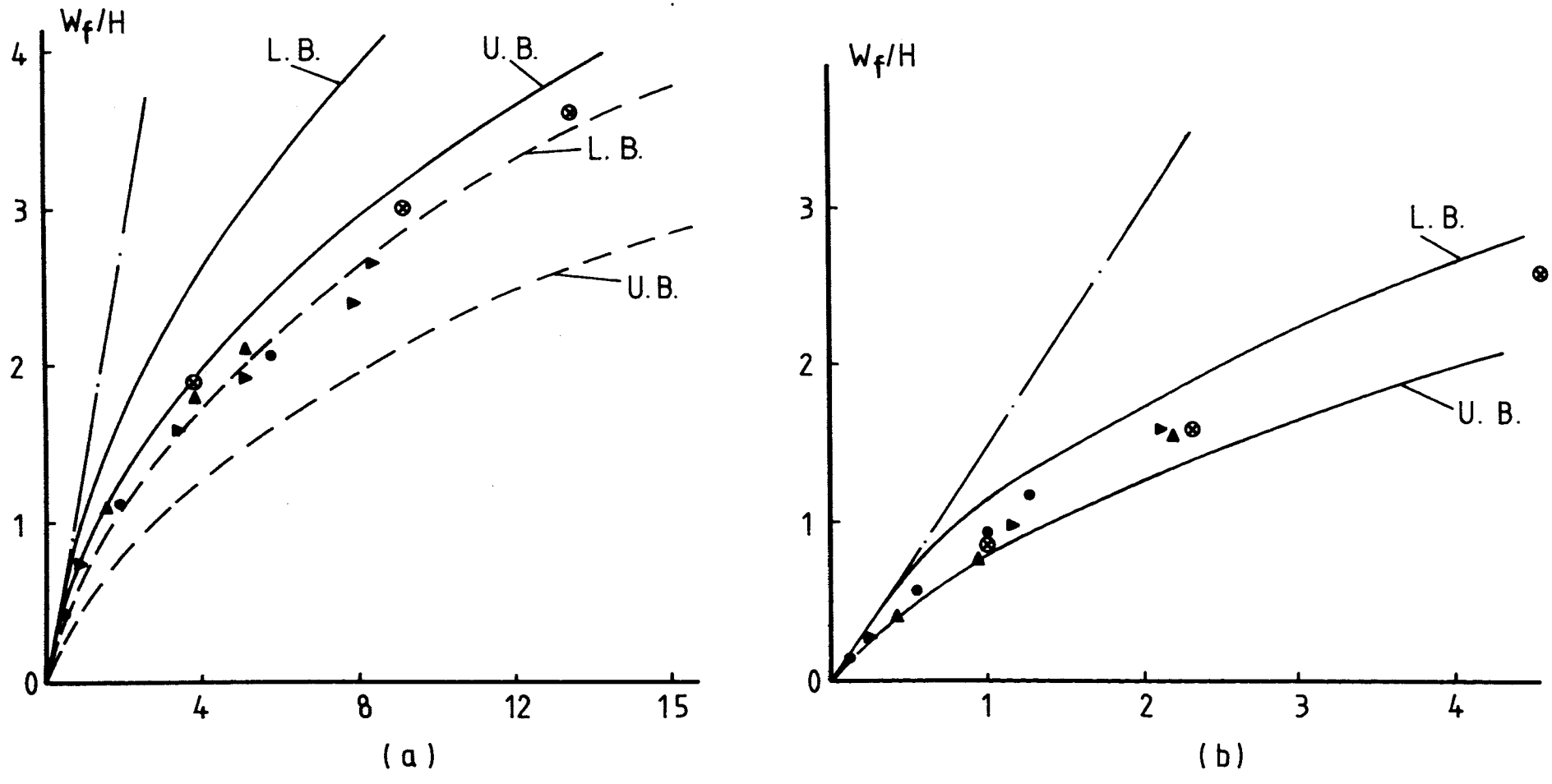

FIG. 68 Variation of $\frac{W_f}{H}$ with λ when ℓ_1 = 1 in. (a) steel beams, (b) aluminium alloy beams.

The symbols are the same as that in Fig. 66.

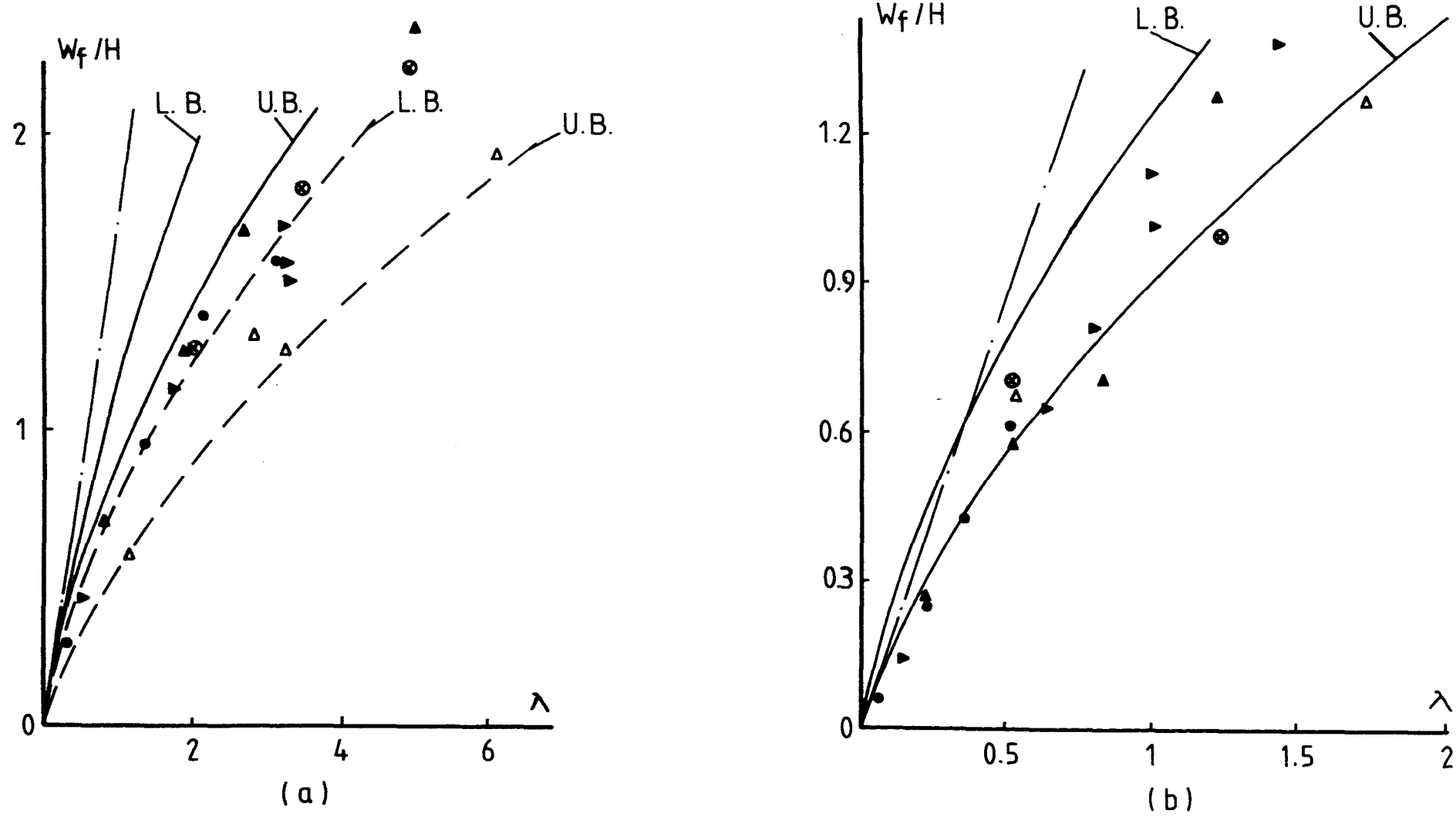

FIG. 69 Variation of $\frac{W_f}{H}$ with λ when ℓ_1 = 0.5 in. (a) steel beams, (b) aluminium alloy beams. The symbols are the same as that in Fig. 66.

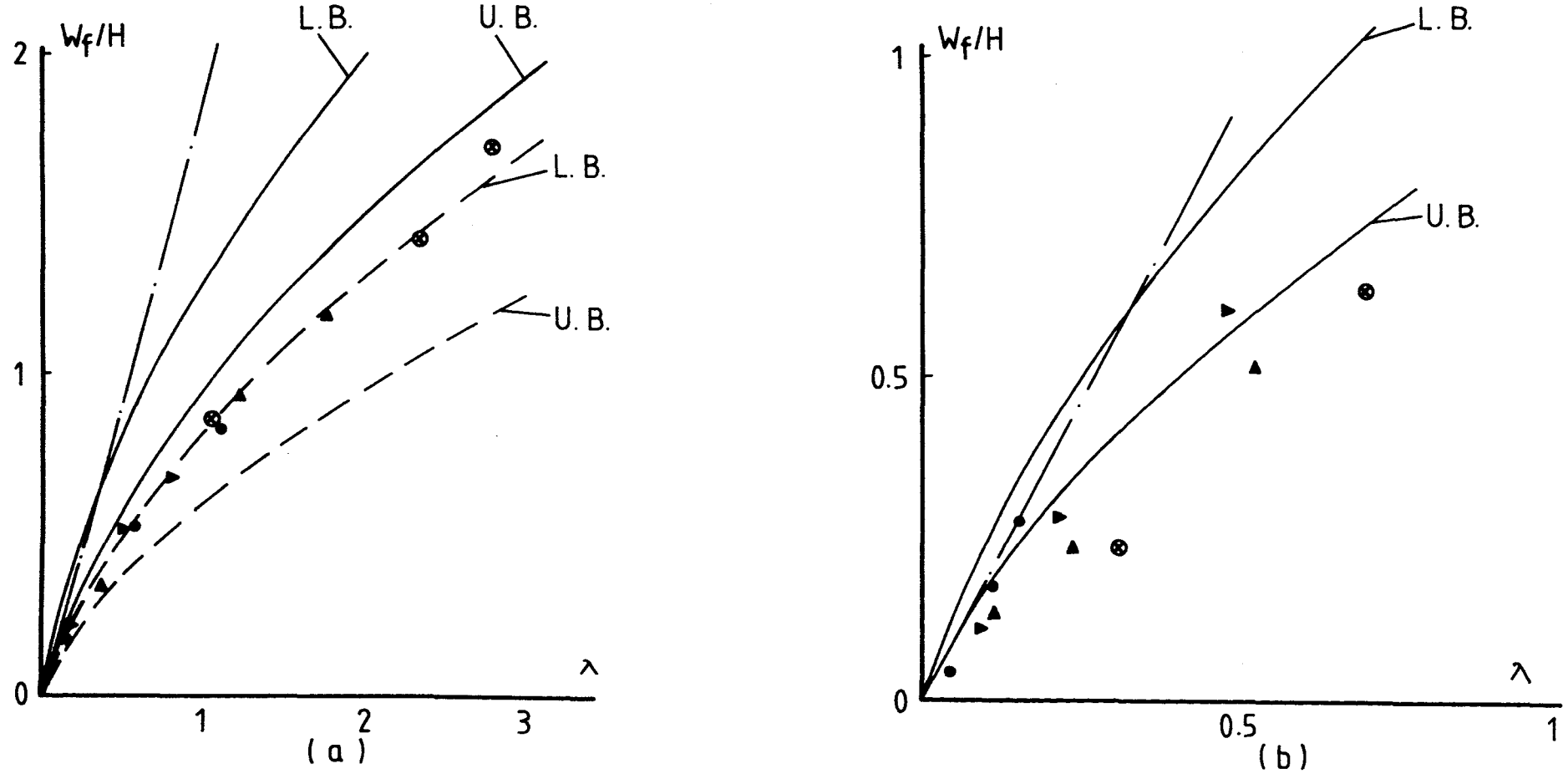

FIG. 70 Variation of $\frac{W_f}{H}$ with λ when ℓ_1 = 0.25 in. (a) steel beams, (b) aluminium alloy beams.

The symbols are the same as that in Fig. 66.

the maximum permanent deformations were obtained, especially for steel beams.

It is evident that the maximum permanent deformations of the beam increase with the increase of the kinetic energy $\lambda = \frac{GV_0^2}{8M_0}\frac{\ell_1}{H}$. The membrane force played an important role on the response of the beam since the maximum permanent deformation is not in proportion to the kinetic energy λ and the difference is very large when λ is large (the maximum permanent deformation of the beam is in proportion to the external dynamic energy in the analyses of the bending only solution [10] and the shear and bending solution discussed in Chapter 3 of this thesis).

It appears that the clamping conditions had no influence on the maximum permanent deformation of the beam provided the impact point was remote from the support (ℓ_1 = 2 in), since the experimental data in Figs. 66a and 66b show that there were no differences occurring between the flat end beams and large end beams. However, the clamping conditions may have an influence when the impact point was close to the supports (ℓ_1 = 0.5 in) shown in Figs. 69a and 69b. More tests on large end beams with different thickness need to be conducted in order to estimate the value of this influence.

Figs. 71 and 72 show that the maximum permanent deformation of the beam struck by the tup with certain value of velocity decreases with the decrease of $r = \ell_1/\ell_2$, especially when the impact point is close to the support the decrease of the maximum permanent deformation is rapid.

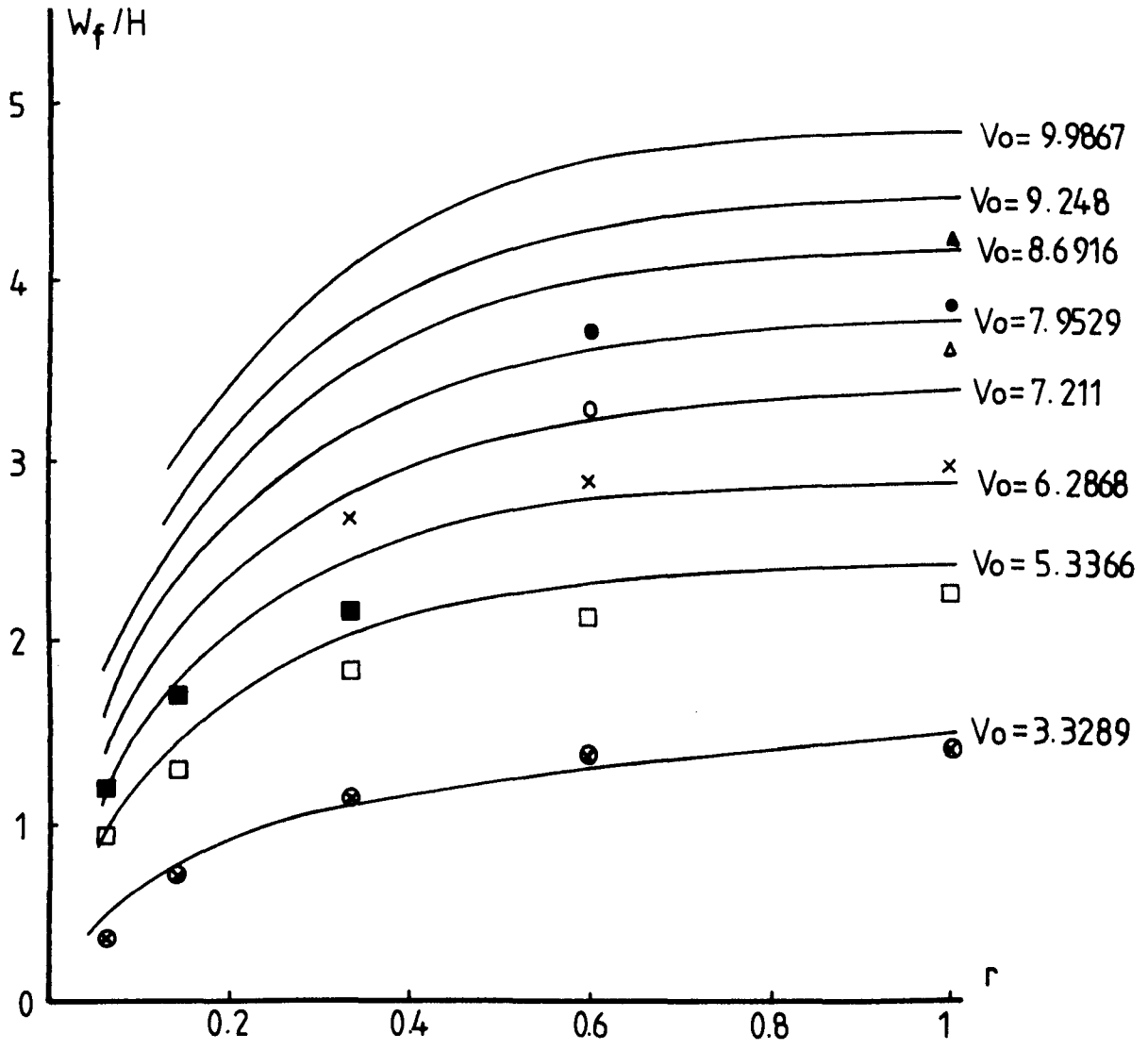

FIG. 71 Variation of maximum permanent deformation $\frac{W_f}{H}$ of flat steel beams with r. ——; theoretical prediction obtained from Chapter 4, ▲ ; experimental result with V_0 = 9.9867 ms^{-1}, ● ; V_0 = 9.248 ms^{-1}, Δ; V_0 = 8.6916 ms^{-1}, ○ ; V_0 = 7.9529 ms^{-1}, × ; V_0 = 7.211 ms^{-1}, ■ ; V_0 = 6.2868 ms^{-1}, □ ; V_0 = 5.3366 ms^{-1}, and ⊗ ; V_0 = 3.3289 ms^{-1}.

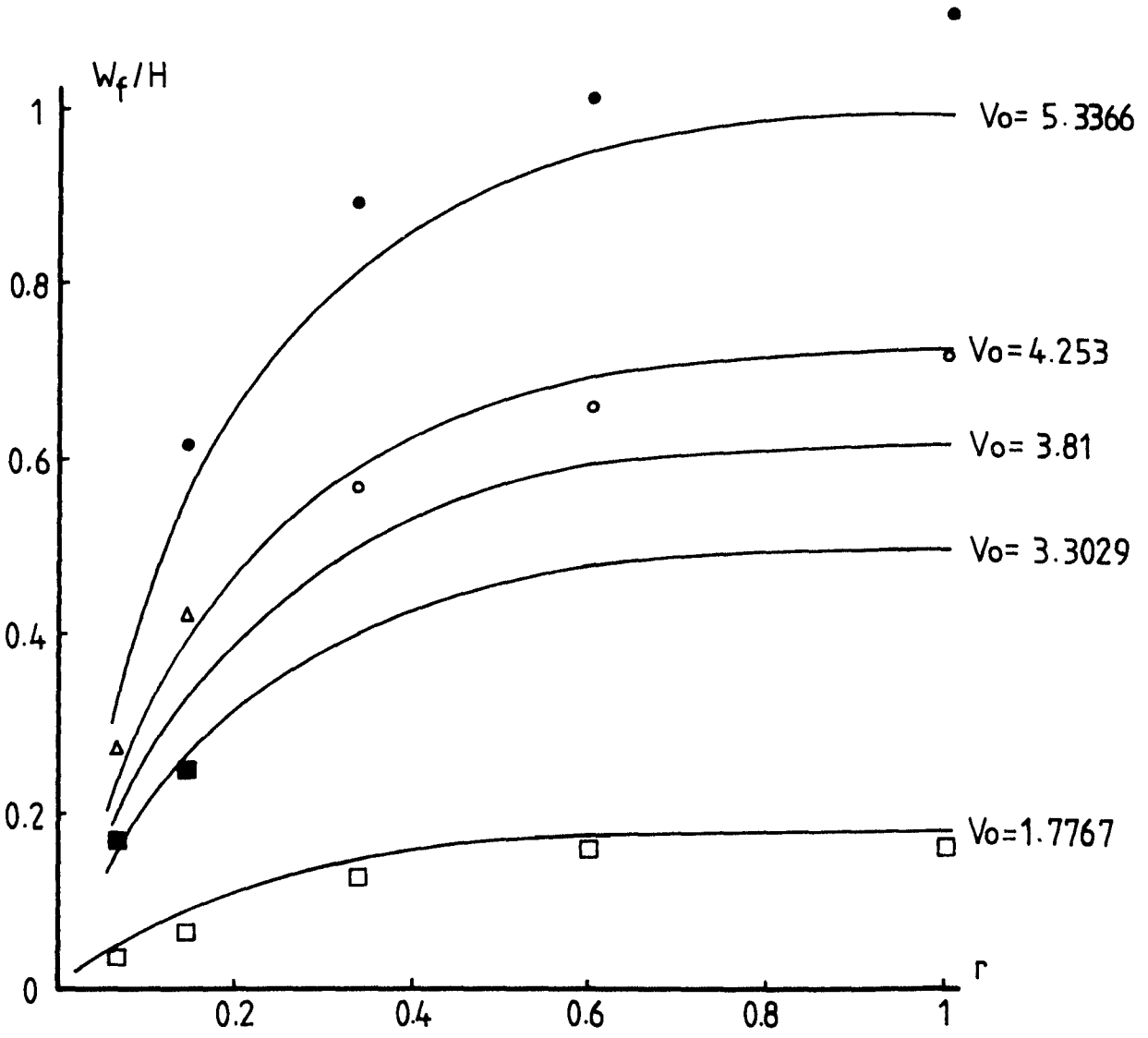

FIG. 72 Variation of maximum permanent deformation $\frac{W_f}{H}$ of flat end aluminium alloy beams with r. ——; theoretical prediction obtained from Chapter 4, ● ; experimental results with V_0 = 5.3366 ms^{-1}, Δ; V_0 = 4.253 ms^{-1}, o; V_0 = 3.81 ms^{-1}, ■; V_0 = 3.3029 ms^{-1}, and □ ; V_0 = 1.7767 ms^{-1}.

It is found that the maximum permanent deformation occurred exactly at the impact point when ℓ_1 = 2 in, 1.5 in and 1.0 in, while for ℓ_1 = 0.5 in and 0.25 in the location of the maximum permanent deformation may slightly deviate from the impact point and approach the centre of the beam.

After test, the dimensions of beams were measured with the travelling microscope and some of dimensions of beams with different impact point and different boundary conditions are plotted in Figs. 73-76. It shows that after test most parts of the beam on both upper surface and lower surface remained straight and the upper surface of beam remained in parallel the lower surface except near the impact point and the supports. The decrease of beam thickness is large near the impact point and the supports. The local effects of compressive force in transverse direction are evident at the impact point and at the support for steel beams. It is clear that after testing the dimensions of the flat and the large end beams were similar except the points near the built-in ends.

There were three clear triangular plastic regions at both the supports and the impact point, shown in Figs. 77 and 78, except the case in which the impact point ℓ_1 was near the support. Fig. 79 shows that when the impact point was close to the support no clear triangular plastic region appeared at the support since the effect of the support was large and the shear force might play an important role on the response of the beam. When the transverse displacement of the beam was small, the

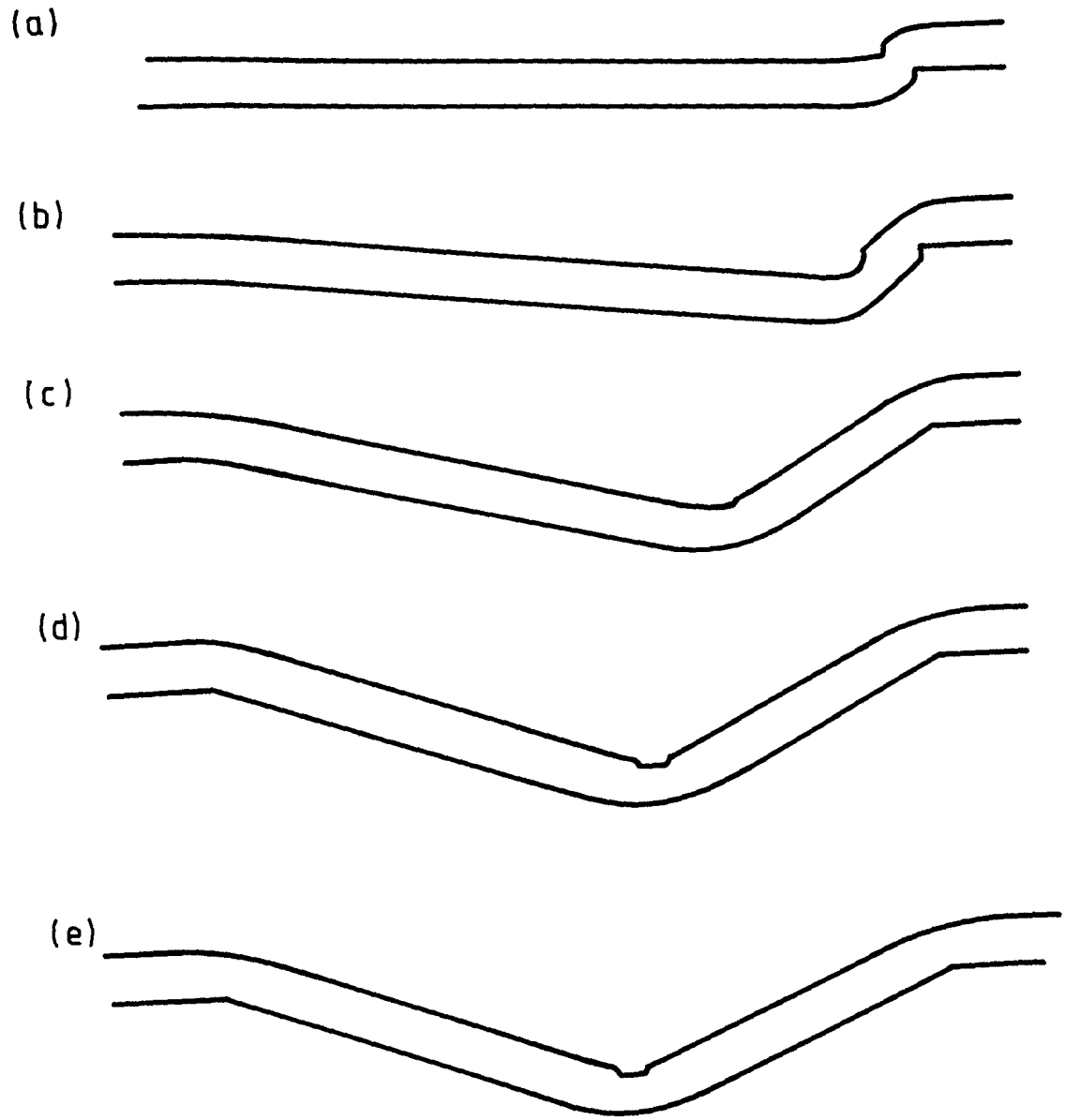

FIG. 73 Dimensions of flat end steel beams (a) ℓ_1 = 0.25 in (6.35 mm), specimen No. STIII17; (b) ℓ_1 = 0. 5 in (12.7 mm), specimen No. STIII15; (c) ℓ_1 = 1 in (25.4 mm), specimen No. STIII12; (d) ℓ_1 = 1.5 in (38.1 mm), specimen No. STIII9; and (e) ℓ_2 = 2 in (50.8 mm), specimen No. STIII4.

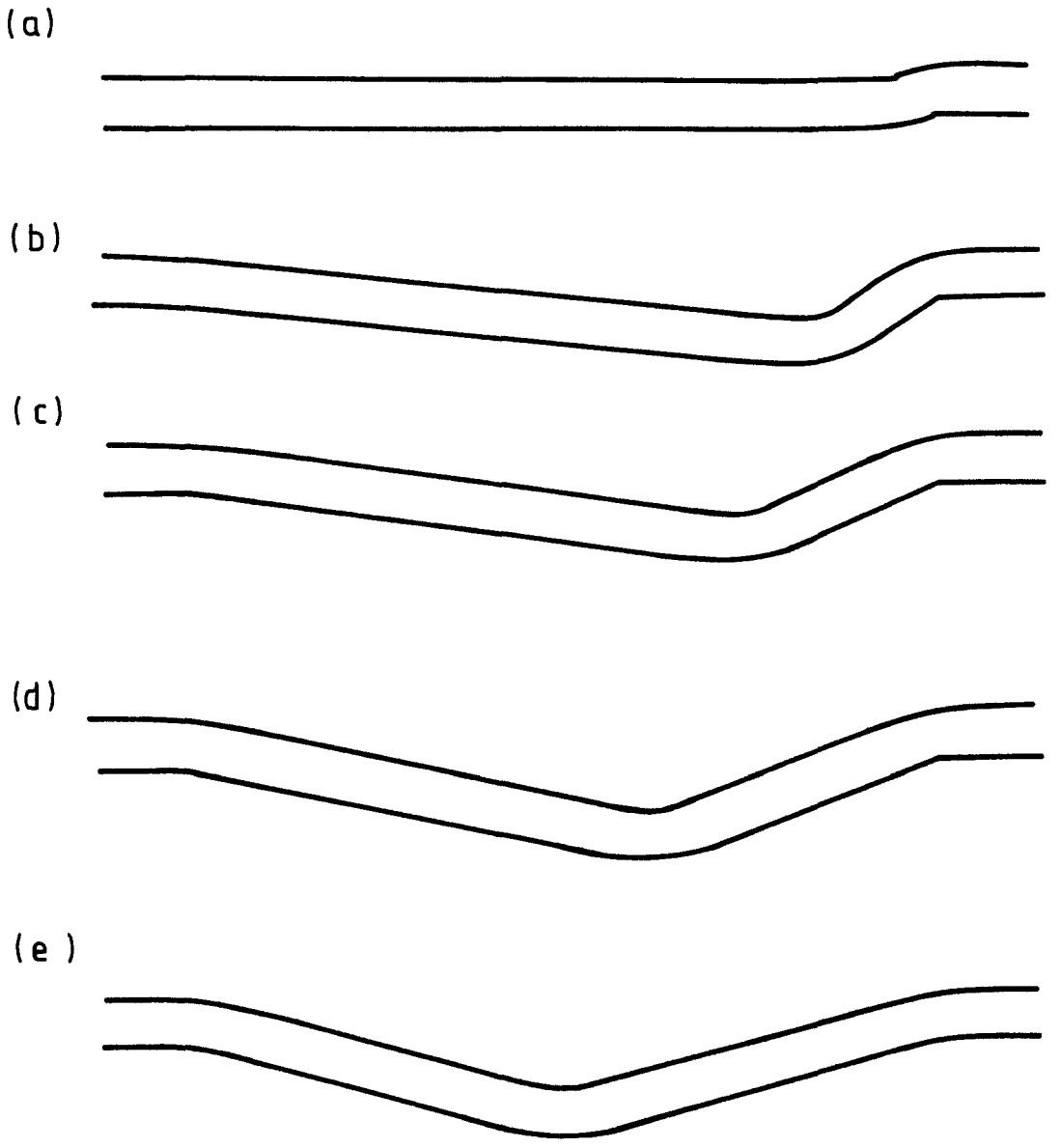

FIG. 74 Dimensions of flat end aluminium alloy beams. (a) ℓ_1 = 0.25 in, specimen No. AℓIII19; (b) ℓ_1 = 0.5 in, specimen No. AℓIII24, (c) ℓ_1 = 1 in, specimen No. AℓIII12, (d) ℓ_1 = 1.5 in, specimen No. AℓIII9; and (e) ℓ_1 = 2 in, specimen No. AℓIII2.

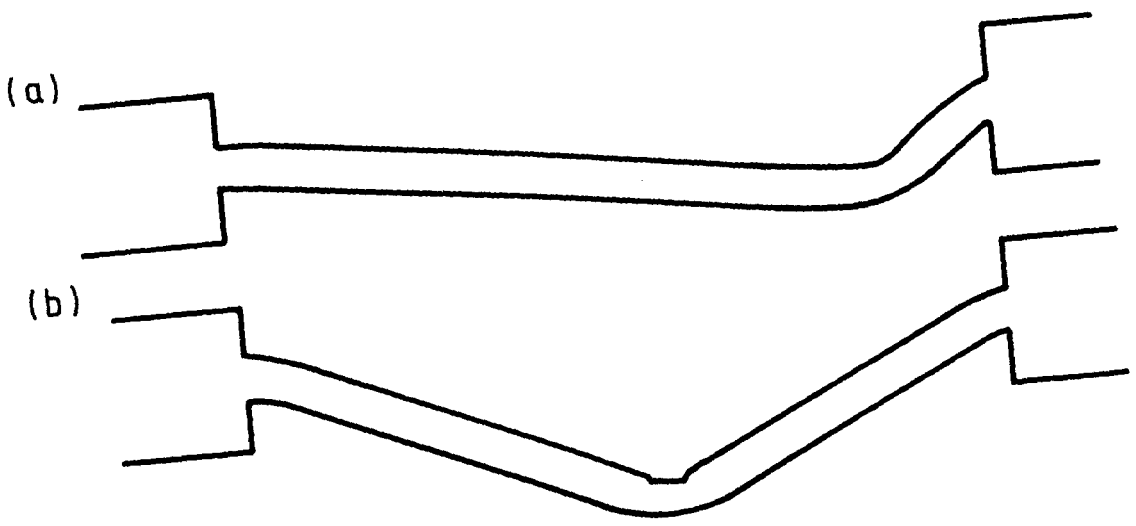

FIG. 75 Dimensions of large end steel beams. (a) ℓ_1 = 0.5 in, specimen No. SII6; (b) ℓ_1 = 2 in, specimen No. SII1.

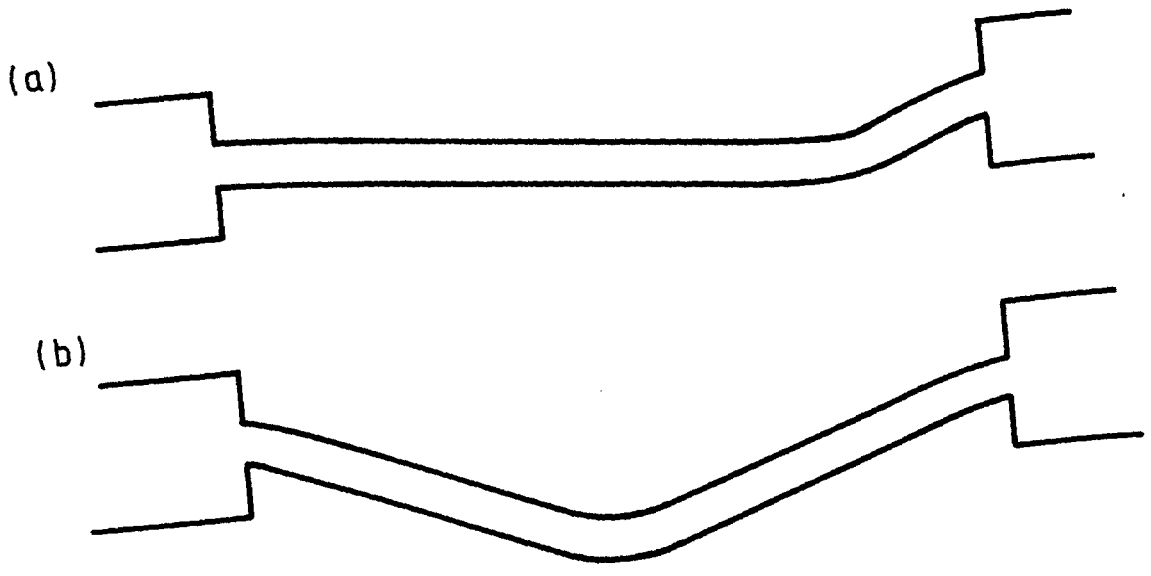

FIG. 76 Dimensions of large end aluminium alloy beams. (a) ℓ_1 = 0.5 in, specimen No. AII8; (b) ℓ_1 = 2 in, specimen No. AII1.

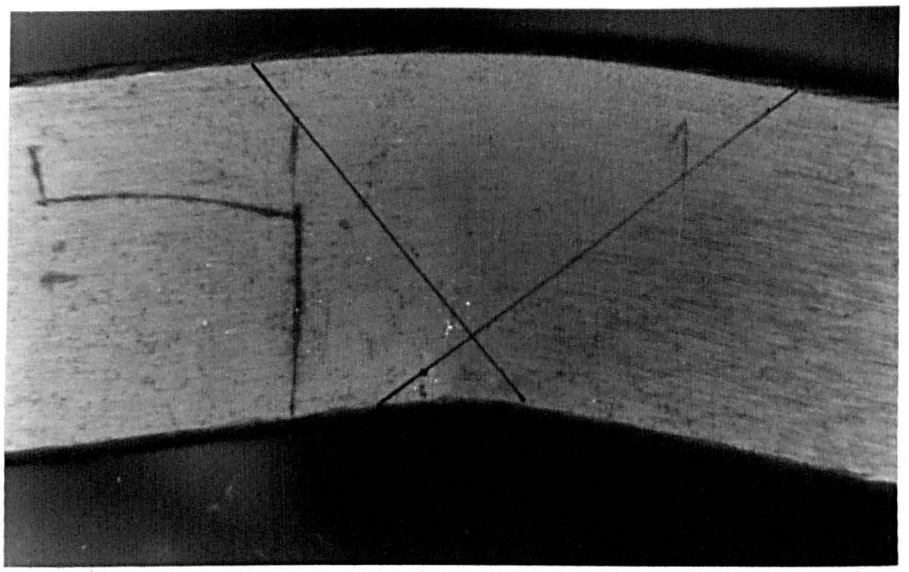

(a)

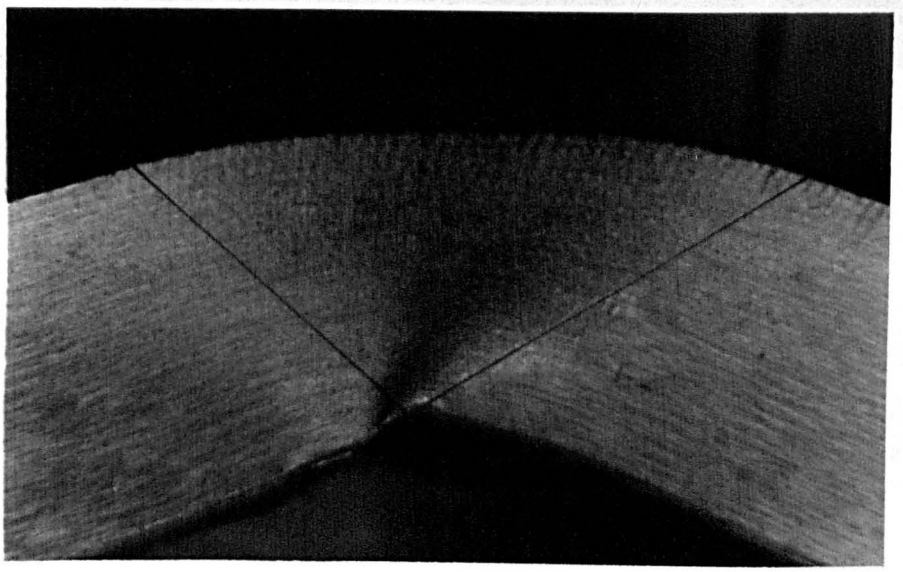

(b)

FIG. 77 Triangular plastic region at the support. (a) two triangles; (b) one triangle.

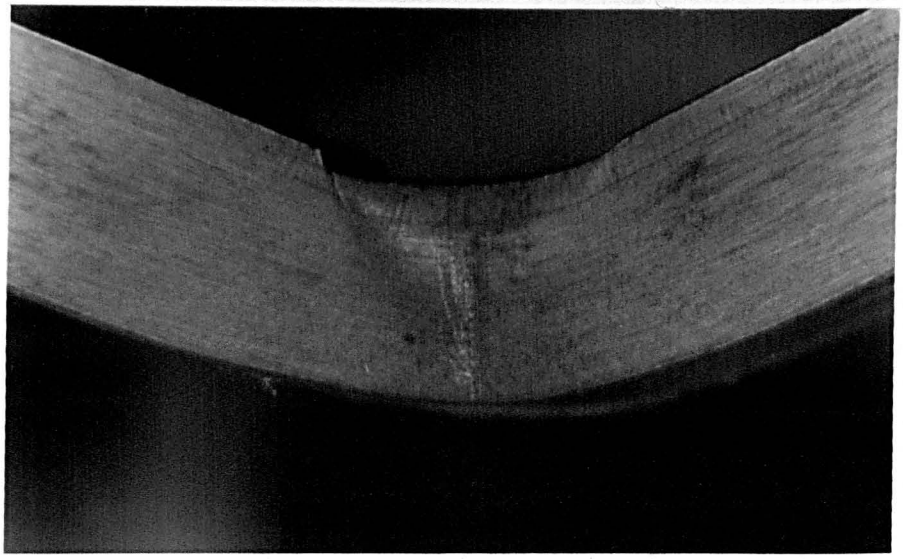

FIG. 78 Plastic deformation at the impact point. The impact point was at the centre of the beam.

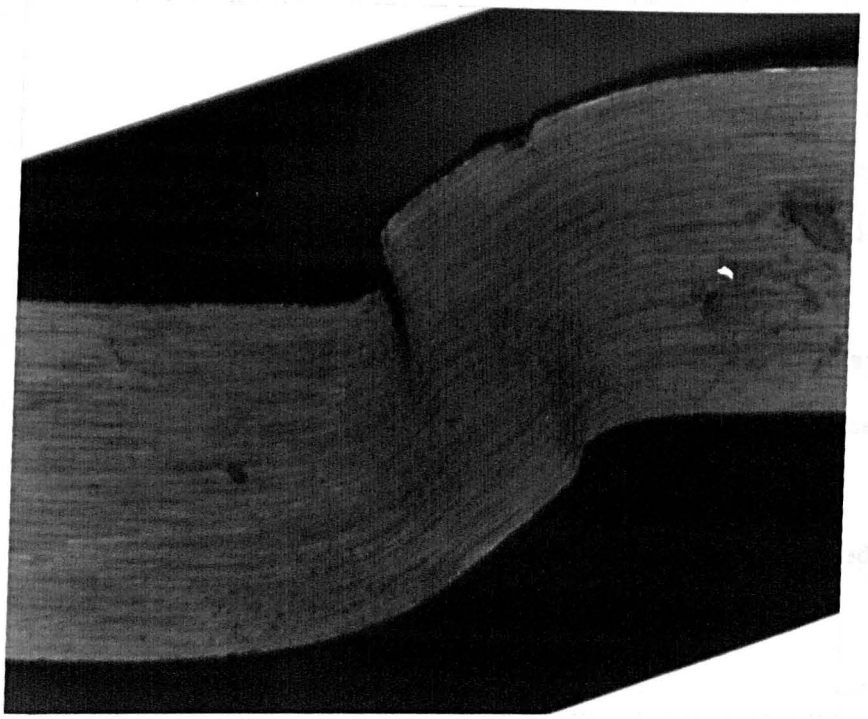

FIG. 79 Plastic deformations at the impact point and at the support when the impact point was close to the support (ℓ_1 = 0.25 in).

plastic region is composed of two triangles shown in Fig. 77a, the larger one on the tension side and the smaller one on the compression side (not clearly shown in Fig. 77a). With the increase of the transverse displacement of the beam, the size of the triangle on the tension side increases, while the size of the other one on the compression side reduces. The plastic region finally becomes one triangle on tension shown in Fig. 77b, provided the transverse displacement is large enough. The sizes of these two triangles was related to the thickness of the beam. The size of the triangle on the tension side increases more slowly for thicker beams and that on the compression side reduces more slowly. The maximum length on the tension side of the plastic region can also be seen on the upper or lower surface of the beam. Within the plastic region, there is a clear reduction of the width of the beam on the upper surface (for the plastic regions at the supports) or on the lower surface (for plastic region at the impact point), shown in Figs. 80.

The plastic regions of the steel beams are similar to those in the aluminium beams and the plastic regions of both the flat end and the enlarged end beams at the impact point are similar. However, the plastic regions at the supports of the flat end beams are larger than those in a corresponding large end beam. The apex of the triangular plastic region at the support occurred exactly at the clamped point for flat end beams shown in Figs. 77, while for the large end beams the apex occurred in the beam section near the connection between the large end and the beam section shown in Fig . 81b.

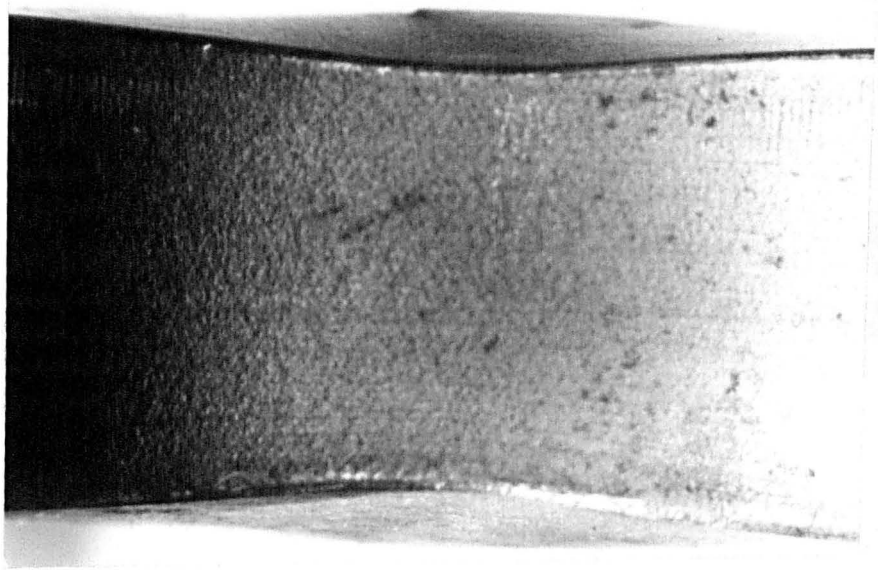

(a)

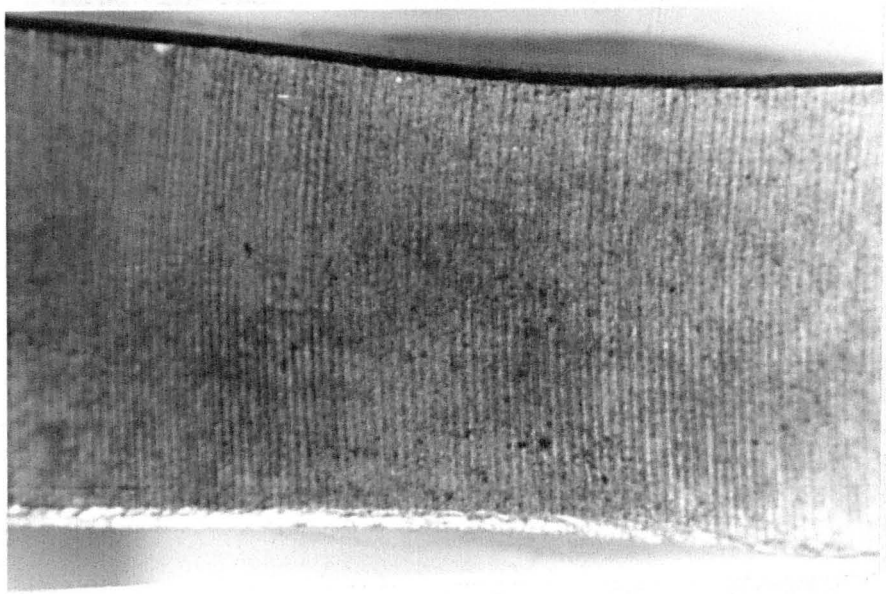

(b)

FIG. 80 Reduction of the beam width at plastic regions. (a) at the impact point; (b) at the support.

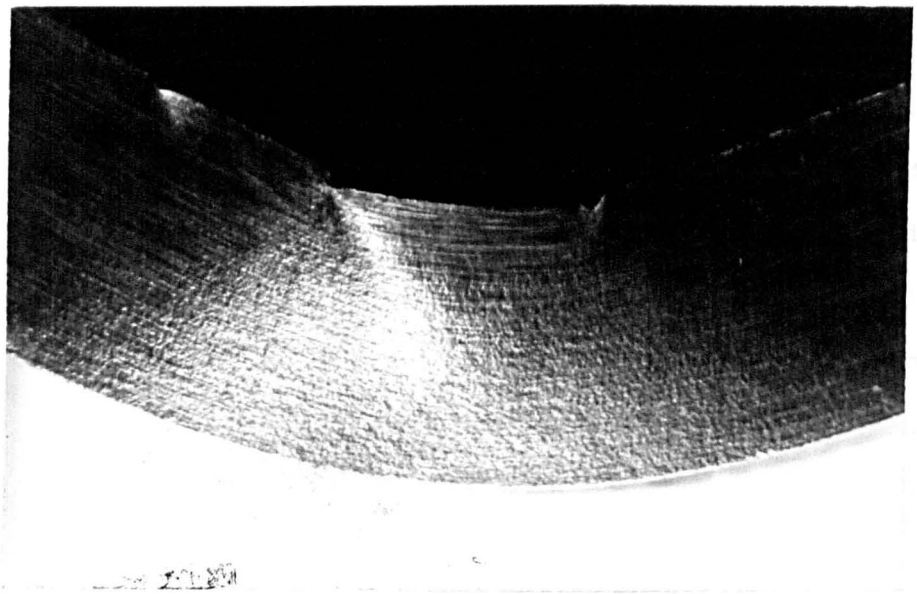

(a)

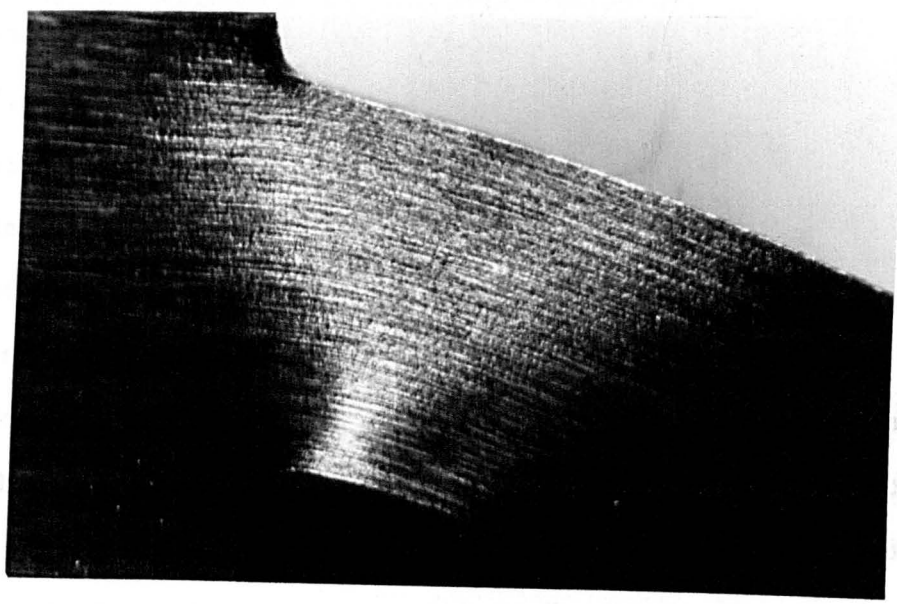

(b)

FIG. 81 Plastic regions of large end beams. (a) plastic region at the impact point; (b) plastic region at the support.

The shear deformation of the beam is difficult to measure since very high local transverse forces occurred at the impact point (between the tup and the beam) and at the support (between the beam and the specimen holder). These transverse forces compressed the beam and some 'plug' deformations shown in Figs. 78 and 79 occurred at the support and at the impact point. However, shear sliding certainly occurred in some beams, especially in those with the impact point ℓ_1 near the support shown in Fig. 79.

6.2 Strain in the Beam

Ten specimens with attached strain gauges were tested with the test arrangement shown in Fig. 62. The impact velocity was 7.3932 ms^{-1} for the steel beams and 5.7336 ms^{-1} for the aluminium alloy beams, respectively. EP type strain gauges which were designed for high-elongation measurements were chosen since the strain at the support and at the impact point of the beam was very large. The strain gauges can measure strains up to 20%. However, it was found that the strain gauges which were stuck at the support and at the impact point separated from the beam before the strain reached 10% approximately, since the curvature of the beam at the support and at the impact point was also very large. Nevertheless, strain-time history traces were recorded with strains up to 9%.

The following analysis of the experimental data is undertaken for the same impact velocity except in those cases when the impact

velocity is defined.

6.2.1 Strain-time history traces

The strain gauge signals which were recorded using DL1080 transient recorders were processed on a BBC microcomputer with an improved programme 'try 8'. Some processed strain-time history traces are shown in Figs. 64 and 82 to 84. It is clear that the strain at the support and at the impact point quickly grew and almost increased linearly in a short time after impact shown in Figs. 82, while the strain obtained from the middle strain gauges went through several cycles after impact and then increased steadily until the beam reached its maximum deformation shown in Figs. 64 and 83.

It was found that the strains at the support and at the impact point increased more quickly with the increase of the thickness of the beam, but the distinction was not large. The strain at the impact point and at the right-hand support was very sensitive to the value of ℓ_1 since the strain increased more quickly when the impact point was near the support. The strain at the impact point was larger than that at the support but the difference was less when the impact point close to the right-hand support. It might appear that the strain at the right-hand support is larger than that at the impact point when the impact point is close enough to the right-hand support. For the flat end aluminium beams, the tensile tearing failure generally started at the impact point when the value of ℓ_1 is large. However, with

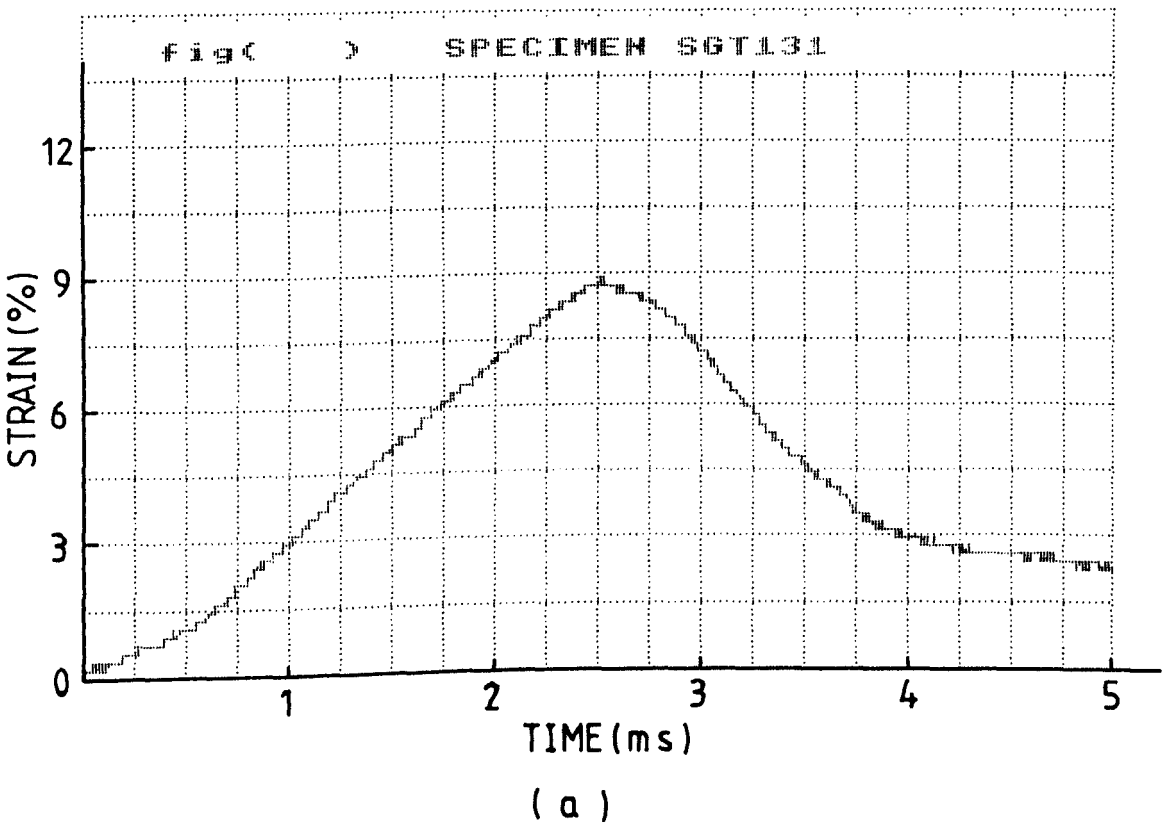

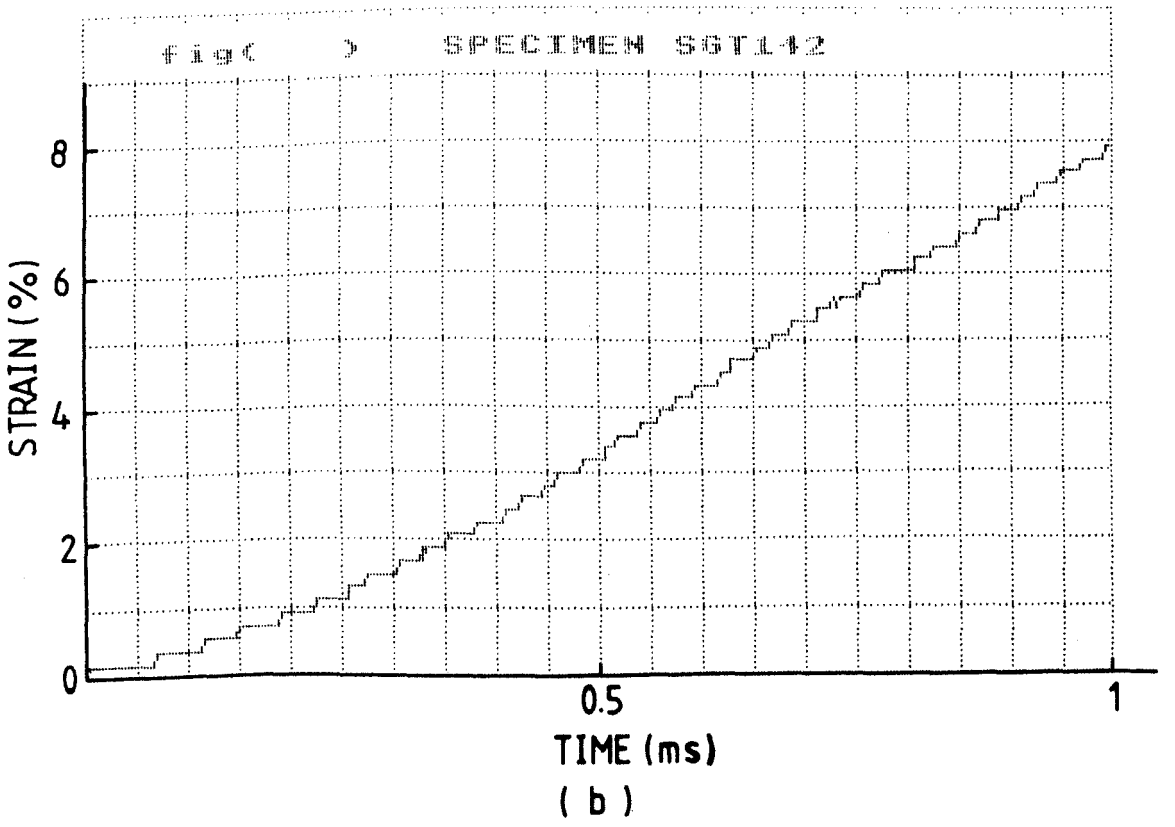

FIG. 82 Strain-time history traces at the support. (a) ℓ_1 = 2 in (50.8 mm), specimen No. AℓI16; (b) ℓ_1 = 1 in, specimen No. AℓIV24.

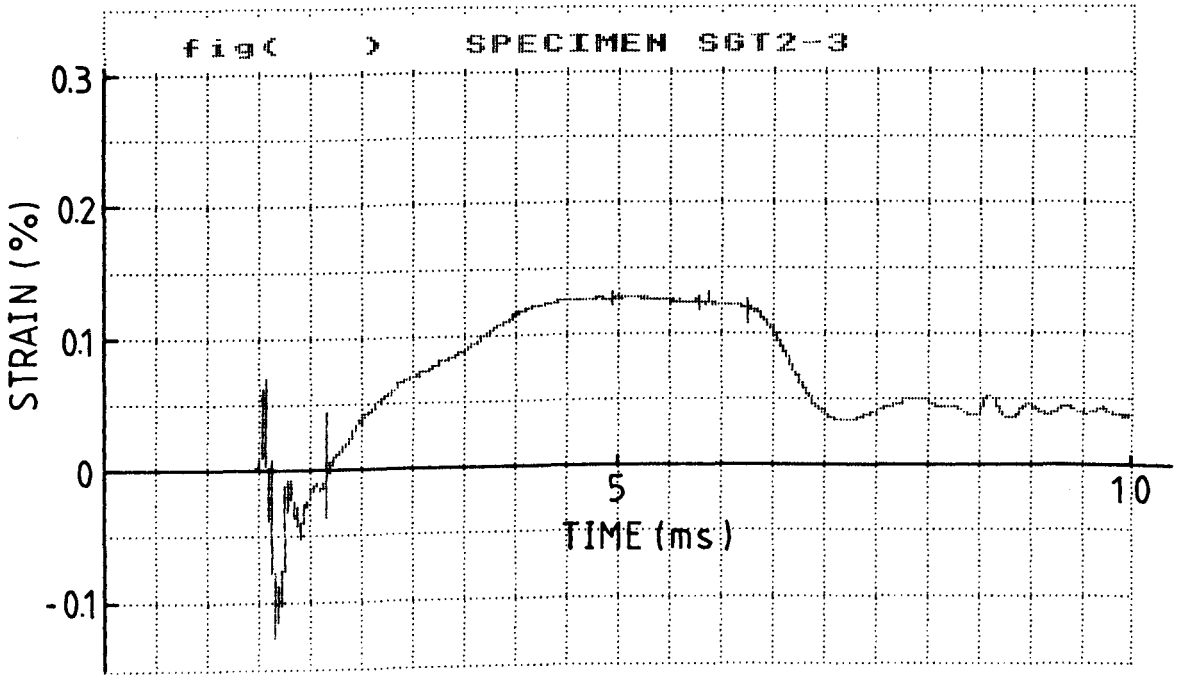

(a)

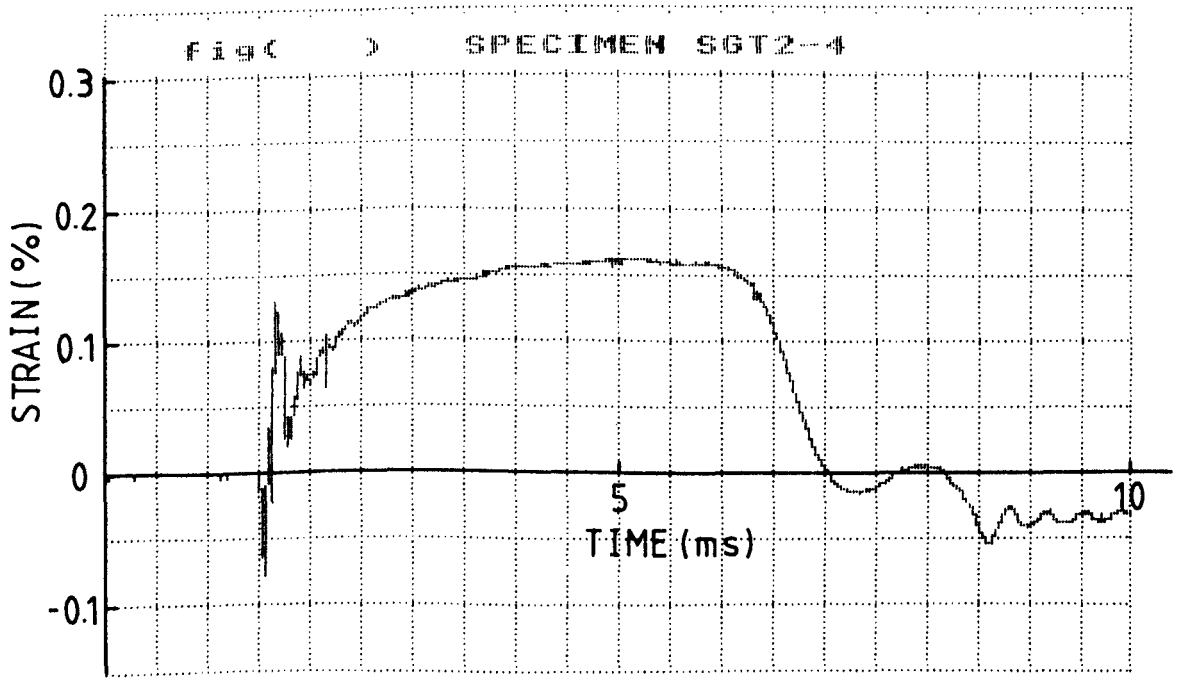

(b)

FIG. 83 Strain-time history traces obtained from middle strain gauges. The specimen No. was STI25 and impacted at ℓ_1 = 2 in (50.8 mm). (a) strain trace from upper surface strain gauge; (b) strain trace from lower surface strain gauge.

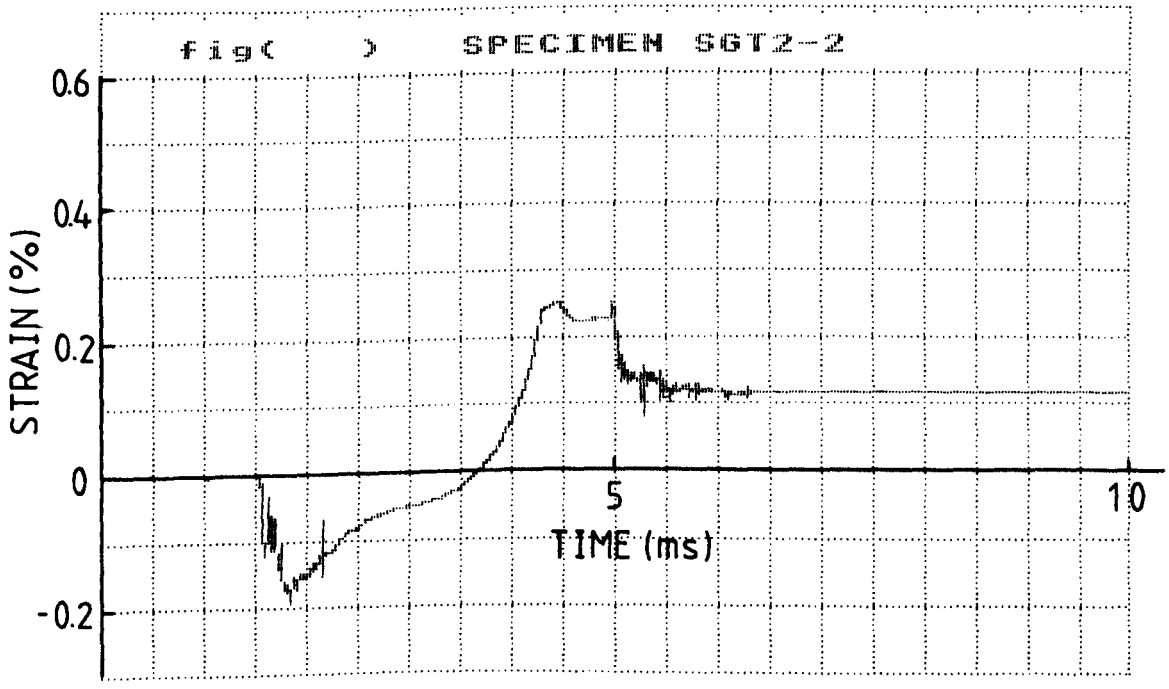

FIG. 84 Strain-time history traces obtained from the strain gauge at the support on the lower surface of the beam. Specimen No. STI25 and impact point ℓ_1 = 2 in (50.8 mm).

the decrease of ℓ_1, the tensile failure may start at the support (the phenomenon of beam failure will be discussed in the next section of this Chapter). At the impact point, the strain in the flat ended beams was similar to that in the large ended beams. However, at the support the strain in the flat ended beams, as expected, was larger than that in beams with enlarged ends since the positions of strain gauges at the support were different as shown in Figs. 62. For flat end beams the centre of strain gauges was exactly at the end of the beam section, while for beams with enlarged ends one end of a strain gauge was at the end of the beam section and, therefore, the measured strain was not the exact strain at the support.

A short time delay was found for the response of strain gauges situated at the supports and at the middle of the beam after the strain gauges at the impact point of the beam were stretched due to the impact of the tup. The duration of delayed time depended on the distance from the impact point. The longer the distance, the longer the delay duration. The duration of delay time for the strain gauge response is related to the propagation of the stress wave in the beam. The response of strain gauges at the supports was delayed about 20-80 microseconds when the impact point ℓ_1 = 2 in.

As previously stated, the first cycle of middle strain gauge traces was due to the travelling plastic hinge. The other cycles might be due to wave reflection in the beam. These cycles were similar for upper surface and lower surface strain gauges. It is evident that after the first cycle the strain gauge on the upper

surface of the beam was compressed and that on the lower surface was stretched as shown in Figs. 64 and 83. However, the strain on both upper surface and lower surface increased with the increase of time and depends on the beam thickness. It may be larger than zero for both upper surface and lower surface shown in Figs. 83. The situation in which the strain on both upper surface and lower surface is larger than zero was called a 'string stage'. (In theoretical analysis, 'string stage' means that not only the whole cross section of the beam is in tensile state but the membrane force in the cross section is equal to fully plastic membrane force of the cross section). It was found that for beams with thickness H of 3.81 mm (0.15 in) and 5.08 mm (0.2 in), the 'string stage' was associated with maximum deformation of 3~5 mm which were obtained by integrating the velocity-time history traces captured by the laser doppler velocimeter. The strain of the middle strain gauge on the thick beam 6.35 mm (0.25 in) and 7.62 mm (0.3 in) was negative on the upper surface of the beam throughout the entire response shown in Figs. 64. However, the value of the strain obtained from the middle strain gauges were very small compared with that at the support and at the impact point. It should be noted that not all cross-sections of the beam entered into a tensile state when both middle strain gauges were stretched. Figs. 83 and 84 show that during 2.2 ms, approximately, after impact the strain which was obtained from the strain gauge which is attached to the support on the lower surface of the beam was less than zero, while both middle strain gauges were stretched since about 0.7 ms after impact.

6.2.2 Strain rate

A short time after impact, the strain rate at the support and the impact point was nearly constant with time shown in Figs. 82. The average value of strain rate at the support was about 45 s^{-1} when the impact point ℓ_1 was 2 in and it may increase with the reduction of ℓ_1. There were no common values of strain rate obtained from middle strain gauges. However, the strain rate from the middle strain gauge traces was very small compared to that at the support and at the impact point (the difference is about two orders of magnitude).

From these ten test results it is difficult to estimate the strain and strain rate etc. for general cases of beams struck by the tup at any point, since there were so many types of test (total 50 types of tests were conducted) and even in the same type of test the strain and strain rate may be different with a different impact velocity. Furthermore, for the later motion of the beam the strain and strain rate at the support and at the impact point are still unknown because the strain gauges separated from the beam and the strain traces with strains over 9% were lost. Nevertheless, a lot of interesting phenomena did emerge from the data.

6.3 Failure of the Beam

Tables 2-5 show that after a test some beams cracked or broke at the supports or at the impact point. Both cracked and broken beams were considered as a beam failure due to the impact.

Of course, there is a difference between cracked and broken beams since dependent on the depth of the cracking through the beam thickness, the beam can absorb some more external energy before it totally breaks. However, this difference is small compared with the energy which the beam can absorb before cracking occurs, provided the thickness of the beam is not very large.

It was found that there were two ways of failure; one is that the cracking started from locations of the maximum tensile strain, i.e. the cracking started from the upper surface (impacted surface) of the beam at the supports or from the lower surface of the beam at the impact point shown in Figs. 85; the other one is that the cracking started from the upper surface of the beam at the impact point shown in Figs. 78 and 79. The first one was classified as tensile tearing failure and the latter one as shear failure* since the first one failed mainly due to bending moment or membrane force while the latter one failed mainly due to shear.

The tensile tearing failure had no regular broken sections and the broken position in the same layer of beam thickness had a large difference along the beam width, in other words, the broken section was convex-concave and was not in a same plane. While for the shear failure the broken section was in a plane and this

---

* The shear failure may occur at the supports for some special cases. Indeed, in preparation for the current test series, a wide beam impacted by a large tup (20 kg) exhibited a clear shear band and a large shear deformation at the support. The failure might have occurred along this shear band if the impact velocity were slightly higher.

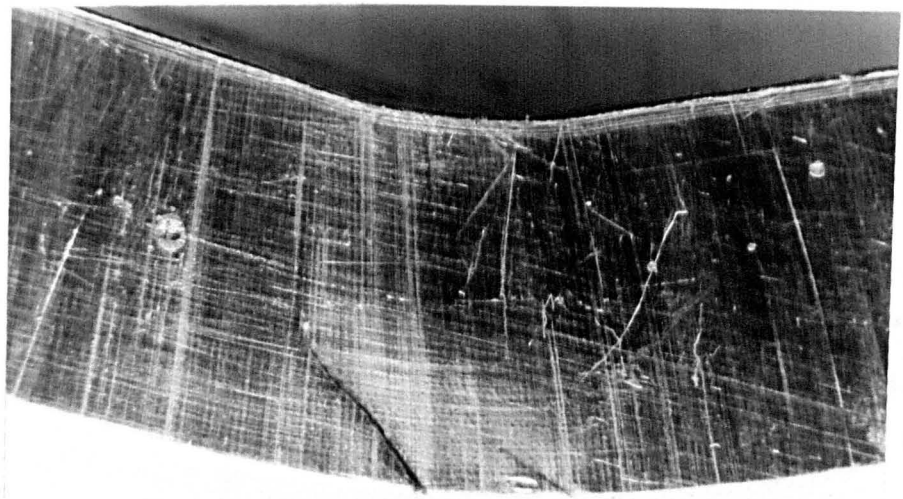

(a)

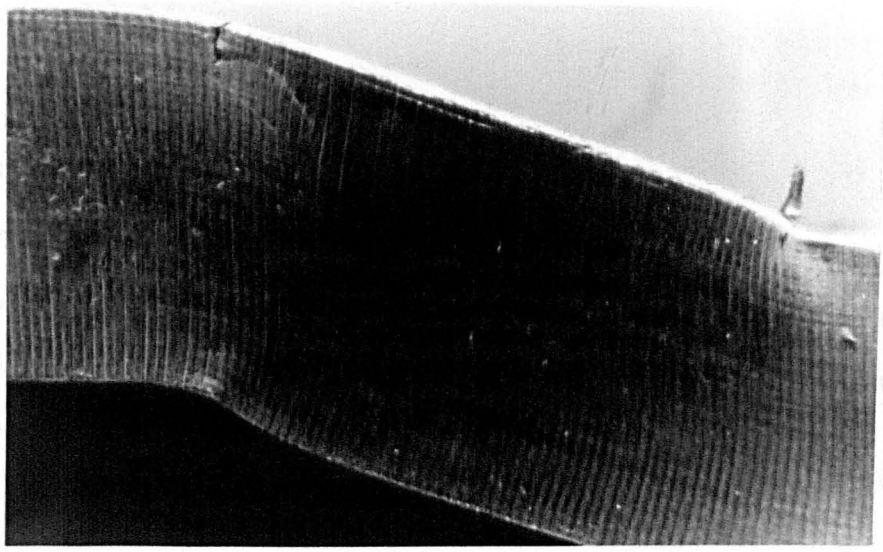

(b)

FIG. 85 Cracking due to tensile tearing.

(a) cracking at the impact point,

(b) cracking at the support.

plane was a cross section of the beam or made an angle of 45^{o} with the lateral axis of the beam, approximately.

It seems that the shape of broken section for tensile tearing failure was influenced by the direction of machining scores on the surfaces of the beam since the cracking of tensile tearing started along these machining scores except the tensile tearing failure occurred at the connection point between the beam section and the large end. After some 'plug' deformation the shear sliding and cracking occurred at the impact point and the machining score had no influence on the failure of shear. The 'plug' deformation was caused by the large concentrated compressive force between the tup and the beam at the impact point.

It should be noted that the shear failure defined herein may differ for some cases from that discussed in reference [29] and in other theoretical work [13-15, etc.]. In references [29] and [13-15], the shear failure is caused by the shear sliding between two adjacent transverse cross sections at one point of the beam and it is defined that the shear failure occurs when the shear sliding $W_s \geqslant kH$. However, shear failure according to the definition herein may be caused by the shear sliding along about 45^{o} direction to the lateral axis of the beam shown in Fig. 78 where the maximum shear stress occurred when the impact point near the centre of the beam. When the impact point was close to the support the phenomenon of shear failure was similar to that defined in references [29, etc.] shown in Fig. 79.

It was found that the type of failure depended on the impact point, clamping conditions and materials (mainly the fracture elongation of the material) of beams.

6.3.1 Flat end beams

A total of 40 types (200 specimens) of test were conducted on flat ended beams of aluminium alloy and steel. After testing, most of these types of test had at least one cracked or broken beam, especially for aluminium beams.

The flat ended aluminium beams generally failed due to tensile tearing except when the impact point was very close to the support. The location of tensile tearing failure changed from the impact point to the support with the reduction of ℓ_1. When the impact point ℓ_1 was 2 in, 1.5 in and 1.0 in the tensile tearing failure occurred at the impact point, while when ℓ_1 was 0.5 in the tensile tearing failure might occur at the impact point or at the support. The shear failure occurred at the impact point or the tensile tearing failure occurred at the support when the impact point ℓ_1 was 0.25 in or less than 0.25 in. It is clear that the shear failure may dominate the type of failure, provided the impact point is very close to the support.

Flat ended steel beams all broke or cracked at the impact point since the limit elongation of steel is much larger than that of aluminium alloy. But the angle of the broken section was different with different impact points. When the impact point was close to the support the shear sliding occurred between two adjacent transverse cross sections shown in Fig. 79, while when

the impact point was in the middle of the beam the shear sliding occurred along about 45^{o} direction to the lateral axis of the beam shown in Fig. 78.

6.3.2 Large end beams

60 enlarged end beams of aluminium alloy and steel were struck at the impact point ℓ_1 2 in (the centre of beam) and 0.5 in. The failure of enlarged end beams was different from the flat ended beams because of the effect of the end clamping conditions.

It is evident that large concentrated stresses may cause yielding at the connection point between the beam section and the enlarged end since the thickness of a specimen suddenly changes at this point, and large concentrated stresses may cause failure of beam at this point. Indeed, it was found that independent of the impact point ℓ_1 large end aluminium beams all cracked or broke at the support (the connection point) due to tensile tearing. Large end steel beams cracked or broke at the impact point due to shear when the impact point was near the centre of the beam, while for small ℓ_1 (0.5 in) the tensile tearing failure occurred at the support (the connection point).

6.3.3 In comparison with the static test

Six enlarged end and six flat ended beams of aluminium and steel were statically loaded in the Dartec testing machine at different points (ℓ_1 = 2 in, 1.0 and 0.5 in) until the beams cracked or broke.

It was found that the type of failure and the location of failure of dynamically loaded beams were the same as those of statically loaded beams which were stated in page 17 in Chapter 2.

6.3.4 Dynamic energy absorbed by cracked or broken beams

The dynamic energy which was absorbed by cracked or broken beams is plotted in Figs. 86-89. For some types of test, the maximum dynamic energy which was absorbed by beams which did not fail is also plotted in these figures.

Figs. 86 and 87 show that the absorbing energy capability of beams decreases sharply when the impact point was close to the support. However, this difference was small between ℓ_1 = 2 in and ℓ_1 = 1.5 in, especially for steel beams.

The variation of dimensionless parameter of dynamic energy $u = \frac{GV_0^2}{2M_0}$, which was absorbed by the beams which failed, with the dimensionless parameter $\frac{H}{\ell}$ is plotted in Figs. 88 and 89 for steel and aluminium alloy beams, respectively. Some maximum values for u which was absorbed by beams without failure is also plotted in these figures. It shows that the absorbing non-dimensional energy capability of beams decreased with the increase of beam thickness and this capability decreases sharply when the impact point ℓ_1 was 2 in and 1.5 in. However, it should be noted that the actual energy $E = \frac{GV_0^2}{2}$ which was absorbed by beams increased with the increase of beam thickness H since the limit plastic bending moment M_0 is the square function of H.

Some approximate curves from the experimental results are

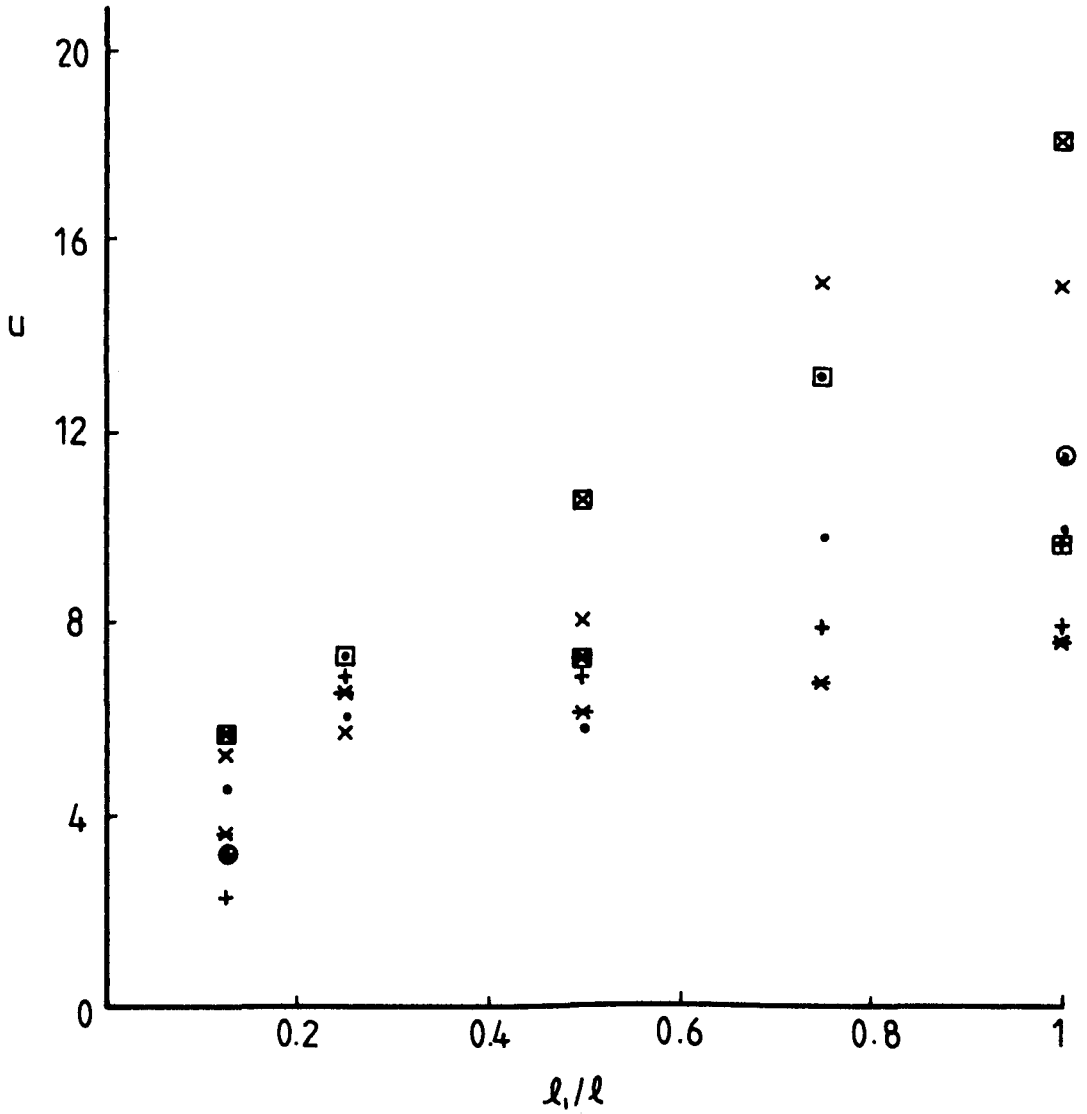

FIG. 86 Variation of dynamic energy u, which was absorbed by flat end steel beams, with the impact point ℓ_1/ℓ, where $\ell = \frac{1}{2}(\ell_1+\ell_2)$ is the half span of the beam. The thickness of the beam; × - H = 0.15 in, • - H = 0.2 in, + - H = 0.25 in, ✱ - H = 0.3 in. □ ; broken beams, ○ ; cracked beams, otherwise, beams without failure.

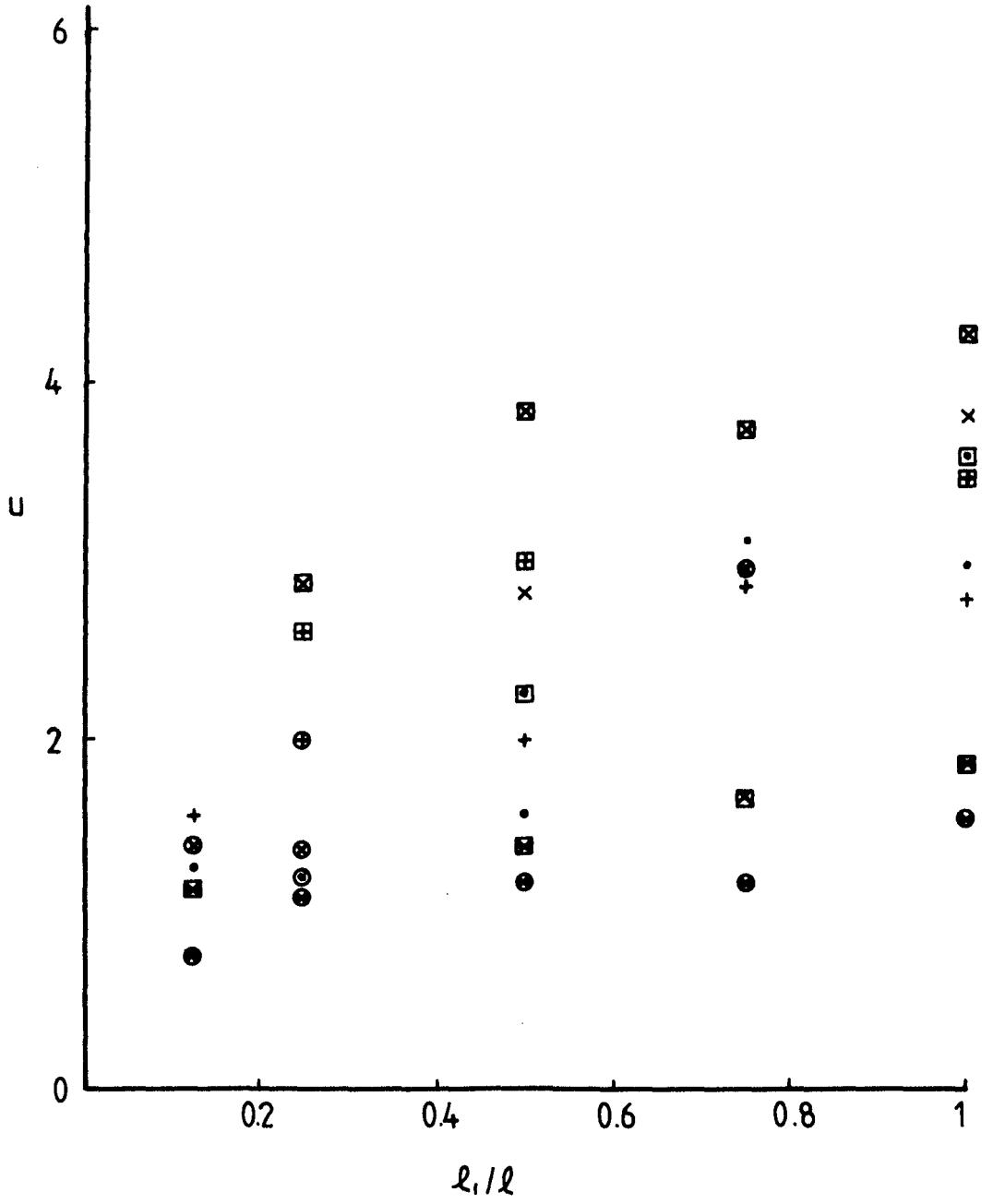

FIG. 87 Variation of dynamic energy u, which was absorbed by flat end aluminium beams, with the impact point ℓ_1/ℓ. The symbols are the same as that in Fig. 86.

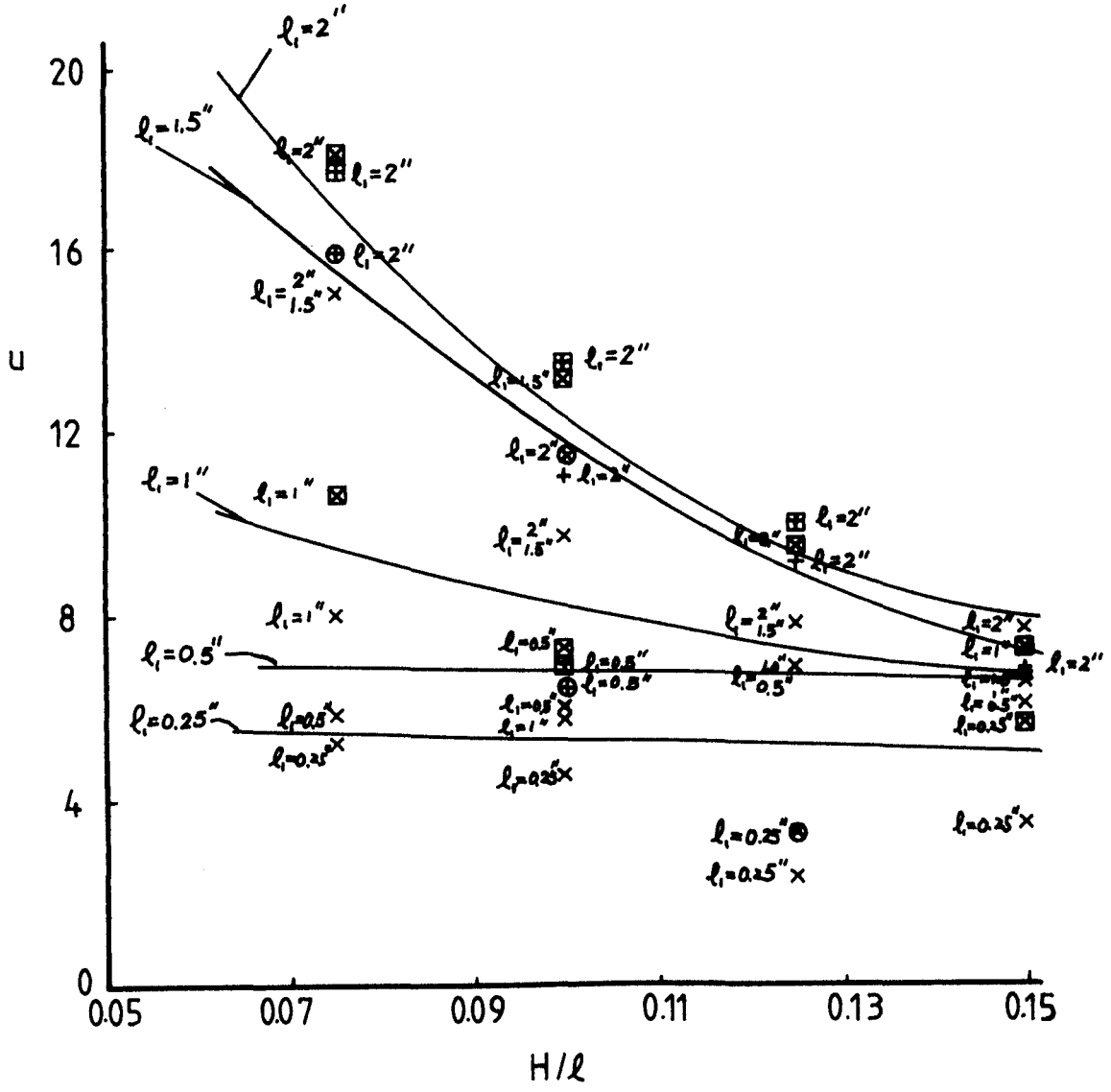

FIG. 88 Variation of dynamic energy u, which was absorbed by steel beams, with the beam thickness H/ℓ. × - flat end beams, + - large end beams. □ ; broken beams, ○ ; cracked beams, otherwise, beams without failure. The curves are the approximate value of dynamic energy which may be absorbed by beams until failure.

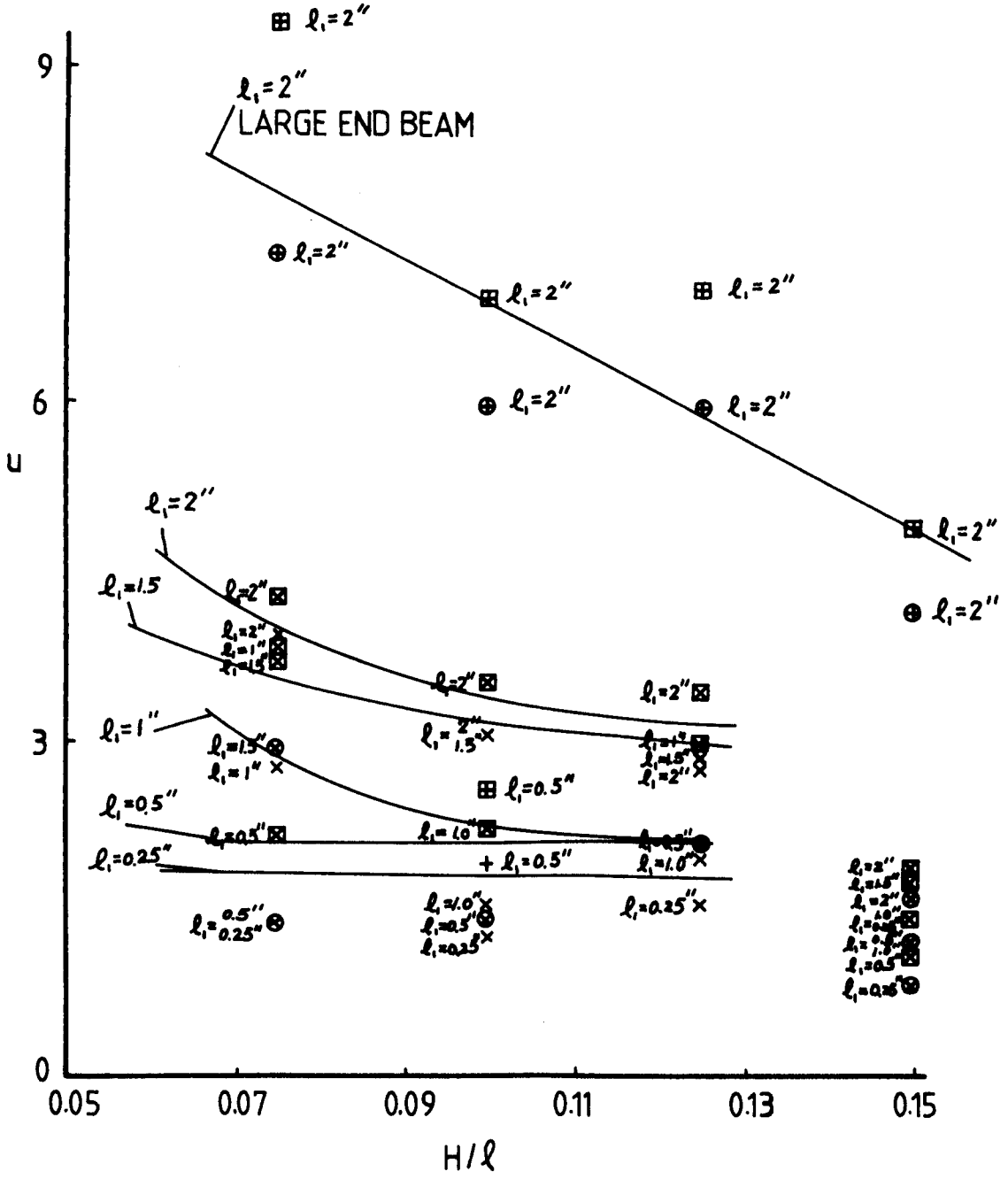

FIG. 89 Variation of dynamic energy u, which was absorbed by aluminium alloy beams, with the beam thickness H/ℓ. The symbols are the same as that in Fig. 88.

drawn in Figs. 88 and 89. These curves give the approximate value of dynamic energy, which can be absorbed by beams until failure, for different beam thickness. The flat end beams with thickness H = 0.3 in were made from a different piece of material as shown in Table 1 and the absorbing energy capability is therefore lower than that of the other flat end beams shown in Fig. 89.

CHAPTER 7

COMPARISON AND DISCUSSION

The bending only solution of a clamped beam struck by a mass at any point of its span was examined by Parkes [10]. It is found in Chapters 3 and 4 of this thesis that according to the rigid-plastic yield condition some yield violations may occur near the impact point where a stationary plastic hinge is assumed. Therefore, in these cases the velocity profiles assumed in reference [10] may not be valid. Nonaka's examination [12] of a clamped beam subjected to an impulsive loading on a concentrated mass at the centre of a beam can be used for the analysis of a clamped beam with a uniform cross section struck by a mass at the centre. The interaction effects of bending moment, membrane force and shear force were considered in reference [12]. Nonaka also considered the influence of strain-rate sensitivity using the Cowper-Symonds empirical expression. Oliveira [15] discussed the shear and bending response of a clamped and a simply supported beam struck by a mass at the centre. He found that when $L \leqslant \lambda(T_1)$, where L, λ and T_1 are defined in reference [15] and $\lambda(T_1)$ can be obtained from equation (15) in reference [15], a shear violation might occur at the supports of the clamped beam and the response of clamped beam would follow a different pattern from that assumed in reference [15]. However, these cases had been omitted in reference [15] since most practical cases have $L > \lambda(T_1)$. Some approximate approaches for examining the dynamic response of

a clamped beam struck by a mass have also been developed in references [20,30].

The theoretical investigation of a clamped beam struck by a mass at any point of its span has been extended to cater for transverse shear and bending response and finite deflection effects which are presented in Chapters 3 and 4 of this thesis, respectively. The interaction effect of bending moment, shear force and membrane force corresponding to a cubic shaped yield surface, which is combined with Fig. 9c and Fig. 42d in this thesis and is similar to Figs. 1 in reference [12], may be obtained in a simple way of combining Chapter 3 with Chapter 4 when the membrane effect is neglected in the shear sliding phases, since the influence of transverse shear forces is important, while the influence of membrane forces is not important, in the early stage of motion when the displacement of the beam remains small [45]. New velocity profiles with a moving plastic bending hinge near the impact point instead of a stationary hinge at the impact point are assumed in Chapters 3 and 4 of this thesis when a bending violation occurs near the stationary hinge at the impact point. These cases were not discussed in reference [10]. The theoretical prediction of threshold external dynamic energy for the onset of plastic failures of tensile tearing and shear sliding of a clamped beam struck by a mass at any point of its span has been discussed in Chapter 5 of this thesis. It appears, according to author's knowledge, that nobody has discussed this problem before except Jones [29] who examined the threshold velocity for onset

of plastic failures of a clamped beam subjected to a uniformly distributed impulsive loading.

Parkes [10] conducted some experimental tests on clamped beams without axial restraint struck by a heavy striker (4 lb.) and a light striker (0.005 lb.) at three different points with r = 0.2, 0.5 and 1 ($r = \ell_1/\ell_2$)*. The ratio r of the lengths of the two parts of the beam varied with the increase of one length (ℓ_2) while the other (ℓ_1) (short one) remained 2 in (some other tests with the length ℓ_1 = 1 in were reported by Parkes in reference [60]). The beam specimens with the same dimensional cross section were made of three different materials - steel, brass and dural. A total of 21 test results was reported in reference [10]. Only one test was performed on each type of test (same impact point, same striker mass and same beam specimen are classified as one type of test). Nonaka [12] conducted some experimental results on clamped beams with or without axial restraint subjected to blast loading at a central concentrated mass. As in his theoretical analysis, these experimental tests may be considered as clamped beams struck by a striker at the centre when the central concentrated mass is equal to the striker mass and the total explosive impulse acted on the central mass is equal to the initial impact momentum of the striker. A total of

---

* The definitions of ℓ_1 and ℓ_2 in this thesis is different from that in reference [10]. In reference [10], ℓ_2 is the length of the short part of the beam while ℓ_1 is the length of the longer part of the beam. However, the definition of ℓ_1 as short length and ℓ_2 as longer length are employed in the whole of this thesis.

30 beam specimens of steel and aluminium alloy was reported in reference [12] and only one test was performed for most types of test. In reference [10] the span of the beam varied from 4 in to 12 in, while in reference [12] the width of the beam varied from 0.47 in to 1.15 in. However, only one beam thickness was used in both references [10] and [12]. It appears that the external dynamic energy which acted on the beam was not very large in references [10,12] in comparison with the maximum energy which can be absorbed by the beam without failure and no failed beams were reported in either of these papers. Furthermore, only the permanent deformation of the beam were reported in references [10,12].

A total of 260 steel and aluminium alloy beam specimens with different impact points (r = 0.067, 0.143, 0.333, 0.6 and 1) were conducted in the Department of Mechanical Engineering at Liverpool University and the experimental results are mainly reported in Chapter 6 of this thesis. The thickness of beam specimens is H = 0.15 in (3.81 mm), 0.2 in (5.08 mm), 0.25 in (6.35 mm) and 0.3 in (7.62 mm). At least 4 tests with different impact velocities were performed for most types of test.

Experimental data, including motion of the beam, strain-time history at some special points, forces between the striker and the beam and permanent deformation, etc., were recorded or processed and these data are discussed in Chapter 6. The comparison between Parkes', Nonaka's experimental test programmes and that reported in this thesis is shown in Table 6.

		Parkes' [10]	Nonaka's [12]	Those reported in this thesis
Test details	Dimension of beam specimens	2ℓ=4, 6 and 12in B=0.25 in H=0.25 in	2ℓ=3.3 in B=0.47 - 1.15 in H=0.11 in	2ℓ=4 in B=0.4 in H=0.15 - 0.3 in
	Material	steel, brass and dural	aluminium alloy and steel	aluminium alloy and steel
	Boundary condition and clamping condition	flat ended beams without axial restraints	flat ended beams without axial restraints and enlarged end beams with axial restraints	flat ended and enlarged end beams with axial restraints
	Impact point	r=0.2, 0.5 and 1	r=1	r=0.067, 0.143, 0.33, 0.6 and 1
	No.of tests for each type of test	1	1 or 2 specimens were tested for most types	for most types of test, at least 4 beams were tested
	Mass of striker	0.005 lb and 4 lb	the ratio of mass g=10	5 kg
	External dynamic energy	moderate	from lower to moderate	from lower to very high
	Total No. of tested specimens	21	30	260
Experimental data presented		only maximum permanent deformation and some permanent deformation profile photos	Max. permanent deformation and some permanent deformation profile photos	a quantity of experimental data have been recorded, processed and measured during the test and after the test which are given and discussed in Chapter 6 of this thesis

Table 6. Comparison of Experimental Tests on Clamped Beams Struck by A Falling Mass.

7.1 Deformation of the Beam

The theoretical analysis which is presented in Chapter 4 shows that when the mass ratio g is very small ($g/r^2 \ll 1$) the deformation of the beam which is yielded in the phases with moving plastic hinges is very small and almost all of the external dynamic energy is absorbed in the last phase of motion in which two parts of beam rotate as rigid bodies about the supports. In these cases, the maximum permanent deformation occurred at the impact point can be approximately expressed as

$$\bar{W}_{0f} = \frac{1}{2\gamma}\left[-1 + \sqrt{1 + \frac{2u\gamma}{(1+r)}}\right]$$

or

$$\frac{W_{0f}}{H} = \frac{1}{2}\left[-1 + \sqrt{1 + \frac{8\lambda}{(1+r)}}\right] \qquad (7\text{-}1)$$

for beams with rectangular cross-sections where $N_0 = BH\sigma_0$ and $M_0 = \frac{1}{4} BH^2 \sigma_0$. Therefore, the maximum permanent deformation $W_{0f/H}$ only depends on the two parameters λ and r. However, when the mass ratio is not small the maximum permanent deformation may depend on the thickness of the beam since g will remain in equation (7-1). This phenomenon can also be observed from the experimental results. The experimental data plotted in Figs. 66-70 lay in narrow regions although the beam thickness is different. However, these data might be more discrete if the mass ratio g were not small. Figs. 66-70 show that equation (7-1) gives fair agreement with the experimental results, especially for aluminium beams with impact point at ℓ_1 = 2 in, 1.5 in and 1 in, while for steel beams the strain rate effect should be considered.

The comparison of maximum permanent deformation predicted by the theoretical analysis and some experimental results are shown in Figs. 90 and 91 (the comparison of the maximum permanent deformation between theoretical analysis and all of the experimental results is shown in Figs. 66-70). It is clear that the difference between the bending only solution and the experimental results is very large when the external dynamic energy is large. However, the theoretical analysis which retains the influence of finite deflections gives good agreement with the experimental results, especially for the aluminium beams. The theoretical lower and upper bound solutions do bound most of the experimental data as shown in Figs. 90 since aluminium is essentially strain rate insensitive at the usual strain rates encountered in practice [42].

It is well-known that mild steel is more sensitive to strain rate. Therefore, the Cowper-Symonds empirical expression

$$\sigma_0' = \sigma_0[1 + (\dot{\varepsilon}/D)^{\frac{1}{p}}] \qquad (7\text{-}2)$$

is employed to revise the theoretical solution, where D and p are equal to 40.4 s^{-1} and 5 [7,8,10, etc.], respectively. It is assumed that the strain rate is a constant in the entire response of the beam and is equal to 45 s^{-1} which was obtained from experimental results in early response of strain gauges (corresponding to the strain less than 9%)*. Therefore, the

---

* One could also use the functions given in references [7,40,45, etc.)

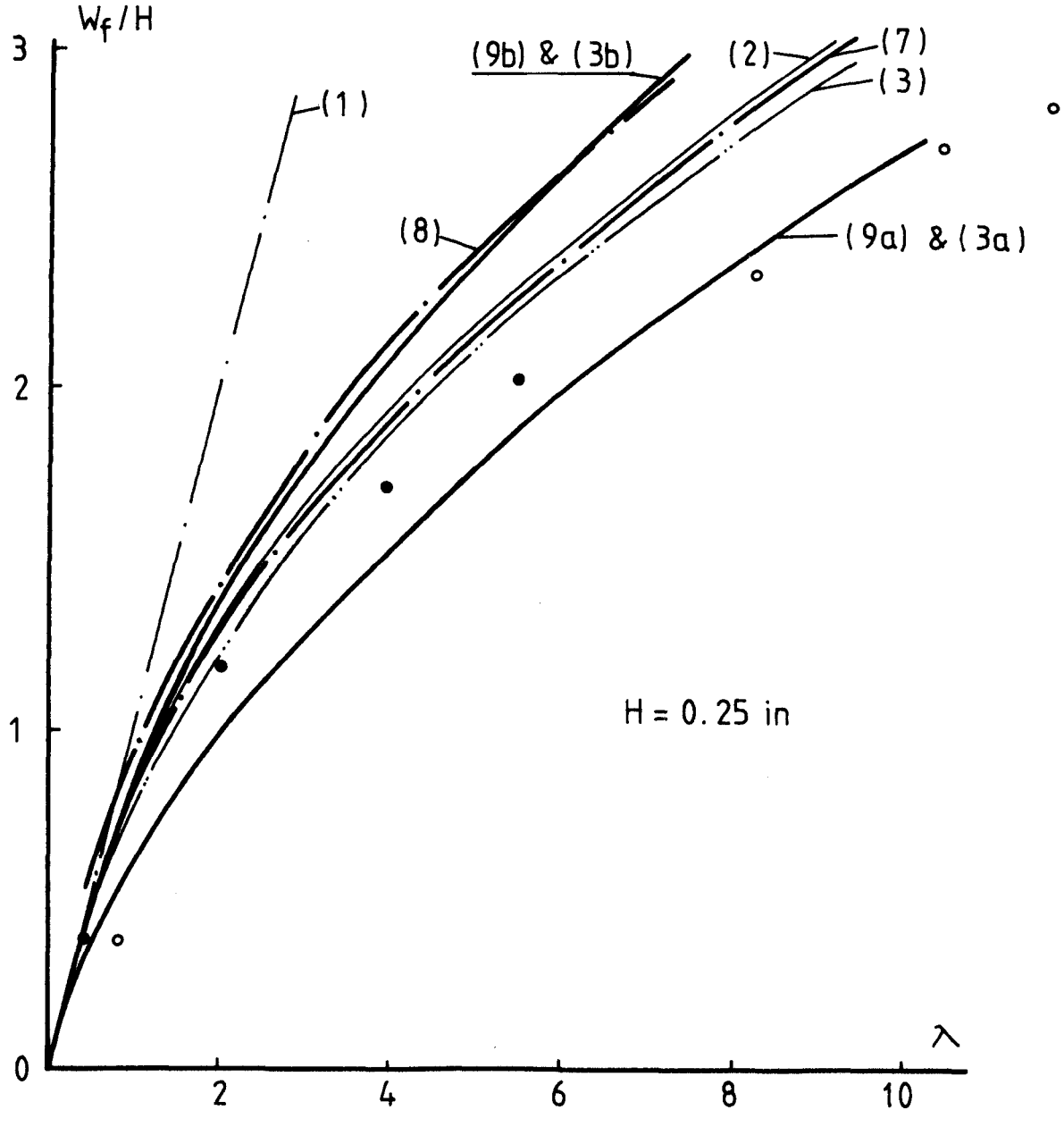

FIG. 90a Variation of maximum permanent deformation $\frac{W_f}{H}$ with external dynamic energy λ for aluminium alloy beams when the impact point ℓ_1 = 2 in (50.8 mm). The symbol (X) indicates that the curve corresponds to the equation (X) given in Appendix II. ● ; experimental results of flat end beams, o ; experimental results of large end beams.

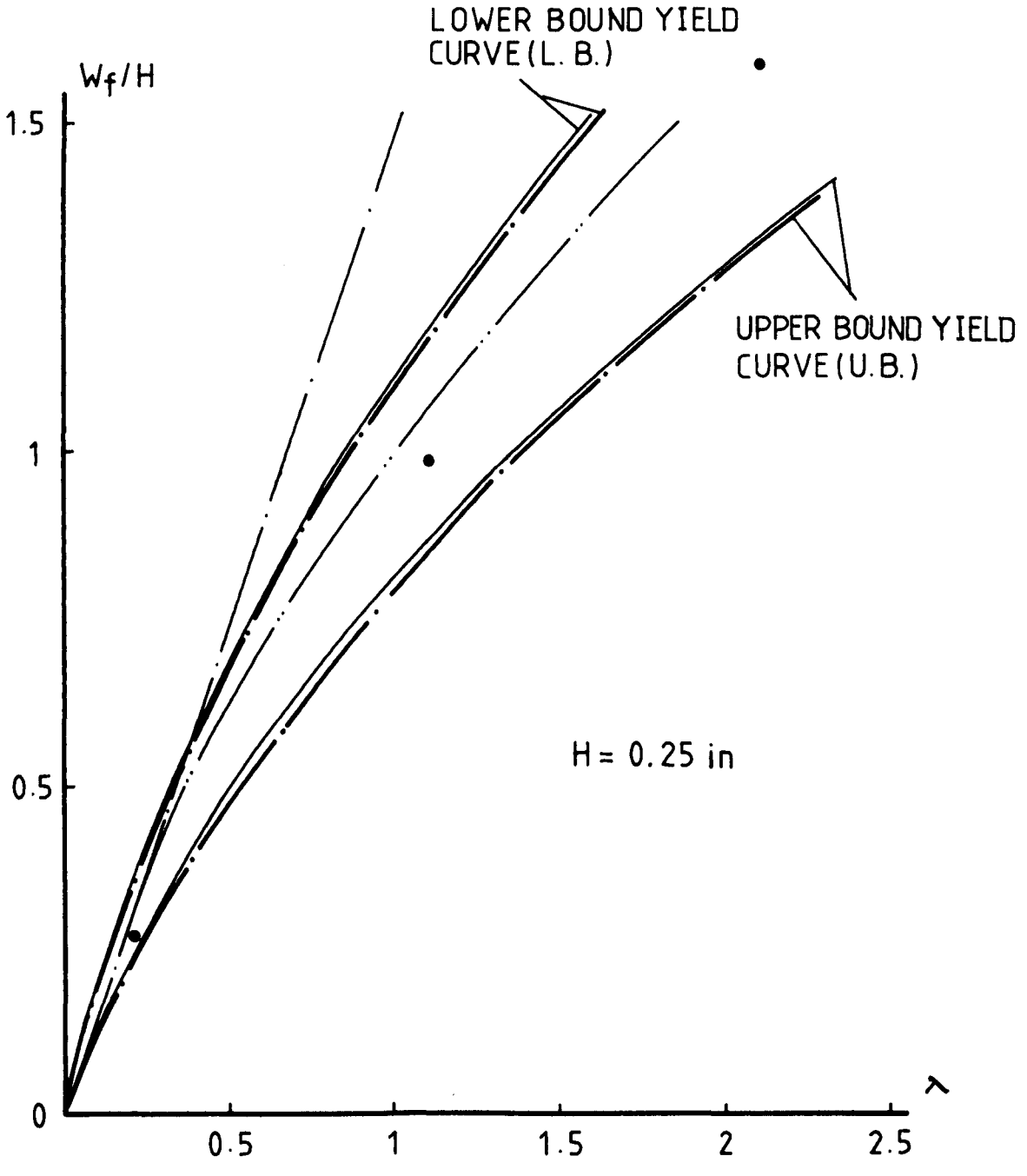

FIG. 90b Variation of W_f/H with λ for aluminium alloy beams when the impact point $\ell_1 = 1$ in (25.4mm). ——·—— ; bending only solution of Ref. [10], ——··—— ; equation (1) Of Ref. [30], ——··—— ; obtained from Ref. [17] with parabolic yield curve, ———— ; obtained from Chapter 4 of this thesis.
● ; experimental results of flat end beams.

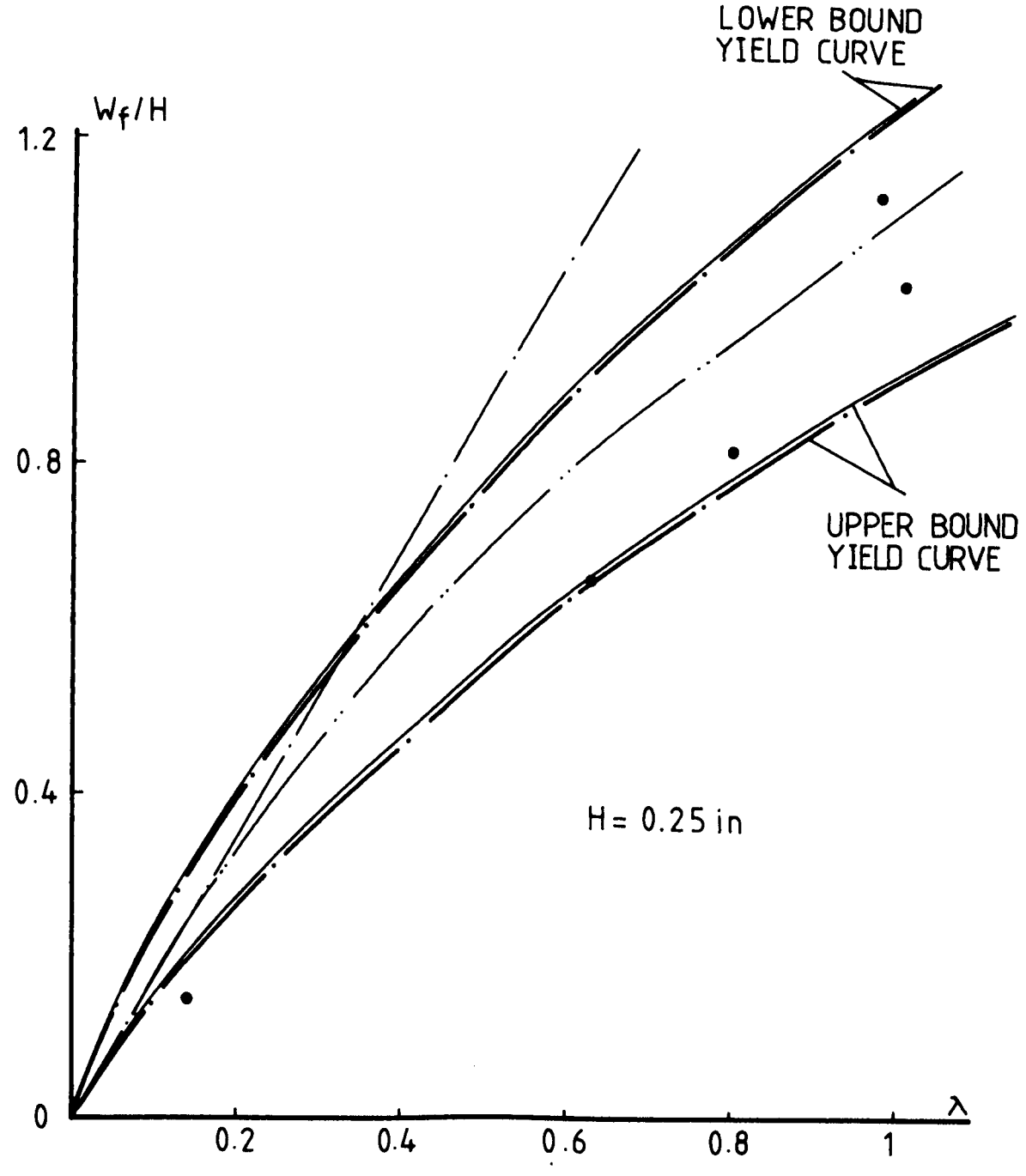

FIG. 90c Variation of $\frac{W_f}{H}$ with λ for aluminium alloy beams when the impact point ℓ_1 = 0.5 in (12.7 mm). See definitions in Fig. 90b.

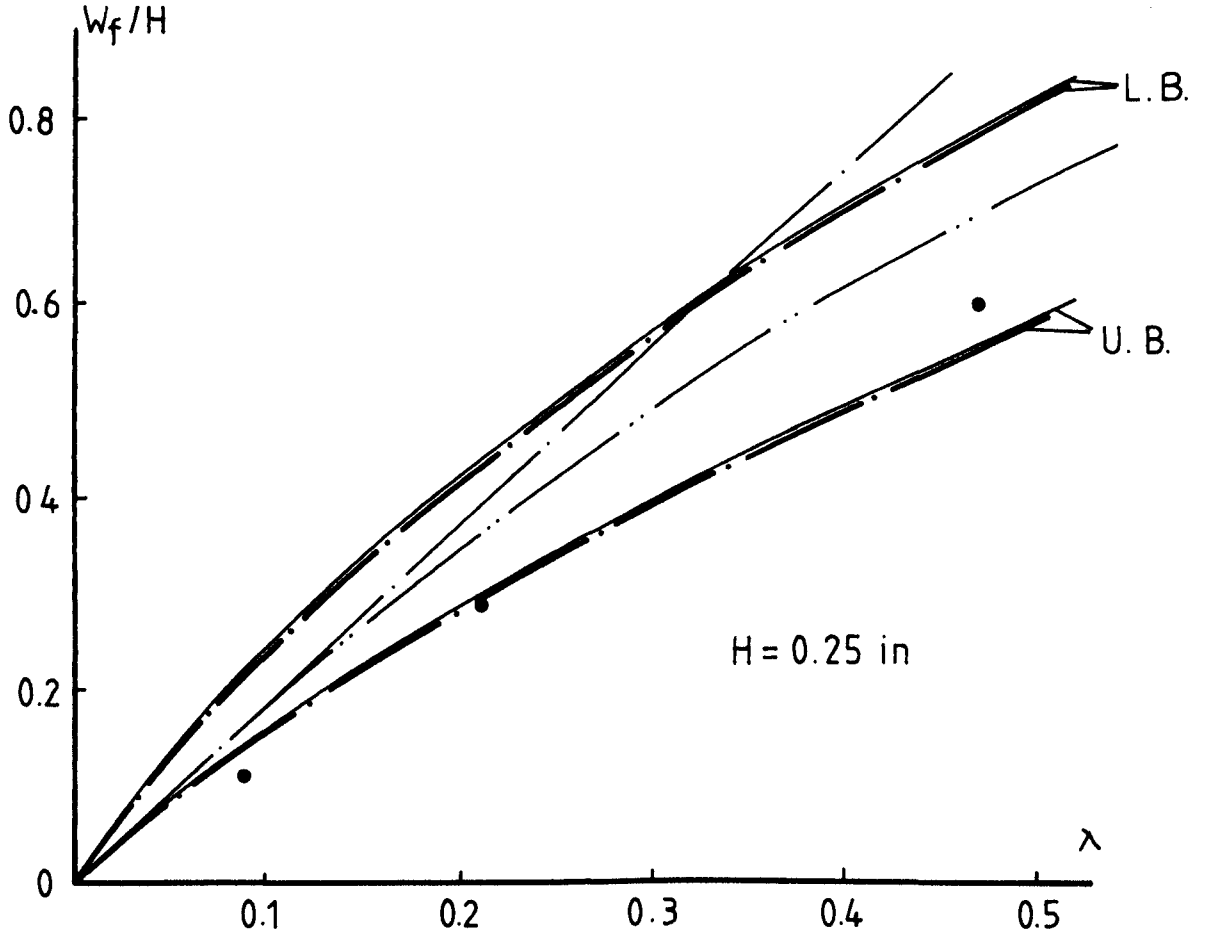

FIG. 90d Variation of $\frac{W_f}{H}$ with λ <u>for aluminium alloy beams when the impact point ℓ_1 = 0.25 in (6.35 mm)</u>. See definitions in Fig. 90b.

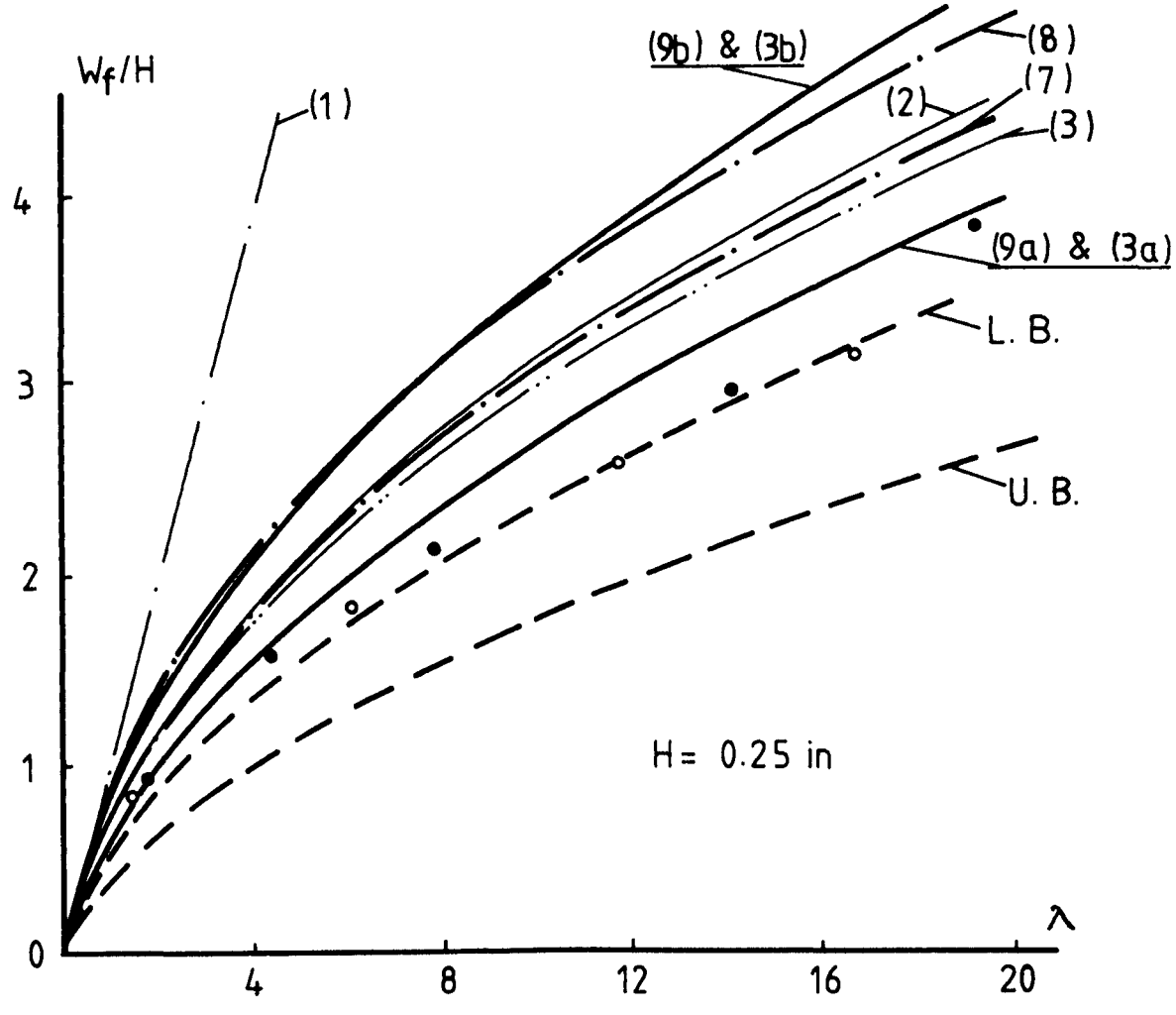

FIG. 91a Variation of maximum permanent deformation $\frac{W_f}{H}$ with external dynamic energy λ for steel beams when the impact point ℓ_1 = 2 in (50.8 mm). The symbol X indicates that the curve corresponds to the equation (X) given in Appendix II.

----; equation (9) in Appendix II with dynamic yield stress σ_o' given by equation (7.3). • ; experimental results of flat end beams, o ; experimental results of large end beams.

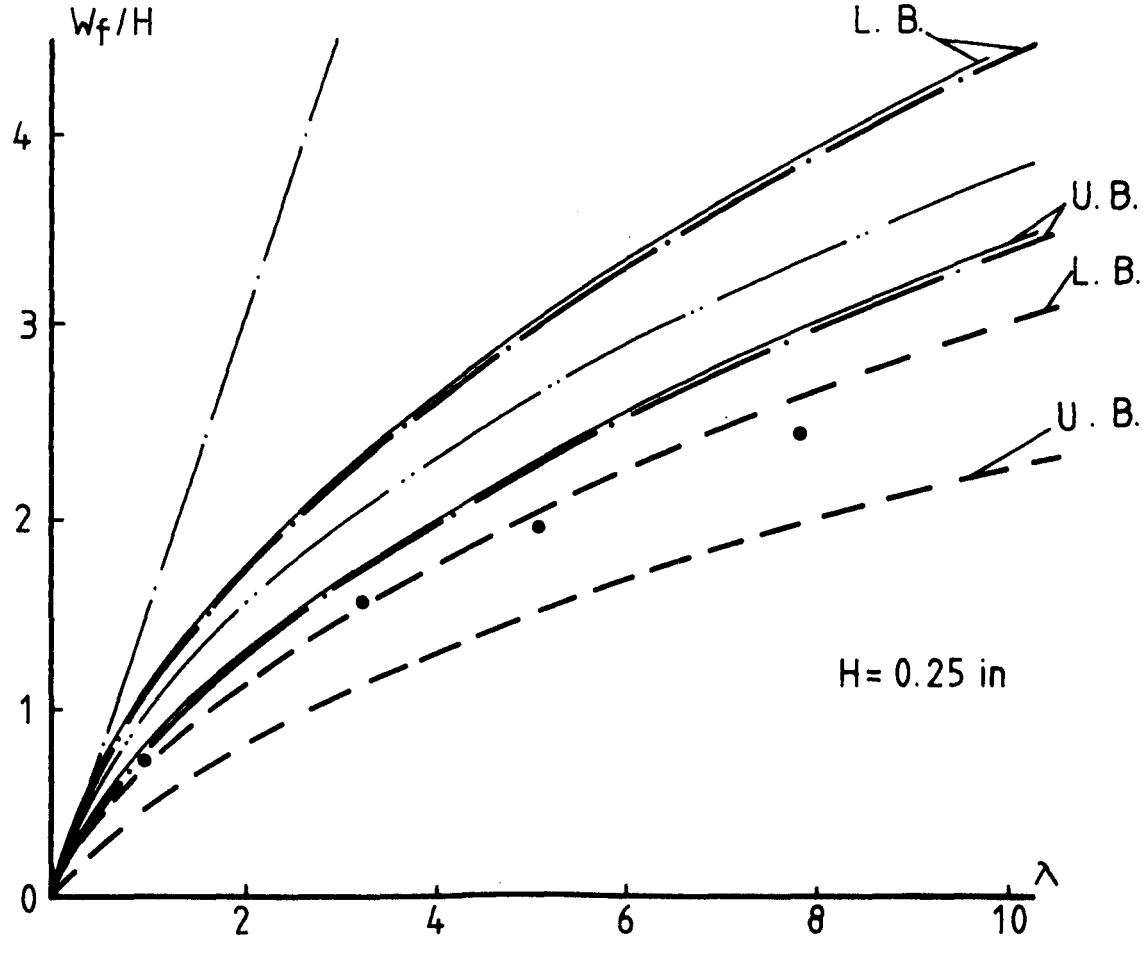

FIG. 91b Variation of W_f/H with λ for steel beams when the impact point $\ell_1 = 1$ in (25.4mm). ——·——; bending only solution of Ref [10], ——·——; equation (1) of Ref. [30], ——··——; obtained from Ref. [17] with a parabolic yield curve, ————; obtained from Chapter 4 of this thesis with static yield stress σ_0, — — —; obtained from Chapter 4 with dynamic yield stress σ_0' given by equation (7.3).
● ; experimental results of flat end beams.

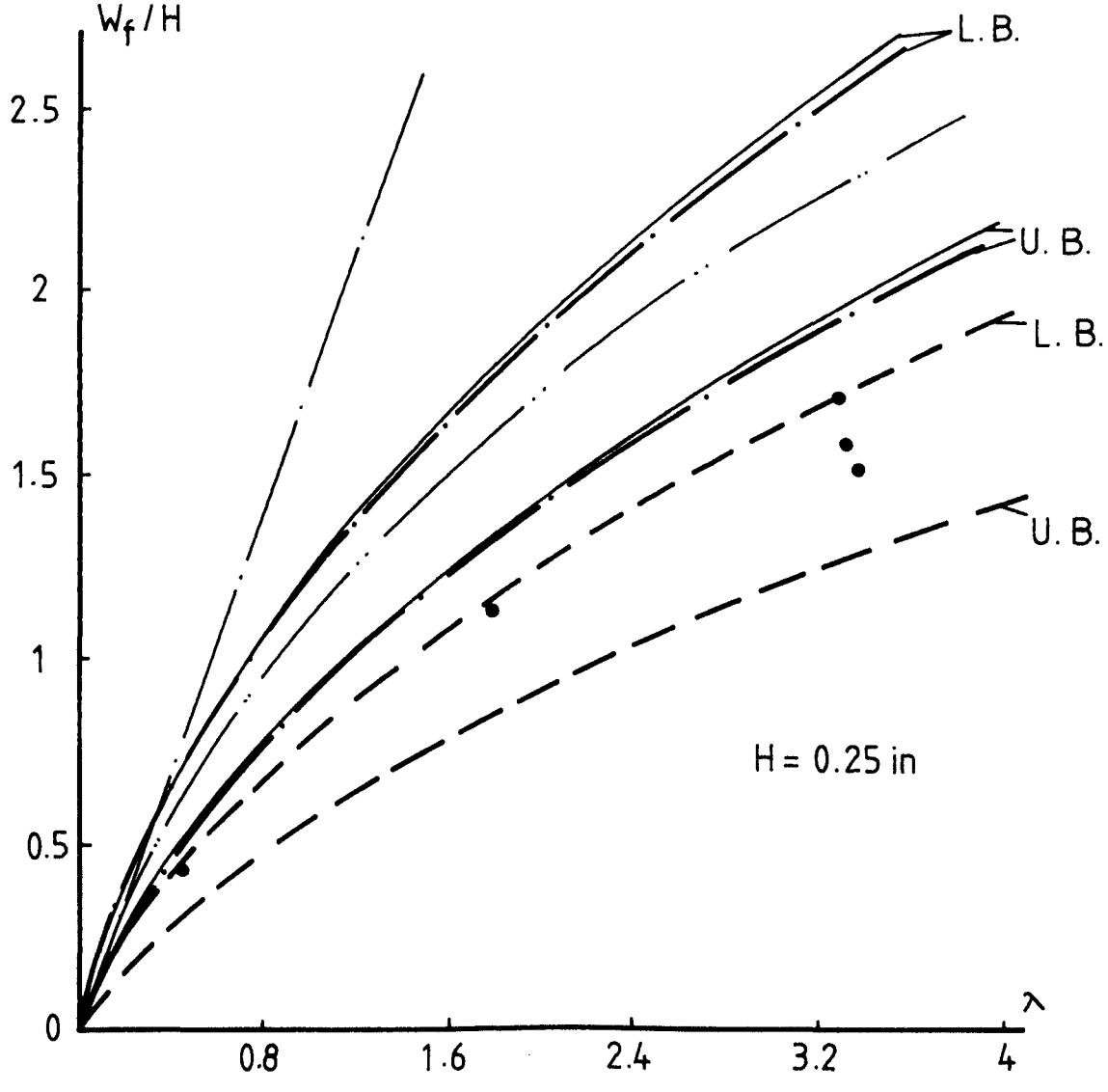

FIG. 91c Variation of $\frac{W_f}{H}$ with λ for steel beams when the impact point ℓ_1 = 0.5 in (12.7 mm). See definitions in Fig. 91b.

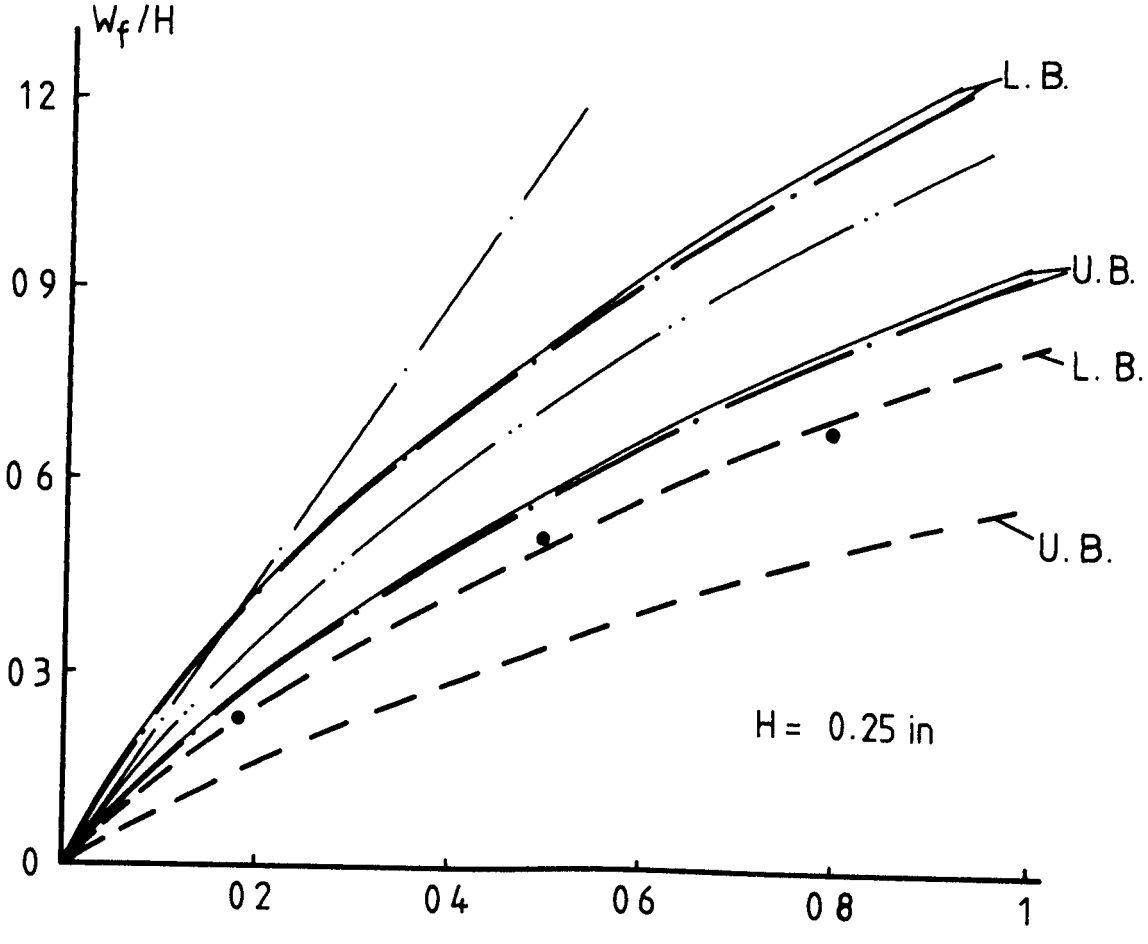

FIG. 91d Variation of $\frac{W_f}{H}$ with λ for steel beams when the impact point ℓ_1 = 0.25 in (6.35 mm). See definitions in Fig. 91b.

dynamic yield stress of steel is

$$\sigma_0' = [1 + 1.0218]\ \sigma_0 = 2.0218\sigma_0. \qquad (7\text{-}3)$$

The revised results are plotted in Figs. 91 using a dashed line. It is evident that the revision of strain rate effects is slightly higher because the strain rate may be less than 45 s^{-1} for later response of the beam. However, it is found that the experimental results agree surprisingly well with the revised upper bound theoretical solution (corresponding to the lower bound yield curve with $\sigma_{0.618} = 0.618\sigma_0$ shown in Fig. 42c). Therefore, good agreement between experimental results and theoretical solution in Chapter 4 will be obtained if the static yield stress σ_0 obtained from static tensile test is replaced by $\sigma_{0.618}$ in equation (7-3), i.e. the dynamic yield stress

$$\sigma_0' = 2.0218 \times 0.618\sigma_0 = 1.249\sigma_0. \qquad (7\text{-}4)$$

It appears from Figs. 91 that the strain rate with lower impact velocity may be less than 45 s^{-1} corresponding to the impact velocity $V_0 = 7.3932$ ms^{-1}, while the strain rate with higher impact velocity may be higher than 45 s^{-1}, since the experimental results with lower impact velocity are larger and those with higher impact velocity are less than the revised upper bound theoretical solution with strain rate 45 s^{-1}. However, this difference is small.

The deformation profile for most of the beam specimens consists of two almost straight parts as shown in Figs. 73-76. This phenomenon also agrees with the theoretical analyses in

Chapters 3 and 4. When the mass ratio g is small, as previously stated, the phase of motion with travelling plastic hinges are very short in the theoretical analysis and almost all of the external dynamic energy is absorbed by a final phase of motion in which two parts of the beam on either side of the impact point rotates as rigid bodies. Therefore, approximate methods in which the phases of motion with travelling hinges are neglected, like equation (7-1) and equation (1) in reference [30] etc., can estimate not only the maximum permanent deformation, as previously stated, but also the deformation profile of the beam except for those points near the impact point and the supports where the curvature of the beam is large, provided the mass ratio g is small. However, when the mass ratio is not small the phases of motion with travelling plastic hinges may play an important role and the deformation profile of the beam may not be linear (the corresponding experimental results with a light striker (0.005 lb.) can be seen in Figs. 15, 16 and 21 in reference [10]). Now, more complex equations in Chapter 4 have to be solved and sometimes even a numerical method is required to solve differential equations (4-32) and (4-36) if a plastic hinge near the impact point moves.

7.2 Failure of Beams

When a structure is subjected to a high intensity and short duration dynamic loading, large plastic deformations are developed in the structure and absorb this external dynamic energy. However, with further increase of the external dynamic

energy the structure may fail due to tensile tearing since a real material has a limited tensile elongation [29], or fail due to transverse shear when the shear sliding reaches some proportion of the thickness of the structure [29]. Of course, the structure may also fail due to the combination of tensile forces and transverse shear.

The theoretical analysis of tensile tearing and shear failure of a clamped beam struck by a mass at any point of its span is discussed in Chapter 5 of this thesis. It appears that the type of failure may change from tensile tearing failure to shear failure with the increase of the limit elongation ε_m of material or with the decrease of the distance ℓ_1 from the impact point to the support. This phenomenon agrees with the experimental test results which is mentioned in Chapter 6. The aluminium beams (with lower value of ε_m) failed due to tensile tearing except some tests with the impact point very close to the support. The steel beams failed with a different type of failure except enlarged end beams with impact point ℓ_1 = 0.5 in or 0.75 in* since flat ended beams and enlarged end beams were made of different materials and the enlarged end beams have a lower value of ε_m (0.31) (the concentrated stress at the connection between beam section and enlarged end may also have an influence on the beam failure).

The comparison of tensile tearing failure between

---

* For enlarged end beams, the impact point ℓ_1 was nominally 2 in and 0.5 in. However, two failed beams had values of ℓ_1 close to 0.75 in which were measured after the tests.

theoretical prediction and experimental test results is given in Tables 7 and 8. Table 7 shows some results of enlarged end beams, while Table 8 shows some results of flat ended beams. It shows that the threshold external dynamic energy λ_t for onset of tensile tearing failure which is obtained from the theoretical analysis in Chapter 5 agrees reasonably well with experimental results, especially for enlarged end beams. The upper and lower theoretical predications do bound most of the corresponding experimental test results. Therefore, from an engineering viewpoint the theoretical analysis in Chapter 5 can be used to estimate the threshold external dynamic energy for the onset of the tensile failure of clamped beams struck by a mass at any points of the span.

Only a few beam specimens which suffered transverse shear failures agree with the theoretical predictions for the threshold external dynamic energy required for the onset of shear failure if the coefficient k is about 0.25 (from theoretical analysis shear failure occurs when shear sliding $W_s = kH$, where $0 < k \leqslant 1$). These few test beams with thicknesses H = 0.25 in and 0.3 in were struck by the falling tup with the impact point very close to the support ($\ell_1 \leqslant 0.25$ in). For most failed beams, the theoretical analysis in Chapter 5 considerably overestimates the threshold external dynamic energy for the onset of shear failure in comparison with the experimental results. This large difference may be attributed to the definition of shear failure between theoretical analysis in Chapter 5 and experimental test results in Chapter 6. The theoretical analysis in Chapter 5

Thickness of beam H (in)	Impact point ℓ_1(in)	Limit elong. of material ε_m	Experimental results		Theoretical results	
			λ Max. value without failure	λ Min. value with failure	λ	$\lambda_{0.618}$
For Enlarged End Aluminium Beams						
0.15	2	0.19	16.334	24.2014C	32.17226	19.88245
0.2	0.5	0.19	0.5441	1.5815B	1.12364	0.69441
	0.75	0.19		1.7354C	2.23027	1.37831
	2	0.19	10.413	14.0675C	19.08565	11.79493
0.25	2	0.19	8.2463	10.419C	12.85057	7.94165
0.3	2	0.19	5.0131	6.5911C	9.36809	5.78948
For Enlarged End Steel Beams						
0.2	0.5	0.31		2.814C	2.42284	1.4973
	0.75	0.31	1.1142	6.1853C	5.07435	3.13595

* C - cracked; B - broken.

Table 7. Tensile Tearing Failure of Enlarged End Beams.

Thickness of beam H (in)	Impact point ℓ_1 (in)	Limit elongation of material ε_m	Experimental results		Theoretical results	
			λ Max. value without failure	λ Min. value with failure	λ	$\lambda_{0.618}$
0.15	0.25	0.19	0.3065	0.6878C	0.58504	0.36156
	0.5		0.5268	1.2327C	1.72367	1.06523
	1		4.5177	6.1558B	6.23657	3.8542
	1.5		5.7576	7.4638C	15.26132	9.4315
	2		18.1376		32.17226	19.88245
0.2	0.25	0.19	0.5135		0.39617	0.24483
	0.5		0.5314	0.8432C	1.12364	0.69441
	1		2.1672	3.2071B	3.84253	2.37469
	1.5		6.0611		9.17936	5.67285
	2		7.4935	7.9523B	19.08565	11.79493
0.25	0.25	0.19	0.4704		0.29648	0.18322
	0.5		0.9804	1.0099C	0.81154	0.50153
	1		2.0997	2.6273B	2.66709	1.65444
	1.5		4.2694		6.25853	3.86777
	2		5.5924	6.6018B	12.85057	7.94165
0.3	0.25	0.15	0.106	0.1489C	0.12729	0.10684
	0.5		0.3687	0.5266C	0.44513	0.27509
	1		0.5231	0.9956C	1.38484	0.85583
	1.5		0.7759	1.4761C	3.09419	1.91221
	2		2.179	2.6034C	6.18034	3.81945

* C - cracked; B - broken

Table 8. Tensile Tearing Failure of Flat End Aluminium Beams.

assumed that transverse shear failure occurs when the shear sliding W_s between two adjacent Transverse Cross Sections is equal to kH. On the other hand, the work in Chapter 6 assumes that the shear failure occurs when cracking starts from the upper surface of the beam at the impact point. After examining the beam specimens, we found that for most beams which failed due to excessive shear cracking did not develop along the transverse cross section but made an angle of 45° to the transverse cross section. Therefore, these beams really failed due to the combined effect of tensile and shear. There are a few beam specimens of H = 0.25 in and 0.3 in with the impact point very close to the support ($\ell_1 \leqslant 0.25$ in) which failed due to shear sliding between two adjacent transverse cross sections. The external dynamic energy of these few beams agrees, as stated in the beginning of this paragraph, with the theoretical predictions. Therefore, the theoretical analysis in Chapter 5 may be used to predict the threshold external dynamic energy for the onset of shear failure of clamped beams struck by a mass at any point of the span, provided the failure is caused by the shear sliding between two adjacent transverse cross sections. While for those failed beams in which the cracking starts from the upper surface at the impact point and develops along an angle of about 45° to the transverse cross section of the beam, further theoretical work is required to predict the threshold external dynamic energy for the onset of plastic failure.

Equations (5-9), (5-11b) and (5-13) in Chapter 5 show that when the tensile strain ε in a clamped beam is given the maximum

deformation W of the beam can be theoretically predicted and it is independent of the load which is acted on the beam, provided the plastic regions in the beam are similar to that assumed in Chapter 5. Therefore, it hints that those equations can be employed to predict the threshold maximum deformation for the onset of tensile tearing failure of both dynamically loaded and statically loaded beams when ε is replaced by the limit elongation ε_m of beam materials. Indeed, theoretical predictions in Chapter 5 agree well with most of experimental data which were obtained from static loading beams. The comparison beween theoretical predictions and experimental results is given in Table 9.

Clamping condition	Specimen No.	Thickness of beam H (in)	Loading point ℓ_1 (in)	Max. permanent deformation	
				experimental results (mm)	theoretical results (mm)
	ALI24	0.15	2	15.4	19.97
flat	ALIII21	0.25	1	10.75	9.93
	ALIV20	0.3	0.5	6.5	4.19
end	STI24	0.15	2	22.5 without failure	40.38
	STIII19	0.25	1	19.5	20.22
	STIV23	0.3	0.5	15	10.26
	AI1	0.15	2	14	19.97
large	AIII1	0.25	1	7.5	9.93
	AIV1	0.3	0.5	5.5	4.19
end	SI1	0.15	2	24.5 without failure	32.53
	SIII1	0.25	1	18	16.3
	SIV1	0.3	0.5	8.25	8.33

Table 9. Comparison of Maximum Permanent Deformation of Statical Loading Beams, Which Failed, between Theoretical Predictions of Equations (5-9), (5-11b) and (5-13) and Experimental Results.

CHAPTER 8

CONCLUSIONS

The theoretical work of Parkes [10] and other authors [12, 13, 15, etc.] has been further developed and extended to examine transverse shear and bending response and finite deflection effects of a clamped beam struck by a mass at any point of the span. The theoretical analysis on shear and bending response in Chapter 3 shows that more mechanisms of motion may occur than in the bending only solution [10] (the theoretical analysis in Chapter 3 can also be reduced to the bending only solution when the fully plastic transverse shear force Q_0 tends to infinity). It is clear that with the increase of the external dynamic energy, a large difference will occur between bending only solution [10], or shear and bending solution in Chapter 3, and one with the influence of finite deflections in Chapter 4. This difference increases sharply when the external dynamic energy is large. It is found that a bending violation may occur near the stationary plastic hinge at the impact point according to rigid-plastic yield condition. Therefore, for these cases which were ignored by Parkes [10] new velocity profiles with a moving plastic hinge instead of the stationary plastic hinge at the impact point are examined in Chapters 3 and 4. The interaction effect of bending moment, shear force and membrane force corresponding to a cubic shaped yield surface may be obtained by combining Chapter 3 with Chapter 4 when the effect of membrane forces is neglected in the shear sliding phases, since

the transverse shear force plays an important role in the early stage of motion when the displacement of the beam remains small [45]. Furthermore, a theoretical method has been developed in Chapter 5 to predict the threshold external dynamic energy for the onset of a tensile tearing failure and a transverse shear failure of a clamped beam struck by a mass at any point of the span.

A total of 260 beam specimens were tested with the impact points varied from the midpoint of the beam to the immediate vicinity of the support. The beam specimens were made of aluminium alloy and steel with flat end and enlarged ends. The thickness of the beams varied from 0.15 in to 0.3 in. A quantity of experimental data have been recorded, processed and measured during the test or after the test, including velocity-time history at the impact point, reactive force-time history between the falling tup and the beam, the motion of the beam and the tup in the whole response, the deformation-time history and strain-time history at some special points, etc. The external dynamic energy varied from small (small plastic deformations in beams) to very large (beam failures). For most types of test, at least 3 unbroken beams with different impact velocities and a failed beam were obtained.

Most of the experimental test results agree reasonably well with the theoretical predictions developed in this thesis. The theoretical predictions in Chapter 4 for the maximum permanent deformation of the beam do bound most of the

results obtained on aluminium beams, while for steel beams good agreement between the theoretical analysis and experimental results is also obtained provided the static yield stress σ_0 is replaced by the dynamic yield stress σ_0' defined by equation (7-4). When the mass ratio g is small, the maximum permanent deformation of the beam can be estimated using a very simple equation (7-1). The theoretical prediction for the threshold external dynamic energy for the onset of tensile tearing failure also bound most of the test results. For those beam specimens which failed due to shear, the theoretical analysis in Chapter 5 can also give reasonable agreement provided the shear cracking develops along the transverse cross section. When the shear cracking develops in an angle of about 45° to the transverse cross section of the beam, further theoretical work is required.

Further theoretical work may be done to predict the maximum permanent deformation of the beam using an 'exact' yield curve (parabolic yield curve) shown in Fig. 42d. The deformation profile of the beam with finite deflection may be obtained if the deformation $\bar{W}(z)$ of the beam at any point which is obtained from bending only solution is replaced by $\bar{W} + \gamma\bar{W}^2$. The deformation $\bar{W}_1$ at the impact point of the beam with finite deflection can be obtained from a bending only solution when $\bar{W}_1$ from the bending only solution is replaced by $\bar{W}_1 + \gamma\bar{W}_1^2$. The theoretical analysis in Chapter 5 may be further developed to predict the failure of beams due to the combined effect of tensile and shear. However, this is a very complex problem and a numerical method may need to be employed.

REFERENCES

1. Symonds, P. S., "Survey of methods of analysis for plastic deformation of structures under dynamic loadings", Brown Univ., Div. of Eng. Report BU/NSRDC/1-67, 1967.
2. Johnson, W., "Impact strength of materials", Arnold, London and Crane Russak (U.S.), 1972.
3. Jones, N., Dumas, J. W., Giannotti, J. G. and Grassit, K. E., "The dynamic plastic behaviour of shells", Dynamic Response of Structure, Eds. G. Herrmann and N. Perrone, Pergamon Press, pp. 1-29, 1972.
4. Jones, N., "A literature review of the dynamic plastic response of structures", The Shock and Vibration Digest, Vol. 7, No. 8, pp. 89-105, 1975.
5. Jones, N., "Recent progress in the dynamic plastic behaviour of structures", The Shock and Vibration Digest, Part 1, Vol. 10, No. 9, pp. 21-33, 1978; Part 2, Vol. 2, No. 10, pp. 13-19, 1978; Part 3, Vol. 13, No. 13, pp. 3-16, 1981; Part 4, Vol. 17, No. 2, pp. 35-47, 1985.
6. Lee, E. H. and Symonds, P. S., "Large plastic deformation of beams under transverse impact", J. Appl. Mech., Vol. 19, pp. 308-314, 1952.
7. Jones, N., "Response of structures to dynamic loading", Mech. Properties at High Rates of Strain , Ed. J. Harding, Inst. of Physics Conf. Series No. 47, pp. 254-276, 1979.

8. Bodner, S. R. and Symonds, P. S., "Experimental and theoretical investigation of the plastic deformation of cantilever beams subjected to impulsive loading", J. Appl. Mech., Vol. 29, pp. 719-728, 1962.

9. Parkes, E. W., "The permanent deformation of a cantilever struck transversely at its tip", Proc. Royal Society, London, Series A, Vol. 228, pp. 462-476, 1955.

10. Parkes, E. W., "The permanent deformation on an encastré beam struck transversely at any point in its span", Proc. Inst. Civil Engr., Vol. 10, pp. 277-304, 1958.

11. Ezra, A. A., "The plastic response of a simply supported beam to an impact load at the center", Proc. 3rd U.S. Nat. Cong. of Appl. Mech., pp. 513-520, 1958.

12. Nonaka, T., "Some interaction effects in a problem of plastic beam dynamics, parts 1-3", J. Appl. Mech., Vol. 34, pp. 623-643, 1967.

13. Symonds, P. S., "Plastic shear deformation in dynamic load problems", Engineering Plasticity, Eds. J. Heyman and F. A. Leckie, pp. 647-664, 1968.

14. Jones, N. and Oliveira, J. G. de, "The influence of rotatory inertia and transverse shear on the dynamic plastic behaviour of beams", J. Appl. Mech., Vol. 46, pp. 303-309, 1979.

15. Oliveira, J. G. de, "Beams under lateral projectile impact", ASCE J. Engrg. Mech. Div., Vol. 108, pp. 51-71, 1982.

16. Cox, A. D. and Morland, L. W., "Dynamic plastic deformations of simply-supported square plates", J. Mech. Phys. Solids, Vol. 7, pp. 229-241, 1959.

17. Jones, N., "A theoretical study of the dynamic plastic behaviour of beams and plates with finite-deflections", Int. J. Solids and Struc., Vol. 7, pp. 1007-1029, 1971.

18. Jones, N., Uran, T. O. and Tekin, S. A., "The dynamic plastic behaviour of fully clamped rectangular plates", Int. J. Solids and Struc., Vol. 6, pp. 1499-1512, 1970.

19. Jones, N. and Walters, R. M., "Large deflections of rectangular plates", J. Ship Res., Vol. 15, pp. 164-171 and 288, 1971.

20. Oliveira, J. G. de, "Design of steel offshore structures against impact loads due to dropped objects", MIT, Dept. Ocean Engrg. Report No. 81-6, June 1981.

21. Conroy, M. F., "Rigid-plastic analysis of a simply supported circular plate due to dynamic circular loading", J. of the Franklin Inst., Vol. 228, pp. 121-135, 1969.

22. Shadbolt, P. J., Corran, R. S. J. and Ruiz, C., "A comparison of plate perforation models in the sub-ordnance impact velocity range", Int. J. Impact Engrg., Vol. 1, pp. 23-49, 1983.

23. Wierzbicki, T. and Kelly, J. M., "Finite deflections of a circular viscoplastic plate subject to projectile impact", Int. J. Solids and Struc., Vol. 4, pp. 1081-1092, 1968.

24. Ivanov, G. V., Nemerovskii, Yu. V. and Rabotnov, Yu. N., "Dynamics of rigid-plastic beam grillages", Izv, Akad, Nauk USSR, OTN, No. 2, pp. 51-58, 1962 (in Russian).

25. Huang, Z. Q. and Liu, J. H., "Rigid-plastic analysis of beam grillages under blast type loading", Int. J. Impact Engrg., Vol. 3, pp. 179-190, 1985.

26. Jones, N. and Abramowicz, W., "Static and dynamic axial crushing of circular and square tubes", Metal Forming and Impact Mechanics, Ed. S. R. Reid, pp. 225-247, 1985.

27. Wang, A. J., "The permanent deflection of a plastic plate under blast loading", J. Appl. Mech., Vol. 22, pp. 375-376, 1955.

28. Jones, N. and Oliveira, J. G. de, "Impulsive loading of a cylindrical shell with transverse shear and rotatory inertial", Int. J. Solids and Struc., Vol. 19, pp. 263-279, 1983.

29. Jones, N., "Plastic failure of ductile beams loaded dynamically", J. Eng. for Industry, Vol. 98, pp. 131-136, 1976.

30. Jones, N. and Liu, J. H., "Local impact loading of beams", Proceedings of the International Symposium on Intense Dynamic Loading and Its Effects, Science Press, Beijing, China, pp. 444-449, 1986.

31. Jones, N. and Guedes Soares, C., "Higher modal dynamic plastic behaviour of beams loaded impulsively", Int. J. Mech. Sci., Vol. 20, pp. 135-147, 1978.

32. Spencer, A. J. M., "Dynamics of ideal fibre-reinforced rigid-plastic beams", J. Mech. Phys. Solids, Vol. 22, pp. 147-159, 1974.

33. Jones, N., "Dynamic behaviour of ideal fibre-reinforced rigid-plastic beams", J. Appl. Mech., Vol. 43, pp. 319-324, 1976.

34. Spencer, A. J. M., "Impulsive loading of fibre-reinforced rigid-plastic plates", Int. J. Eng. Sci., Vol. 17, pp. 35-47, 1979.

35. Oliveira, J. G. de and Jones, N., "Some remarks on the influence of transverse shear on the plastic yielding of structure", Int. J. Mech. Sci., Vol. 20, pp. 759-765, 1978.

36. Jones, N., "Bound methods for transverse shear effects in the dynamic plastic behaviour of structures", Int. J. Impact Engrg., Vol. 3, pp. 273-291, 1985.

37. Jones, N. and Oliveira, J. G. de, "Dynamic plastic response of circular plates with transverse shear and rotatory inertia", J. Appl. Mech., Vol. 47, pp. 27-34, 1980.

38. Symonds, P. S. and Mentel, T. J., "Impulsive loading of plastic beams with axial constraints", J. Mech. Phys. Solids, Vol. 6, pp. 186-202, 1958.

39. Jones, N., "Influence of strain-hardening and strain-rate sensitivity on the permanent deformation of impulsively loaded rigid-plastic beams", Int. J. Mech. Sci., Vol. 9, pp. 777-796, 1967.

40. Symonds, P. S. and Jones, N., "Impulsive loading of fully clamped beams with finite plastic deflections and strain-rate sensitivity", Int. J. Mech. Sci., Vol. 14, pp. 49-69, 1972.

41. Walters, R. M. and Jones, N., "An approximate theoretical study of the dynamic plastic behaviour of shells", Int. J. Nonlinear Mech., Vol. 7, pp. 255-273, 1972.

42. Symonds, P. S., "Viscoplastic behaviour in response of structures to dynamic loading", Behaviour of Material Under Dynamic Loading , Ed. N. J. Huffington, ASME, pp. 106-124, 1965.

43. Perrone, N. and Bhadra, P., "A simplified method to account for plastic rate sensitivity with large deformations", J. Appl. Mech., Vol. 46, pp. 811-816, 1979.

44. Menkes, S. B. and Opat, H. J., "Broken beams", Experimental Mechanics, Vol. 13, pp. 480-486, 1973.

45. Jones, N., "Some comments on the dynamic plastic behaviour of structure", presented at International Symposium on Intense Dynamic Loading and Its Effects, Beijing, China, June 3-7, 1986.

46. Duwez, P. E., Clark, D. S. and Bohnenblust, H. F., "The behaviour of long beams under impact loading", J. Appl. Mech., Vol. 17, pp. 27-34, 1950.

47. Corran, R. S. J., Shadbolt, P. J. and Ruiz, C., "Impact loading of plates - an experimental investigation", Int. J. Impact Engrg., Vol. 1, pp. 3-22, 1983.

48. Humphreys, J. S., "Plastic deformation of impulsively loaded straight clamped beams", J. Appl. Mech., Vol. 32, pp. 7-10, 1965.

49. Florence, A. L. and Firth, R. D., "Rigid-plastic beams under uniformly distributed impulse", J. Appl. Mech., Vol. 32, pp. 481-488, 1965.

50. Florence, A. L., "Circular plate under a uniformly distributed impulse", Int. J. Solids and Struc., Vol. 2, pp. 37-47, 1966.

51. Wierzbicki, T. and Florence, A. L., "A theoretical and experimental investigation of impulsively loaded clamped circular viscoplastic plates", Int. J. Solids and Struc., Vol. 6, pp. 553-568, 1970.

52. Jones, N., Griffin, R. N. and Van Duzer, R. E., "An experimental study into the dynamic plastic behaviour of wide beams and rectangular plates", Int. J. Mech. Sci., Vol. 13, pp. 721-735, 1971.

53. Jones, N., "Scaling of inelastic structural members loaded dynamically", Structural Impact and Crashworthiness, Vol. 1, Ed. G. A. O. Davies, pp. 45-74, 1984.

54. Jones, N., Jouri, W. S. and Birch, R. S., "On the cutting of mild steel plate", Dept. of Mechanical Engineering Report ES/09/83, University of Liverpool, 1983.

55. Jones, N., "Dynamic plastic behaviour of structures", Cambridge University Press, to be published.

56. Birch, R. S., "Dynamic buckling of stiffened structural members", Ph. D. Thesis, Dept. of Mechanical Engineering, University of Liverpool, 1986.

57. Reid, S. R. and Hendry, S. R., "Impact response of fluid-backed metal beams", Comput. Struct., Vol. 20, pp. 321-338, 1985.

58. Jones, N., "Dynamic behaviour of rigid-plastic plates with finite-deflections", Notes on 11th November, 1969.

59. Jones, N., "Tearing threshold", Notes on 19th July, 1985.

60. Parkes, E. W., "Some simple experiments on the dynamic plastic behaviour of mild steel beams", Brit. Weld. J., Vol. 3, pp. 362-366, 1956.

APPENDIX I

Details of the proof of static admissibility conditions for Chapter 3 are given in this Appendix. We will see that this examination into the static admissibility conditions is a considerable exercise. However, it is necessary. Otherwise, we cannot be sure that the velocity profiles which we assumed in the theoretical analysis give the correct solution, since an 'exact' solution for the dynamic response of structure must satisfy both kinematic and static admissibility conditions relating to the yield surface which we chose.

The general shear force and bending moment expressions (3-6) with velocity profile (3-3) can be used for most cases discussed in Chapter 3. Substituting equation (3-3) into (3-6), we obtain

$$q_2 = 0\,, \quad m_2 = -1 \qquad \text{for } -\tfrac{1}{\gamma} \le z \le -z_2 \qquad (1a,b)$$

$$q_2 = q_{20} + \frac{g\ddot{W}_2}{8uV_1 z_2}(2z_2 + z)z - \frac{g\dot{W}_2 \dot{z}_2}{8uV_1 z_2^2} z^2$$

$$m_2 = 1 + 2q_{20}V_1 z + \frac{g\ddot{W}_2}{12uz_2}(3z_2 + z)z^2 - \frac{1}{12}\frac{g\dot{W}_2 \dot{z}_2}{u z_2^2} z^3 \qquad \text{for } -z_2 \le z \le 0^- \qquad (1c,d)$$

$$q_1 = q_{10} + \frac{g\ddot{W}_1}{8uV_1 z_1}(2z_1 - z)z + \frac{g\dot{W}_1 \dot{z}_1}{8uV_1 z_1^2} z^2$$

$$m_1 = 1 + 2q_{10}V_1 z + \frac{g\ddot{W}_1}{12uz_1}(3z_1 - z)z^2 + \frac{g\dot{W}_1 \dot{z}_1}{12u z_1^2} z^3 \qquad \text{for } 0^+ \le z \le z_1 \qquad (1e,f)$$

$$q_1 = 0 \quad \text{and} \quad m_1 = -1. \qquad \text{for } z_1 \le z \le 1 \qquad (1g,h)$$

Differentiating equations (1) with respect to z, we obtain

$$q_2' = 0, \quad m_2' = 0 \qquad \text{for } -\tfrac{1}{\gamma} \le z \le -z_2 \qquad (2a,b)$$

$$q_2' = \frac{g\ddot{W}_2}{4uV_1 z_2}(z_2 + z) - \frac{g\dot{W}_2 \dot{z}_2}{4uV_1 z_2^2} z$$

$$m_2' = 2q_{20}V_1 + \frac{g\ddot{W}_2}{4uz_2}(2z_2 + z)z - \frac{g\dot{W}_2 \dot{z}_2}{4u z_2^2} z^2 \qquad \text{for } -z_2 \le z \le 0^- \qquad (2c,d)$$

$$q_1' = \frac{g\ddot{W}_1}{4uv_1z_1}(z - z_1) + \frac{g\dot{W}_1\dot{z}_1}{4uv_1z_1^2}z \qquad \text{for } 0^+ \le z \le z_1 \qquad (2e,f)$$

$$m_1' = 2q_{10}v_1 + \frac{g\ddot{W}_1}{4uz_1}(2z_1 - z)z + \frac{g\dot{W}_1\dot{z}_1}{4uz_1^2}z^2$$

$$q_1' = 0 \quad \text{and} \quad m_1' = 0 \qquad \text{for } z_1 \le z \le 1 \qquad (2g,h)$$

where $(\ )' = \frac{\partial(\ )}{\partial z}$.

Differentiating equations (1) twice, we obtain

$$q_2'' = 0\,, \quad m_2'' = 0 \qquad \text{for } -\tfrac{1}{\gamma} \le z \le -z_2 \qquad (3a,b)$$

$$q_2'' = \frac{g\ddot{W}_2}{4uv_1z_2} - \frac{g\dot{W}_2\dot{z}_2}{4uv_1z_2^2}$$

$$m_2'' = \frac{g\ddot{W}_2}{2uz_2}(z_2 + z) - \frac{g\dot{W}_2\dot{z}_2}{2uz_2^2}z \qquad \text{for } -z_2 \le z \le 0^- \qquad (3c,d)$$

$$q_1'' = -\frac{g\ddot{W}_1}{4uv_1z_1} + \frac{g\dot{W}_1\dot{z}_1}{4uv_1z_1^2}$$

$$m_1'' = \frac{g\ddot{W}_1}{2uz_1}(z_1 - z) + \frac{g\dot{W}_1\dot{z}_1}{2uz_1^2}z \qquad \text{for } 0^+ \le z \le z_1 \qquad (3e,f)$$

$$q_1'' = 0 \quad \text{and} \quad m_1'' = 0. \qquad \text{for } z_1 \le z \le 1 \qquad (3g,h)$$

1. Case I, $\nu_2 \ge \nu_1 > 3$

A) Phase 1, shear sliding $0 \le t \le t_s$

In this phase, equations (3-10) give

$$\ddot{W}_2 = \ddot{W}_1 = \frac{8}{3}\frac{v_1^2u}{g} > 0\,, \quad z_1 = z_2 = \frac{3}{v_1}\,,$$

$$q_{10} = -q_{20} = -1 \quad \text{and} \quad \dot{z}_1 = \dot{z}_2 = 0 \qquad (4a\text{-}d)$$

substituting equations (4) into (2) and (3), we obtain

$$q_2' = \tfrac{2}{3}v_1\left(1 + \frac{z}{z_2}\right) \ge 0\,, \quad q_2'' > 0 \qquad \text{for } -z_2 \le z \le 0^- \qquad (5a,b)$$

$$m_2' = 2v_1 + \tfrac{4}{3}v_1^2 z + \frac{2}{3}\frac{v_1^2}{z_2}z^2 \ge 0 \qquad \text{for } -z_2 \le z \le 0^- \qquad (5c)$$

since $m_2' = 0$ at $z = -z_2$ and $m_2'' = \frac{4}{3}v_1^2\left(1 + \frac{z}{z_2}\right) \ge 0$, (5d)

$$q_1' = \frac{2}{3} v_1 \left(1 - \frac{z}{z_1}\right) \geq 0, \quad q_2'' < 0 \qquad \text{for } 0^+ \leq z \leq z_1 \qquad (5e,f)$$

$$m_1' = -2v_1 + \frac{4}{3} v_1^2 z - \frac{2}{3} \frac{v_1^2}{z_1} z^2 \leq 0 \qquad \text{for } 0^+ \leq z \leq z_1 \qquad (5g)$$

since $m_2' = 0$ at $z = -z_2$ and $m_2'' = \frac{4}{3} v_1^2 \left(1 + \frac{z}{z_2}\right) \geq 0$. (5h)

Equations (1a,b), (1g,h) and (5) give

$$0 \leq q_2 \leq 1, \quad -1 \leq m_2 \leq 1, \quad -1 \leq q_1 \leq 0 \text{ and } -1 \leq m_1 \leq 1$$

since $q_2 = 0$ and $m_2 = -1$ at $z = -z_2$, $q_2 = 1$ and $m_2 = 1$ at $z = 0^-$, $q_1 = -1$ and $m_1 = 1$ at $z = 0^+$ and $q_1 = 0$ and $m_1 = -1$ at $z = z_1$.

The distributions of shear force and bending moment are shown in Fig. 3(c,d).

B) Phase 2, $t_s < t \leq t_1$

Equations (3-12) and (3-13a) give

$$\ddot{W}_1 = -\frac{24u}{z_1(2+gz_1)}, \quad \dot{W}_1 = \frac{2u}{(1+gz_1)} \text{ and } \dot{z}_1 = \frac{12(1+gz_1)^2}{(2+gz_1)gz_1}. \qquad (6a-c)$$

Substituting equations (6) into (2) and (3), we obtain

$$q_1' = -\frac{6}{v_1 z_1^2 (2+gz_1)} \left(gz_1 - 2gz - \frac{z^2}{z_1}\right) \qquad (7a)$$

$$m_1' = \frac{\ddot{W}_1}{4u} + \frac{g\ddot{W}_1}{4uz_1}(2z_1 - z)z - \frac{\ddot{W}_1}{4uz_1^2}(1+gz_1)z^2$$

$$= \frac{\ddot{W}_1}{4u}\left[1 - \frac{z^2}{z_1^2} + 2gz\left(1 - \frac{z}{z_1}\right)\right] \leq 0 \qquad \text{for } 0^+ \leq z \leq z_1 \qquad (7b)$$

since $\ddot{W}_1 < 0$ and $\frac{z}{z_1} < 1$.*

$$q_1'' = \frac{6}{v_1 z_1^2 (2+gz_1)} \left(2g + \frac{1}{z_1}\right) > 0 \qquad (7c)$$

---

* Equation (3-5e) give $q_{10} = -q_{20} = \frac{\ddot{W}_1}{8uv_1}$. Equations (6a-c) give $\dot{W}_1 \dot{z}_1 = -\frac{\ddot{W}_1}{g}(1 + gz_1)$.

$$m_1'' = \frac{\ddot{W}_1}{4u}\left[2g\left(1-\frac{z}{z_1}\right)-2g\frac{z}{z_1}-2\frac{z}{z_1}\right] = \frac{\ddot{W}_1}{4u}\left[2g-2\frac{z}{z_1}-4g\frac{z}{z_1}\right]. \qquad (7d)$$

Assumed that $q_1' = 0$, equation (7a) give

$$z_{1\min} = \frac{g z_1^2}{1+2g z_1}. \qquad (7e)$$

Substituting $z_{\min}$ into equation (1e), we obtain

$$q_{1\min} = -\frac{3}{v_1 z_1}\frac{(1+g z_1)^2}{(2+g z_1)(1+2g z_1)} > -\frac{3}{v_1 z_1} \geq -1 \qquad (7f)$$

since $z_1 \geq \frac{3}{v_1}$.

Equations (7b) and (7f) with $q_1 = -1$ and $m_1 = 1$ at $z = 0^+$ and $q_1 = 0$ and $m_1 = -1$ at $z = z_1$ give

$$-1 \leq q_1 \leq 0, \quad -1 \leq m_1 \leq 1, \quad 0 \leq q_2 \leq 1 \text{ and } -1 \leq m_2 \leq 1$$

due to $q_1 = -q_2$, $m_1 = m_2$ in this phase.

C) Phase 3, $t_1 < t \leq t_2$

In this phase, $z_1 = 1$, $\dot{z}_1 = 0$ and $\dot{\bar{W}}_0 = \dot{\bar{W}}_1 = \dot{\bar{W}}_2$. Equations (3-17) give

$$\ddot{\bar{W}}_1 = -\frac{8u(3+z_2)}{z_2(z_2 g+4+\frac{4}{3}g)} \quad \text{and} \quad \dot{\bar{W}}_1 \dot{z}_2 = -\frac{\ddot{\bar{W}}(\frac{4}{3}g+2+3z_2+z_2^2)}{3+2z_2}. \qquad (8a,b)$$

Equations (3-5d,e) with equation (8b) give

$$q_{20} = \frac{g}{8uv_1}(z_2\ddot{\bar{W}}_1+\dot{\bar{W}}_1\dot{z}_2) \quad \text{and} \quad q_{10} = q_{20}+\frac{\ddot{\bar{W}}_1}{4uv_1}. \qquad (8c,d)$$

Equations (2) and (3) with equations (8) give

$$q_2' = \frac{g\ddot{\bar{W}}_1}{4uv_1 z_2}(z_2+z) + \frac{g\ddot{\bar{W}}_1}{4uv_1 z_2^2}\frac{(\frac{4}{3}g+2+3z_2+z_2^2)}{3+z_2}$$

$q_2'' < 0$ since $\ddot{\bar{W}}_1 < 0$ and $\dot{\bar{W}}_1\dot{z}_2 > 0$. Assumed that $q_2' = 0$, we

obtain

$$z_{2max} = \frac{\ddot{w}_2 z_2^2}{\dot{w}_2 \dot{z}_2 - \ddot{w}_2 z_2} \tag{8e}$$

Substituting equation (8e) into (1c), we obtain

$$q_{2max} = q_{20} + \frac{g \ddot{w}_1^2 z_2^2}{8 u v_1 (\dot{w}_1 \dot{z}_2 - \ddot{w}_1 z_2)} = \frac{g}{8 u v_1} \frac{\dot{w}_1^2 \dot{z}_2^2}{(\dot{w}_1 \dot{z}_2 - \ddot{w}_2 z_2)}$$

$$= \frac{g}{v_1 z_2} \frac{(\frac{6}{g} + 2 + 3 z_2 + z_2^2)}{(z_2 g + 4 + \frac{4}{3} g)} < \frac{6 + 2g + 3 g z_2 + g z_2^2}{v_1 (z_2^2 g + 4 z_2 + \frac{4}{3} g z_2)}$$

$$= \frac{3}{v_1} \frac{2 + \frac{2}{3} g + g z_2 + \frac{1}{3} g z_2^2}{z_2^2 g + 4 z_2 + \frac{4}{3} g z_2} < \frac{3}{v_1} \frac{\frac{2}{3} g z_2^2 + \frac{4}{3} g z_2 + 2 z_2}{z_2^2 g + \frac{4}{3} g z_2 + 4 z_2} < 1 \tag{9a}$$

since $z_2 \geq 1$ and $\nu_1 > 3$ in this phase.

$$q_1' = \frac{g}{4 u v_1} \ddot{w}_1 (1 - z) \leq 0 \qquad \text{for } 0^+ \leq z \leq 1$$

since $z_1 = 1$, $\dot{z}_1 = 0$ and $\ddot{w}_1 < 0$. The minimum value of q_1 occurs at $z = 1$ and it is equal to

$$q_{1min} = q_{10} + \frac{g \ddot{w}_1}{8 u v_1} = \frac{g}{8 u v_1} (z_2 \ddot{w}_1 + \dot{w}_1 \dot{z}_2) + \frac{\ddot{w}_1}{4 u v_1} + \frac{g \ddot{w}_1}{8 u v_1}$$

$$= -\frac{1}{v_1} \frac{(g z_2^2 + 4 z_2 + g + 2 g z_2)}{g z_2^2 + 4 z_2 + \frac{4}{3} g z_2} > -1 \tag{9b}$$

since $\nu_1 > 3$ and $z_2 \geq 1$.

$$m_2' = 2 q_{20} v_1 + \frac{g \ddot{w}_1}{4 u z_2} (2 z_2 + z) z - \frac{g \dot{w}_2 \dot{z}_2}{4 u z_2^2} z^2 \geq 0, \text{ if } 2 q_{20} v_1 \geq 0, \text{ for } -z_2^+ \leq z \leq 0 \tag{9c}$$

since $m_2'' < 0$ and $m_2' > 0$ at $t = 0$ if $2q_{20}\nu_1 \geq 0$.

$$2 q_{20} v_1 \geq 0 \rightarrow z_2 \ddot{w}_1 + \dot{w}_1 \dot{z}_2 \geq 0 \quad \text{or} \quad \frac{3}{g} \geq \frac{1}{2} z_2^2 - 1 \tag{9d}$$

$$m_1' = 2 q_{10} v_1 + \frac{g \ddot{w}_1}{4 u} (2 - z) z \leq 0, \text{ if } 2 q_{10} v_1 \leq 0, \text{ for } 0^+ \leq z \leq 1 \tag{9e}$$

since $m_1'' < 0$ and $m_1' \leq 0$ at $z = 0^+$ if $2q_{10}\nu_1 \leq 0$.

$$2Q_{10}V_1 \le 0 \longrightarrow \frac{u}{g} \ge \frac{2}{z_2} - z_2 \qquad (9f)$$

Equations (9) give

$0 \le Q_2 \le 1$, $-1 \le m_2 \le 1$ if $\frac{\ddot{z}}{g} \ge \frac{1}{2}z_2^2 - 1$

$-1 \le Q_1 \le 0$, $-1 \le m_1 \le 1$ if $\frac{u}{g} \ge \frac{2}{z_2} - z_2$

since $q_2 = 0$, $m_2 = -1$ at $z = -z_2^+$, $m_1 = m_2 = 1$ at $z = 0$ and $m_1 = -1$ at $z = 1$.

For $\frac{4}{g} < \frac{2}{z_2(t_1)} - z_2(t_1)$, the shear force and bending moment expressions (1) are no longer valid since the plastic hinge previously occurred at $z = 0$ now transfer to the point $z = z_0$.

In this case, the distribution of shear force is

$$Q_2 = \begin{cases} 0 & \text{for } -\frac{1}{\gamma} \le z \le -z_2^- \\ \frac{g}{8uV_1}\left[\ddot{W}(z_0^-) + \ddot{W}(z)\right](z - z_0) - \frac{1}{4uV_1}\ddot{W}(0) & \text{for } -z_2^+ \le z \le 0^- \\ \frac{g}{8uV_1}\left[\ddot{W}(z_0^-) + \ddot{W}(z)\right](z - z_0) & \text{for } 0^+ \le z \le z_0^- \end{cases} \qquad (10a)$$

$$Q_1 = \frac{g}{8uV_1}\left[\ddot{W}(z_0^+) + \ddot{W}(z)\right](z - z_0) \qquad \text{for } z_0^+ \le z \le 1 \qquad (10b)$$

substituting equations (3-24) into equations (10), we obtain

$$Q_2 = \begin{cases} \frac{g}{8uV_1}\left[\ddot{W}_3 + \frac{\dot{W}_3\dot{z}_0}{z_2+z_0} + \ddot{W}_3\frac{z_2+z}{z_2+z_0} + \dot{W}_3\frac{z_0\dot{z}_2 - z_2\dot{z}_0 - z(\dot{z}_2+\dot{z}_0)}{(z_2+z_0)^2}\right](z_2 - z_0) - \frac{1}{4uV_1}\ddot{W}_{(0)} & \text{for } -z_2^+ \le z \le 0^- \\ \frac{g}{8uV_1}\left[\ddot{W}_3 - \frac{\dot{W}_3\dot{z}_0}{z_2+z_0} + \dot{W}_3\frac{z_2+z}{z_2+z_0} + \dot{W}_3\frac{z_0\dot{z}_2 - z_2\dot{z}_0 - z(\dot{z}_2+\dot{z}_0)}{(z_2+z_0)^2}\right](z_2 - z_0) & \text{for } 0^+ \le z \le z_0^- \end{cases} \qquad (11a)$$

$$Q_1 = \frac{g}{8uV_1}\left[\ddot{W}_3 + \frac{\dot{W}_3\dot{z}_0}{1-z_0} + \ddot{W}_3\frac{1-z}{1-z_0} + \dot{W}_3\dot{z}_0\frac{(1-z)}{(1-z_0)^2}\right](z - z_0) \qquad \text{for } z_0^+ \le z \le 1 \qquad (11b)$$

$$Q_2' = \frac{g}{4uV_1}\frac{1}{(z_2+z_0)}\left[\ddot{W}_3(z_2+z) - \dot{W}_3\dot{z}_0\frac{(z_2+z)}{(z_2+z_0)} - \dot{W}_3\dot{z}_2\frac{z}{(z_2+z_0)}\right] \qquad \text{for } -z_2^+ \le z \le z_0^- \qquad (11c)$$

$$Q_1' = \frac{g}{4uV_1}\frac{(1-z)}{(1-z_0)}\left[\ddot{W}_3 + \frac{\dot{W}_3\dot{z}_0}{1-z_0}\right] = \frac{g}{4uV_1}\frac{(1-z)}{(1-z_0)}\left[-\frac{12u}{g(1-z_0)^2}\right] \le 0 \qquad (11d)$$

$$\text{for } z_0^+ \le z \le 1$$

$$q_2'' = \frac{g}{4\mu v_1}\frac{1}{(z_2+z_0)}\left[\ddot{w}_3 - \dot{w}_3\dot{z}_0\frac{1}{z_2+z_0} - \dot{w}_3\dot{z}_2\frac{1}{z_2+z_0}\right]$$

$$= -\frac{12}{v_1(z_2+z_0)}\frac{g(z_2+z_0)+1}{[g(z_2+z_0)^3+4(z_2^2+z_0z_2+z_0^2)]} < 0 \qquad (11e)$$

$$q_1'' = \frac{3}{v_1(1-z_0)^3} > 0. \qquad (11f)$$

Assumed that $q_2' = 0$, we obtain

$$z^*_{max} = \frac{\dot{w}_3\dot{z}_0z_2 - \ddot{w}_3z_2(z_2+z_0)}{\ddot{w}_3(z_2+z_0) - \dot{w}_3\dot{z}_0 - \dot{w}_3\dot{z}_2}. \qquad (11g)$$

Equations (11a,g) and (3-26) give

$$q_{2max} = \frac{3}{2v_1}\frac{z_2(z_2+2z_0)[g^2(z_2+z_0)^4+4z_2^2+4gz_2(z_2+z_0)^2]}{(z_2+z_0)^3[g^2(z_2+z_0)^4+4(z_2^2-z_0z_2+z_0^2)+g(5z_2^3+3z_2^2z_0+3z_2z_0^2+5z_0^3)]} \qquad (11h)$$

The minimum value of shear force q_1 occurs at $z = 1$ and it equals

$$q_{1min} = -\frac{3}{2v_1(1-z_0)}. \qquad (11i)$$

It shows from equations (11a-i) that

$$q_2 \geq 0 \quad \text{and} \quad q_1 \leq 0$$

since $q_2 = 0$ at $z = -z_2$, $q_2 = 0$ at $z = z_0^-$, $q_1 = 0$ at $z = z_0^+$ and

$$q_2(0^-) = \frac{6}{v_1}\frac{z_0z_2g(z_2+z_0)+z_2^2}{(z_2+z_0)[g(z_2+z_0)^3+4(z_2^2-z_0z_2+z_0^2)]} > 0. \qquad (11j)$$

Therefore, we can obtain

$$-1 \leq m_1 \leq 1 \quad \text{and} \quad -1 \leq m_2 \leq 1$$

since $m_2' = 2q_2\nu_1$, $m_1' = 2q_1\nu_1$, $m_2 = -1$ in $-\frac{1}{r} \leq z \leq -z_2$, $m_1 = m_2 = 1$ at $z = z_0$ and $m_1 = -1$ at $z = -1$.

---

* It is clear from equations (11e) and (3-26a,b) that z^*_{max} is negative.

For $\frac{3}{g} < \frac{1}{2} z_2^2 - 1$, the plastic hinge previously occurred at $z = 0$ now transfers to the point $z = -z_0$. The distributions of shear force can be expressed as

$$q_2 = \begin{cases} 0 & \text{for } -\frac{1}{\nu} \le z \le -z_2^- \\ \frac{g}{8uv_i}[\ddot{w}(-z_0^-) + \ddot{w}(z)](z_0+z) & \text{for } -z_2^+ \le z \le -z_0^- \end{cases} \quad (12a)$$

$$q_1 = \begin{cases} \frac{g}{8uv_i}[\ddot{w}(-z_0^+) + \ddot{w}(z)](z_0+z) & \text{for } -z_0^+ \le z \le 0^- \\ \frac{g}{8uv_i}[\ddot{w}(-z_0^+) + \ddot{w}(z)](z_0+z) + \frac{1}{4uv_i}\ddot{w}(0) & \text{for } 0^+ \le z \le 1 \end{cases} \quad (12b)$$

Substituting equation (3-27) into equations (12), we obtain

$$q_2 = \frac{g}{8uv_i}\left[\ddot{w}_3 + \dot{w}_3\dot{z}_0\frac{1}{z_2-z_0} + \ddot{w}_3\frac{z_2+z}{z_2-z_0} + \dot{w}_3\frac{z_2\dot{z}_0 - \dot{z}_2 z_0 - z(\dot{z}_2-\dot{z}_0)}{(z_2-z_0)^2}\right](z_0+z) \quad (13a)$$

for $-z_2^+ \le z \le -z_0^-$

$$q_1 = \begin{cases} \frac{g}{8uv_i}\left[\ddot{w}_3 - \frac{\dot{w}_3\dot{z}_0}{1+z_0} + \ddot{w}_3\frac{1-z}{1+z_0} - \dot{w}_3\frac{(1-z)\dot{z}_0}{(1+z_0)^2}\right](z_0+z) & \text{for } -z_0^+ \le z \le 0^- \\ \frac{g}{8uv_i}\left[\ddot{w}_3 - \frac{\dot{w}_3\dot{z}_0}{1+z_0} + \ddot{w}_3\frac{1-z}{1+z_0} - \dot{w}_3\frac{(1-z)\dot{z}_0}{(1+z_0)^2}\right](z_0+z) + \frac{1}{4uv_i}\left[\ddot{w}_3\frac{1}{1+z_0} + \frac{\dot{w}_3\dot{z}_0}{(1+z_0)^2}\right] & \text{for } 0^+ \le z \le 1 \end{cases} \quad (13b)$$

Differentiating equation (13a,b) with respect to z, we obtain

$$q_2' = \frac{g}{4uv_i}\left\{\ddot{w}_3\frac{(z_2+z_0)}{(z_2-z_0)} + \frac{\dot{w}_3}{(z_2-z_0)^2}\left[(z_2+z)\dot{z}_0 - (z_0+z)\dot{z}_2\right]\right\} \quad (13c)$$

$$q_1' = \frac{g}{4uv_i}\left[\ddot{w}_3(1+z_0) - \dot{w}_3\dot{z}_0\right]\frac{(1-z)}{(1+z_0)^2} \le 0 \quad (13d)$$

$$q_2'' = \frac{g}{4uv_i}\left[\ddot{w}_3(z_2-z_0) + \dot{w}_3(\dot{z}_0-\dot{z}_2)\right]\frac{1}{(z_2-z_0)^2} < 0 \quad (13e)$$

$$q_1'' = \frac{g}{4uv_i}\left[\dot{w}_3\dot{z}_0 - \ddot{w}_3(1+z_0)\right]\frac{1}{(1+z_0)^2} > 0 \quad (13f)$$

since equations (3-29) give

$$\ddot{w}_3(1+z_0) - \dot{w}_3\dot{z}_0 = -\frac{4u(1+z_0)^2}{\left[\frac{1}{3}g(1+z_0)^3+1\right]} < 0 \quad (13g)$$

and $$\ddot{w}_3(z_2-z_0) + \dot{w}_3(\dot{z}_0-\dot{z}_2) = -\frac{48u}{g(z_2-z_0)} < 0 \quad (13h)$$

Assumed that $q_2' = 0$, we obtain

$$z_{max} = -z_2 + \frac{\ddot{w}_3 \dot{z}_2 (z_2 - z_0)}{\ddot{w}_3 (\dot{z}_2 - \dot{z}_0) - (z_2 - z_0)\dddot{w}_3} \quad . \tag{13i}$$

Substituting equation (13i) into (13a), we obtain

$$q_{2max} = \frac{g}{8uv_i} \frac{[\ddot{w}_3 \dot{z}_0 + (z_2 - z_0)\ddot{w}_3]^2}{(\dot{z}_2 - \dot{z}_0)\ddot{w}_3 - (z_2 - z_0)\dddot{w}_3} = \frac{3}{2v_i (z_2 - z_0)} \quad . \tag{13j}$$

The minimum value of shear force q_1 occurs at $z = 1$ and it equals

$$q_{1min} = -\frac{g(1+z_0)^2 + 2}{2v_i [\frac{1}{3} g (1+z_0)^3 + 1]} \quad . \tag{13k}$$

It shows from equations (13a-k) that

$$q_2 \geq 0 \text{ in } -\frac{1}{r} \leq z \leq -z_0^- \text{ and } q_1 \leq 0 \text{ in } -z_0^+ \leq z \leq 1$$

since $q_2 = 0$ in $-\frac{1}{r} \leq z \leq -z_2$ and $q_1 = q_2 = 0$ at $z = -z_0$. Therefore, we can obtain that $-1 \leq m_2 \leq 1$ and $-1 \leq m_1 \leq 1$ since $m_2' = 2V_1 q_2$, $m_1' = 2V_1 q_1$, $m_2 = -1$ in $-\frac{1}{r} \leq z \leq -z_2$, $m_2 = m_1 = 1$ at $z = -z_0$ and $m_1 = -1$ at $z = 1$.

D) Phase 4, $t_2 < t \leq t_f$

Equation (3-31) give

$$\ddot{w}_1 = \frac{-4ur(1+r)}{\frac{1}{3}(1+r)g + r} \quad . \tag{14}$$

Substituting equation (14) with $z_2 = \frac{1}{r}$, $z_1 = 1$, $\dot{z}_1 = \dot{z}_2 = 0$ and $\dot{w}_1 = \dot{w}_2$ into equations (1), (2) and (3), we obtain

$$q_2 = q_{20} - \frac{gzr(2+rz)(1+r)}{[\frac{1}{3}(1+r)g + r]2v_i} \qquad \text{for } -\frac{1}{r} \leq z \leq 0^- \tag{15a}$$

$$q_1 = q_{10} - \frac{gzr(2-z)(1+r)}{2v_i[\frac{1}{3}(1+r)g + r)} \qquad \text{for } 0^+ \leq z \leq 1 \tag{15b}$$

$$q_2' = -\frac{gr(1+zr)(1+r)}{v_i[\frac{1}{3}(1+r)g + r]} < 0 \qquad \text{for } -\frac{1}{r} \leq z \leq 0^- \tag{15c}$$

$$q_1' = -\frac{gr(1-z)(1+r)}{v_1[\frac{1}{3}(1+r)g+r]} < 0 \qquad \text{for } 0^+ \le z \le 1 \qquad (15d)$$

$$q_2'' = -\frac{gr^2(1+r)}{v_1[\frac{1}{3}(1+r)g+r]} < 0 \qquad \text{for } -\frac{1}{r} \le z \le 0^- \qquad (15e)$$

$$q_1'' = \frac{gr(1+r)}{v_1[\frac{1}{3}(1+r)g+r]} > 0 \qquad \text{for } 0^+ \le z \le 1 \qquad (15f)$$

where q_{20} and q_{10} are defined by equations (3-5a,c) and (14) and they are

$$q_{20} = \frac{r}{v_1[\frac{1}{3}(1+r)g+r]}[\tfrac{1}{3}g(1+r)(1-\tfrac{1}{r})+r] \qquad (15g)$$

and

$$q_{10} = -\frac{\frac{1}{3}g(1-r^2)+r}{v_1[\frac{1}{3}(1+r)g+r]} < 0 \qquad (r \le 1) \qquad (15h)$$

Equations (15c,d) shows that the maximum absolute values of shear force q_2 and q_1 occurs at the supports $z = -\frac{1}{r}$ and $z = 1$, respectively. They are

$$q_{2max} = \frac{g(\frac{1}{3}r^2+\frac{1}{6}+\frac{1}{2}r)+r^2}{v_1[\frac{1}{3}(1+r)g+r]} < 1 \qquad (15i)$$

$$q_{1min} = -\frac{g(1+r)(\frac{1}{3}+\frac{r}{6})+r}{v_1[\frac{1}{3}(1+r)g+r]} = -\frac{g(\frac{1}{3}+\frac{r}{2}+\frac{r^2}{6})+r}{v_1[\frac{1}{3}(1+r)g+r]}$$

$$= -\frac{3}{2v_1}\frac{g(\frac{2}{3}+r+\frac{r^2}{3})+2r}{g(1+r)+3r} > -1 \qquad (15j)$$

since $v_1 > 3$ and $r \le 1$.

Equations (15a-j) showed that

$$-1 < q_2 < 1 \quad \text{and} \quad -1 < q_1 < 0$$

since $q_{2max} < -q_{1min} < 1$. Equations (15a-j) also give

$$q_2 \ge 0 \quad \text{if} \quad q_{20} \ge 0, \text{ or } \frac{3}{g} \ge \frac{1}{r^2} - 1, \quad \text{and} \quad q_1 < 0.$$

Therefore, we can obtain

$$-1 \le m_2 \le 1 \quad \text{if} \quad \frac{3}{g} \ge \frac{1}{r^2} - 1 \quad \text{and} \quad -1 \le m_1 \le 1$$

since $m_2' = 2\nu_1 q_2$, $m_1' = 2\nu_1 q_1$, $m_2 = -1$ at $z = -\frac{1}{r}$, $m_2 = m_1 = 1$ at $z = 0$ and $m_1 = 1$ at $z = 1$.

For $\frac{3}{g} < \frac{1}{r^2} - 1$, the plastic hinge previously occurred at $z = 0$ now transfer to the point at $z = -z_0$. The shear forces are

$$q_2 = \frac{g}{8u\nu_1}\left[\ddot{\bar{w}}(-z_0^-) + \ddot{\bar{w}}(z)\right](z_0 + z) \qquad \text{for } -\tfrac{1}{r} \le z \le -z_0^- \tag{16a}$$

$$q_1 = \begin{cases} \frac{g}{8u\nu_1}\left[\ddot{\bar{w}}(-z_0^+) + \ddot{\bar{w}}(z)\right](z_0 + z) & \text{for } -z_0^+ \le z \le 0^- \\ \frac{g}{8u\nu_1}\left[\ddot{\bar{w}}(-z_0^+) + \ddot{\bar{w}}(z)\right](z_0 + z) + \frac{1}{4u\nu_1}\ddot{\bar{w}}(0) & \text{for } 0^+ \le z \le 1 \end{cases} \tag{16b}$$

Equations (3-36) and (16) give

$$q_2 = \frac{g}{8u\nu_1}\left[\ddot{\bar{w}}_3 + \frac{\dot{\bar{w}}_3 \dot{z}_0 r}{(1 - z_0 r)} + \ddot{\bar{w}}_3 \frac{1 + z_0 r}{1 - z_0 r} + \dot{\bar{w}}_3 \dot{z}_0 \frac{(1 + z_0 r) r}{(1 - z_0 r)^2}\right](z_0 + z) \qquad \text{for } -\tfrac{1}{r} \le z \le -z_0^- \tag{17a}$$

$$q_1 = \begin{cases} \frac{g}{8u\nu_1}\left[\ddot{\bar{w}}_3 - \frac{\dot{\bar{w}}_3 \dot{z}_0}{1 + z_0} + \ddot{\bar{w}}_3 \frac{1 - z}{1 + z_0} - \dot{\bar{w}}_3 \dot{z}_0 \frac{(1 - z)}{(1 + z_0)^2}\right](z_0 + z) & \text{for } -z_0^+ \le z \le 0^- \\ \frac{g}{8u\nu_1}\left[\ddot{\bar{w}}_3 - \frac{\dot{\bar{w}}_3 \dot{z}_0}{1 + z_0} + \ddot{\bar{w}}_3 \frac{1 - z}{1 + z_0} - \dot{\bar{w}}_3 \dot{z}_0 \frac{(1 - z)}{(1 + z_0)^2}\right](z_0 + z) + \frac{1}{4u\nu_1}\left[\frac{\ddot{\bar{w}}_3}{1 + z_0} - \frac{\dot{\bar{w}}_3 \dot{z}_0}{(1 + z_0)^2}\right] & \text{for } 0^+ \le z \le 1 \end{cases} \tag{17b}$$

$$q_2' = \frac{g}{4u\nu_1} \frac{1 + z r}{(1 - z_0 r)^2}\left[\ddot{\bar{w}}_3 (1 - z_0 r) + \dot{\bar{w}}_3 \dot{z}_0 r\right] < 0 \qquad \text{for } -\tfrac{1}{r} \le z \le -z_0^- \tag{17c}$$

$$q_1' = \frac{g}{4u\nu_1} \frac{1 - z}{(1 + z_0)^2}\left[\ddot{\bar{w}}_3 (1 + z_0) - \dot{\bar{w}}_3 \dot{z}_0\right] < 0 \qquad \text{for } -z_0^+ \le z \le 1 \tag{17d}$$

$$q_2'' = \frac{g}{4u\nu_1} \frac{r}{(1 - z_0 r)^2}\left[\ddot{\bar{w}}_3 (1 - z_0 r) + \dot{\bar{w}}_3 \dot{z}_0 r\right] < 0 \qquad \text{for } -\tfrac{1}{r} \le z \le -z_0^- \tag{17e}$$

$$q_1'' = -\frac{g}{4u\nu_1} \frac{1}{(1 + z_0)^2}\left[\ddot{\bar{w}}_3 (1 + z_0) - \dot{\bar{w}}_3 \dot{z}_0\right] > 0 \qquad \text{for } -z_0^+ \le z \le 1 \tag{17f}$$

since $$\ddot{\bar{w}}_3 (1 - z_0 r) + \dot{\bar{w}}_3 \dot{z}_0 r = -\frac{12u r^2}{g(1 - z_0 r)} < 0 \tag{17g}$$

and $$\ddot{\bar{w}}_3 (1 + z_0) - \dot{\bar{w}}_3 \dot{z}_0 = -\frac{4u(1 + z_0)^2}{\left[\frac{1}{3} g (1 + z_0)^3 + 1\right]} < 0 \tag{17h}$$

Equations (17c) and (17d) show that the maximum absolute value of shear force q_1 and q_2 occur at the supports $z = -\frac{1}{r}$ and $z = 1$, respectively. They are

$$q_{2max} = \frac{g}{8uv_i}\left[\ddot{w}_3 + \frac{\dot{w}_3 \dot{z}_0 r}{(1-z_0 r)}\right](z_0 - \frac{1}{r}) = \frac{3}{2}\frac{r}{v_i(1-z_0 r)} \qquad (17i)$$

$$q_{1min} = \frac{g}{8uv_i}\left[\ddot{w}_3(1+z_0) - \dot{w}_3 \dot{z}_0\right] + \frac{1}{4uv_i}\frac{1}{(1+z_0)^2}\left[\ddot{w}_3(1+z_0) - \dot{w}_3 \dot{z}_0\right]$$

$$= -\frac{\frac{g}{2}(1+z_0)^2 + 1}{\frac{1}{3}g(1+z_0)^3 + 1} \qquad (17j)$$

Equations (17c) and (17d) also show that $q_2 \geq 0$ and $q_1 \leq 0$ since $q_2 = q_1 = 0$ at $z = -z_0$. Therefore, we can obtain that

$$-1 \leq m_2 \leq 1 \text{ for } -\frac{1}{r} \leq z \leq -z_0 \text{ and } -1 \leq m_1 \leq 1 \text{ for } -z_0 \leq z \leq 1$$

since $m_2 = -1$ at $z = -\frac{1}{r}$, $m_2 = m_1 = 0$ at $z = -z_0$ and $m_1 = -1$ at $z = 1$.

2. Case II, $1 < \nu_1 \leq 3$ and $\nu_2 > 3$

A) Phase 1, shear sliding

a. $0 < t < t_{s1}$

Equations (2c) and (2e), give $q_2' \geq 0$ and $q_1' \geq 0$ with $\dot{z}_2 = \dot{z}_1 = 0$ and $z_1 = 1$, since the accelerations $\ddot{\bar{w}}_1$ and $\ddot{\bar{w}}_2$ which are defined by equations (3-39c) and (3-39d) are positive. $q_2' \geq 0$ and $q_1' \geq 0$ mean that $0 \leq q_2 \leq 1$ and $-1 \leq q_1 \leq 0$ since $q_2 = 0$ in $-\frac{1}{r} \leq z \leq -z_2$, $q_2 = 1$ at $z = 0^-$, $q_1 = -1$ at $z = 0^+$ and $q_1 \leq 0$ at $z = 1$. We can also obtain from $q_2 \geq 0$ and $q_1 \leq 0$ that $-1 \leq m_2 \leq 1$ and $-1 \leq m_1 \leq 1$ since $m_2' = 2\nu_1 q_2$, $m_1' = 2\nu_1 q_1$, $m_2 = -1$ in $-\frac{1}{r} \leq z \leq -z_2$, $m_2 = m_1 = 1$ at $z = 0$ and $m_1 = -1$ at $z = 1$.

b. $t_{s1} \leq t \leq t_{s2}$

For $\frac{3}{2} \leq \nu_1 < 3$

Equations (3-40a-c) give

$$\ddot{\bar{W}}_1 = -\frac{12\mu(1+\nu_1)}{(3+\beta)}, \quad \ddot{\bar{W}}_2 = \frac{\beta}{3}\frac{\mu}{\beta}\nu_1^2 \quad \text{and} \quad z_2 = \frac{3}{\nu_1}. \tag{18a-c}$$

The shear force q_{10} can be obtained from equation (3-5e) with q_{20} = 1 and $\ddot{\bar{W}}_0 = \ddot{\bar{W}}_1$, it equals

$$q_{10} = \frac{\beta\nu_1 - 3}{(3+\beta)\nu_1} \tag{18d}$$

Substituting equations (18) with $\dot{z}_1 = \dot{z}_2 = 0$ and $z_1 = 1$ into equations (1), (2) and (3), we can obtain that

$$0 \leq q_2 \leq 1 \quad \text{and} \quad -1 \leq m_2 \leq 1 \qquad \text{for} \quad -\frac{1}{r} \leq z \leq 0^- \tag{19a,b}$$

since $q_2' \geq 0$ and $m_2' \geq$ in $-\frac{1}{r} \leq z \leq 0^-$, $q_2 = 0$ and $m_2 = -1$ in $-\frac{1}{r} \leq z \leq -z_2$ and $q_2 = 1$ and $m_2 = 1$ at $z = 0^-$; and

$$q_{1min} = -\frac{\nu_1\beta + 3\beta + 6}{2(3+\beta)\nu_1} \geq -1, \quad \text{if} \quad \frac{3}{\beta} \geq \frac{3-\nu_1}{2(\nu_1-1)} \tag{19c}$$

$$m_1' = 2\nu_1 q_{10} - 3\beta(1+\nu_1)(2-z)z/(3+\beta)$$
$$= \frac{1}{(3+\beta)}[2\beta\nu_1 - 6 - 3\beta(1+\nu_1)(2-z)z] \leq 0 \quad \text{if} \quad 2\nu_1 q_{10} \leq 0 \text{ or } \frac{3}{\beta} \geq 4 \tag{19d}$$

since $q_1' \leq 0$, $m_2'' \leq 0$ in $0^+ \leq z \leq 1$.

Equations (18d), (19c) and (19d) show that

$$-1 \leq q_1 \leq 0 \quad \text{and} \quad -1 \leq m_1 \leq 1 \qquad \text{for} \quad 0^+ \leq z \leq 1 \tag{19e,f}$$

if $\frac{3}{g} \geq \nu_1$, since $q_1 \leq 0$, $m_1 = 1$ at $z = 0^+$, $q_{1min} \geq -1$* and $m_1 = -1$ at $z = 1$.

For the following motion, it can be shown that all static admissibility conditions which appear in phase 3 and phase 4 of case I are satisfied provided $\nu_1 > \frac{3}{2}$.

If $\frac{3}{g} < \nu_1$, the shear force distributions are

$$q_2 = \begin{cases} 0 & \text{for } -\frac{1}{\gamma} \leq z \leq -z_2^- \\ \frac{g}{8u\nu_1}\left[\ddot{W}(0^-) + \ddot{W}(z)\right]z + 1 & \text{for } -z_2^+ \leq z \leq 0^- \\ \frac{g}{8u\nu_1}\left[\ddot{W}(z_0^-) + \ddot{W}(z)\right](z - z_0) & \text{for } 0^+ \leq z \leq z_0^- \end{cases} \quad (20a)$$

$$q_1 = \frac{g}{8u\nu_1}\left[\ddot{W}(z_0^+) + \ddot{W}(z)\right](z - z_0) \qquad \text{for } z_0^+ \leq z \leq 1 \quad (20b)$$

Substituting equation (3-41) into equations (20), we obtain

$$q_2 = \begin{cases} 0 & \text{for } -\frac{1}{\gamma} \leq z \leq -z_2^- \\ \frac{g\ddot{W}_2}{8u\nu_1 z_2}(2z_2 + z)z - \frac{g\dot{W}_2 \dot{z}_2}{8u\nu_1 z_2^2} z^2 + 1 & \text{for } -z_2^+ \leq z \leq 0^- \\ \frac{g}{8u\nu_1}\left[\frac{\ddot{W}_2}{z_0}(z^2 - z_0^2) - \frac{\ddot{W}_1}{z_0}(z - z_0)^2 - (\dot{W}_3 - \dot{W}_1)\frac{\dot{z}_0}{z_0^2}(z^2 - z_0^2)\right] & \text{for } 0^+ \leq z \leq z_0^- \end{cases} \quad (21a)$$

$$q_1 = \frac{g}{8u\nu_1}\left[\frac{\ddot{W}_3}{1 - z_0}(2 - z_0 - z) + \frac{\dot{W}_3 \dot{z}_0}{(1 - z_0)^2}(2 - z_0 - z)\right](z - z_0) \quad \text{for } z_0^+ \leq z \leq 1 \quad (21b)$$

Differentiating equations (21a,b), we obtain

---

* We can show that $\nu_1 \geq \frac{3 - \nu_1}{2(\nu_1 - 1)}$ if $\nu_1 \geq \frac{3}{2}$. Therefore, equation (19c) is satisfied, provided $\frac{3}{g} \geq \nu_1$.

$$q_2' = \begin{cases} \frac{g\ddot{W}_2}{4\mu\nu_1 z_2}(z_2+z) - \frac{g\dot{W}_2\dot{z}_2}{4\mu\nu_1 z_2^2} z & \text{for } -z_2^+ \le z \le 0^- \\ \frac{g}{4\mu\nu_1}\left[\frac{\ddot{W}_3}{z_0} z - \frac{\ddot{W}_1}{z_0}(z-z_0) - (\dot{W}_3-\dot{W}_1)\frac{\dot{z}_0}{z_0^2} z\right] & \text{for } 0^+ \le z \le z_0^- \end{cases} \quad (21c)$$

$$q_1' = \frac{g}{4\mu\nu_1}\left[\frac{\ddot{W}_3}{1-z_0} + \frac{\dot{W}_3\dot{z}_0}{(1-z_0)^2}\right](1-z) < 0 \qquad \text{for } z_0^+ \le z \le 1 \quad (21d)$$

$$q_2'' = \begin{cases} \frac{g\ddot{W}_2}{4\mu\nu_1 z_2} - \frac{g\dot{W}_2\dot{z}_2}{4\mu\nu_1 z_2^2} & \text{for } -z_2^+ \le z \le 0^- \\ \frac{g}{4\mu\nu_1}\left[\frac{\ddot{W}_3}{z_0} - \frac{\ddot{W}_1}{z_0} - (\dot{W}_3-\dot{W}_1)\frac{\dot{z}_0}{z_0^2}\right] & \text{for } 0^+ \le z \le z_0^- \end{cases} \quad (21e)$$

$$q_1'' = -\frac{g}{4\mu\nu_1(1-z_0)^2}\left[\ddot{W}_3(1-z_0) + \dot{W}_3\dot{z}_0\right] > 0 \qquad \text{for } z_0^+ \le z \le 1 \quad (21f)$$

Equations (21a-f) give

$$q_{1\min} = -\frac{3}{2\nu_1(1-z_0)} \quad \text{and} \quad -1 \le m_1 \le 1 \quad \text{in } z_0^+ \le z \le 1, \quad (21g,h)$$

since $q_1 = 0$, $m_1 = 1$ at $z = z_0^+$, $m_1 = -1$ at $z = 1$ and $m_1' = 2\nu_1 q_1 < 0$.

The shear forces and bending moments in $-\frac{1}{r} \le z \le z_0^-$ can be obtained from equation (21a) and the following equations

$$m_2 = \begin{cases} -1 & \text{for } -\frac{1}{r} \le z \le -z_2^- \\ \frac{g}{12\mu}\left[\frac{2\dot{W}_2\dot{z}_2}{z_2} + \ddot{W}_2\left(1+\frac{z}{z_2}\right) - \dot{W}_2\dot{z}_2\frac{z}{z_2^2}\right](z+z_2)^2 - 1 & \text{for } -z_2^+ \le z \le 0^- \\ 1 + \frac{g}{12\mu}\left[2\ddot{W}_3 - 2(\dot{W}_3-\dot{W}_1)\frac{\dot{z}_0}{z_0} + \ddot{W}_1 + (\ddot{W}_3-\ddot{W}_1)\frac{z}{z_0} - (\dot{W}_3-\dot{W}_1)\frac{\dot{z}_0 z}{z_0^2}\right](z-z_0)^2 & \text{for } 0^+ \le z \le z_0^- \end{cases} \quad (21i)$$

For $1 < \nu_1 < \frac{3}{2}$, equations (3-44a,c,d) give

$$\ddot{W}_1 = \frac{12\mu}{g}(\nu_1 - 1) > 0 \quad (22a)$$

$$\ddot{W}_2 = -\frac{8\mu(2z_2\nu_1+3)}{4z_2+gz_2^2} < 0 \quad (22b)$$

and $$\dot{W}_2\dot{z}_2 = \frac{12u}{gz_2} + \frac{4u(2z_2v_1+3)}{4+gz_2} \qquad (22c)$$

Substituting equation (22a) with $\dot{z}_1 = 0$ and $z_1 = 1$ into equations (1-3), we obtain

$$-1 \le q_1 < 0,\ q_1' > 0,\ q_1'' > 0 \text{ and } -1 \le m_1 \le 1 \text{ in } 0^+ \le z \le 1 \qquad (23a\text{-}d)$$

since $m_1' = 2\nu_1 q_1$, $q_1 = -1$ and $m_1 = 1$ at $z = 0^+$ and $m_1 = -1$ at $z = 1$.

Equations (1-3) and (22b,c) give

$$q_{2max} = \left(\frac{6}{v_1 z_2} + 4\right) \frac{(12gz_2 + 6gz_2^2v_1 + 12 + 3g^2z_2^2 + 2g^2v_1z_2^3)}{(4+gz_2)(12gz_2 + 6gz_2^2v_1 + 12)} - 1 \qquad (23e)$$

since $$q_2'' < 0 \text{ and } q_{20} = -\frac{\ddot{W}_2}{4uv_1} - 1. \qquad (23f,g)$$

Equation (23e) shows that

$$(q_{2max})_{max} = 2\,\frac{3g\bar{z}_2 + \frac{1}{2}g\bar{z}_2^2v_1 + 3 + \frac{3}{4}g^2\bar{z}_2^2 + \frac{1}{4}g^2\bar{z}_2^3v_1}{5g\bar{z}_2 + 2g\bar{z}_2^2v_1 + 4 + g^2\bar{z}_2^2 + \frac{1}{2}g^2\bar{z}_2^3v_1} - 1 < 1 \qquad (23h)$$

where $\bar{z}_2 = \frac{3}{\nu_1}$ is the position of left side plastic hinge at $t = t_{s1}$, since $(q_{2max})'_{z_2} < 0$. It shows that $q_2 \geq 0$ in $-\frac{1}{r} \leq z \leq 0^-$ if $q_{20} \geq 0$ since $q_2'' < 0$ and $q_2 = 0$ in $-\frac{1}{r} \leq z \leq -z_2$. Therefore, we can obtain

$$0 \le q_2 \le 1 \text{ and } -1 \le m_2 \le 1 \text{ if } q_{20} \ge 0 \text{ or } \frac{6}{g} \ge v_1 z_2^2 \qquad (23i,j)$$

since $m_2' = 2\nu_1 q_2$, $m_2 = -1$ in $-\frac{1}{r} \leq z \leq -z_2$ and $m_2 = 1$ at $z = 0$.

If $r^2 < \frac{1}{2}(\nu_1 - 1)$, it appears for following motion that all static admissibility conditions discussed in phase 3 and phase 4 of case I are satisfied with $z_2 \geq \sqrt{\frac{2}{\nu_1 - 1}}$, $1 < \nu_1 < \frac{3}{2}$ and $r^2 < \frac{1}{2}(\nu_1 - 1)$.

If $r^2 \geq \frac{1}{2}(\nu_1 - 1)$, the shear sliding at $z = 0^+$ continues until $t = t_{s2}$ which defined by equation (3-46f) and the examination of static admissibility condition is similar to that used for $t_{s1} \leq t \leq t_{s2}$. Equations (1), (2), (3) and (3-46b,c) with $\dot{z}_1 = \dot{z}_2 = 0$, $z_1 = 1$ and $z_2 = \frac{1}{r}$ give

$$q_{2max} = \frac{3}{2}\left(\frac{r}{\nu_1}+1\right)\frac{g+2r}{g+3r} - 1 < 1 \qquad (24a)$$

since $\frac{r}{\nu_1} = \frac{1}{\nu_2} < \frac{1}{3}$ and

$$0 \leq q_2 < 1 \quad \text{and} \quad -1 \leq m_2 \leq 1 \quad \text{if } q_{20} \geq 0 \text{ or } \frac{3}{g} \geq \frac{\nu_1}{r^2} \qquad (24b)$$

and $$-1 \leq q_1 < 0 \quad \text{and} \quad -1 \leq m_1 \leq 1 \qquad (24c)$$

It shows that for $t > t_{s2}$ the static admissibility conditions discussed in phase 4 of case I are all satisfied except equation (15j) may not be satisfied when $\nu_1 < 1 + 0.5gr(1+r)/[g(1+r) + 3r]$.

For $\frac{6}{g} < \nu_1 z_2^2$, the shear force distributions are

$$q_2 = \begin{cases} 0 & \text{for } -\frac{1}{r} \leq z \leq -z_2^- \\ \frac{g}{g\nu_1}\left[\ddot{w}(-z_0^-) + \ddot{w}(z)\right](z_0+z) & \text{for } -z_2^+ \leq z \leq -z_0^- \end{cases} \qquad (25a)$$

$$q_1 = \begin{cases} \frac{g}{g\nu_1}\left[\ddot{w}(-z_0^+) + \ddot{w}(z)\right](z_0+z) & \text{for } -z_0^+ \leq z \leq 0^- \\ \frac{g}{g\nu_1}\left[\ddot{w}(0^+) + \ddot{w}(z)\right]z - 1 & \text{for } 0^+ \leq z \leq 1 \end{cases} \qquad (25b)$$

Substituting equations (3-47) into equations (25), we obtain

$$q_2 = \begin{cases} 0 & \text{for } -\frac{1}{r} \leq z \leq -z_2^- \\ \frac{g}{g\nu_1}\left[\ddot{w}_3 + \frac{\dot{\bar{w}}_3 \dot{z}_0}{\dot{z}_2 - \dot{z}_0} + \ddot{w}_3\frac{z_2+z}{z_2-z_0} + \dot{\bar{w}}_3\frac{z_2\dot{z}_0 - \dot{z}_2 z_0 - z(\dot{z}_2 - \dot{z}_0)}{(z_2-z_0)^2}\right](z_0+z) & \text{for } -z_2^+ \leq z \leq -z_0^- \end{cases} \qquad (26a)$$

$$q_1 = \begin{cases} \frac{g}{8\mu v_1}\left[\ddot{w}_3 + (\dot{w}_2 - \dot{w}_3)\frac{\dot{z}_0}{z_0} + (\ddot{w}_2 - \ddot{w}_3)\frac{z}{z_0} + \ddot{w}_2 - (\dot{w}_2 - \dot{w}_3)\frac{\dot{z}_0}{z_0^2} z\right](z_0 + z) & \text{for } -z_0^+ \le z \le 0^- \\ \frac{g}{8\mu v_1}\left[\ddot{w}_1 + \ddot{w}_1(1-z)\right]z - 1 & \text{for } 0^+ \le z \le 1 \end{cases} \quad (26b)$$

Equation (26a) with equations (3-49d,e) give

$$q_{2max} = \frac{3}{2v_1(z_2 - z_0)} \quad \text{and} \quad q_2 \ge 0 \quad \text{in } -\frac{1}{r} \le z \le -z_0^- \quad (26c,d)$$

since $q_2'' < 0$ and $q_2 = 0$ in $-\frac{1}{r} \le z \le -z_2$ and at $z = -z_0^-$. Therefore, we can obtain $-1 \le m_2 \le 1$ in $-\frac{1}{r} \le z \le -z_0^-$, since $m_2' = 2v_1 q_2$, $m_2 = -1$ in $-\frac{1}{r} \le z \le -z_2$ and $m_2 = 1$ at $z = -z_0$.

Differentiating equation (26b) with respect of z, we obtain

$$q_1' = \begin{cases} \frac{g}{4\mu v_1}\left[\frac{\ddot{w}_2}{z_0}(z_0 + z) - \frac{\ddot{w}_3}{z_0} z - (\dot{w}_2 - \dot{w}_3)\frac{\dot{z}_0}{z_0^2} z\right] = \frac{g}{4\mu v_1}\left[-\ddot{w}_1 z + \ddot{w}_2\right] & \text{for } -z_0^+ \le z \le 0^- \\ \frac{g}{4\mu v_1}\ddot{w}_1(1-z) > 0 & \text{for } 0^+ \le z \le 1 \end{cases} \quad (26e)$$

$$q_1'' = \begin{cases} -\frac{g}{4\mu v_1}\ddot{w}_1 < 0 & \text{for } -z_0^+ \le z \le 0^- \\ -\frac{g}{4\mu v_1}\ddot{w}_1 < 0 & \text{for } 0^+ \le z \le 1 \end{cases} \quad (26f)$$

since $\ddot{w}_1 > 0$ and $\ddot{w}_2 < 0$. Equations (26e-f) show that the static admissibility conditions in $-z_0^+ \le z \le 1$ are satisfied since $-1 \le q_1 \le 0$, provided

$$\frac{g}{8\mu v_1}\ddot{w}_1 \le 1 \quad \text{and} \quad \ddot{w}_1 z_0 + \ddot{w}_2 \le 0. \quad (26g,h)$$

Equations (26g,h) must be checked during the numerical calculation.

3. Case III, $0 < \nu_1 \le 1$ and $\nu_2 > 3$

A) Phase 1, shear sliding

a) $0 \le t \le t_{s1}$, equations (1), (2) and (3) with $\dot{z}_1 = \dot{z}_2 = 0$, $q_{10} = -q_{20} = -1$, $\ddot{w}_2 > 0$ and $\ddot{w}_1 = 0$ give

$$0 \le q_2 \le 1 \quad \text{and} \quad -1 \le m_2 \le 1 \qquad \text{for } -\frac{1}{r} \le z \le 0^- \tag{27a,b}$$

$$q_1 = -1 \quad \text{and} \quad -1 \le m_1 \le 1 \qquad \text{for } 0^+ \le z \le 1 \tag{27c,d}$$

since $q_2' > 0$, $q_2'' > 0$, $q_2 = 0$ and $m_2 = -1$ in $-\frac{1}{r} \le z \le -z_2$, $q_2 = 1$ and $m_2 = -1$ at $z = 0^-$, $q_1 = -1$ in $0^+ \le z \le 1$ and $m_1 = 1$ at $z = 0$.

b) $t_{s1} < t \le t_2$, equations (22b,c) and (23e-j) are valid. In other words, we can obtain

$$0 \le q_2 \le 1 \quad \text{and} \quad -1 \le m_2 \le 1 \quad \text{if } q_{20} \ge 0 \text{ or } \frac{6}{g} \ge v_1 z_2^2. \tag{28a,b}$$

It also shows that $q_1 = -1$ and $-1 \le m_1 \le 1$ in $0^+ \le z \le 1$ since $\ddot{\bar{w}}_1 = 0$.

If $\frac{6}{g} < v_1 z_2^2$, the shear force distributions are

$$q_2 = \begin{cases} 0 & \text{for } -\frac{1}{r} \le z \le -z_2^- \\ \frac{g}{8uv_1}\left[\ddot{\bar{w}}(-z_0^-) + \ddot{\bar{w}}(z)\right](z_0+z) & \text{for } -z_2^+ \le z \le -z_0^- \end{cases} \tag{29a}$$

$$q_1 = \begin{cases} \frac{g}{4uv_1}\ddot{\bar{w}}(-z_0^+)(z_0+z) & \text{for } -z_0^+ \le z \le 0^- \\ -1 & \text{for } 0^+ \le z \le 1 \end{cases} \tag{29b}$$

Substituting equation (3-55) with $\ddot{\bar{w}}_3 = \ddot{\bar{w}}_2$ into equations (29), we obtain

$$q_2 = \begin{cases} 0 & \text{for } -\frac{1}{r} \le z \le -z_2^- \\ \frac{g}{8uv_1}\left[\ddot{\bar{w}}_2 + \frac{\dot{\bar{w}}_2 \dot{z}_0}{(z_2 - z_0)} + \ddot{\bar{w}}_2 \frac{z_2+z}{z_2-z_0} + \dot{\bar{w}}_2 \frac{z_2\dot{z}_0 - z_0\dot{z}_2 - z(\dot{z}_2 - \dot{z}_0)}{(z_2 - z_0)^2}\right](z_0+z) & \text{for } -z_2^+ \le z \le -z_0^- \end{cases} \tag{30a}$$

$$q_1 = \begin{cases} \frac{g}{4uv_1}\ddot{\bar{w}}_2(z_0+z) & \text{for } -z_0^+ \le z \le 0^- \\ -1 & \text{for } 0^+ \le z \le 1 \end{cases} \tag{30b}$$

Equation (29a) with equations (3-57) give

$$q_{2max} = \frac{3}{2\nu_1(z_2 - z_0)} \quad \text{and} \quad q_2 \geq 0 \quad \text{in} \quad -\frac{1}{r} \leq z \leq -z_0^- \tag{30c}$$

since $q_2'' < 0$ and $q_2 = 0$ in $-\frac{1}{r} \leq z \leq -z_2$ and at $z = -z_0^-$. Therefore, we obtain $-1 \leq m_2 \leq 1$ in $-\frac{1}{r} \leq z \leq -z_0$ since $m_2 = -1$ in $-\frac{1}{r} \leq z \leq -z_2$, $m_2 = 1$ at $z = -z_0$ and $m_2' = 2q_2\nu_1$ in $-\frac{1}{r} \leq z \leq -z_0^-$.

Equation (29b) with equation (3-57) gives

$$-1 \leq q_1 \leq 0 \quad \text{in} \quad -z_0^+ \leq z \leq 1 \tag{30d}$$

since $q_1 = 0$ at $z = -z_0^+$, $q_1 = -1$ in $0 \leq z \leq 1$ and $\ddot{\bar{w}}_2 < 0$. According to $m_1' = 2\nu_1 q_1$, we can obtain

$$m_1(1) = 1 - \frac{\nu_1}{(g z_0 - 1)}(2 + g z_0^2 + 2 g z_0) \tag{30e}$$

since $m_1 = 1$ at $z = -z_0$ and m_1 is continuous at $z = 0$.

Equation (30e) shows that the velocity profile given by equation (3-55) is only valid when $m_1(1) \geq -1$ or

$$(g z_0 + 1)(1 - \nu_1) \geq \frac{1}{2} g \nu_1 z_0^2 \tag{30f}$$

If equation (30f) is not satisfied, the motion is governed by equations (3-47) and (3-49) and the examination of static admissibility conditions is given in equations (25) and (26).

c. $t_2 < t \leq t_f$, equations (1), (2) and (3) with $\dot{z}_2 = 0$, $z_2 = \frac{1}{r}$ and $\ddot{\bar{w}}_2 < 0$ give

$$q_{2max} = \frac{3}{2}\left(\frac{1}{\nu_2} + 1\right)\frac{(2\nu + g)}{(3\nu + g)} - 1 \quad < 1 \tag{31a}$$

since $\nu_2 > 3$. Therefore, we can obtain that

$0 \leq q_2 < 1$ and $-1 \leq m_2 \leq 1$ if $q_{2_0} \geq 0$ or $\frac{3}{g} \geq \frac{\nu_1}{r^2}$ in $-\frac{1}{r} \leq z \leq 0^-$, (31b,c)

$q_2 = -1$ and $-1 \leq m_1 \leq 1$ in $0^+ \leq z \leq 1$ (31d,e)

since $q_2' > 0$ in $-\frac{1}{r} \leq z \leq 0^-$, $m_2 = -1$ at $z = -\frac{1}{r}$, $m_2 = m_1 = 1$ at $z = 0$, $\ddot{\bar{W}}_1 = 0$ and $\nu_1 \leq 1$.

If $\frac{3}{g} < \frac{\nu_1}{r^2}$, the equations (29) and (30) are still valid if $\dot{z}_2$ and z_2 are replaced by 0 and $\frac{1}{r}$, respectively.

4. Case IV, $1 < \nu_1 \leq \nu_2 \leq 3$

A) Phase 1, shear sliding

a. $0 \leq t \leq t_{s1}$

Equations (1) and (2) with equations (3-61b,c) $\dot{z}_2 = \dot{z}_1 = 0$, $z_2 = \frac{1}{r}$ and $z_1 = 1$ give

$$q_{2_{min}} = 1 - \frac{3}{2}\left(1 - \frac{1}{\nu_2}\right) \leq 1 - \frac{3}{2}\left(1 - \frac{1}{3}\right) = 0 \qquad (32a)$$

$$q_{1_{max}} = -1 + \frac{3}{2}\left(1 - \frac{1}{\nu_1}\right) \geq 0 \qquad (32b)$$

or $q_2 > 0$ in $-\frac{1}{r} < z < 0^-$ and $q_1 < 0$ in $0^+ < z < 1$ since $\nu_1 < \nu_2 < 3$. Therefore, we can obtain

$$0 \leq q_2 \leq 1 \text{ and } -1 \leq m_2 \leq 1 \text{ in } -\frac{1}{r} \leq z \leq 0^-, \qquad (32c,d)$$

$$-1 \leq q_1 \leq 0 \text{ and } -1 \leq m_1 \leq 1 \text{ in } 0^+ \leq z \leq 1 \qquad (32e,f)$$

since $m_2 = -1$ at $z = -\frac{1}{r}$, $q_2 = 1$ and $m_2 = 1$ at $z = 0^-$, $q_1 = -1$ and $m_1 = 1$ at $z = 0^+$, $m_1 = -1$ at $z = 1$, $m_2' = 2\nu_1 q_2$ in $-\frac{1}{r} \leq z < 0^-$ and $m_1' = 2\nu_1 q_1$ in $0^+ \leq z \leq 1$.

b. $t_{s1} < t \leq t_{s1}$

If $v_1 \geq 1 + r$, equations (1), (2) and (3) with $\dot{z}_1 = \dot{z}_2 = 0$, $z_2 = \frac{1}{r}$, $z_1 = 1$, $\ddot{\bar{w}}_1 < 0$ and $\ddot{\bar{w}}_2 > 0$ give

$$0 < q_2 \leq 1 \text{ and } -1 \leq m_2 \leq 1 \text{ in } -\frac{1}{r} \leq z \leq 0^- , \tag{33a,b}$$

$$q_{1min} = \frac{1}{v_1}\,\frac{gv_1 + 3g + 6}{2g + 6} \geq -1 \text{ if } v_1 \geq \frac{3(2+g)}{6+g} \tag{33c,d}$$

and $$-1 \leq m_1 \leq 1 \text{ in } 0^+ \leq z \leq 1 \text{ if } q_{1,0} \leq 0 \text{ or } \frac{3}{g} \geq v_1 \tag{33e,f}$$

since $m_2 = -1$ at $z = -\frac{1}{r}$, $m_2 = 1$ and $q_2 = 1$ at $z = 0^-$, $m_1 = 1$ at $z = 0^+$, $q_1' < 0$ in $0^+ \leq z \leq 1$ and

$$q_{1,0} = 1 + \frac{\ddot{\bar{w}}_1}{4v_1} = 1 - \frac{3(v_1+1)}{v_1(3+g)} \tag{33g}$$

If $\frac{3}{g} < v_1$, the equations (21) are valid when $\dot{z}_2$ and z_2 are replaced by 0 and $\frac{1}{r}$, respectively.

If $v_1 < 1 + r$, equations (1), (2) and (3) with $\dot{z}_2 = \dot{z}_1 = 0$, $z_2 = \frac{1}{r}$, $z_1 = 1$, $\ddot{\bar{w}}_2 < 0$ and $\ddot{\bar{w}}_1 > 0$ give

$$q_{2max} = \frac{3rg + 6r^2 + v_1 g}{2v_1(g+3r)} \leq 1, \text{ if } v_1 \geq \frac{3r(g+2r)}{g+6r} , \tag{34a,b}$$

$$-1 \leq m_2 \leq 1, \text{ if } q_{2,0} \geq 0 \text{ or } \frac{3}{g} \geq \frac{v_1}{r^2} \tag{34c,d}$$

since $q_2' < 0$ in $-\frac{1}{r} \leq z \leq 0^-$, $m_2 = -1$ at $z = -\frac{1}{r}$, $m_2 = 1$ and

$$q_{2,0} = -1 + \frac{3(v_1+r)r}{(3r+g)v_1} \tag{34e}$$

at $z = 0^-$; and

$$-1 \leq q_1 \leq 0 \text{ and } -1 \leq m_1 \leq 1 \text{ in } 0^+ \leq z \leq 1 \tag{34f,g}$$

since $q_1 = -1$ and $m_1 = 1$ at $z = 0^+$, $m_1 = 1$ and $q_1 \leqslant 0$ at $z = 1$ and $q_1' > 0$ in $0^+ \leqslant z \leqslant 1$.

If $\frac{3}{g} < \frac{\nu_1}{r^2}$, equations are valid if $\dot{z}_2$ and z_2 are replaced by 0 and $\frac{1}{r}$, respectively.

B) Phase 2, $t_{s2} < t \leqslant t_f$

The motion is the same as that of phase 4 in case I and equations (14-17) are valid, but equation (15j) is satisfied only when $1 < \nu_1 < 1 + \frac{1}{2} r^2$.

5. Case V, $0 < \nu_1 \leqslant 1$ and $1 < \nu_2 \leqslant 3$

a. $0 \leqslant t \leqslant t_{s1}$

It is clear from equations (1), (2) and (3) that

$$0 < q_2 \leq 1 \text{ and } -1 \leq m_2 \leq 1 \text{ in } -\tfrac{1}{r} \leq z \leq 0^- \qquad (35a,b)$$

$$q_1 = -1 \text{ and } -1 \leq m_1 \leq 1 \text{ in } 0^+ \leq z \leq 1 \qquad (35c,d)$$

since $\dot{z}_2 = \dot{z}_1 = 0$, $z_2 = \frac{1}{r}$, $z_1 = 1$, $m_2 = -1$ at $z = -\frac{1}{r}$, $q_2 = 1$ and $m_2 = 1$ at $z = 0^-$, $q_1 = -1$, $m_1 = 1$ at $z = 0^+$, $\ddot{\bar{w}}_2 > 0$ and $\ddot{\bar{w}}_1 = 0$.

b. $t_{s1} < t \leqslant t_f$

Equations (1), (2) and (3) show that equations (34) are valid except $q_1 = -1$ and $\ddot{\bar{w}}_1 = 0$ in $0^+ \leqslant z \leqslant 1$.

If $\frac{3}{g} < \frac{1}{r^2}$, the equations (30) are valid if $\dot{z}_2$ and z_2 are replaced by 0 and $\frac{1}{r}$, respectively.

6. Case IV, $0 < \nu_1 \leq \nu_2 \leq 1$

It is easy to obtain that

$$q_2 = 1 \quad \text{and} \quad -1 \leq m_2 \leq 1 \qquad \text{in} \quad -\tfrac{1}{\gamma} \leq z \leq 0^- , \tag{36a,b}$$

$$q_1 = -1 \quad \text{and} \quad -1 \leq m_1 \leq 1 \qquad \text{in} \quad 0^+ \leq z \leq 1 \tag{36c,d}$$

since $\ddot{\bar{W}}_1 = \ddot{\bar{W}}_2 = \dot{z}_1 = \dot{z}_2 = 0$.

APPENDIX II

Formulae of maximum permanent deformation of a clamped beam with rectangular cross section struck by a falling body at the centre. Parke's bending only solution [10]

$$\frac{W_f}{H} = \frac{u\ell}{12gH}\left[\frac{g}{1+g} + 2\ln(1+g)\right] \tag{1}$$

Nonaka's formula [12] with influence of finite deflection is

$$\frac{W_f}{H} + \frac{1}{3}\left(\frac{W_f}{H}\right)^3 = \frac{u\ell}{12gH}\left[\frac{g}{1+g} + 2\ln(1+g)\right] \quad \text{for } \frac{W_f}{H} \le 1 \tag{2a}$$

and

$$\frac{W_f}{H} = \sqrt{\left\{\frac{u}{24g}\left[\frac{g}{1+g} + 2\ln(1+g)\right] + \sqrt{1+\left(\frac{\ell}{H}\right)^2} - \frac{2H}{3\ell}\right\}^2 - \left(\frac{\ell}{H}\right)^2} \tag{2b}$$

$$\text{for } \frac{W_f}{H} > 1$$

Jones' formulae [17 or 30] with square yield curves

$$\frac{W_f}{H} = \frac{1}{2}\left(\sqrt{1 + \frac{u\ell(2g+3)}{3(1+g)^2H}} - 1\right) \tag{3a}$$

or

$$\frac{W_f}{H} = \frac{1}{2}\left(\sqrt{1 + \frac{u\ell(2g+3)}{0.618\times 3(1+g)^2H}} - 1\right) \tag{3b}$$

Jones' formula [17] with parabolic yield curve

$$\frac{W_f}{H} + \frac{1}{2}\left(\frac{W_f}{H}\right)^3 = \frac{u\ell(2g+3)}{12(1+g)^2H} \quad \text{for } \frac{W_f}{H} \le 1 \tag{4a}$$

and

$$\frac{W_f}{H} = \sqrt{1 + \frac{2g+3}{12}\left[\frac{u\ell}{(1+g)^2H} - \frac{18}{3+2g}\right]} \quad \text{for } \frac{W_f}{H} > 1 \tag{4b}$$

Oliveira's formulae [20]

$$\frac{W_f}{H} = \left\{1 + \left(\frac{8}{\pi^2}\right)\left(\frac{\frac{2g}{\pi^2}+1}{1+g}\right)^2 \frac{3g}{(3+2g)}\left[\frac{3u\ell}{4(3+2g)H} - \frac{4}{3}\right]\right\}^{\frac{1}{2}} \tag{5}$$

$$\frac{W_f}{H} = \frac{\sqrt{2u\frac{\ell}{H}g}}{\pi(1+g)} \tag{6}$$

$$\frac{W_f}{H} = \sqrt{\frac{3ul}{4(3+2g)H}} - \frac{1}{3} \tag{7}$$

$$\frac{W_f}{H} = \sqrt{\frac{3ul}{\pi(3+2g)H}} - \frac{1}{2} \tag{8}$$

Formulae obtained in Chapter 4

$$\frac{W_f}{H} = \frac{1}{2}\left\{-1+\sqrt{1+\frac{ul}{3gH}\left[\frac{g}{1+g}+2\ln(1+g)\right]}\right\} \tag{9a}$$

or

$$\frac{W_f}{H} = \frac{1}{2}\left\{-1+\sqrt{1+\frac{ul}{0.618\times 3gH}\left[\frac{g}{1+g}+2\ln(1+g)\right]}\right\} \tag{9b}$$